TOPOGRAPHIC AND GEOMORPHOLOGIC ANALYSES OF VOLCANIC AND IMPACT-RELATED LANDFORMS ON EARTH AND MARS

A DISSERTATION SUBMITTED TO THE GRADUATE DIVISION OF THE UNIVERSITY OF HAWAI'I IN PARTIAL FULFILLMENT OF THE REQUIREMENTS FOR THE DEGREE OF

DOCTOR OF PHILOSOPHY

IN

GEOLOGY AND GEOPHYSICS

DECEMBER 2008

By
Aisha Renee Morris

Dissertation Committee:

Peter J. Mouginis-Mark, Chairperson
F. Scott Anderson
Sarah A. Fagents
Scott Rowland
Ross Sutherland

We certify that we have read this thesis and that, in our opinion, it is satisfactory in scope and quality as a dissertation for the degree of Doctor of Philosophy in Geology and Geophysics.

DISSERTATION COMMITTEE

_____
Chairperson

_____

_____

_____

_____

ACKNOWLEDGEMENTS

I will admit it. This process has been the cause of elation and pride at its best and sleepless nights and tears at its worst. It has been a journey through which I have arrived at the end knowing I am stronger and more durable than I thought I was at the beginning. Despite the many challenges I have faced along the way, the support and love from a colorful cast of characters has enabled me to persevere through one of the hardest, yet most rewarding, things I have undertaken thus far.

Jeff Karson, formerly of Duke University, was one of the first people to encourage me to explore the world of geology. He took me on a research dive to the bottom of the ocean in the Alvin submersible, and needless to say, I was hooked.

My committee. Peter Mouginis-Mark, F. Scott Anderson, Sarah Fagents, Scott Rowland, and Ross Sutherland. You all have immeasurable patience and I truly appreciate the time and effort you have put in to my graduate education and preparation for the "real world." Thank you for answering my (oftentimes silly) questions without kicking me out of graduate school. I have learned from all of you.

My friends. Near and far, you have all been amazing in your ability to encourage and support me. Your kind words and simple gestures have not gone unnoticed and have enabled me to balance life and work in a manner that kept me sane. I would especially like to acknowledge the taekwondo crew. It is amazing how things seem to come into perspective when you are able to kick something for an hour.

My family. Thank you for providing me with more love, support and encouragement than I could ever need. I am so blessed to have a family that has never

asked for more than I can do or settled for any less than my best. Thank you for encouraging me despite the 3 a.m. phone calls and thank you for celebrating the triumphs with me, no matter how great or small. You all never cease to amaze me with your strength, thoughtfulness, selflessness and love.

Last, but certainly not least, God. Some people know Him, some people don't. I do, and without Him, I would not have made it through the tears and sleepless nights, or truly appreciated the joys and triumphs. He is my strength.

ABSTRACT

In this work, high-resolution topography and imaging datasets are utilized to illuminate the formation processes of enigmatic surface features on Mars and lava flows on Kilauea Volcano. Thermally distinct craters are identified on a deposit flanking Hrad Vallis, Elysium Planitia, Mars. In THEMIS IR nighttime images, the craters have cool interiors surrounded by warm ejecta haloes and in daytime IR the craters have warm interiors surrounded by cool ejecta, suggesting coarser material in the ejecta than in the surrounding terrain. The craters exhibit varying degrees of concentric fracturing and blocks up to several meters across are visible in HiRISE images. The distribution and morphology of the craters suggest that they are the result of interaction between a hot deposit and ice.

Previous studies of the one-dimensional roughness characteristics of volcanic surfaces indicate that information regarding the formation and evolution of the surface may be gleaned from roughness statistics. In this work, the 1D technique is carried into the second dimension, where roughness statistics are mapped using topography at varying resolutions. Lava flows in Kilauea caldera, emplaced by a variety of processes, provide a useful location to apply the 2D model. The 2D model results indicate that features formed during emplacement and modification of the flows exhibit statistically distinct roughness signatures and provides a tool for unit mapping based on surface roughness.

Four candidate examples of impact melt flows and debris flows have been identified on the southern rim and interior wall at Tooting crater, a young, 29 km diameter impact crater in Amazonis Planitia, Mars. The flows are analyzed using HiRISE, CTX, and THEMIS VIS images, and a stereo-derived HiRISE DEM. The

impact melt flows are fractured on the meter- to decameter scale, have ridged, leveed lobes and flow fronts. The debris flows exhibit varying morphologies, from a channelized, leveed flow with arcuate ridges in the channel, to a rubbly flow with a channel but no obvious levees. Extensive structural failure has modified the northern half of the crater and is interpreted to have caused the destruction of both the volatile-rich wall rock and any impact melt emplaced.

TABLE OF CONTENTS

Acknowledgements iii

Abstract v

List of Tables x

List of Figures xi

Chapter 1. Introduction 1

Figures 11

Chapter 2. Thermally Distinct Craters Near Hrad Vallis, Elysium Planitia, Mars 12

Abstract 13

1. Introduction 14

2. Background 15

3. Data and analysis 17

4. Description of craters 18
   4.1. Thermal properties 18
   4.2. Morphology and ejecta distribution 20
   4.3. Distribution of craters 22

5. Additional quasi-circular features 23
   5.1. Pits and hollows 24
   5.2. "Low-relief features" to north of ridged mountain 25

6. Discussion 26

7. Summary 30

Acknowledgements 31

Tables 32

Figures 33

Chapter 2 Addendum. HiRISE Views of Hrad Vallis Thermally Distinct Craters 45

1. New HiRISE Data 46

2. HiRISE Observations 47
   2.1. Terrain surrounding thermally distinct craters 47
   2.2. Thermally distinct craters 47
   2.3. "Pits" and "Hollows" 49
   2.4. "Low-relief features" north of ridged mountain 50

3. Discussion 50

4. Conclusions 52

Figures 54
Chapter 3. The Roughness of Hawaiian Volcanic Terrains 68
1. Abstract 69
1. Introduction 70
2. Background 72
2.1. Surface Roughness 72
2.2. Lava flow emplacement and volcano dynamics 74
2.3. Summary 75
3. Data 76
3.1. TOPSAR 76
3.2. Airborne LIDAR 77
3.3. Tripod-mounted LIDAR 77
4. Field sites 78
5. Two-dimensional roughness method 81
6. Kilauea results: Application to T-LIDAR, airborne LIDAR and TOPSAR data 85
6.1. Site A 87
6.2. Site B 88
6.3. Site C 89
6.4. Site D 90
6.5. Site E 90
6.6. Site F 91
7. Discussion 92
7.1. Comparison to previous methods 93
7.2. Influence of topography 100
8. Conclusions 102
Acknowledgements 104
Tables 105
Figures 108
Chapter 4. Possible Impact Melt and Debris Flows at Tooting Crater, Mars 121
Abstract 122
1. Introduction 123
2. Geologic Setting of Tooting crater 125
3. Types of flows observed in HiRISE and CTX data 127
3.1. Flow Type 1: Smooth, polygonally fractured material 128
3.2. Flow Type 2: Hummocky and smooth lobes 129
3.3. Flow Type 3: Hybrid lobe (Flow 3) 131

3.4. Flow Type 4: Leveed, ridged, channelized flow (Flow 4) 131
4. Discussion 139
4.1. Two major flow groups 140
4.2. Volatiles 146
4.3. Flow Distribution 148
4.4. Proposed flow formation sequence 150
4.5. Future targeting 153
5. Conclusions 155
Acknowledgements 156
Tables 157
Figures 159
Appendices 177
1. Appendix A: Additional Hrad Vallis Crater Data (Chapter 2) 177
2. Appendix B: Individual Topographic Profiles From Flow 4 (Chapter 4) 182
References 202

LIST OF TABLES

Chapter 2.
Table 1. Thermally distinct crater information……..32

Chapter 3.
Table 1. Hurst exponents derived from 2D and 1D studies……...…..105
Table 2. Y-intercepts derived from T-LIDAR, airborne LIDAR and TOPSAR.106
Table 3. RMS deviations at 1 m from 2D and 1D studies……...……107

Chapter 4.
Table 1. Morphometric data for Tooting crater...…….....157
Table 2. Correlation coefficients for Flow D and Mauna Loa lava flow…….158

LIST OF FIGURES

Chapter 1
Figure 1. Global view of TES-derived albedo and MOLA shaded relief....11

Chapter 2
Figure 1. MOLA shaded relief of Elysium region....33
Figure 2. Viking Orbiter mosaic of Elysium region....34
Figure 3. THEMIS IR images of Craters 11 and 12....35
Figure 4a. MOC images of Crater 11....36
Figure 4b. MOC image of Crater 2....37
Figure 4c. MOC image of Crater 3....38
Figure 5. MOLA profile across Crater 2....39
Figure 6. THEMIS VIS image identifying Craters 1-3....40
Figure 7. THEMIS VIS image identifying Craters 7-10....41
Figure 8. Sketch map of units identified from Viking mosaic....42
Figure 9. MOC image showing portion of lobe extending from main flow unit....43
Figure 10. MOC image of quasi-circular features....44

Chapter 2 Addendum
Figure 11. Viking Orbiter mosaic of Hrad Vallis region....54
Figure 12a. HiRISE image PSP_006881_2145 detailing Crater 1....55
Figure 12b. HiRISE image PSP_006881_2145, ejecta of Crater 1....56
Figure 12c. HiRISE image PSP_006881_2145, ejecta of small crater....57
Figure 13a. HiRISE image PSP_005813_2150 detailing Crater 11....58
Figure 13b,c. HiRISE image PSP_005813_2150, cones and ejecta near Crater 11....59
Figure 13d,e. HiRISE image PSP_005813_2150, surface and rays of Crater 11....60
Figure 14a. HiRISE image PSP_008384_2150 detailing Crater 12....61
Figure 14b, c. HiRISE image PSP_008384_2150, ejecta of Crater 12....62
Figure 15. HiRISE anaglyph of Crater 11....63
Figure 16. HiRISE image PSP_007237_2140 detailing flow lobe....64
Figure 17a. HiRISE image PSP_007672_2155 detailing low-relief features....65
Figure 17b. HiRISE image PSP_007672_2155 detailing low-relief features....66
Figure 17c. HiRISE image PSP_007672_2155 detailing layering in deposit....67

Chapter 3
Figure 1. SRTM shaded relief image of Big Island....108
Figure 2. TOPSAR shaded relief of Kilauea Volcano....109
Figure 3. Airborne LIDAR shaded relief of Kilauea caldera....110
Figure 4. T-LIDAR topographic data....111
Figure 5. Sketch map of Kilauea caldera....112
Figure 6. Representative images of field sites....113
Figure 7. Hurst exponent and y-intercept maps derived from TOPSAR....114
Figure 8. Hurst exponent and y-intercept maps derived from airborne LIDAR....115
Figure 9. Site A Hurst exponent and y-intercept maps from T-LIDAR....116

Figure 10. Deviograms of six field sites at three dataset resolutions 117
Figure 11. Deviograms of field areas described in text 118
Figure 12. Comparison of RMS deviation, Hurst exponent and cell size 119
Figure 13. Comparison of Hurst exponent for decreasing deviogram sizes 120

Chapter 4
Figure 1. THEMIS VIS mosaic of Tooting crater.....159
Figure 2. CTX image of Tooting crater cavity and immediate rim.....160
Figure 3. HiRISE image detailing fractured flows on southern rim.....161
Figure 4. Stereo-derived DEM of southern rim 162
Figure 5. HiRISE image detailing overhang of fractured flows and rubbly flow.....163
Figure 6. HiRISE image detailing near-rim lobate flows 164
Figure 7a. HiRISE image detailing Flow 2 and related flows 165
Figure 7b, c. HiRISE image detailing Flow 2 and related flows 166
Figure 8. HiRISE image detailing Flow 3 167
Figure 9. HiRISE image detailing proximal and distal regions of Flow 3 168
Figure 10. HiRISE image detailing Flow 4.....169
Figure 11. Stereo-derived DEM of Flow 4 170
Figure 12. Graphs of elevation vs. channel morphometry of Flow 4.....171
Figure 13. Graphs of Flow 4 whole flow and channel morphometry 172
Figure 14. Maps of Flow 4 surface roughness characteristics 173
Figure 15. Pyroclastic deposits from Mt. St. Helens compared to Flow 3 174
Figure 16. Comparison of Flow 4 and Flow 2 175
Figure 17. Graphs of Flow 4 whole flow and channel morphometry vs. gradient....176

CHAPTER 1. INTRODUCTION

The primary focus of this work is to utilize newly available remote sensing data and terrestrial field studies to understand enigmatic geological features on Mars. Mars is a terrestrial planet that has experienced a range of geological processes, similar to the Earth, and although the environment is not currently Earth-like, the planet's surface bears evidence of an active geological history [Greeley and Guest, 1987; Scott and Tanaka, 1986; Tanaka and Scott, 1987]. Large volcanic centers are observed, including shield volcanoes not unlike Hawaiian shield volcanoes. From remote spectroscopic studies of the surface [Bandfield et al., 2000] correlated with studies of meteorites from Mars [Hamilton et al., 2003], as well as in situ rover spectroscopic investigations [McSween et al., 2004], researchers have determined that the surface is primarily basaltic. In addition to the large central volcanic structures, such as Olympus Mons, Alba Patera and Elysium Mons (Figure 1), extensive lava plains have been identified in several regions of the planet [Greeley and Guest, 1987; Scott and Tanaka, 1986].

The Vallis Marineris, a vast canyon system, dissects the surface of the planet just east of the Tharsis rise, a large structural and volcanic center that straddles the equator

(Figure 1). Whereas large outflow channels provide evidence for catastrophic releases of liquid water in the Hesperian [Carr, 1979], valley networks in the highly cratered Noachian-aged highlands suggest liquid water was physically stable on the surface some time in the distant past [Carr and Clow, 1981; Malin and Edgett, 2003], primarily prior to the end of the late heavy bombardment (2.8-3.8 Gyr BP) [Gulick and Baker, 1989]. This observation has been used to argue for a warmer, wetter Mars early in the history of the planet [Craddock and Howard, 2002]. However, the role of volatiles in the history of the planet [Baker, 2001; McEwen et al., 2007b] is still under investigation. The role of volatiles in valley network formation [Ansan et al., 2008], impact cratering processes [Osinski, 2006], and volcanic processes [Fagents et al., 2002; Hort and Weitz, 2001] is a primary focus of recent studies. High spatial resolution, temporally varying image data and topography studies have shown evidence for recent, episodic seepage of water within gullies on Mars [Malin and Edgett, 2000; Malin et al., 2006; Pelletier et al., 2008]. The timing, distribution and state of water has been an active topic in the Mars community [McEwen et al., 2007b; Okubo and McEwen, 2007; Osinski, 2006].

Here I provide some evidence from enigmatic features on the Martian surface for the presence of liquid water in the geologically recent (late Amazonian) time. Using high resolution panchromatic imaging data, thermal infrared data and field techniques, my studies range from the formation of enigmatic craters on a young sedimentary deposit flanking an outflow channel in the northern lowlands (Chapter 2: Hrad Vallis), to the development of a terrain analysis technique using two-dimensional quantification of surface roughness of lava flows on Kilauea Volcano (Chapter 3), to the morphological and surface roughness analysis of newly identified flow features on an extremely young,

nearly pristine impact crater on Mars (Chapter 4: Tooting crater). At first glance, these studies may appear widely disparate, yet as will be discussed in the following section, they are all related to the ongoing study of surface processes on terrestrial planets, and Mars in particular.

Two of my dissertation chapters deal with the role of volatiles in shaping the surface we see today. The history of water on Mars is a complicated story, as water is unstable in liquid form at the current obliquity (~25º) [Head et al., 2003; Ward, 1992] and under current atmospheric conditions [Carr and Clow, 1981]. Nevertheless, we see obvious evidence that water flowed on the surface in the past, such as large-scale outflow channels in Chryse Planitia [Ivanov and Head, 2001] and Elysium Planitia [Russell and Head, 2003], as well as relatively high order (maximum Strahler order of 5) drainage systems such as in the Aeolis region [Ansan et al., 2008] within Terra Cimmeria (Figure 1). In addition to evidence that water flowed on the ancient surface of Mars, there is also evidence from the Gamma Ray Spectrometer onboard the Mars Odyssey spacecraft that water is present in the subsurface today, particularly at high latitudes [Boynton et al., 2002]. Furthermore, while imaging the Martian surface, the Mars Orbiter Camera (MOC) has observed changes in the appearance of gully features between images obtained seven years apart, hinting that even today, given suitable conditions, liquid water may still flow on the surface in short bursts [Malin et al., 2006].

In Chapter 2, I examine possible formation processes for enigmatic craters in a proposed mud deposit in the Elysium volcanic region of Mars (Figure 1). Hrad Vallis is a large channel located to the northwest of the Elysium rise. A lobate deposit proposed to be a large mudflow that formed as a result of volcano-ice interaction flanks the source

region [De Hon et al., 1999; Wilson and Mouginis-Mark, 2003]. Within the deposit are 12 enigmatic craters that lack raised rims, exhibit extensive concentric fracturing, and display distinct thermal signatures in Thermal Emission Imaging System (THEMIS) infrared (IR) data. Using MOC images [Malin et al., 1992], THEMIS IR and visible images (VIS) [Christensen et al., 2004] and Mars Orbiter Laser Altimeter (MOLA) topography [Zuber et al., 1992], I examine the morphology, thermal characteristics and topography of the craters and associated ejecta. I determine that the craters likely formed as the result of explosions within the mudflow due the interaction of the hot mudflow with a frozen, volatile-rich substrate. This initial study was published in the journal *Icarus* in February of 2006 as Morris and Mouginis-Mark, and since the initial publication, the High Resolution Imaging Science Experiment (HiRISE) onboard the Mars Reconnaissance Orbiter spacecraft [McEwen et al., 2007a] has acquired images covering two of the thermally distinct craters and a portion of the proposed mudflow at spatial resolutions of 25 cm/pixel. These additional data provide views of the surface of the mudflow, crater ejecta and fractures surrounding the central depressions of the craters, and I have added an addendum following Chapter 2 describing the new results. The new HiRISE data provide additional evidence for ejecta surrounding the thermally distinct craters. Meter-scale boulders surround the depressions and are nearly absent from the surfaces beyond the ejecta haloes. In addition, small channels are observed emanating from features identified as rays in Chapter 2, consistent with the hypothesis that volatiles were involved in the formation of the thermally distinct craters.

The history of Mars is diverse in volcanic structures and eruption products [Mouginis-Mark et al., 1992; Plescia, 2004]. Work on terrestrial basaltic volcanoes has

demonstrated how the type of eruption products observed on a volcanic construct give insight into the internal volcano dynamics. Terrestrial studies have determined that explosive volcanism (fragmentation of the melt) is typically driven by magmatic volatiles [Morrissey and Mastin, 2000; Vergniolle and Mangan, 2000] and effusive lava flows result from less energetic release of magma [Kilburn, 2000]. Additionally, work by Rowland and Walker [1990] indicates that pahoehoe flows on Kilauea and Mauna Loa, on the Big Island of Hawaii, are typical of an open conduit system where magmatic gases decouple from the melt, resulting in long periods of sustained flow at low volumetric rates. In contrast, the 'a'a flows on these volcanoes are inferred to be the products of high discharge rates from the vent, likely due to the rapid release of volume from the subsurface magma storage chamber [Rowland and Walker, 1990]. Remote determination of whether an extraterrestrial lava flow exhibits characteristics typical of a pahoehoe flow or more closely resembling an 'a'a flow may provide information regarding the dynamics of the associated volcanic edifice or flow field. Previous terrestrial studies have exploited the use of high-resolution topography to calculate the surface roughness of lava flows for the purpose of extracting information regarding formation processes from the characteristic surface roughness [Campbell and Shepard, 1996; Shepard et al., 1995; Shepard and Campbell, 1999; Shepard et al., 2001]. These techniques have been applied to Mars using the MOLA data, although information regarding the meter-scale surface roughness of individual flows and flow fields is not available due to the resolution of the MOLA shots (300 m between shots along-track) [Campbell et al., 2003; Kreslavsky and Head, 2000]. HiRISE is providing unprecedented views of the surface of Mars at spatial resolutions of 25 cm/pixel. In addition to wide-coverage, high-resolution images, HiRISE

is also obtaining stereo observations of the surface of Mars, allowing high-resolution stereo-derived topographic data to be generated using MOLA shots to obtain absolute elevations [McEwen et al., 2007a].

In Chapter 3, in anticipation of these high spatial and vertical resolution stereo-derived topographic data, particularly over varying volcanic surfaces, I perform a multi-resolution topographic study of sample flow surfaces in Kilauea caldera, Hawaii, in order to quantitatively examine the association between surface roughness and known formation processes on a shield volcano. I focus on potential terrestrial analogs for young volcanic terrains on Mars. I use TOPSAR (10 m/pixel), airborne LIDAR (1 m/pixel) and tripod-mounted LIDAR (2-3 cm/pixel) data to calculate the scale-dependent surface roughness of six field sites on Kilauea caldera. I build upon previous studies that utilized one-dimensional profiles of these field sites to calculate scale-dependent surface roughness statistics in order to correlate these values with known flow emplacement mechanisms. I advance this method by developing a two-dimensional technique to calculate the surface roughness statistics from digital elevation models (DEMs) to provide a map view of roughness and roughness scaling properties. I correlate these roughness statistics with the known formation mechanism (determined from published literature and fieldwork) and the previous 1D results. This work is currently in press in the *Journal of Geophysical Research-Planets* as Morris, Anderson, Mouginis-Mark, Haldemann, Brooks and Foster.

Geomorphologic and topographic studies of the present surface provide clues to the history of water on Mars [Carr, 1996]. The impact cratering process excavates materials located at depth, potentially allowing for the emplacement of wet ejecta on the

surrounding landscape [Strom et al., 1992]. Identifying a large pristine impact crater and associated ejecta may allow the state of water to be inferred at the time of impact. To date, no definitive evidence for water reaching the surface during the terminal phase(s) of this process has been documented [Barlow and Perez, 2003]. In Chapter 4, I present geomorphic evidence (observations of lobate flows) that suggests that water was close to the surface in the recent past. I study recently identified flow features on an extremely young crater on Mars [Mouginis-Mark et al., 2007]. Tooting crater (Figure 1) fits the criteria of being large and very young, and is located just west of the Olympus Mons aureole, on relatively featureless layered basaltic flows in the Amazonis Planitia [Mouginis-Mark and Garbeil, 2007]. Tooting crater is a multi-layered ejecta crater, and the formation of this type of ejecta morphology has been an ongoing debate in the cratering community [Barlow et al., 2000; Barlow and Perez, 2003]. The debate concerns the mechanism for fluidization of the discrete ejecta lobes within the ejecta blanket [Barlow et al., 2000]. One hypothesis proposes that the fluidization of the ejecta lobes is a result of the interaction between volatiles in the target material and the impact ejecta [Carr et al., 1977; Mouginis-Mark, 1979]. The competing hypothesis proposes that interaction between the atmosphere and impact ejecta produces the multi-layered ejecta blankets [Barnouin-Jha and Schultz, 1998; Schultz and Gault, 1979]. I address these hypotheses by analyzing flow features observed in recent high-resolution image data. Recent HiRISE (25 cm/pixel) [McEwen et al., 2007a] and Context Imager (CTX, 6 m/pixel) [Malin et al., 2007] images are providing unprecedented views of the morphology and high-resolution topography of this young impact crater, and changing the way we understand the details of crater formation on Mars. The technique developed

in Chapter 3 provides a useful tool for examining the surface roughness characteristics of one flow in particular. One theoretical study of terrestrial impact structures hypothesized that the more volatile-rich a target, the less likely impact melt would be preserved after an impact event, particularly on Mars [Kieffer and Simonds, 1980]. In contrast, Tooting crater appears to have evidence for the existence of coeval impact melt and debris flows, suggesting that a volatile-rich target was capable of producing and preserving both volatile-rich flows and coherent impact melt sheets. In addition, the discovery of these flows has also provided evidence to support the interaction of target volatiles with impact ejecta as the primary fluidization mechanism forming multi-layered ejecta blankets on Mars. The work presented in Chapter 4 will soon be submitted for publication as Morris and Mouginis-Mark.

The preceding description of the work performed for the completion of this dissertation suggests that this work has contributed to the understanding of surface roughness of lava flows on Earth, with applications to other terrestrial planetary bodies. The technique applied in Chapter 3 is applicable to any topographic dataset, from bathymetry data of coral reefs, to global studies of possible climate effects on Mars, to centimeter-scale studies of lava flow surfaces. In addition to terrestrial applications, I anticipate that the results of the surface roughness study will be useful in terrain analysis on Mars as high-resolution stereo-derived topographic datasets from HiRISE become increasingly available.

In addition to surface roughness studies, this work has contributed to our knowledge of the distribution of volatiles in the shallow subsurface of Mars. The identification of explosion craters within a mudflow deposit suggests that not only was

the mudflow at a significantly higher temperature than the substrate, but also that volatiles were available in the shallow subsurface at the time of flow emplacement. The presence of coeval debris flows and impact melt on Tooting crater, an extremely young impact crater, suggests that many more Martian craters may have had these features at the time of formation, but the evidence has since been destroyed.

Future research avenues will provide additional information for these topics. For instance, the recent and ongoing acquisition of HiRISE images will enable detailed morphologic and morphometric studies of the thermally distinct craters. What is the morphology of the crater floors compared to the surrounding terrain? Are there similar craters observed in other regions of the planet? What are the similarities and differences among these crater populations, particularly at the meter scale? Is there a global trend regarding the distribution of thermally distinct craters and the associated deposits? At the meter scale, do we see ejecta around all of the craters? Will a fracture analysis provide information regarding the formation of the thermally distinct craters?

Additionally, questions remain regarding the state and nature of the proposed volatiles at Tooting crater. What is the relative chronology among the varying lobate flows on the outer rim and interior wall of Tooting crater? Additionally, what is the chronology of the flow features relative to the impact cratering event? What state were the proposed volatiles in at the time of the impact event? Are there other craters on the surface of Mars that contain flow features similar to those identified on Tooting crater?

As described above, many questions regarding the evolution of the surface of terrestrial planets still remain. I hope that this work will aid in future avenues of research in terrain analysis on Earth, on Mars and the other terrestrial planets. For example, the

data returning from the Messenger mission to Mercury hold promise for new directions in which to take terrain analysis techniques. In particular, evidence of volcanism has recently been identified on the surface of Mercury. Application of the surface roughness method described in Chapter 3 to the Mercury Laser Altimeter topography data may enable researchers to understand the nature of the volcanic products on the surface of Mercury.

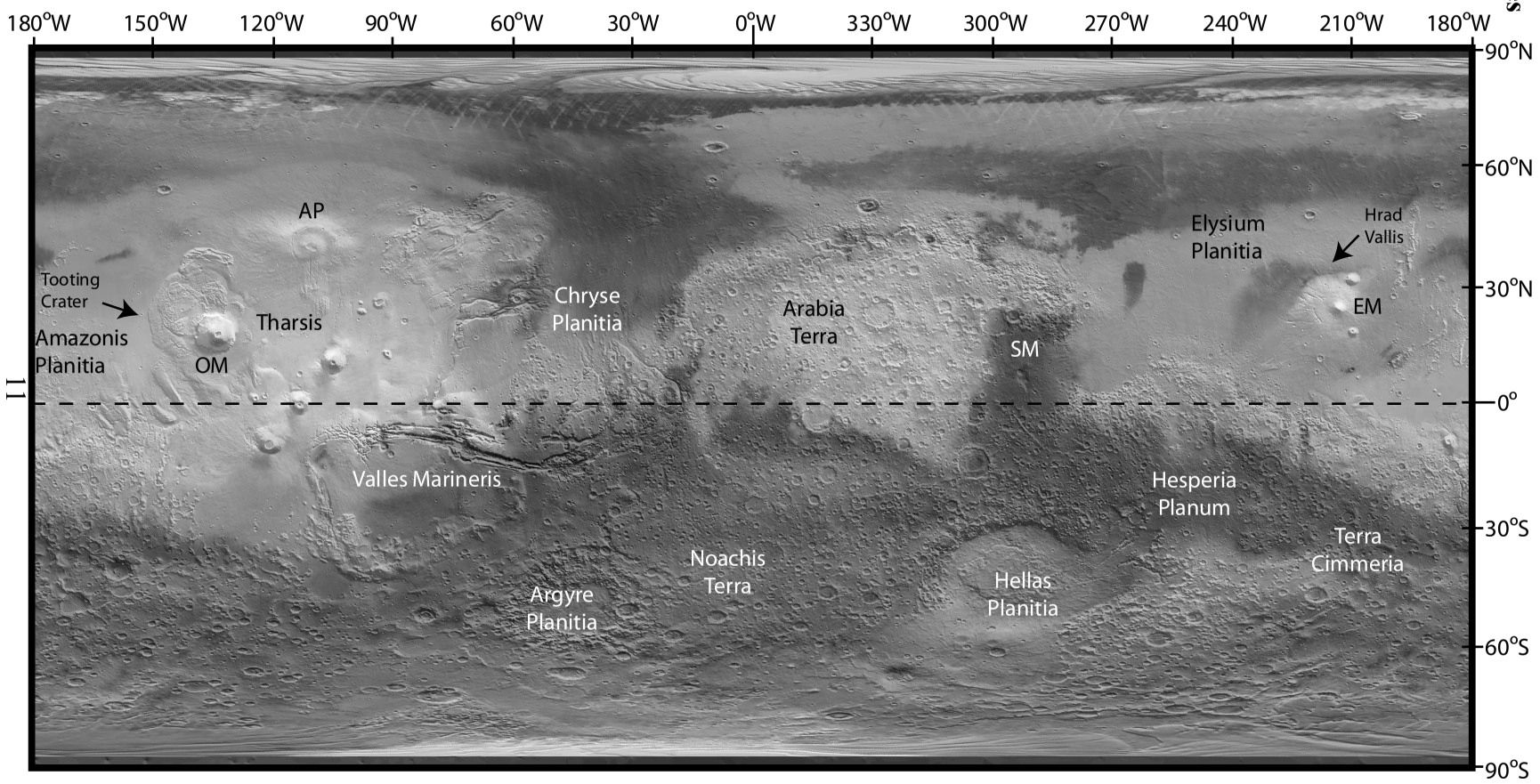

Figure 1. Simple cylindrical map of Mars showing Thermal Emission Spectrometer (TES) albedo over Mars Orbiter Laser Altimeter (MOLA) shaded relief [Christensen et al. 2001]. Data are gridded at 8 pixels per degree, resulting in a grid cell size of 7.5 km. Major terrains are labeled. OM: Olympus Mons, AP: Alba Patera, SM: Syrtis Major, EM: Elysium Mons. The locations of Hrad Vallis (Chapter 2) and Tooting crater (Chapter 4) are identified by arrows.

CHAPTER 2. THERMALLY DISTINCT CRATERS NEAR HRAD VALLIS, ELYSIUM PLANITIA, MARS

Published in its present form as Morris, A. R. and P. J. Mouginis-Mark (2006), Icarus, 180, 335-347.

Abstract

Evidence of volcano-ground ice interactions on Mars can provide important constraints on the timing and distribution of Martian volcanic processes and climate characteristics. Northwest of the Elysium Rise is Hrad Vallis, a ~370 m deep, 800 km long sinuous valley that begins in a source region at 34ºN, 218ºW. Flanking both sides of the source region is a lobate deposit that extends ~50 km perpendicular from the source and is an average of ~40 m thick. Previous studies have suggested the formation of the Hrad Vallis source region was the result of explosive magma-ice interaction and that the lobate deposit is a mudflow; here we use newly available MOLA, MOC and THEMIS data to investigate the evidence supporting this hypothesis. Within the lobate deposit we have identified 12 craters with thermal infrared signatures and morphologies that are distinct from any other craters or depressions in the region. The thermally distinct craters are distinguished by their cool interiors surrounded by warm ejecta in the nighttime THEMIS IR data and warm interiors surrounded by cool ejecta in the daytime THEMIS IR data. The craters are typically 1,100-1,800 m in diameter (one crater is ~2,300 m across) and 30-40 m deep, but may be up to 70 m. The craters are typically circular and have central depressions (several with interior dune fill) surrounded by ~1 to >6 concentric fracture sets. The distribution of the craters and their morphology suggests that they are likely the result of the interaction between a hot mudflow and ground ice.

1. Introduction

The search for, and documentation of, evidence for volcano-ice interactions on the surface of Mars has been a primary focus in Martian volcanology studies for many years. Many different unusual features on the planet have been suggested to be evidence for the interaction of hot volcanic material and near-surface ground ice [Allen, 1979; Chapman et al., 2000; Fagents et al., 2002; Mouginis-Mark, 1985]. Northwest of the Elysium Rise is a region covered by extensive deposits thought to be the result of widespread volcano-ground ice interactions [Christiansen, 1989; Mouginis-Mark, 1985; Russell and Head, 2003].

Hrad Vallis, a ~370 m deep, 800 km long sinuous valley, begins in a source region located at 34ºN, 218ºW (Figure 1). The source region is flanked by a geologically unique feature on Mars, a lobate deposit that extends a maximum of ~50 km from the source (Figure 2) [Wilson and Mouginis-Mark, 2003]. Within the deposit is a population of craters that exhibit distinct characteristics in the thermal infrared. Previous investigations have proposed that the craters are the result of the interaction of a hot mudflow deposit and cold substrate, or the explosive release of volatiles from within a hot mudflow [De Hon et al., 1999; Wilson and Mouginis-Mark, 2003]. A study by De Hon [1992] suggested that the landscape surrounding the source region of Hrad Vallis may be the result of karstification or thermokarst activity. The origin of the craters appears to be intimately linked with the origin of the deposit surrounding the Hrad Vallis source region. Constraining crater origin, the subject of this study, will therefore aid in

the interpretations of the Hrad Vallis region, a terrain interpreted to be the result of extensive volcano-ice interaction.

2. Background

The terrain surrounding the source area for Hrad Vallis is geologically distinct from the surrounding landscape. The region is characterized by unusual flow-like deposits and channel systems that extend radially from the slopes of the Elysium Rise [Christiansen, 1989]. Various formation mechanisms have been proposed for Hrad Vallis based on observations from Viking Orbiter [Christiansen, 1989; De Hon, 1992; De Hon et al., 1999; Wilson and Mouginis-Mark, 2003] and Mars Orbiter Camera (MOC) images and Mars Orbiter Laser Altimeter (MOLA) topography [Wilson and Mouginis-Mark, 2003].

Previous studies have examined the Hrad Vallis region and noted the unique morphology of the deposit that surrounds the source area. Based on photogeologic mapping of Viking Orbiter images, early workers postulated that the formation of the northwest Elysium deposits occurred as heat associated with magmatism within Elysium Rise released subsurface volatiles, generating mega-lahars that traveled down slope toward the northern lowlands [Christiansen, 1989; Christiansen and Greeley, 1981]. Mouginis-Mark et al. [1984] described the regional geology of Elysium Planitia and identified plausible morphological evidence for volcano-ground ice interactions by analyzing Viking Orbiter data. This evidence includes the diversity of crater morphology, presence of knobby and chaotic terrain, and possible explosive behavior of Hecates Tholus [Mouginis-Mark et al., 1984]. Mouginis-Mark [1985] examined the Elysium Planitia region, including Hrad Vallis, to determine the origin for a range of enigmatic

features such as collapse pits and anomalous craters. Based on geomorphologic interpretations of Viking Orbiter images, Mouginis-Mark [1985] proposed interaction between subsurface volatiles and volcanic heat as a potential source for the features, although he acknowledged that the craters could potentially be impact craters formed after the initial emplacement of the mudflow forming the region around Hrad Vallis.

De Hon [1992] studied the Hrad Vallis region to gain insight into the formation mechanism of the channel and the landscape surrounding the depression. He suggested a formation by karstification or thermokarst processes in the substrate of the region leading to collapse of the surface. In this model, elongation and coalescence of the collapse troughs along structural trends lead to formation of composite valleys. Subsequent prolonged release of water into the valley formed by non-fluvial processes results in formation of an incised channel on the floor of the valley. De Hon [1992] proposed the fractured, chaotic terrain and mudflow material near the head of the valley suggest thixotropic behavior of saturated, clay-rich materials. However, De Hon [1992] did not directly address the anomalous craters within the deposit surrounding the Hrad Vallis source region.

Using high-resolution MOC images in conjunction with MOLA topographic data, Wilson and Mouginis-Mark [2003] re-examined the Hrad Vallis region to further constrain the formation mechanism for the depression and the deposit surrounding the source region. MOLA altimetry provided topographic data from which they noted the estimated thickness of the deposit was an average of 40 m, although it is likely as thick as 80 m on the western side of Hrad Vallis and possibly 25 m thick on the eastern side. Wilson and Mouginis-Mark [2003] suggested the variation in flow thickness was the

result of the flow traveling a greater distance to the east from the source region. After noting the presence of a greater number of crater features than would be expected on the deposit (the overlying unit has many craters while the underlying unit has relatively few), they attempted to explain the anomalous craters as phreatic or phreatomagmatic explosion craters within a mud deposit generated during the formation of the Hrad Vallis source region ([Wilson and Mouginis-Mark, 2003]; their Figure 6). This model suggests that the craters result from explosions due to rapid heating and explosive release of ice or water contained within the hot mudflow deposit or within an ice-rich substrate.

Several of the aforementioned studies noted the presence of distinct craters within the flow deposit (Figure 2) that appear to have been formed by processes other than impact cratering and proposed origins potentially related to the emplacement of a smooth deposit bounding the source region of Hrad Vallis [Mouginis-Mark, 1985; Mouginis-Mark et al., 1984; Wilson and Mouginis-Mark, 2003]. Presently, no models exist to explain the formation of these distinct craters. The primary goal of the current study is to assess possible formation mechanisms for the craters by way of a geomorphologic and topographic examination utilizing a variety of data that have become available since the earlier studies.

3. Data and analysis

To understand the origin of the craters, we used publicly available MOLA profiles and MOC images, Thermal Emission Imaging System visible wavelength (THEMIS VIS), and day and night THEMIS infrared (THEMIS IR) image data, which provide insight into the topographic, morphologic and thermal properties of craters in the Hrad

Vallis region. We were unable to use compositional data from the THEMIS instrument due to the perennially cold temperatures in the middle latitudes where Hrad Vallis is located [Christensen et al., 2004]. The MOLA, THEMIS and MOC data were inspected for evidence consistent with any one of four different processes: (1) impact cratering, (2) a formation resulting from collapse, (3) by explosive activity within the flow deposit (which may be a mudflow), or (4) a combination of these processes. In this study, a "thermally distinct" crater is defined as a crater having a warm interior surrounded by a cool halo relative to the surrounding terrain in the daytime IR and a low-temperature interior surrounded by a high temperature halo relative to the adjacent surfaces in the nighttime IR data (Figure 3). The thermally distinct craters appear to have temperature characteristics that are different from both the surrounding terrain and other obvious impact craters in the region. The relative temperatures acquired from the THEMIS IR images are discussed in the following section.

4. Description of craters

4.1. Thermal properties

Previous studies of thermally distinct impact craters have been conducted using low spectral resolution, high spatial resolution Termoskan data obtained during the Phobos '88 mission to Mars [Betts and Murray, 1993]. The Termoskan instrument was a two-band scanning radiometer with one band in the visible wavelengths at 0.5-1.0 μm and one band in the thermal infrared at 8-12 μm. The thermal data used in the study had resolutions of 1.8 km/pixel and 300 m/pixel [Betts and Murray, 1993]. Betts and Murray [1993] examined the thermal character of crater ejecta on the plains near Valles Marineris

and identified a strong dependence on Hesperian terrains for the presence of thermally distinct ejecta blankets. The study indicated that ejecta blankets distinct in the thermal infrared (EDITH) were spatially or temporally dependent on terrains of Hesperian age. The EDITH craters exhibited varying thermal relationships with the surrounding terrain, where some ejecta appeared warmer than the surrounding terrain and other ejecta blankets were cooler. Betts and Murray [1993] concluded that the EDITH craters were the result of exhumation of thermally distinct material of Noachian age from beneath a younger, thinner layer of Hesperian aged material.

In our study, the primary criterion used to define the crater dataset is the thermal properties of the craters. By definition, all the craters included in our sample have distinct thermal properties in the thermal infrared data. The thermally distinct craters at Hrad Vallis are characterized by ejecta blankets that consistently appear cooler than the surrounding material in the daytime IR and warmer than the surrounding material in the nighttime IR. Of the craters covered by THEMIS VIS or MOC data, some with IR signatures have visible ejecta, while others do not appear to have ejecta in the visible wavelength images (Table 1). In the THEMIS nighttime IR brightness temperature data, the innermost regions of the craters are relatively cooler than the surrounding terrain, while the crater ejecta are relatively warmer than the surrounding terrain (Figure 3). Christensen et al. [2003] suggested that the cool daytime and warm nighttime ejecta on the rims of the craters are typical of a surface that is either blockier than the surroundings or more highly indurated than the surrounding terrain, while the low-temperature nighttime IR signature of the central portion of the craters is characteristic of a dusty or fine-grained material. In contrast, typical examples of impact craters in the region are

characterized by ejecta that appear warm in the daytime IR and cool in the nighttime IR. A total of 12 craters have these unusual attributes at Hrad Vallis and they will be discussed in detail in the following sections.

4.2. Morphology and ejecta distribution

The measured crater diameters are typically ~1,100-1,800 m (Table 1), although Crater 11 is ~2,300 m (Figure 4a). The typical crater morphology includes a central depression surrounded by concentric fractures and faults resulting in disrupted terrain on the outside of the central region (Figure 4). The majority of the craters have a double-ring center, characterized by a coherent inner raised ring within the central depression. Where MOLA profiles cross the craters, the outer rims of the craters do not have raised rims and the central portions of the craters appear to be ~30-40 m deep, but may be as much as 70 m deep (Figure 5, Appendix A: Figures 3 and 4). The THEMIS VIS and MOC data also do not show raised rims on the craters. The lack of raised rims is potentially indicative of a non-impact origin for the thermally distinct craters. Crater ejecta are evident in the visible wavelength on the outer rims of the three craters covered by MOC images and some of the craters covered by THEMIS VIS data. On the craters where ejecta are obvious in the visible wavelengths, the ejecta blankets typically reach radial distances of 400-1,000 m from the rims of the craters (Appendix A: Figures 1 and 2). Although not all of the thermally distinct craters have visible ejecta, in the THEMIS nighttime IR their defining thermal ejecta signatures typically extend ~2/3 of a crater radius away from the crater rim.

Variations in dune population, degree of fracturing, and ejecta morphology are visible at THEMIS VIS and MOC resolutions (~19 and 1.5-6.44 m/pixel, respectively) (Figure 4). The majority of the interior depression and the area between the fractures within Crater 2 is covered by dune fields, while only the innermost region of Crater 11 is sparsely covered in dunes and the dune population in Crater 3 is intermediate between Craters 2 and 11 (Figure 4). Dunes are not observed on the terrain surrounding the outermost fractures of any of the craters covered by MOC images. There is also no morphologic evidence for extensive eolian mantling or stripping.

The degree of fracturing surrounding the central depression varies from one major fracture set surrounding Crater 2 to extensive fracturing on the outer region of Craters 3 and 11 (Figure 4). Crater 1 appears to have slightly less extensive fracturing than Crater 3, and more fracturing than Crater 2 (Figure 6). Craters 7-10 have more extensive fracturing than Crater 2, with Craters 7 and 8 exhibiting degrees of fracturing similar to Crater 1 (Figure 7).

The definition of the thermally distinct craters by the identification of a thermal anomaly in the THEMIS IR data is likely not applicable to the smaller features observed in Figure 7. A smaller-scale phreatic event may produce only a weak ejecta blanket, which may be only a few pixels wide in the THEMIS IR data. Examination of the high-resolution THEMIS VIS and MOC images reveals that the smaller depressions that at first appear similar to the thermally distinct craters have morphologies inconsistent with the thermally distinct craters. The smaller craters lack the concentric disruption of the surrounding terrain that characterizes the thermally distinct craters. Even at the highest resolution data available, ejecta is not visible on any of the smaller depressions.

MOC images show that Craters 2, 3 and 11 have evidence for ejecta on the rim (Figure 4). The ejecta surrounding Craters 3 and 11 appear to have been more fluidized than the ejecta from Crater 2. Differences also exist in ejecta morphology between Craters 3 and 11. The ejecta surrounding Crater 11 are more visible in the MOC images than the ejecta surrounding Crater 3, although the craters have similar degrees of concentric faulting and fracturing. The differences in the apparent amount of ejecta between Craters 3 and 11 are potentially related to the size variation between the two craters, as Crater 11 is twice the diameter of Crater 3. The ejecta surrounding Crater 2 exhibit a distribution consistent with ballistic trajectories, forming a uniformly wide halo of material around the central depression (Figure 4b). Assuming the ejecta surrounding all three craters is the same material from a similar depth, it is possible that the material ejected from Craters 3 and 11 may have had a slightly higher volatile content or may have been emplaced at a much lower angle to the substrate than the material ejected from Crater 2. At this time, detailed analysis of ejecta from the nine other thermally distinct craters is not possible due to limitations in MOC image coverage of the region.

4.3. Distribution of craters

The craters identified as thermally distinct craters based on the THEMIS daytime and nighttime IR data were mapped on a mosaic of Viking images (Figure 8). Twelve craters were identified, all located in a region mapped as Apf (Amazonian fluted plains material) by De Hon et al. [1999]. The Apf unit is identified as smooth, level plains material having low-relief fluting and an intersecting pattern of linear hollows and is interpreted as dune fields or a mudflow originating from the source of Hrad Vallis and

Galaxias Fossae [De Hon et al., 1999]. Following the geologic map of De Hon et al. [1999], Wilson and Mouginis-Mark [2003] further subdivided the Apf unit into two separate mudflow units near the source region of Hrad Vallis (Figure 8).

Close examination of Figure 8 indicates that the thermally distinct craters are restricted to the "upper mudflow unit" identified by Wilson and Mouginis-Mark [2003]. A search of publicly available (as of March 2005) THEMIS IR data in the regions surrounding Hrad Vallis and the western and northwestern flank of the Elysium rise reveals no other evidence for similar examples of the thermally anomalous craters on geologic units other than the upper mudflow unit near the source region of Hrad Vallis. The isolated nature of the crater locations is consistent with an origin linked to the emplacement of the unit within which they are contained.

5. Additional quasi-circular features

In addition to the thermally distinct craters in the smooth unit bordering the source region of Hrad Vallis and obvious impact craters, there are at least three additional populations of quasi-circular features in the region. All three additional populations of identified features lack the thermal signature that distinguishes the craters previously discussed. Furthermore, in terms of location in the Hrad Vallis region, the additional populations of quasi-circular features and the thermally distinct craters are mutually exclusive. In the available image data, we do not see evidence of the quasi-circular features on the upper smooth unit, nor do we see the thermally distinct craters on the lower units.

5.1. Pits and hollows

Two of the additional populations are depressions that we call "pits" and "hollows" present on the lobe of material extending westward away from the source region of Hrad Vallis (Figure 6). The ~4 km wide lobe of material extends ~25 km to the west from the edge of the smooth deposit and is ~80-100 m thick as determined from MOLA topographic profiles (e.g. orbits 00457, 10786, 12616). The edges of the lobe exhibit margin-parallel fractures, hinting at post-emplacement deformation (Figure 9). Although the lobe appears to be the result of fluidized movement of unconsolidated material, at MOC resolution (3.21 m/pixel) flow features are not preserved on the current surface of the deposit. The presence and high numbers of the pits and hollows on this lobe of material relative to the surrounding substrate was one of the key attributes suggested by Wilson and Mouginis-Mark [2003] as evidence for an endogenic origin of the anomalous craters identified elsewhere on the deposit flanking the Hrad Vallis source region. The recent acquisition of more extensive MOC coverage of the region now allows us to examine the thermally anomalous craters and pits and hollows in greater detail than the earlier studies.

The first population on the lobe comprises amorphous "pits" resulting in a potholed appearance in the Viking Orbiter, THEMIS VIS and MOC images. The amorphous pits are depressions with irregular edges in plan view, occur primarily along the middle axis of the lobe, and (from individual MOLA profiles) are typically 400-500 m in diameter and 10-20 m deep. The edges of the amorphous pits do not appear raised relative to the surrounding material and an ejecta mantle surrounding the pits is not

observed (Figure 9). The floors of the pits are smooth, flat to bowl-shaped and consistently contain dunes.

We refer to the second population of sub-circular depressions on the lobe as "hollows" (Figure 6). The hollows display relatively low relief compared to the pits and the contact between the depression and the surrounding material is smooth and gradual. The hollows are ~500-1000 m in diameter and occur primarily in the near-source portion of the lobe. The interiors of the hollows exhibit morphologies similar to the surrounding terrain (Figure 6).

Based on our assessment of the recent MOC images and the THEMIS VIS images, unavailable at the time Wilson and Mouginis-Mark [2003] made their original assessment, we find that the pits, hollows and thermally distinct craters are in fact three separate populations of depressions within the lobate deposit, and likely represent the products of three separate formation processes.

5.2. "Low-relief features" to north of ridged mountain

The third population of quasi-circular features is observed in the region to the east and north of the smooth deposit on the eastern side of the Hrad Vallis source region, just northeast of the mountain block (Figure 10). We refer to the these features as "low-relief features." These low-relief features are typically non-circular and 100-300 m across, although four larger features have measured diameters of 320, 480, 580 and 970 m (Figure 10). They occur on what Wilson and Mouginis-Mark [2003] referred to as the "lower mudflow." From available MOC images, it appears that the largest features are clustered in an area of ~3-4 km in radius. Typically, the morphology of the features

includes a circular to sub-circular ring of material, often enclosing a relatively flat central region. Based on shadow and illumination observations from the MOC images, few of the features appear to have negative relief. No definitive evidence has been found for ejecta surrounding any of the features within the area. Additionally, the low-relief features to the east and north of Hrad Vallis do not have thermal signatures in the THEMIS IR data. This may be a problem of image resolution, as the THEMIS IR resolution is ~100 m/pixel and many of the features are in the 100-200 m diameter range, making any possible thermal signature only one or two pixels large. Assuming the features formed separated by geologically distinct periods of time based on their presence in superposed geologic units, the relative age of the features may also cause differences in the thermal signatures of the low-relief features and the thermally distinct craters.

6. Discussion

The origin of the thermally distinct craters in the Hrad Vallis region is an enigma, although several mechanisms have been invoked. Mouginis-Mark [1985] hypothesized that the craters were pseudocraters formed when the hot mudflow overrode a volatile-rich substrate, causing highly energetic vaporization of volatiles in the form of monogenetic explosion craters in the mudflow. He also suggested they may be impact craters formed after the emplacement of the smooth unit. De Hon et al. [1999] hypothesized the origin of the depressions in the smooth deposit surrounding Hrad Vallis was actually the result of infilling of impact craters by a mudflow originating from Hrad Vallis. Wilson and Mouginis-Mark [2003] proposed that the craters are the result of the highly energetic release of volatiles concentrated within the mudflow, causing explosion craters on the

surface of the flow. These mechanisms will now be discussed in light of the observations from the newly available data.

An origin of the thermally distinct craters due to impact cratering or infilling of pre-existing impact craters is not compatible with the observations described in the preceding sections. Infilling of existing impact craters is inconsistent with the presence of thermally distinct ejecta in the THEMIS IR data. The thermally distinct craters are similar sizes and are all located on what appears to be a single geologic unit. There appears to be a relative lack of craters in a similar crater diameter range outside of the geologic unit containing the thermally distinct craters. Additionally, the morphology of the thermally distinct craters is inconsistent with an impact crater origin. At the resolution of the THEMIS VIS images, not all of the thermally distinct craters appear to have ejecta, despite having a distinct thermal signature in the thermal infrared wavelengths. Furthermore, the concentric fracturing of the crater rims is inconsistent with typical 1-2 km impact crater terrace formation. The concentric fracturing, lack of a raised rim and lack of visible ejecta, despite the location in a geologically young unit, all argue against impact cratering as the process responsible for the thermally distinct craters.

Our observations suggest impact cratering was not responsible for the formation of the concentrically fractured, thermally distinct craters on the mudflow deposit, so we must investigate the other options mentioned above. The craters are circular, implying a point source, with thermally distinct ejecta on the outer edges of the depressions. Based on the above observations, the thermally distinct craters exhibit morphologies consistent with formation by explosion (ejecta surrounding the depression) and subsequent collapse of the surrounding material (fractures cutting some ejecta). At infrared wavelengths, the

ejecta surrounding the craters extend to varying distances from the crater rim, although only a weak correlation between crater diameter and ejecta blanket width can be observed. The varying degree of fracturing on the outer regions of the thermally distinct craters is suggestive of a spatially or temporally varying process causing collapse of the crater wall. It is likely the lower degree of fracturing of Crater 2 than Craters 3 and 11, and the more equally distributed ejecta halo around Crater 2, are both related to the origin of the thermally distinct craters.

Our preferred model for the origin of the mudflow is intimately related to the origin of Hrad Vallis. A previous model for the origin of Hrad Vallis invokes a large dike that propagated from a magma reservoir toward the west-northwest (as suggested by Wilson and Mouginis-Mark [2003] and Russell and Head [2003]). As put forth by Wilson and Mouginis-Mark [2003], in the case of Hrad Vallis, the hot magmatic material intermixed with the melted ground ice and was explosively released onto the surface to form the mudflow within which the craters studied here are located. The interaction between the hot mudflow and remaining ice, whether contained in the mudflow or, more likely, in the still-frozen substrate, caused some explosion craters as the remaining ice rapidly flashed to steam.

A phreatic explosion within a mudflow would be expected to produce ejecta surrounding the central depression, akin to maar-forming terrestrial explosions [Self et al., 1980], although the exact volume of material ejected from the crater versus the volume of material that falls back into the crater is unknown. The observation that only the largest Hrad craters have ejecta visible in the available images may be consistent with the hypothesis that the larger craters are the result of a more energetic explosion that was

more efficient at ejecting material out of the crater onto the surrounding terrain. The empty volume caused by the liberation of the locally concentrated volatiles may result in slumping of the newly formed crater walls in response to the free surface exposed within the crater. With the data currently available, we are not able to determine whether the volatiles were released from the substrate or from within the mudflow. Compositional data showing the make-up of the ejecta versus that of the mudflow would be highly useful, but the region is too cool and dust-covered to obtain reliable compositional information. Fagents et al. [2002] describe pseudocraters identified in several regions of Mars and observed in Iceland. These craters are typically a few hundred meters in diameter, and if resolved at all, a thermal signature in the THEMIS IR images would be only a few pixels wide and inadequate to fully characterize the feature. Although the features described in Fagents et al. [2002] typically have positive relief, the thermally distinct craters near Hrad Vallis may be an interesting new variant of pseudocrater on Mars because we can identify their ejecta using MOC and THEMIS VIS images.

The lobate deposit containing the thermally distinct craters on the flanks of the source region of Hrad Vallis appears to be a unique geological feature on the surface of Mars [Wilson and Mouginis-Mark, 2003]. We have searched the publicly available THEMIS VIS image database and find no other examples elsewhere on Mars. It is possible that the location of the feature is the primary reason for the unusual formation, as the source region for Hrad Vallis is at the highest latitude and lowest elevation of all the major outflow channels on the planet. In addition, the head region of Hrad Vallis is located at the break in slope between the Elysium Rise, the second largest volcanic province on Mars, and the northern lowlands, a region thought to have been extensively

modified by near-surface ground-ice [Mouginis-Mark et al., 1984]. The sequence of events and the characteristics of the region may all conspire to make the craters in Hrad Vallis unique, although searching for similar craters elsewhere on Mars may help to identify other hot meltwater eruptions.

7. Summary

We have documented 12 thermally anomalous craters in the diameter range of ~1,100-1,800 m flanking the source region for Hrad Vallis, near Elysium, Mars. We observe that all the craters are circular, not elongate, and all lack the raised rims commonly associated with relatively fresh impact craters. Ejecta with distinct thermal signatures that are all typical of coarser-grained or blocky material surround the craters. The depths of the craters are approximately equal to the thickness of the lobate deposit and in high-resolution image data we see that multiple concentric collapse events surround the central crater depression. The characteristics of the craters are consistent with a formation initiated by an explosive event followed by collapse of the region surrounding the depression. Initiating such explosive events must rely on an unusual combination of mudflow temperature (hotter than normal?) and the existence of isolated pockets of ice close to the surface that could be heated to vaporization temperature. Further numerical modeling of the dynamics of this interaction is essential to adequately resolve the origin of the craters, but such work is beyond the scope of this investigation. Additional high-resolution images specifically targeting the thermally distinct craters using the MOC instrument and the High Resolution Imaging Science Experiment (HiRISE) on the Mars Reconnaissance Orbiter might address some of the remaining

questions concerning the meter-scale morphology of the thermally distinct craters. New information regarding the crater morphology, such as the spatial extent and characteristics of ejecta as well as better knowledge of the interior structure, will aid in the determination of the origin of the craters.

Acknowledgements

This work was supported by NASA grant NAG5-13323 (PMM, PI) under the Mars Data Analysis Program. We wish to gratefully acknowledge helpful discussions with Lionel Wilson. Computer programming by Harold Garbeil also proved especially useful for the collation of THEMIS and MOLA datasets. We thank Robert Craddock and an anonymous reviewer for their thoughtful reviews, which greatly improved the manuscript.

Table 1. Thermally distinct crater information

Crater ID	Latitude (ºN)	Longitude (ºE)	Diameter (m)	Visible ejecta	Relative Ejecta Temp. Daytime IR	Relative Ejecta Temp. Nighttime IR
1	34º 12' 40.59"	141º 4' 31.56"	1700	no	cool	warm
2	34º 12' 40.59"	141º 10' 37.21"	1650	yes	cool	warm
3	34º 2' 21.80"	141º 19' 31.62"	1200	yes	slightly cool	possibly warm
4	33º 38' 27.33"	141º 11' 5.34"	1100	no	cool	warm
5	33º 30' 57.30"	141º 28' 54.16"	1100	n/a	cool	warm
6	33º 48' 17.99"	142º 10' 9.31	1300	no	cool	warm
7	34º 7' 31.19"	141º 57' 29.89"	1600	no	no apparent ejecta	warm
8	34º 14' 33.09"	141º 58' 26.14"	1200	no	slightly cool	small amount warm
9	34º 23' 27.50"	142º 3' 35.54"	1300	no	slightly cool	large region warm
10	34º 32' 50.04"	142º 5' 56.17"	1200	no	cool	warm
11	34º 48' 18.22"	141º 52' 20.50"	2300	yes	cool rayed	warm, rayed
12	34º 39' 23.81"	141º 46' 42.97"	1800	n/a	very cool	very warm

Figures

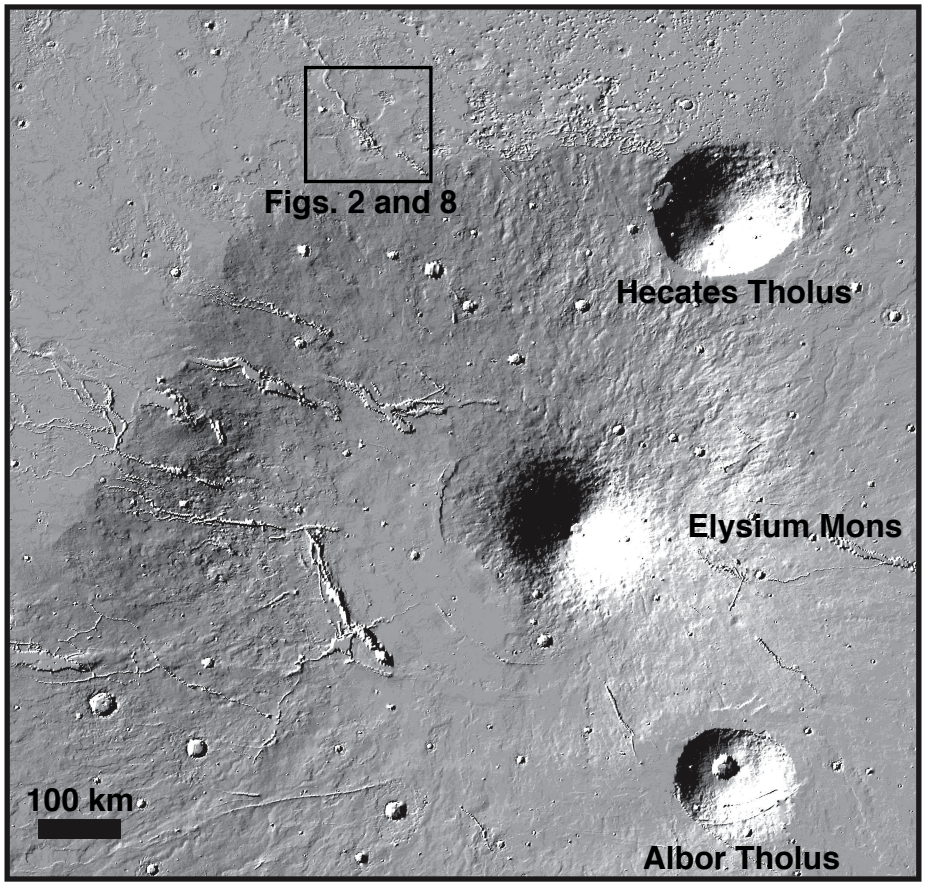

Figure 1. MOLA shaded relief image of Elysium region made using MOLA 128 pixels/degree Digital Elevation Model (DEM). Coverage area extends from 17.0º-37.0ºN, 206.5º-226.5ºW. The three main Elysium volcanoes are identified. North is to the top, with artificial illumination from southeast. Black box shows location of Figs. 2 and 8.

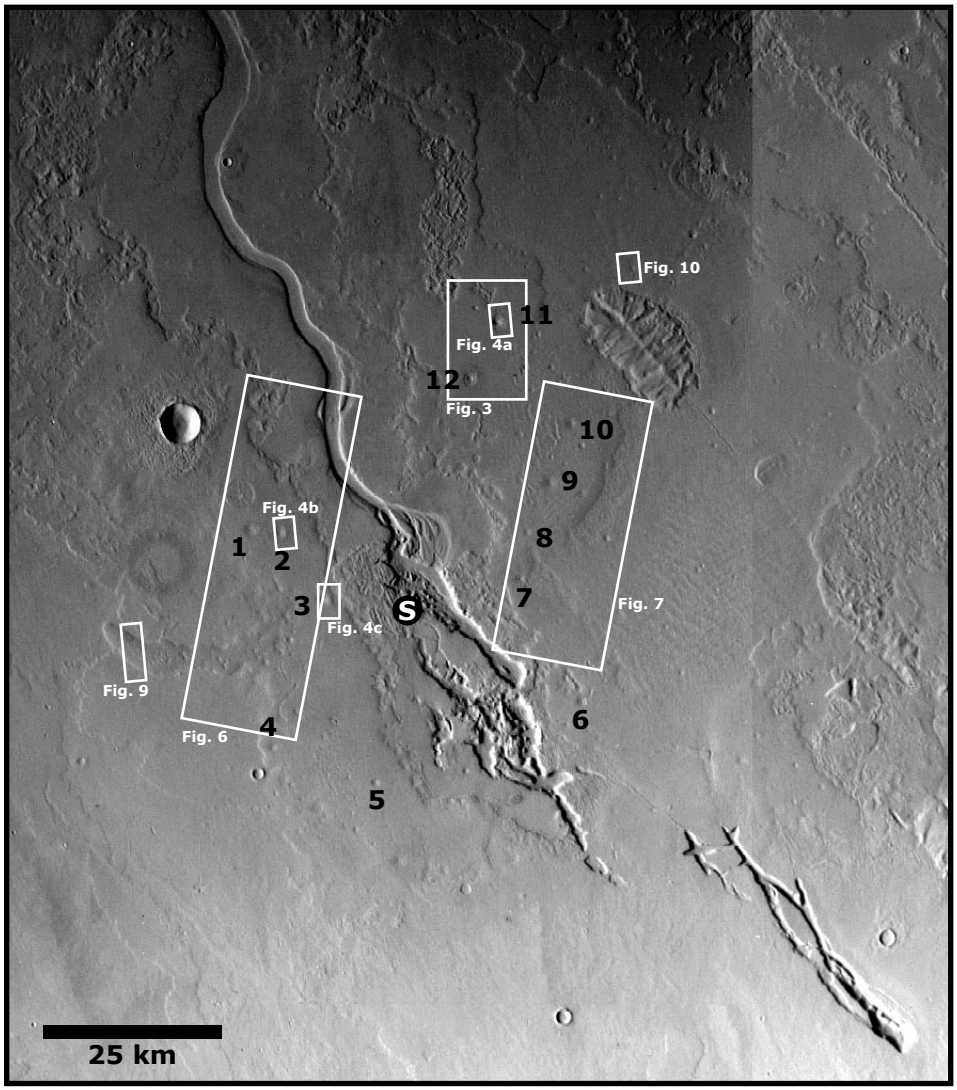

Figure 2. Viking Orbiter mosaic of Hrad Vallis region. Thermally distinct craters identified by numbers. Location of subsequent figures identified by boxes. White "S" identifies jumbled, chaotic source region for Hrad Vallis. Image composed of Viking Orbiter frames 541A10-12. See Fig. 1 for location.

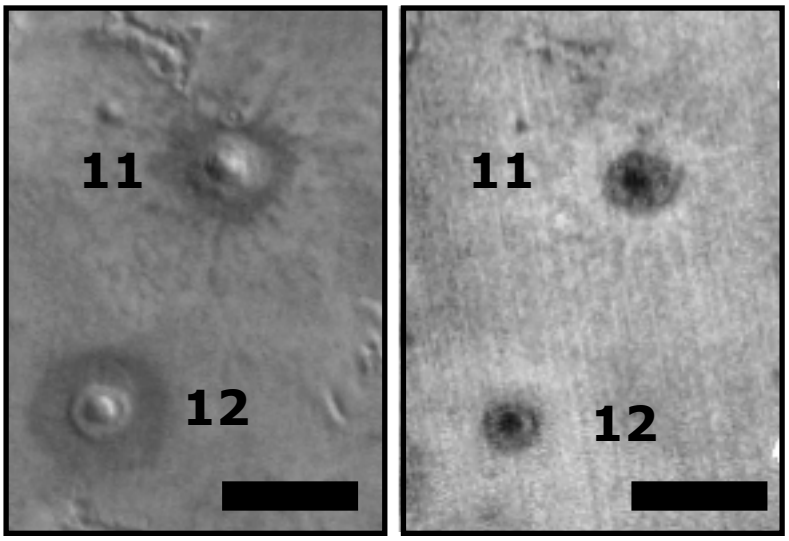

Figure 3. THEMIS IR images of Craters 11 and 12. Daytime image (left) is I01518016 acquired at L_S 360, local start time 13:57:06.204. Nighttime image (right) is I01462006 acquired at L_S 359, local start time 22:40:18.495. Scale bars are 5 km in length. See Fig. 2 for location.

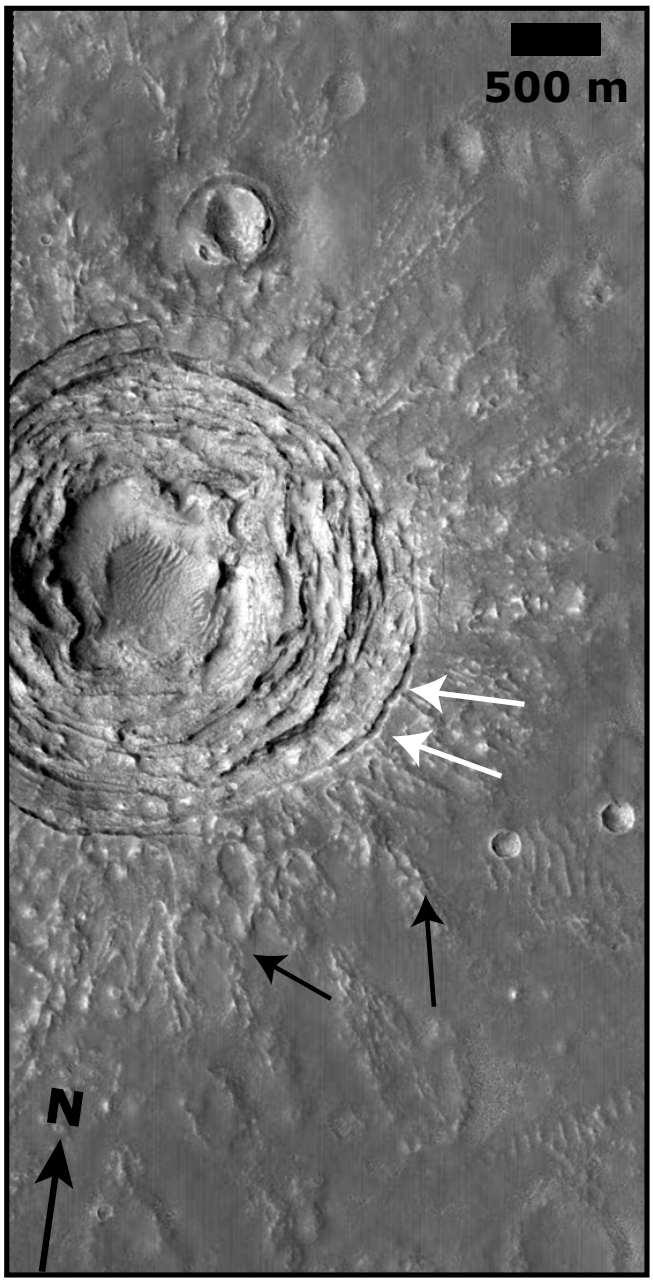

Figure 4. (a) MOC image of Crater 11. Note the minimal dune coverage in central portion of depression. Possible ejecta rays noted by black arrows. White arrows identify potential locations where fractures cut the ejecta. Note fracturing of terrain surrounding depression. See Fig. 2 for location. Portion of MOC image E2200273 (6.44 m/pixel). (b) MOC image of Crater 2. Diffuse ejecta halo surrounds dune-filled central crater. Note single fracture system cutting surrounding terrain identified by black arrows. See Fig. 2 for location. Portion of MOC image E2300531 (3.22 m/pixel). (c) Portion of MOC image R1004518 (6.44 m/pixel) of Crater 3. Image is processed but not map-projected. Note moderate dune coverage of interior portions of depression surrounded by fairly extensive fracturing of surrounding terrain. Possible ejecta material identified by black arrows. See Fig. 2 for location.

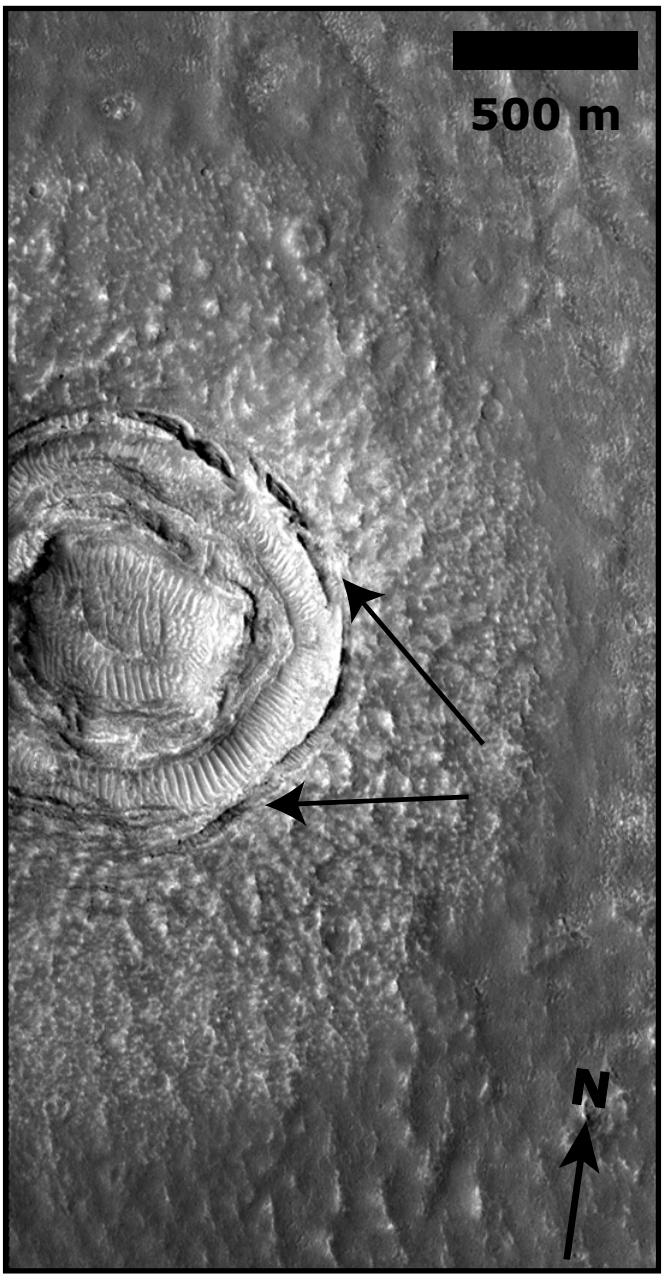

Figure 4b.

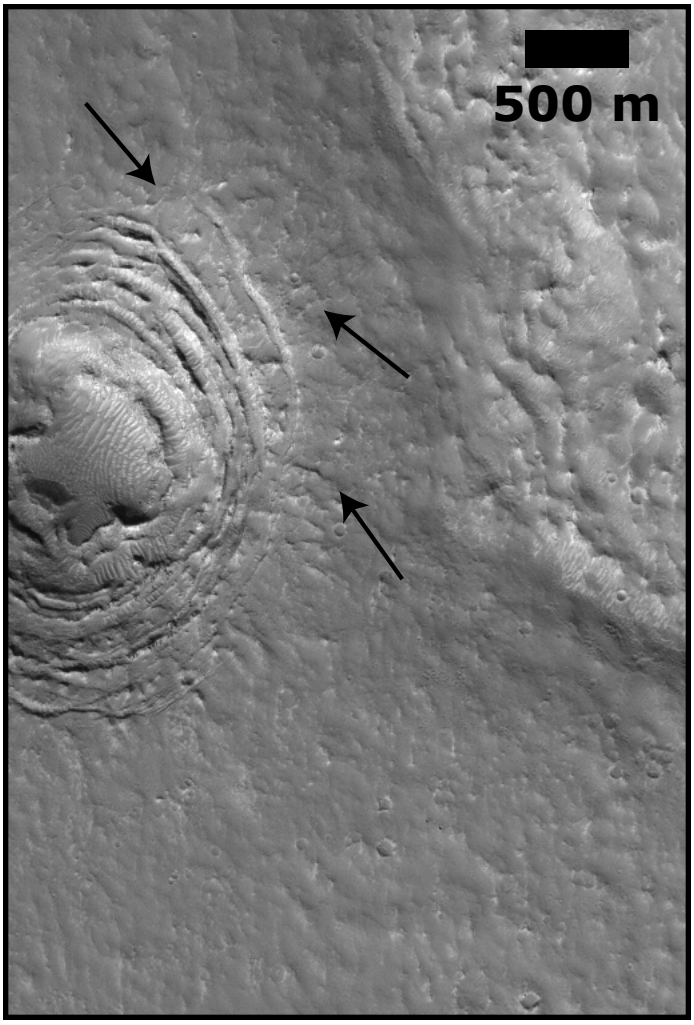

Figure 4c.

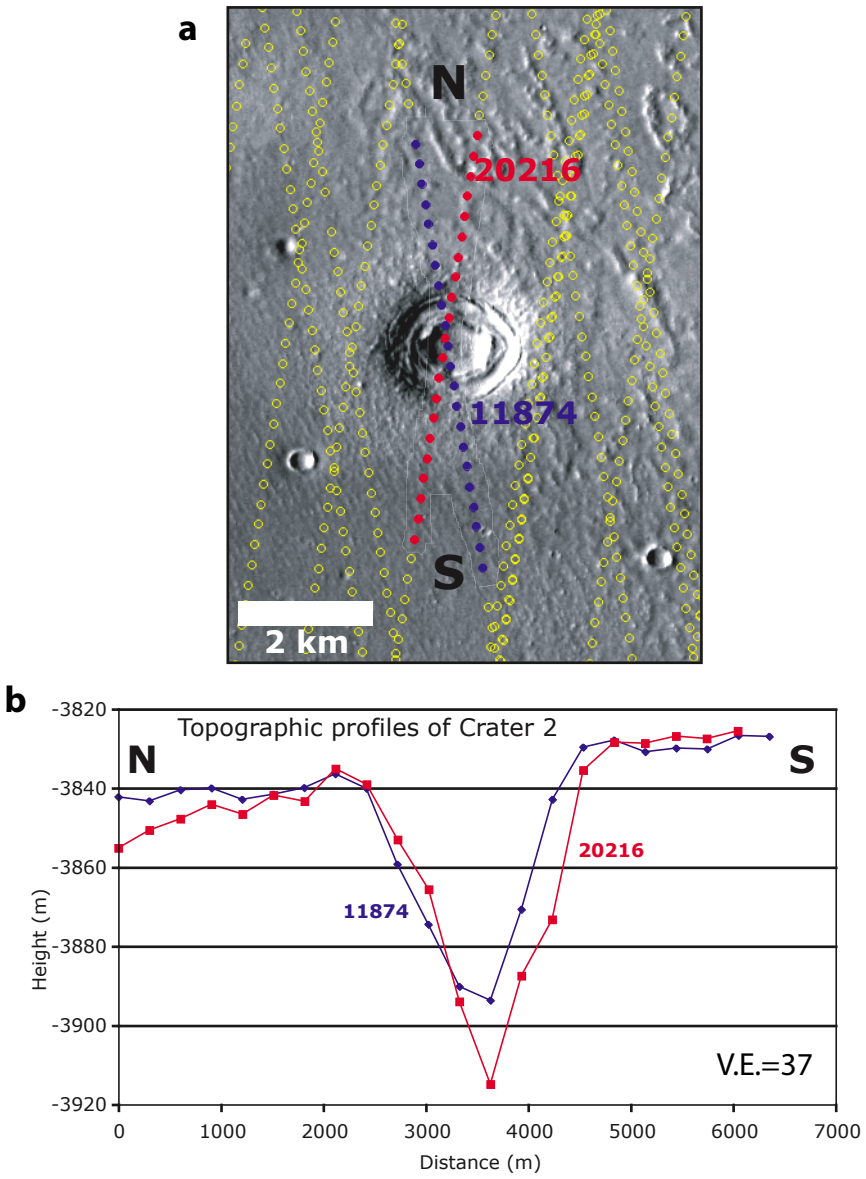

Figure 5. MOLA profiles across central region of Crater 2. (a) Image is portion of THEMIS VIS image V05263019, with co-located MOLA ground shots indicated by circles. Blue closed circles indicate selected shots from MOLA orbit 11874 and red closed circles indicate selected shots from MOLA orbit 20216. Yellow open circles show locations of other MOLA data, not used here, but indicate the general spatial coverage of the altimetry. (b) Graph of selected MOLA shots showing topography of Crater 2. Red line shows profile from MOLA orbit 20216, blue line shows orbit 11874. Note lack of substantial rim.

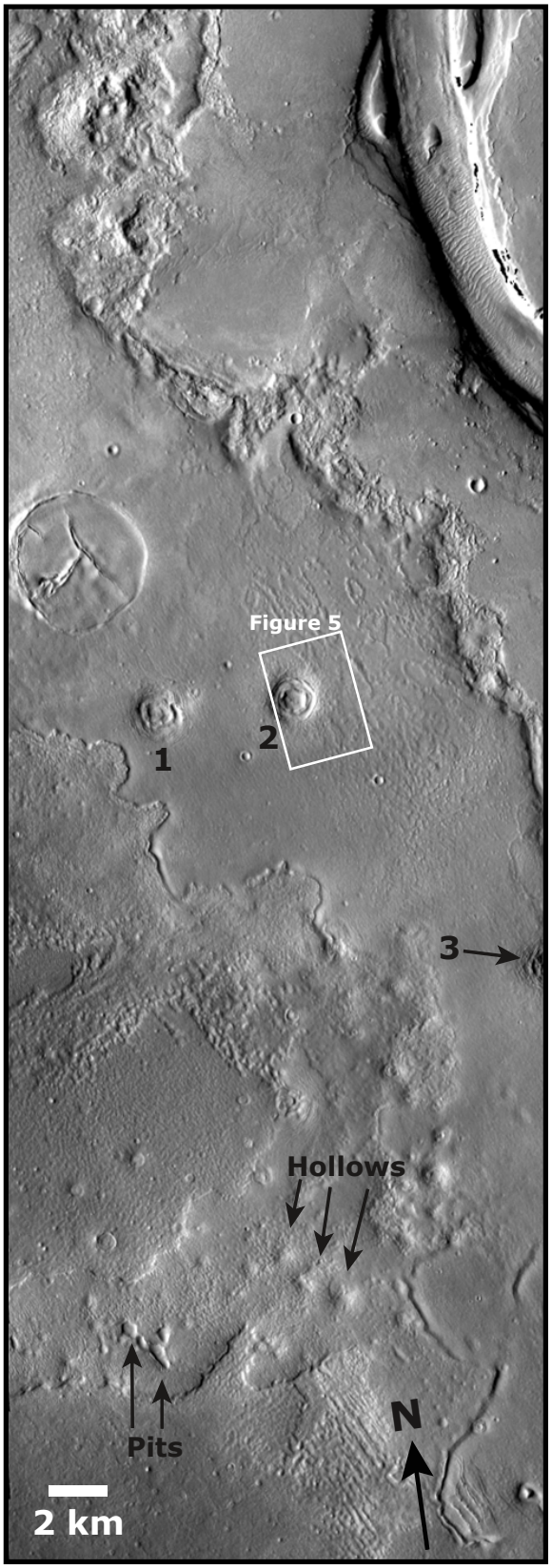

Figure 6. Thermally distinct Craters 1-3 identified by numbers. Pits and hollows are discussed in text. Circular feature to north of Crater 1 is likely a pre-existing impact crater filled by the mudflow from Hrad Vallis, where cooling cracks created a “peace sign” in the central portion of the feature. White box denotes location of Fig. 5. THEMIS VIS image V05263019. See Fig. 2 for location.

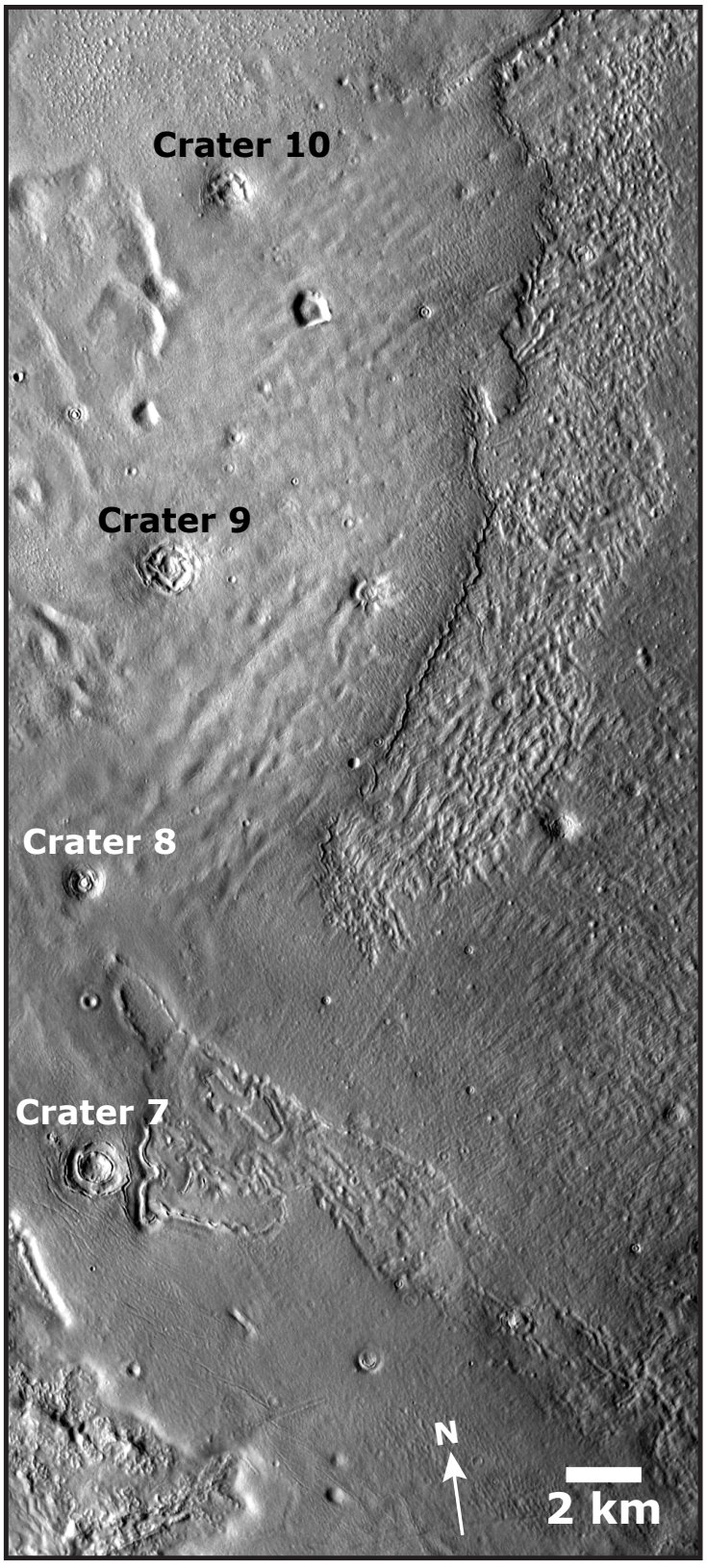

Figure 7. Craters 7-10 identified by numbers. THEMIS VIS image V05238007. See Fig. 2 for location.

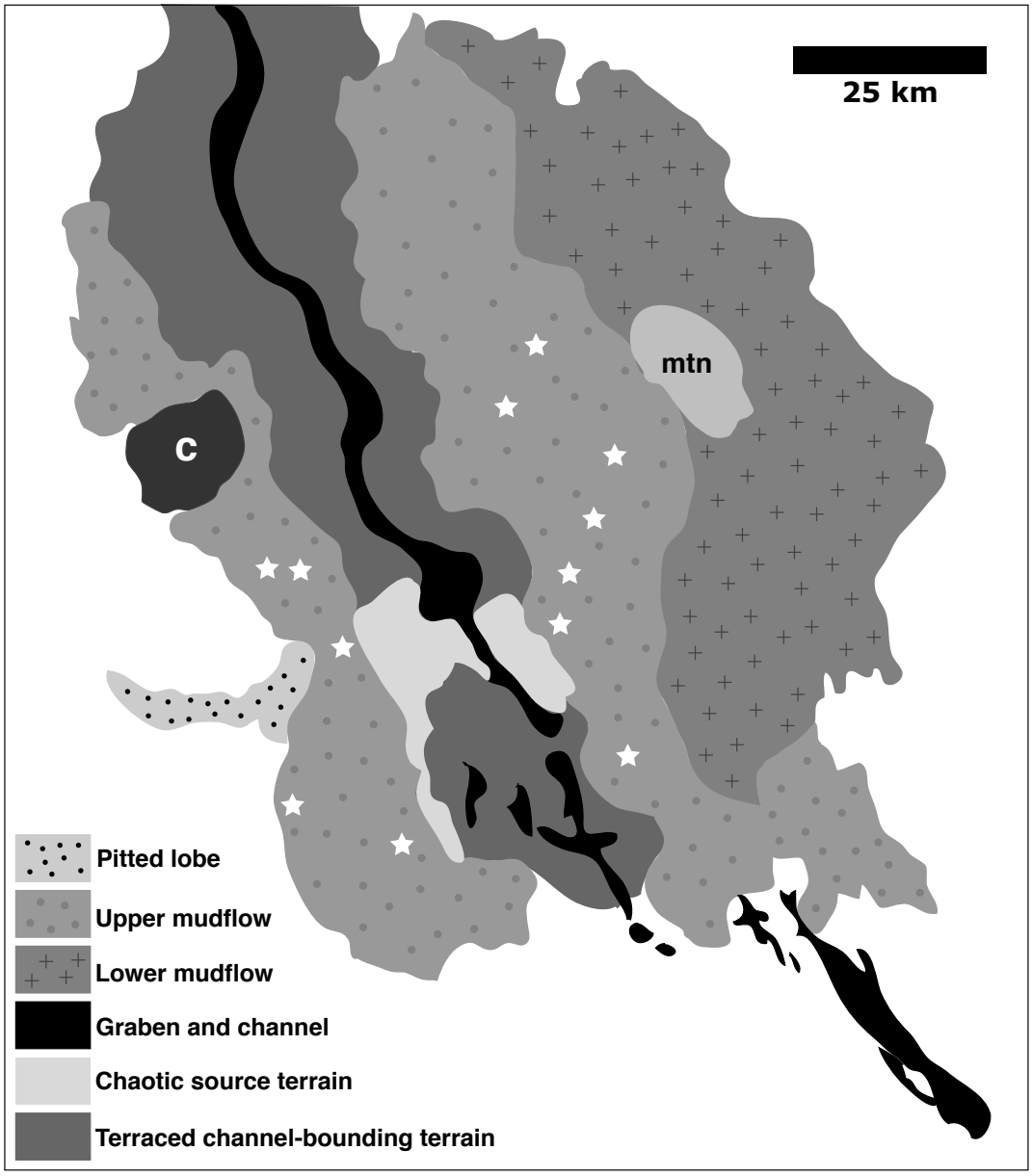

Figure 8. Sketch map of units identified from Viking mosaic (see Fig. 2) after Wilson and Mouginis-Mark (2003). White stars indicate the location of the thermally distinct craters. The unit containing the thermally distinct craters is identified as the "upper mudflow unit" and the unit within which the low-relief quasi-circular features are located is identified as the "lower mudflow unit" by Wilson and Mouginis-Mark (2003). The unit containing the pits and hollows is the "pitted lobe." "C" refers to a 6 km diameter impact crater and the associated crater ejecta. "Mtn" identifies the mountain block surrounded by the lower mudflow unit.

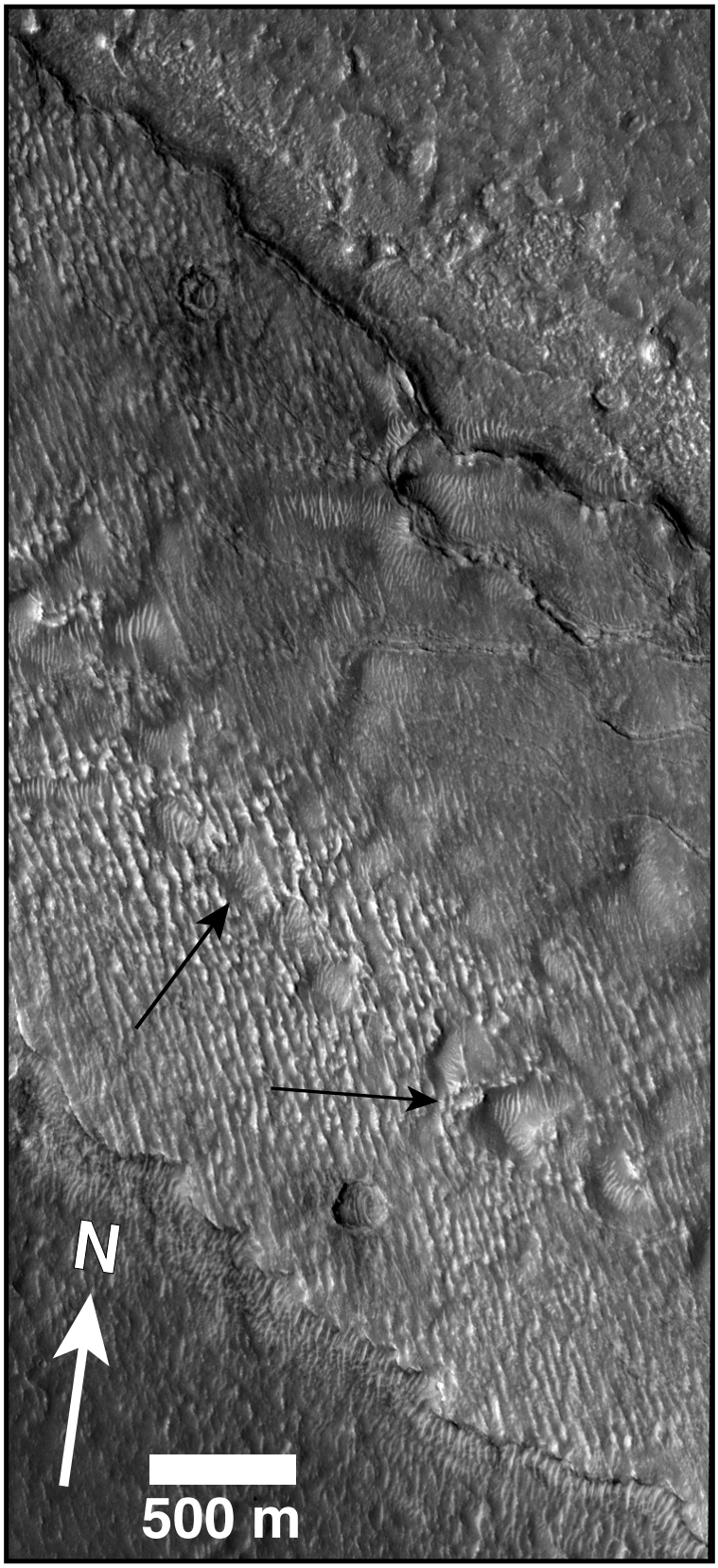

Figure 9. Portion of lobe extending westward away from main body of mudflow unit. Amorphous pits identified by black arrows. MOC image R0100413 (3.21 m/pixel). See Fig. 2 for location.

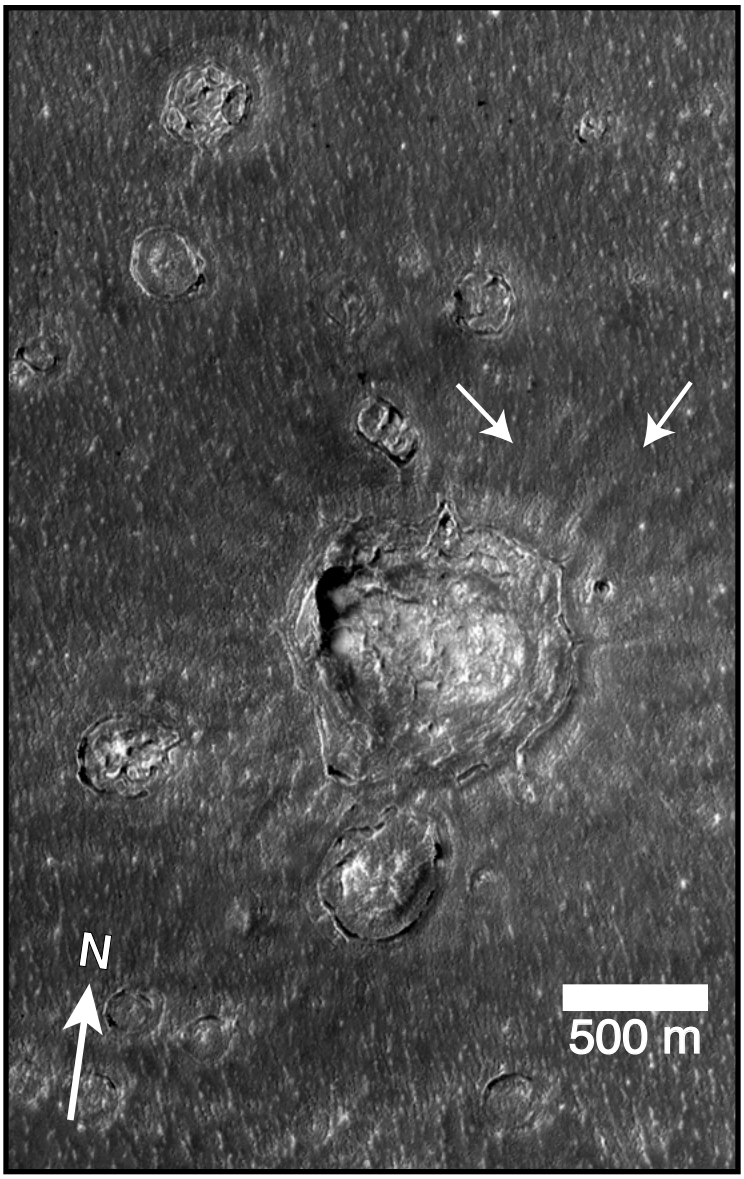

Figure 10. Low-relief quasi-circular features (largest ~1 km) to north of mountain block. Arrows point to possible ejecta rays. Portion of MOC image M2201275 (4.61 m/pixel). See Fig. 2 for location.

CHAPTER 2 ADDENDUM. HIRISE VIEWS OF HRAD VALLIS THERMALLY DISTINCT CRATERS

1. New HiRISE Data

Recent high-resolution images obtained by HiRISE (0.25-0.30 m/pixel), the High-Resolution Imaging Science Experiment [McEwen et al., 2007a], have provided unprecedented views of three of the thermally distinct craters and a portion of the pits and hollows on the lobe discussed in Chapter 2 (Figure 11). The HiRISE coverage over the Hrad Vallis deposit is still increasing, but the currently available data offer insight into answering some of the remaining questions from the previous THEMIS, MOC and MOLA-based study. Our previous study lacked the ability to examine the detailed morphology of the crater ejecta (or lack thereof), the fractures surrounding the thermally distinct craters, and the meter-scale morphology of the additional quasi-circular features in the deposit surrounding Hrad Vallis. These new data allow investigation of the meter-scale characteristics of the terrain surrounding three of the thermally distinct craters. We are also able to clarify the meter-scale morphology of the crater ejecta and fractures. Additionally, we examine the meter-scale morphology of the low-relief features to the east of the primary, or upper, mudflow deposit (see Chapter 2, Figure 8). Finally, one HiRISE image covers a portion of the lobe of material extending westward away from the primary deposit. This image enables us to examine the morphology of the surface of the lobe as well as the previously identified pits and hollows. In the following sections, several questions remaining from the previous chapter will be presented and subsequently addressed using the newly acquired HiRISE data. In essence, we have an unusual opportunity to test our previously published hypotheses during the course of my dissertation research.

2. HiRISE Observations

2.1. Terrain surrounding thermally distinct craters

New HiRISE images cover three of the previously identified thermally distinct craters and the terrain surrounding each crater. HiRISE image PSP_006881_2145 details Crater 1 (Figure 12a), PSP_005813_2150 details Crater 11 (Figure 13a), and image PSP_008384_2150 details part of Crater 12 (Figure 14a; there is a data gap in the center of the crater). At HiRISE resolution, the terrain surrounding the thermally distinct craters, mapped as Apf (Amazonian fluted plains) by De Hon et al. [1999], exhibits kilometer-scale variations in surface morphology. Patches of terrain appear smooth at the meter scale, while fields of cones populate the regions to the southwest and east-southeast of Crater 11 and to the north-northeast of Crater 12 (Figures 13a and 14a). The cones are typically ~30-50 m across at the summit, and ~60-80 m across at the base (Figures 13b and 14b). Many of the cones have flat summits, while some have a summit crater. The larger cones exhibit channels extending radially away from the summit and decameter-scale pits are often observed at the base of many of the cones (Figure 13b). Near Crater 12, the cones are also observed within the crater ejecta (Figure 14b).

2.2. Thermally distinct craters

As inferred in Chapter 2, the ejecta of Craters 1, 11 and 12 (the only craters imaged by HiRISE to date) appear to contain a large population boulder-sized (~1-5 m across) material (Figures 12b, 13c, 14c). The boulders in the ejecta halo of Craters 1 (Figure 12b) and 12 (Figure 14c) appear to generally be smaller than those in the ejecta rays of Crater 11 (Figure 13c). Few boulders are present within the fractures, and dunes

cover much of the visible surface of floors of the fractures (Figures 12b, 13c and 14c). Additionally, Figure 13d illustrates the absence of large boulders and blocks on the surface beyond the crater ejecta halo. The walls of the fractures appear massive, lacking extensive layering of the material (Figures 12b, 13c and 14c). One new observation of the ejecta from Crater 12 is the apparent presence of parallel ridges within the ejecta blanket (Figure 14c). The ridges are typically 35-40 m in wavelength and are oriented NW-SE around the entire crater (Figure 14a).

In Chapter 2 we noted that the ejecta surrounding Crater 11 appeared to have a slight "rayed" appearance based on THEMIS VIS and MOC data. High-resolution views of the proposed rays reveal that these are positive-relief features composed of fine-grained material with boulders within the unit, and channel forms appear to extend from some of the rays onto the surrounding terrain (Figure 13e). The observed channel forms emanating from the rays are typically < 100 m long and ~ 2 m wide. The source regions for the channel forms appear to be the local topographic highs formed by the rays.

The HiRISE images also provide information regarding the smaller craters (< 600 m) previously observed in the THEMIS VIS and MOC images. Based on the previously available images, the smaller craters were not included as thermally distinct craters, but the new HiRISE data provide evidence for boulder-sized ejecta (1-5 m across) and concentric fractures surrounding the smaller features (Figure 12c).

In addition, the HiRISE team has used images from two different look directions to produce a stereo anaglyph over Crater 11 (Figure 15), allowing relative topography of the crater to be examined. The edges of Crater 11 do not appear to be noticeably raised, and the sides of the depression, beginning with the outermost fracture, appear to step

down gradually along the faults bounding the crater. Additionally, the ejecta "rays" appear to be fairly thin.

2.3. "Pits" and "Hollows"

HiRISE image PSP_007237_2140 covers the pits and hollows on a portion of the lobe extending away from the proposed mudflow deposit (Figure 16a). At HiRISE resolution, the surface of the lobe is generally covered with a population of 1-5 m boulders to the east. The grain size of the material on the surface of the lobe appears to decrease westward, or down-flow as interpreted from the THEMIS VIS and Viking data (see Chapter 2). The edges of the widest sections of the lobe (both to the north and the south) are covered by a series of approximately flow-perpendicular ridges, oriented ~NW-SE along the lobe and highlighted by high albedo dunes (Figure 16b). The central ~2 km of the lobe has more subtle ridges than those observed on the outer edges, and contains the pits and hollows discussed in Chapter 2. The width of the central, subdued-ridge area of the lobe is relatively consistent in the portion of the lobe visible in the HiRISE image (Figure 16a). The contact between the ridged outer portion and the subdued ridges of the inner portion is not distinct, and relative formation times are not clear (Figure 16b).

In the new high-resolution data, it is clear that the pits and hollows exhibit different morphologies from the thermally anomalous craters described in Chapter 2. The pits are surrounded by one set of fractures (Figure 16c), while the hollows appear to be surrounded by narrow, incipient fractures (if the surface has been broken at all), as the surfaces appear depressed without extensive disruption of the lobe material. The fractures

bordering the pits are typically 20-50 m across and are often bounded by concentrations of meter-scale boulders (Figure 16c). The floors of the pits typically lack boulders and contain linear dunes with varying orientations, while floors of the hollows exhibit morphologies similar to the surface of the lobe surrounding the hollows (Figure 16c).

2.4. "Low-relief features" north of ridged mountain

HiRISE images PSP_007672_2155 details the region to the north of the ridged mountain, including the "low-relief" features in that area (Figure 17a). In Chapter 2, we note that we did not observe a thermal anomaly associated with these craters, and in the HiRISE image, we do not observe ejecta around the low-relief features (Figure 17b). The deposit in which the low-relief features formed abuts the base of the ridged mountain. Where the deposit contacts the ridged mountain, it has formed fractures parallel to the edge of the deposit. Within the fractures, there are few meter-scale boulders and the deposit exhibits layering (Figure 17c).

3. Discussion

The recent high-resolution images obtained by HiRISE permit examination of the thermally distinct craters and surrounding terrains at scales unavailable when Chapter 2 was published. These new data have provided additional evidence for the explosive interaction of a hot material overriding a volatile-rich substrate. The fields of small cones observed on the surface near Craters 11 and 12 suggest that small-scale explosions may have formed rootless cones similar to those described by Fagents et al. [2002]. Based on field research of features in Iceland, the formation of rootless cones is typically attributed

to violent interaction of lava flows and volatile-rich ground [Greeley and Fagents, 2001]. We suggest that a hot mudflow, as proposed by Wilson and Mouginis-Mark [2003], overrode a volatile-rich substrate, creating rootless cones in a similar fashion. The relationship between the cones and the large, thermally distinct craters is still unclear, and we hope that additional HiRISE data over some of the other previously identified thermally distinct craters will provide additional clues.

The observation that the ejecta of Craters 1, 11 and 12 contain many boulders is consistent with the interpretation of Christensen et al. [2003] that the higher nighttime THEMIS IR temperature and cooler daytime temperatures (see Chapter 2, Figure 3) are due to the presence of either blockier material or more indurated material. In this case, the boulders cause a higher nighttime and lower daytime temperature of the material in comparison to the surrounding terrain. The lack of boulders within the fractures of Craters 1, 11 and 12 suggests that the boulders were emplaced on the surface of the deposit prior to formation of the concentric fractures. Additionally, extensive boulders are not identified beyond the crater ejecta halo, suggesting the source for the boulders on the surface of the proposed mudflow is the thermally distinct craters. The identification of ejecta surrounding the smaller concentric craters has led to the addition of the smaller craters to the thermally distinct crater group. The "rays" surrounding Crater 11 appear to include boulder-sized ejecta, suggesting they are related to the formation of Crater 11. Additionally, we observe ~100 m long, ~2 m wide channel forms emanating from some of the rays, suggesting the formation of the rays may be intimately related to the presence of liquid water.

The subdued ridges observed on the central portion of the lobe containing the pits and hollows are likely to be the result of one of two possible formation scenarios. The ridges may have formed equally across the entire lobe, but relaxed in the central portion of the lobe, or the ridges may not have formed in the central portion of the lobe due to material variations across the lobe. Both possibilities suggest that the outer portion of the lobe and the inner regions exhibit different material properties, whether during formation or during post-emplacement modification of the flow. The presence of the pits and hollows only within the central portion of the lobe suggests that the material within the inner region of the lobe was more volatile-rich than the edges. The pits and hollows may be akin to kettle lakes in glaciated terrains [Summerfield, 1991]. In this scenario, pockets of volatiles contained within the lobe passively disappeared, leaving behind a depression on the surface once occupied by interstitial volatiles. The identification of fractures surrounding the pits and incipient fractures surrounding the hollows suggests that the pits and hollows may be two forms of the same feature. Contrary to our assessment in Chapter 2 that the pits and hollows are features created by separate processes, we now suggest that the hollows may be the initial form of the pits. In this model, the pits develop when significant subsurface voids have been created, allowing full subsidence of the surface. The presence of dunes on the floors of the pits and the lack of dunes on the floors of the hollows appear to support this relative age interpretation.

4. Conclusions

In summary, it appears we must revise our initial interpretations from Chapter 2 as a result of the new information from the HiRISE images. We were correct in our interpretation of the thermal signature of the anomalous craters was due to the presence

of coarser material in the regions surrounding the craters. The lack of ejecta surrounding the low-relief features to the north of the ridged mountain indicates that we were also correct in our interpretation that these features were not formed in a similar manner as the thermally distinct craters. Contrary to our previous assumption that the smaller, concentrically fractured craters are not similar to the larger craters, the presence of 1-5 m blocks of ejecta surrounding the smaller craters indicates that these are indeed the same type of craters. Finally, contrary to our previous interpretation that two separate processes formed the pits and hollows, we now believe that these are two forms of the same feature.

In addition to evaluating our previous interpretations, the new HiRISE images have provided new information regarding the nature of the surface surrounding the source region for Hrad Vallis. We have identified the presence of fields of small cones on the surface of the flow. The larger cones have channels extending from their summits and the majority of the cones have meter to decameter scale pits at the contact between the flanks of the cone and the flow surface. We have also identified channel forms emanating from some of the ray-like features surrounding Crater 11. A thorough survey of the rays is yet to be done, but this observation may provide important evidence for the involvement of volatiles in the formation of the thermally distinct craters.

Figures

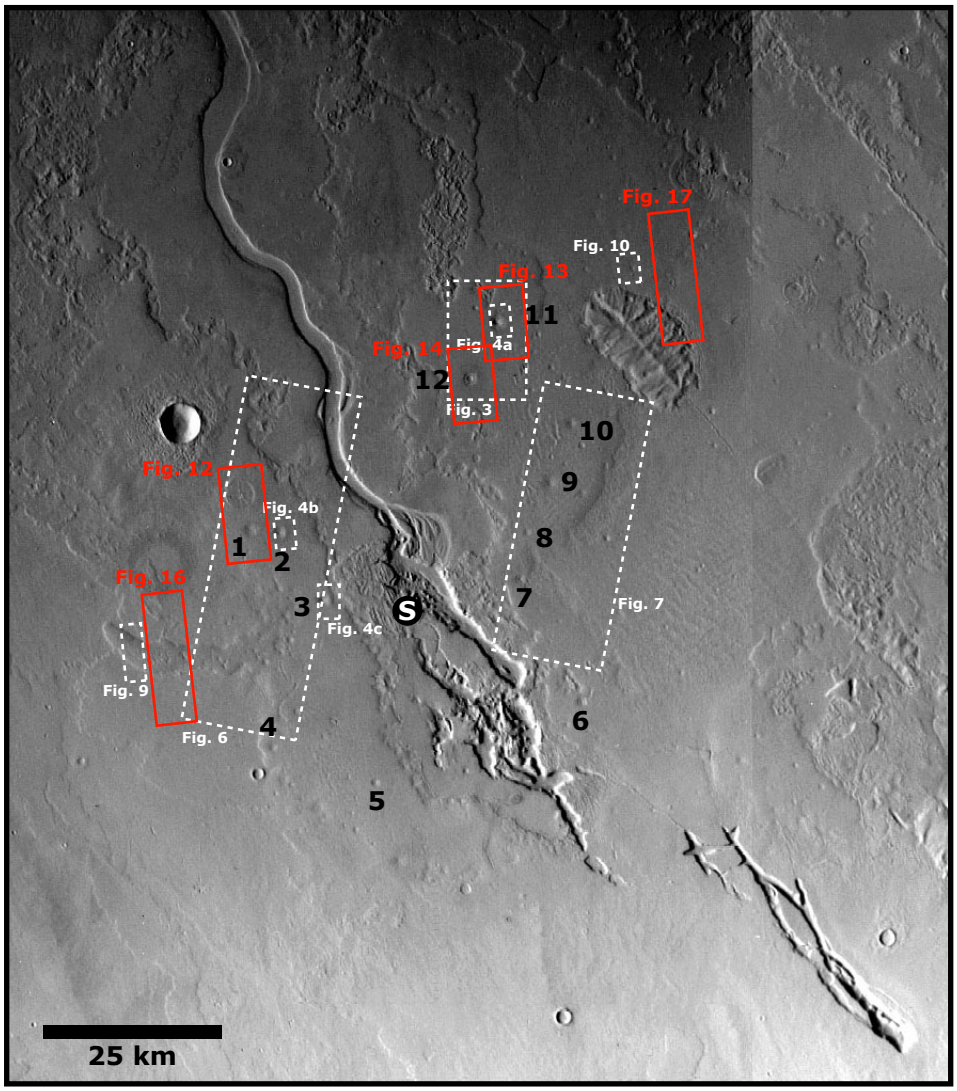

Figure 11. Viking Orbiter mosaic of Hrad Vallis region after Chapter 2 Figure 1. Thermally distinct craters are identified by numbers. Location of figures from Chapter 2 and are identified by dashed white boxes. New HiRISE figures from Chapter 2 addendum are identified by red boxes. White "S" identifies jumbled, chaotic source region for Hrad Vallis. Image composed of Viking Orbiter frames 541A10-12. See Figure 1 from Chapter 2 for location.

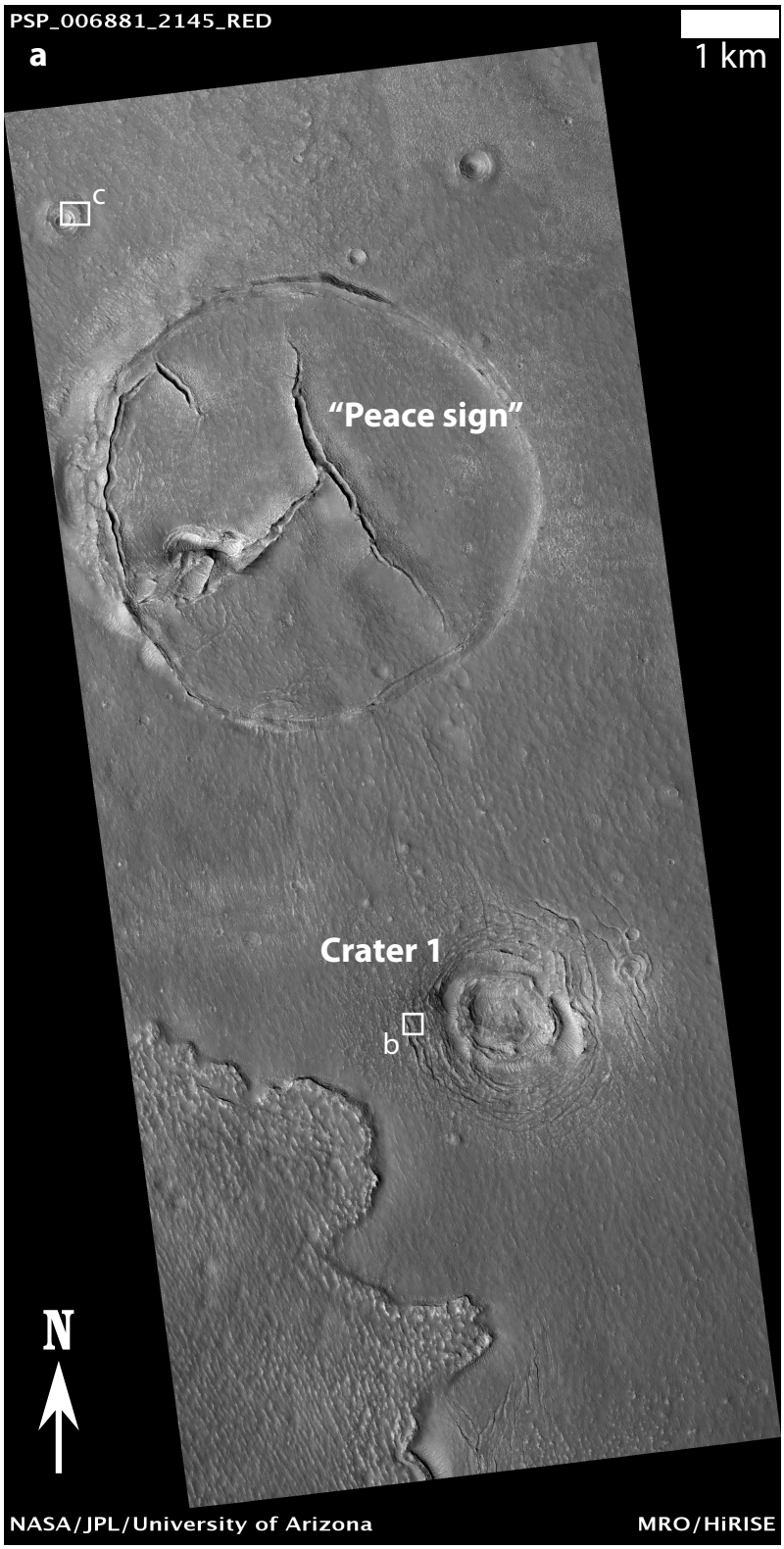

Figure 12 a) HiRISE image PSP_006881_2145 detailing Crater 1 and "peace sign." White boxes identify the locations of figures 12b and 12c. b) Detail of ejecta and fractures surrounding Crater 1. c) Detail of fracture and boulder-sized ejecta of small crater north of "peace sign."

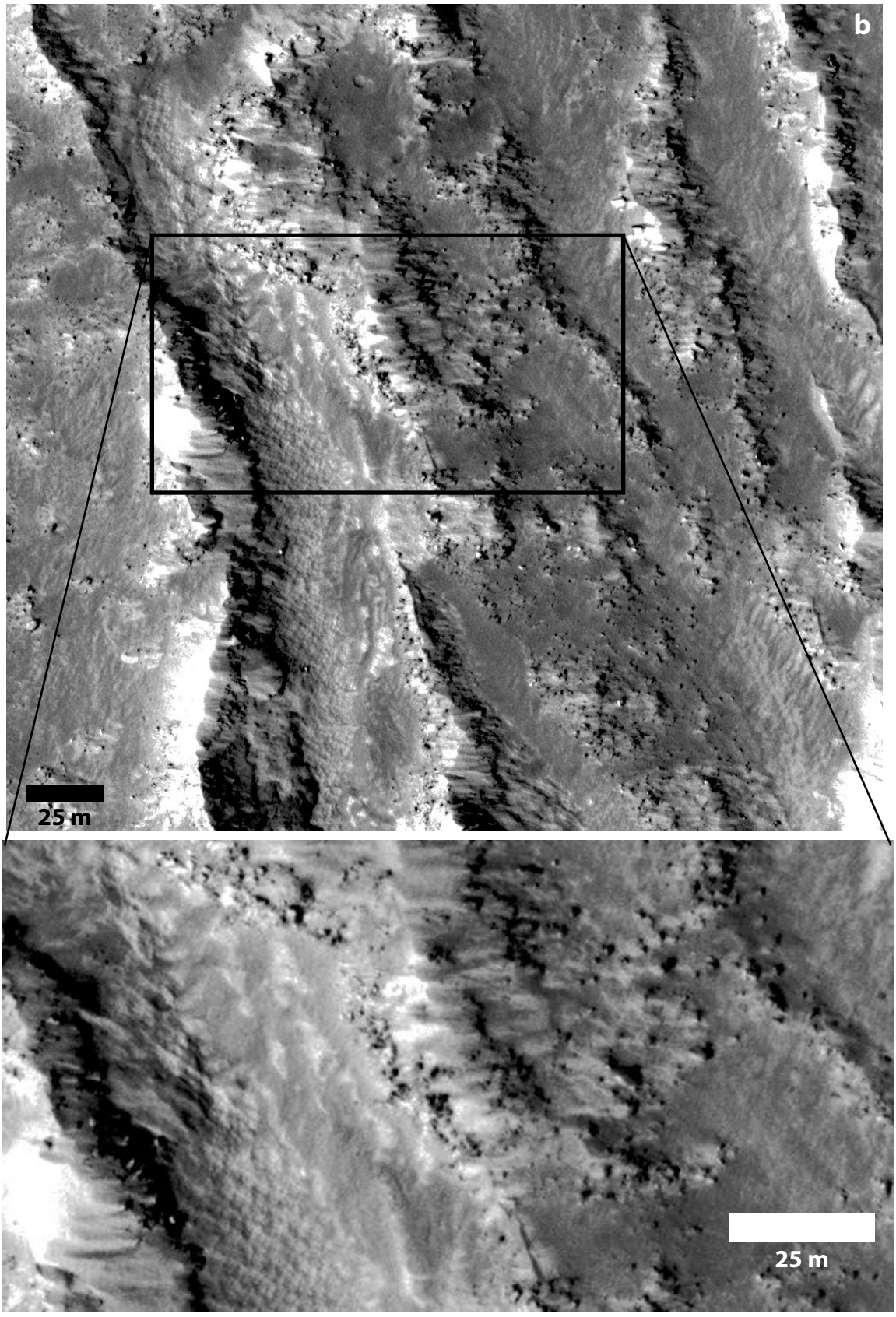

Figure 12b.

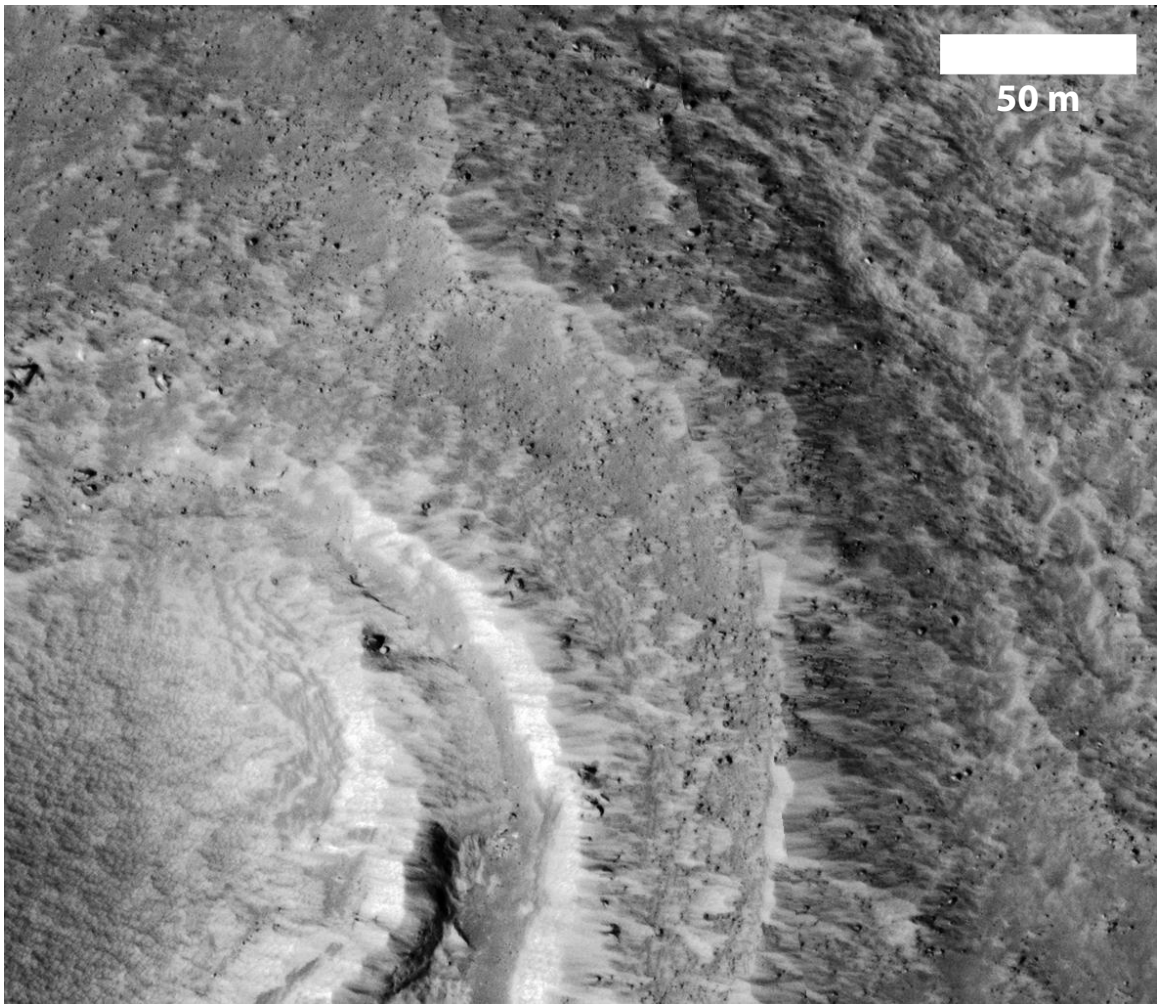

Figure 12c.

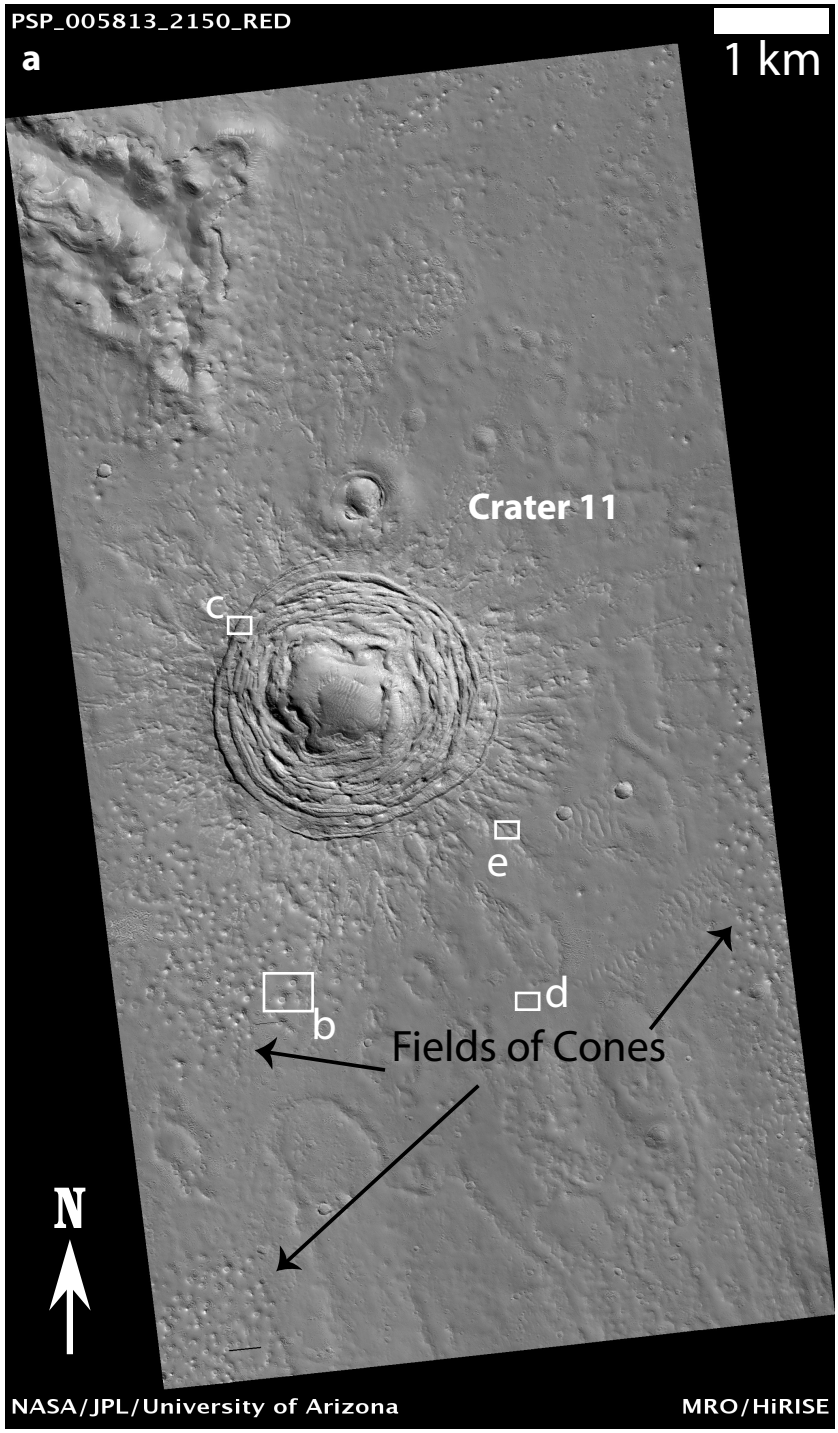

Figure 13. a) HiRISE image PSP_005813_2150 detailing Crater 11 from Chapter 2. Boxes identify locations of 13b, 13c and 13d. Image courtesy of NASA/JPL/University of Arizona. b) Detail of cones observed in terrain surrounding Crater 11. c) Detail of fracture cutting ejecta on Crater 11. d) Surface of proposed mudflow beyond crater ejecta. Note absence of large blocks. e) Detail of ejecta "ray" material with channels. Black arrows identify southern edge of ejecta "ray." White arrows identify channels emanating from ejecta "ray."

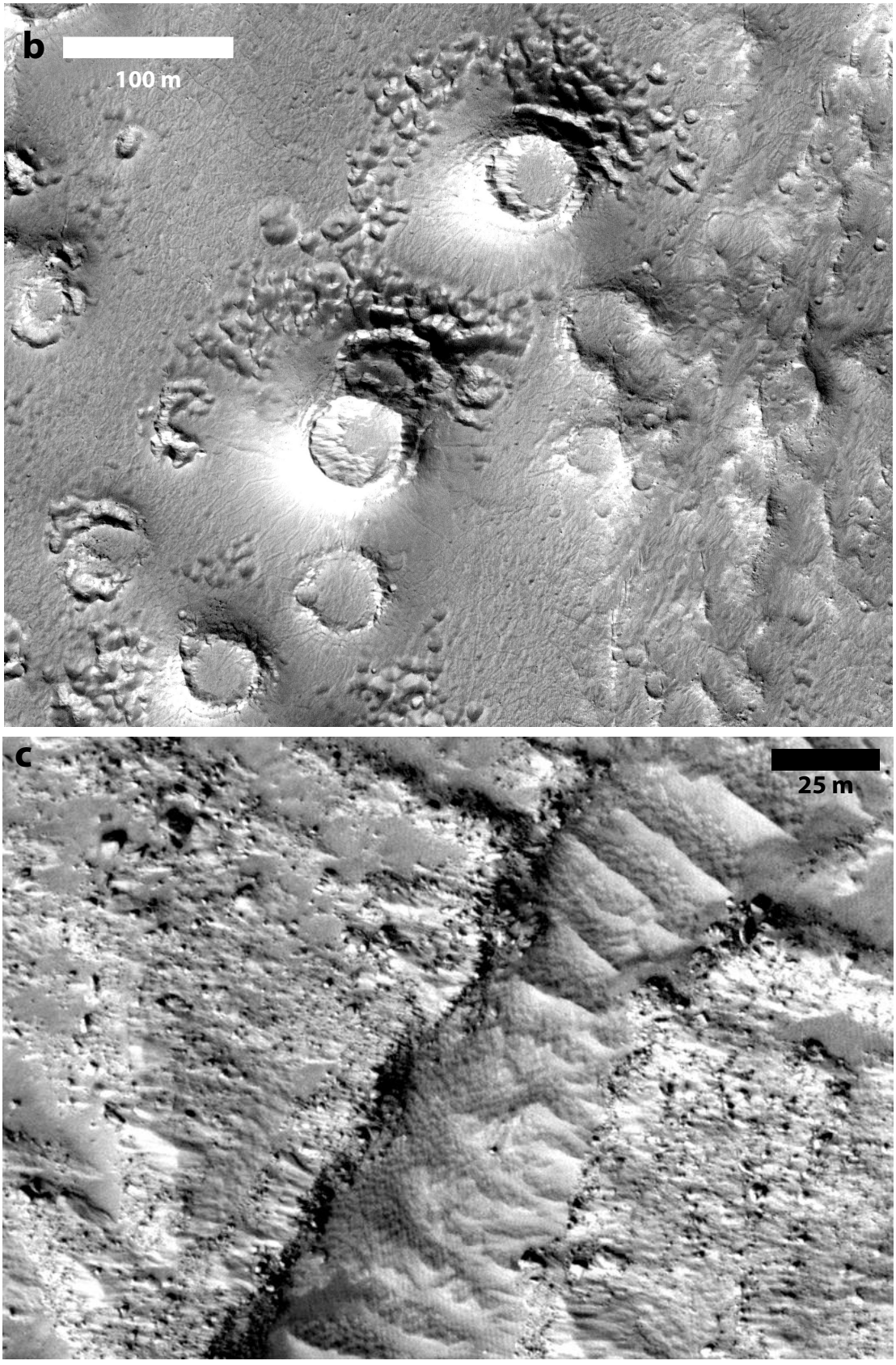

Figure 13b, c.

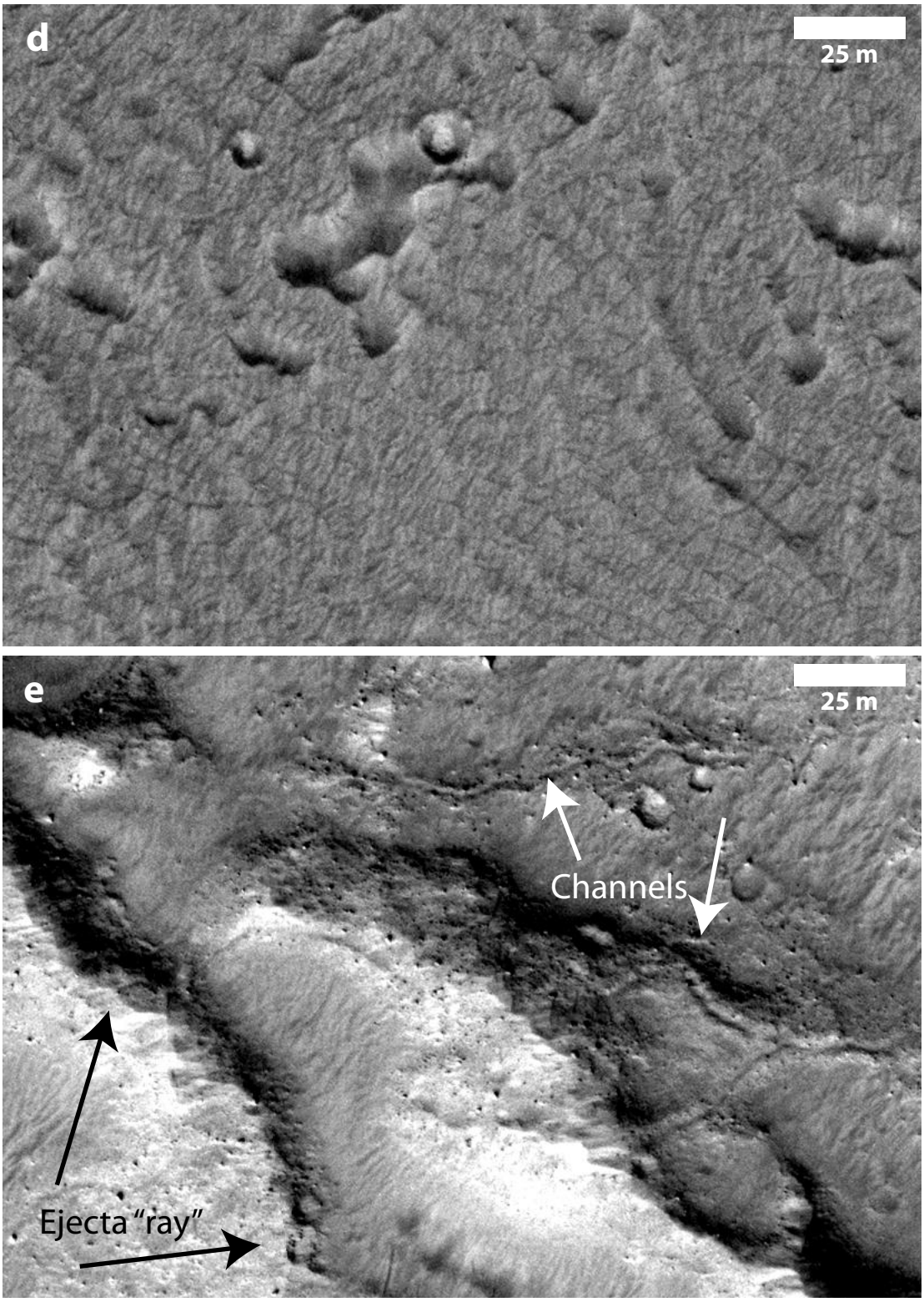

Figure 13d, e.

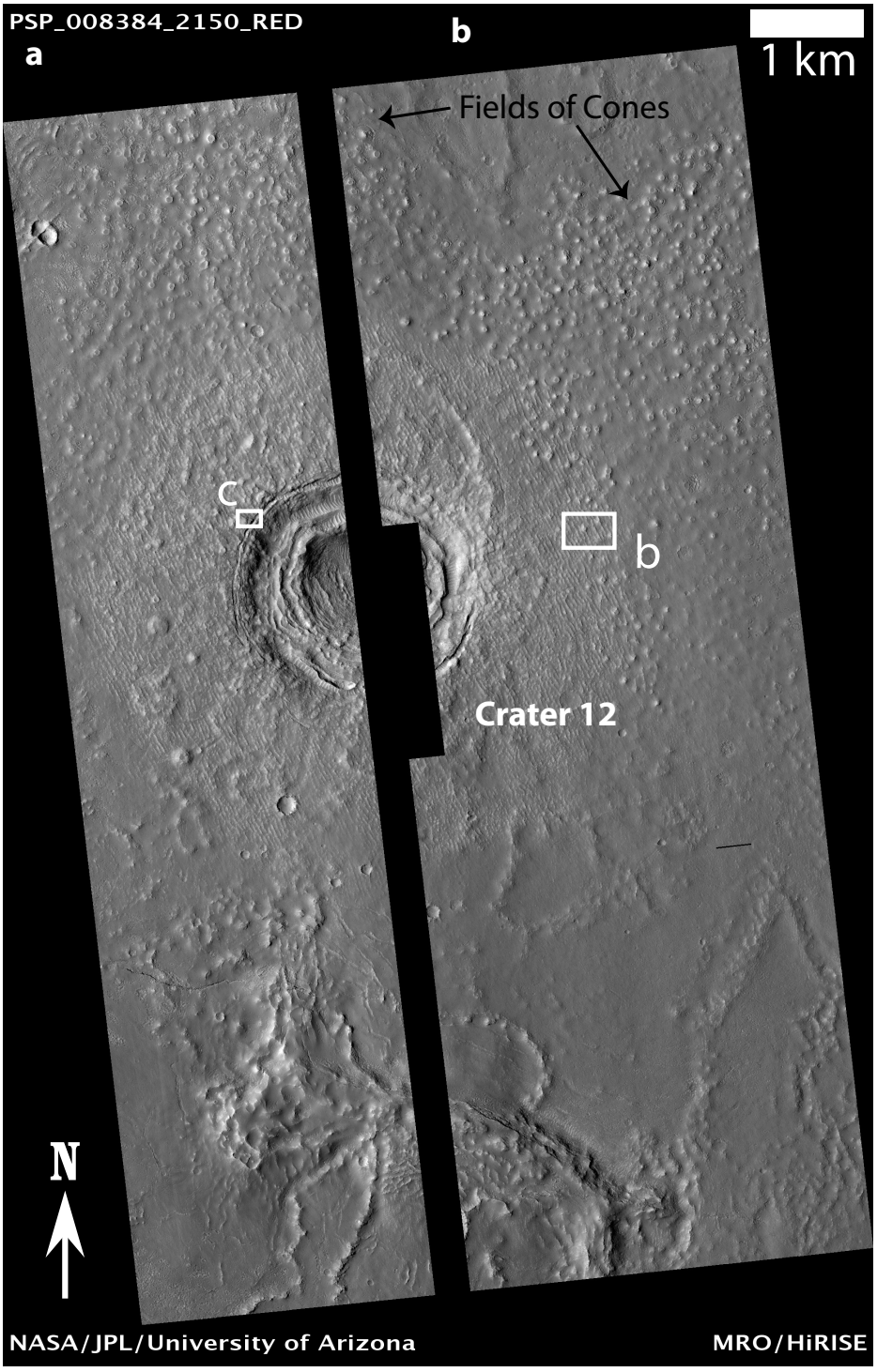

Figure 14. a) HiRISE image PSP_008384_2150 detailing Crater 12 from Chapter 2. Boxes identify locations of 14b and 14c. Image courtesy of NASA/JPL/University of Arizona. b) Detail of ridges and cones observed in terrain surrounding Crater 12. Arrows identify cones observed within ridged ejecta. c) Detail of ejecta and outer fracture to the NW of Crater 12.

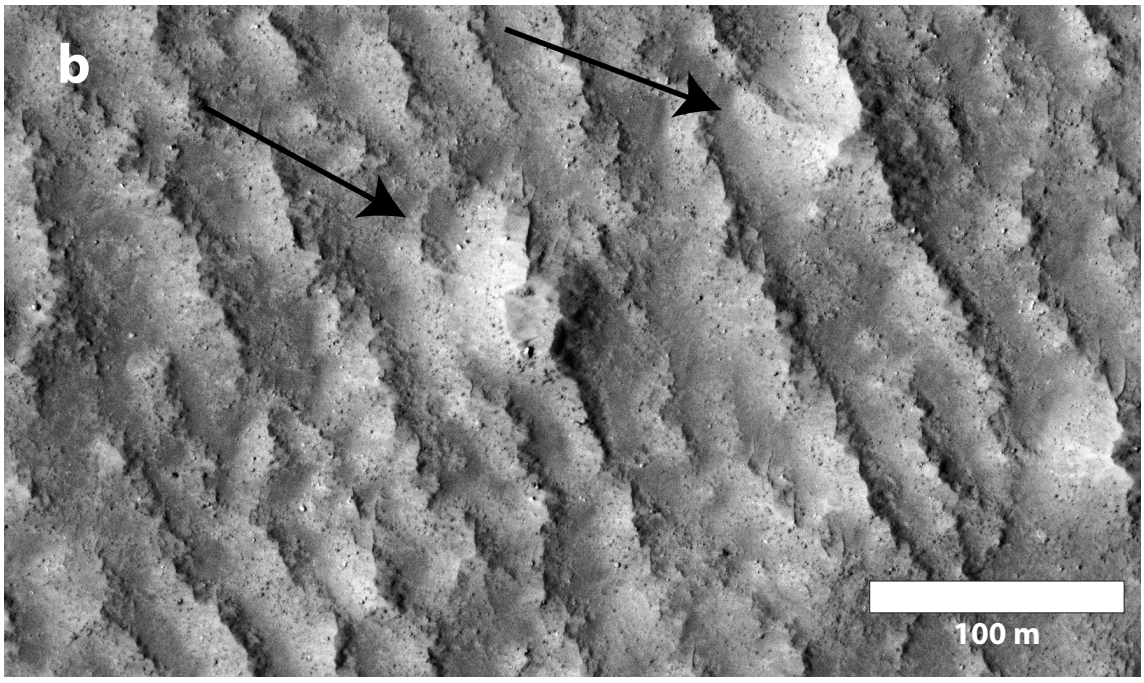

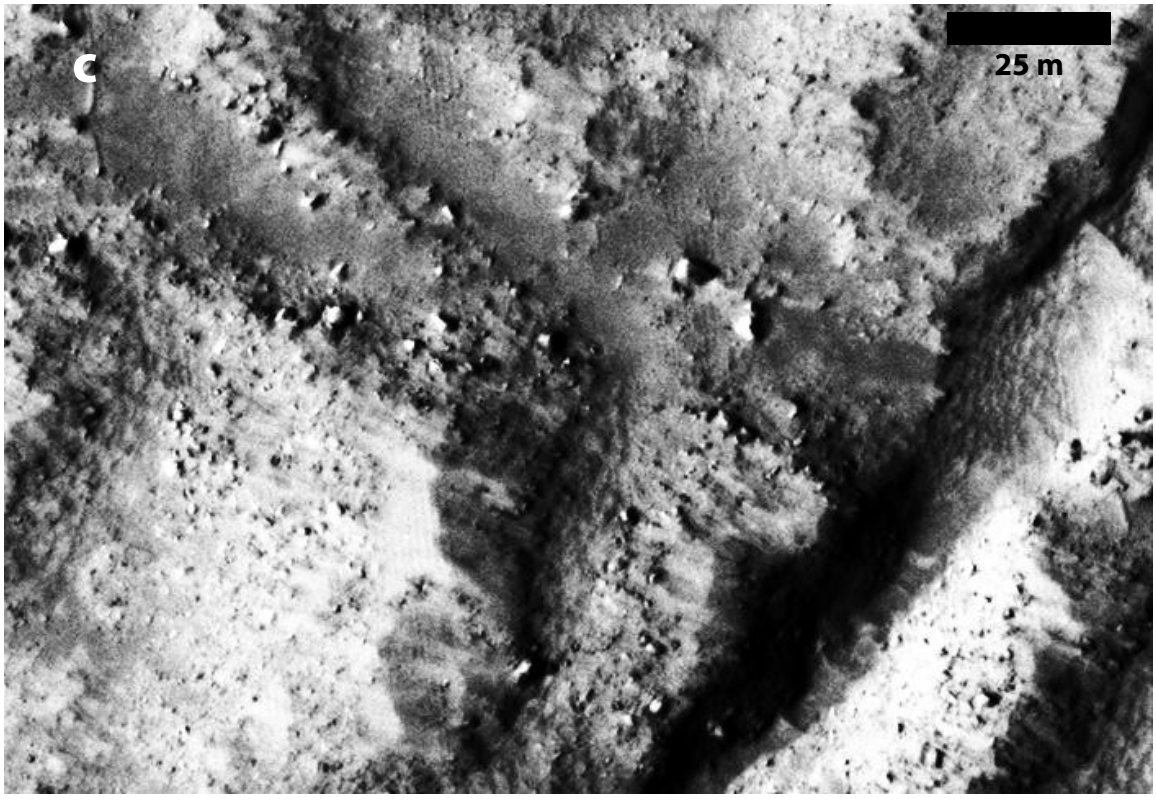

Figure 14b, c

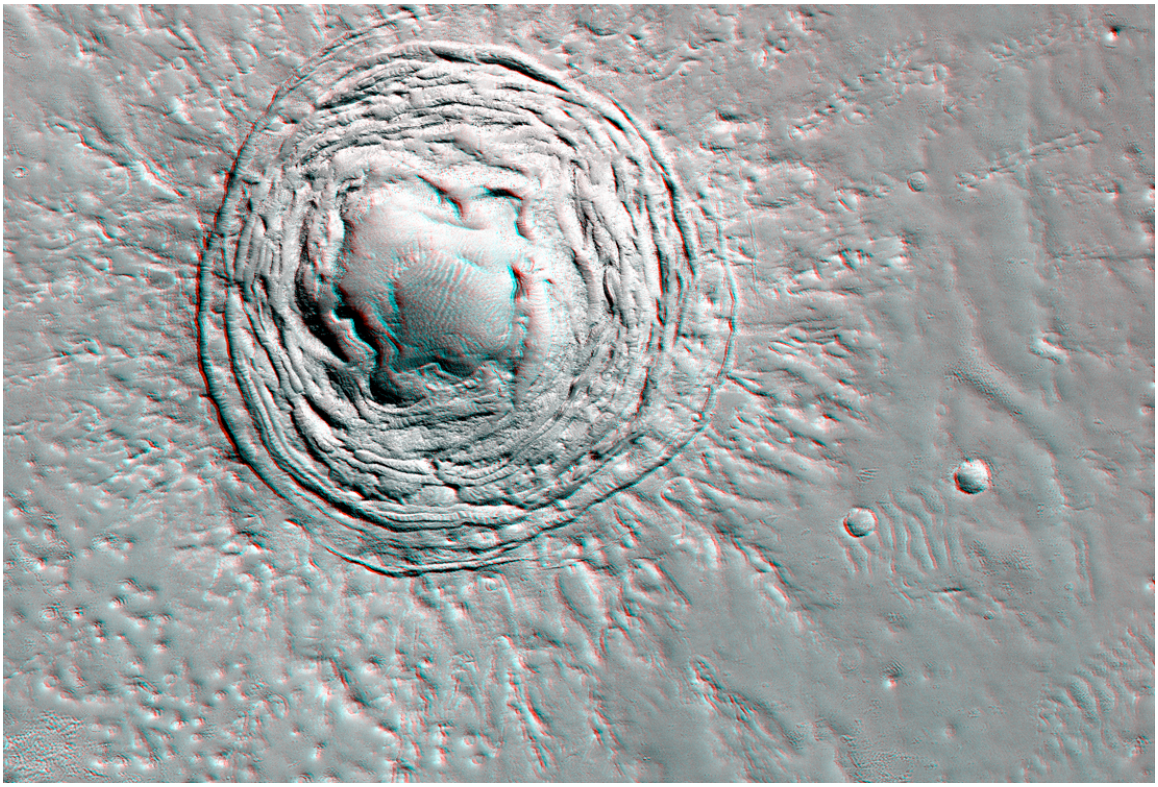

Figure 15. Stereo anaglyph of Crater 11 produced by the HiRISE team at the University of Arizona. Anaglyph derived from HiRISE image PSP_005813_2150 and PSP_005879_2150. Image courtesy of NASA/JPL/University of Arizona.

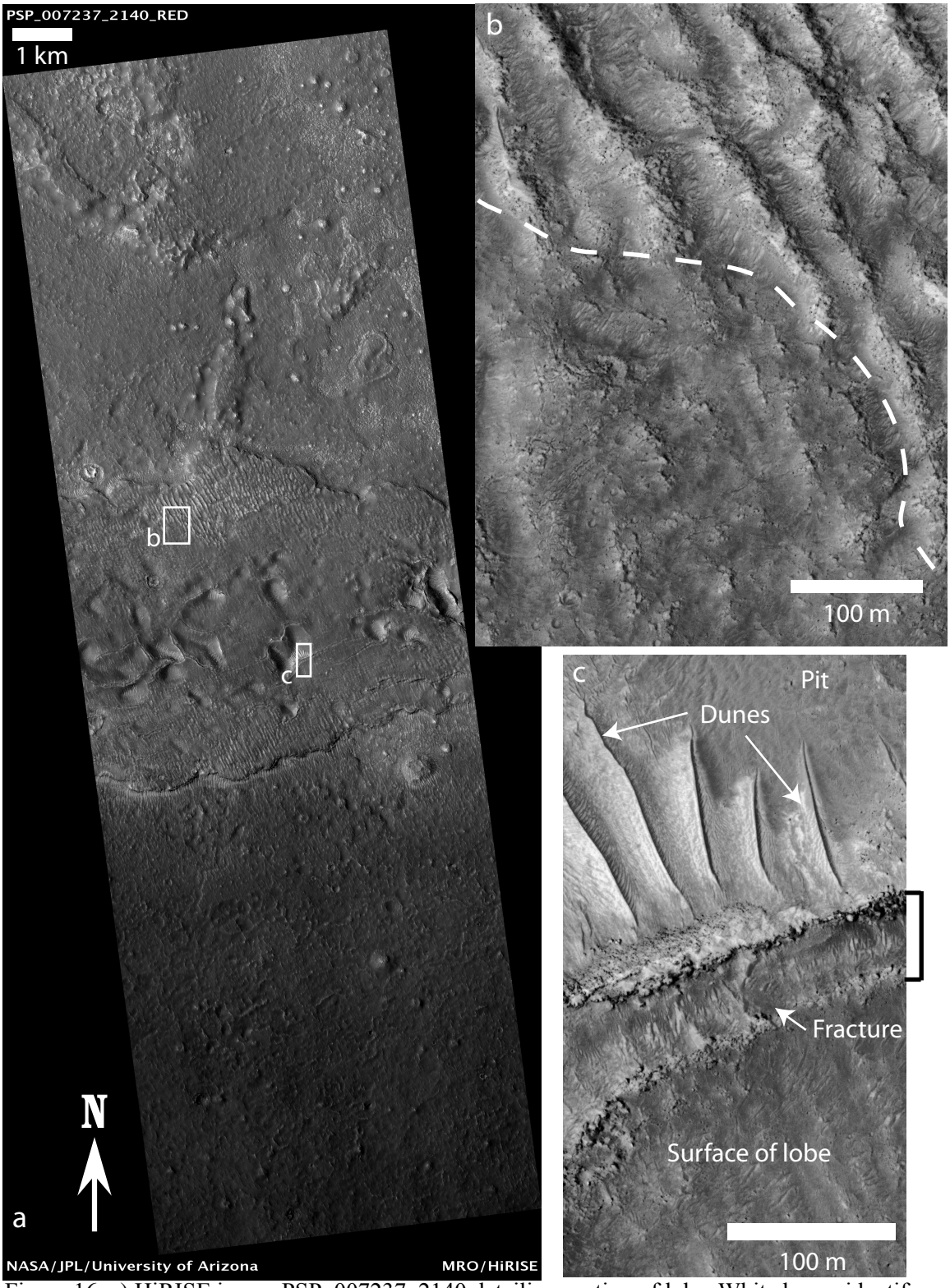

Figure 16. a) HiRISE image PSP_007237_2140 detailing portion of lobe. White boxes identify locations of 16b and 16c. Image courtesy of NASA/JPL/University of Arizona. b) Dashed white line indicates contact between ridges and subdued ridges of lobe. c) Detail of fracture bounding a pit in center of lobe. Width of the fracture is highlighted by the black lines to the right of (c).

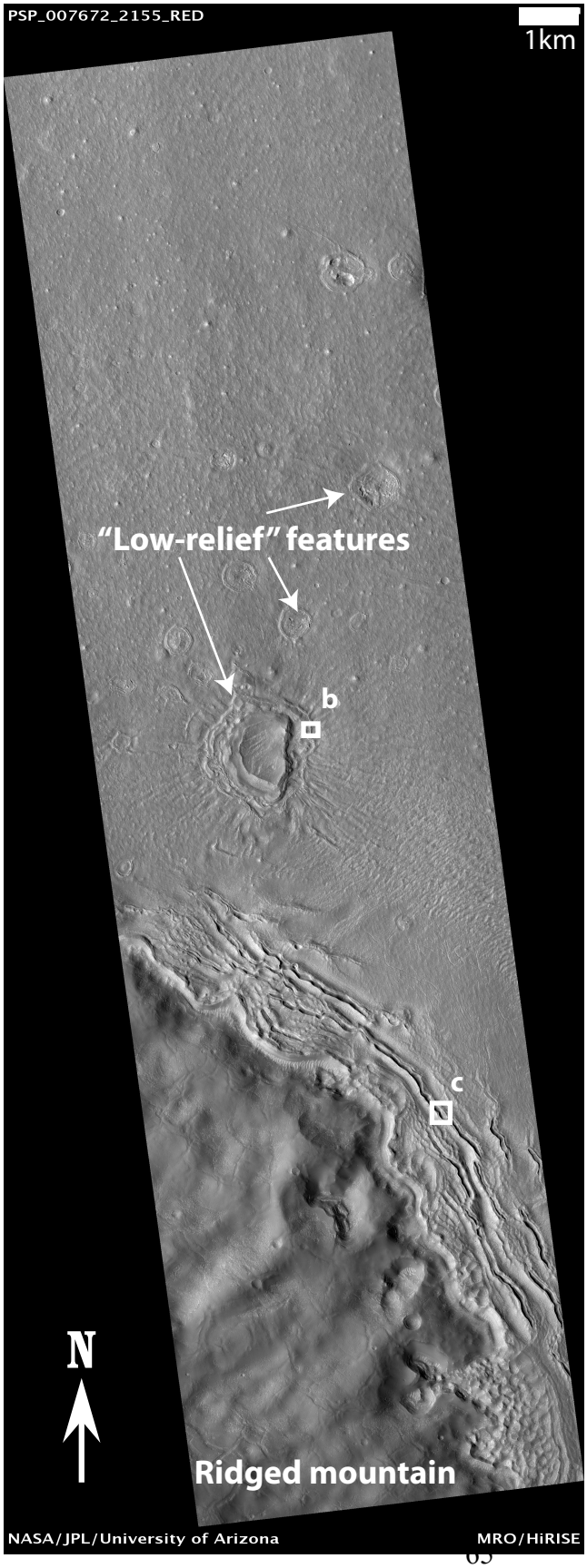

Figure 17 a) HiRISE image PSP_007672_2155 detailing region of "low-relief" features to the northeast of the ridged mountain block. The white boxes identify the locations of 17b and 17c. b) Edge of "low-relief" feature. Note lack of boulder-sized ejecta. c) Detail of fracture near edge of lower mud-flow deposit (see Chapter 2, Figure 8). Note layering on interior of fracture.

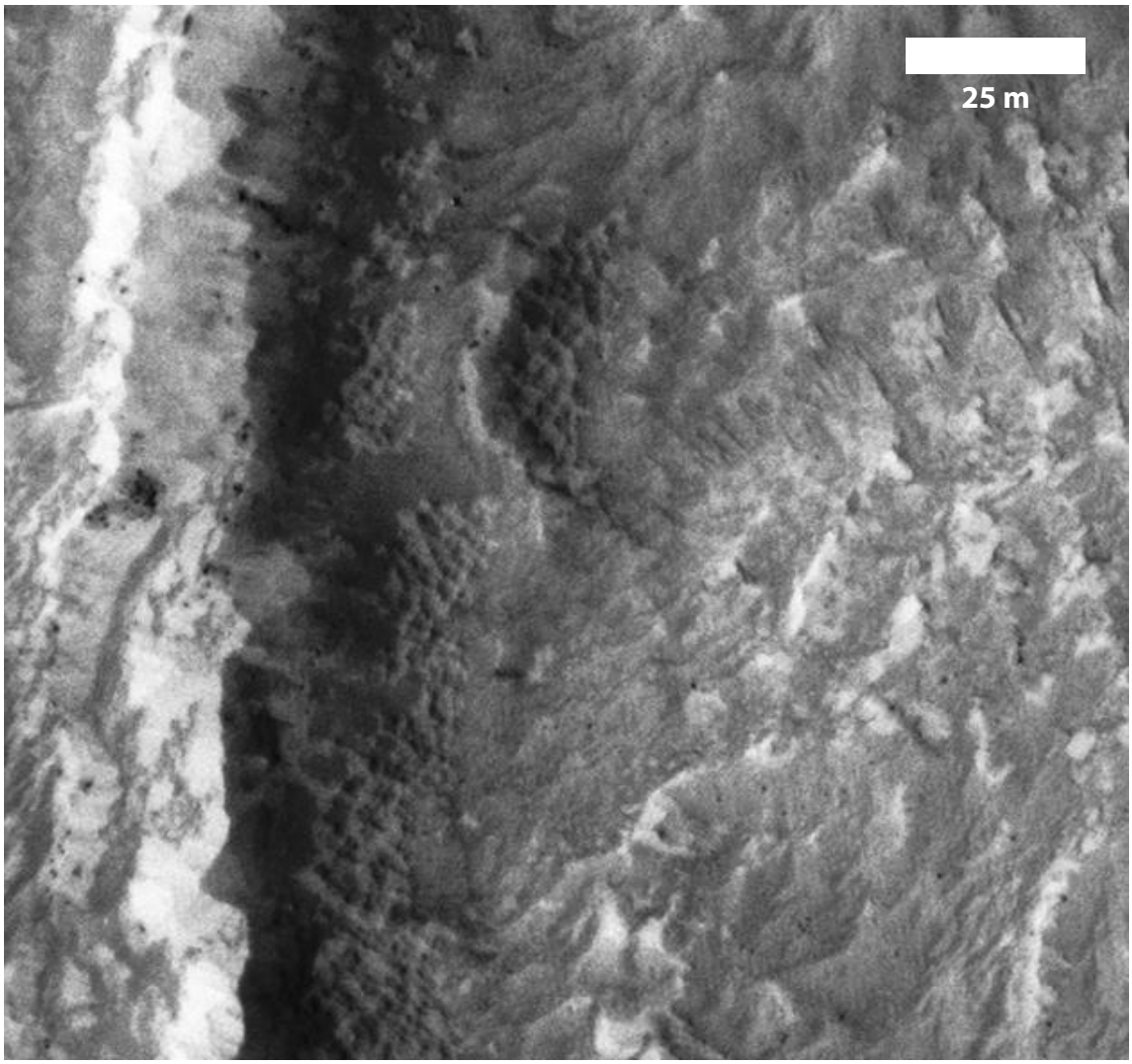

Figure 17b.

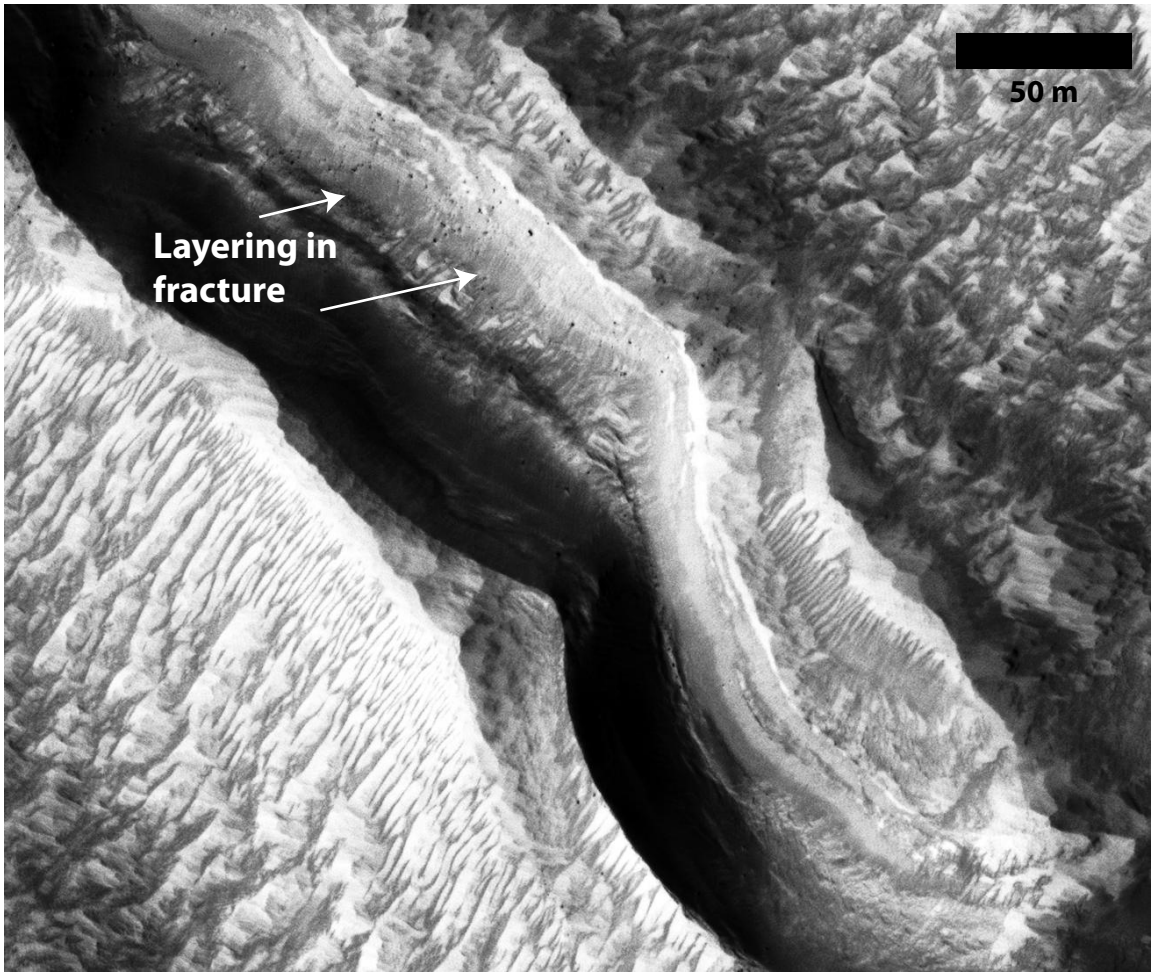

Figure 17c.

CHAPTER 3. THE ROUGHNESS OF HAWAIIAN VOLCANIC TERRAINS

Published in its present form as Morris, A. R., F. Scott Anderson, Peter J. Mouginis-Mark, Albert F. C. Haldemann, Benjamin A. Brooks and James Foster (2008), Journal of Geophysical Research, doi:10.1029/2008JE003079, in press.

Abstract

We performed analyses of topographic variation (surface roughness) using a new 2D mapping method which shows that understanding the relationship between data resolution, Hurst exponent, y-intercept, RMS deviation, and cell size is important for assessing surface processes. We use this new method to assess flows at six field sites in Kilauea caldera, Hawaii, using three datasets at different resolutions, TOPSAR (10 m/pixel), airborne LIDAR (1 m/pixel) and tripod-mounted LIDAR (0.02-0.03 m/pixel). The flows studied include ponded pahoehoe flows, compound pahoehoe flows and jumbled, slabby pahoehoe. The 2D quantification of surface roughness for the Kilauea lava flows indicates that features formed during emplacement and modification of the flows exhibit statistically distinct roughness signatures. The 2D method provides a tool for unit mapping based on surface roughness. Key findings indicate that the new 2D method provides more robust results than 1D methods for surface roughness due to larger 2D sample sizes and the removal of 1D directional bias leading to a reduction in error. Furthermore, dataset resolution relative to the scale of the features under study is important to consider when designing a 2D surface roughness study. Future applications to topographic datasets from Mars will provide information on flow emplacement conditions and spatial and temporal evolution of volcanic provinces on Mars.

1. Introduction

The statistical roughness of a planetary surface is a useful characteristic for planetary mapping [Kreslavsky and Head, 2000], investigating potential landing sites for surface rover mobility [Anderson et al., 2003; Golombek et al., 2003], constraining surface scattering models used in radar investigations [Orosei et al., 2003; Shepard et al., 1995], and interpreting formation and modification processes that affect surface topography [Shepard et al., 2001]. Surface roughness is the expression of the topography at horizontal scales from sub-meter to hundreds of meters and is commonly self-affine, or fractal [Mandelbrot, 1982; Turcotte, 1992]. Self-affine topography can be statistically quantified using the RMS deviation, which is calculated from the RMS (root mean square) of the difference in topography between points separated by a lag or a step [Mandelbrot, 1982; Turcotte, 1992]. However, there are caveats to roughness analysis; for example, Campbell et al. [2003] suggest that the vertical and spatial resolution of altimetry and imaging datasets influence interpretation of surface roughness, particularly extrapolation of roughness estimates below the resolution of the dataset under consideration. Additionally, previous terrestrial studies have demonstrated that the use of linear profiles to characterize surfaces can result in bias due to insufficient sampling of any anisotropic features along the surface [Shepard et al., 2001].

In this paper we examine the effects of variations in the horizontal and vertical resolution of the topographic data on the interpretation of volcanic features on Kilauea Volcano in Hawaii using a new two-dimensional method of calculating surface roughness. Our method uses digital elevation models (DEMs) to calculate three roughness statistics, the RMS deviation at 1 m, the Hurst exponent (H) and the y-

intercept of the line fit in log-log space (see Section 5), which can be compared with results from previous 1D surface roughness studies. We then map and classify these parameters, enabling the identification of flow boundaries and inter- and intra-flow effects such as changes in emplacement mechanism.

Ultimately, we seek to understand the effects of limited-resolution topographic data on the interpretation of volcanic features on the surface of Mars. Unfortunately, current data for the topography of the Martian surface from the Mars Orbiter Laser Altimeter (MOLA) have insufficient resolution for roughness studies of flow emplacement processes [Campbell et al., 2003; Kreslavsky and Head, 2000]. However, current and future topography derived from the Mars Exploration Rovers (MER) [Li et al., 2006; Li et al., 2007] or from the High Resolution Imaging Science Experiment (HiRISE) onboard the Mars Reconnaissance Orbiter (MRO) [McEwen et al., 2007a] with higher resolution will soon be available, suggesting the need to study the behavior of roughness at smaller scales in order to understand how best to use the roughness to map and interpret the surface of Mars. We have therefore tested our methods on the volcanic terrains on the Big Island of Hawaii, which have been extensively measured with spatial resolutions from 2 cm to 10 m, and are useful analogs for Martian topography. Recognizing that Martian flows are more dust mantled than flows in Hawaii, we are using these higher resolution topography datasets and new 2D methods to understand the required resolution for enabling the use of roughness methods to assess terrestrial and Martian flow emplacement processes. In addition, we have assessed ground-truth for our terrestrial observations due to the relative accessibility of the location, enhancing our

ability to interpret the results, and strengthening future interpretation of surfaces we cannot directly observe.

In addition to previously stated goals, we examine the assumptions inherent in using statistical measures of roughness such as RMS deviation and Hurst exponent for studying the behavior of natural self-affine, or scale-dependent, surfaces. We also identify the key factors that must be considered for global-scale surface roughness mapping, such as the Hurst exponent, dataset resolution, RMS deviation at a fixed step size and cell size. In the following sections, we first discuss the previous studies of surface roughness and lava flow emplacement and volcano dynamics. Then we describe the various types of topographic data used in this analysis, including both remotely sensed information and field measurements. Next, we detail the development of the two-dimensional method used to calculate surface roughness statistics, followed by the results of the 2D technique for the field and remotely sensed datasets, as well as discussion of these results.

2. Background

2.1. Surface Roughness

Many surfaces exhibit a power-law relationship between horizontal length scales and statistical measures of vertical roughness, or topographic variation, and are called self-affine, or fractal [Mandelbrot, 1982; Shepard et al., 1995]. We consider one quantitative measure of topographic variation, RMS deviation, as well as the Hurst exponent and y-intercept (the topographic variation of the sample). The power-law dependence between horizontal length scale and RMS deviation is represented by the

Hurst exponent ($0<H<1$), a value characterizing the scaling properties of the topography over a particular range of horizontal scales [Shepard et al., 2001]. Field-based investigations have shown that it is possible for H to change as a function of horizontal scale [Shepard et al., 2001], suggesting that H correlates with the physical processes responsible for surface roughness at a particular horizontal scale [Shepard et al., 2001]. The relationship between surface roughness and H is non-unique, but provides clues to the horizontal scales at which closer examination of physical processes should be undertaken. The description of topographic variation requires the use of at least two separate parameters [Brown and Scholz, 1985; Sayles and Thomas, 1978]. In this study we use H, RMS deviation and y-intercept, as it has been established that the topographic variation is a function of the length of the sample because surface roughness is nonstationary [Brown and Scholz, 1985; Sayles and Thomas, 1978]. Additionally, we examine the coefficient of the power law relationship between horizontal scale and RMS deviation, the y-intercept of the line fit in log-log space. Combining the Hurst exponent and y-intercept allows us to make quantitative interpretations of the surface roughness. Topographic datasets derived from instruments such as MOLA (~465 m/pixel global DEM), the High Resolution Stereo Camera (HRSC, ~12 m/pixel) and HiRISE (~1 m/pixel) can be used to examine the surface roughness of Mars at increasingly finer resolutions, but the relationships among the roughness calculated at each resolution are poorly understood.

2.2. Lava flow emplacement and volcano dynamics

In comparative planetary studies of volcanic landforms, the discrimination between pahoehoe and ‘a‘a lava flows has important implications for the interpretation of the formation and evolution of volcanic activity. For example, studies of the morphology of lava flows on Kilauea Volcano on the Big Island of Hawaii have yielded important information regarding the temporal and spatial evolution of the emplacement of both ‘a‘a and pahoehoe lava flows [Kauahikaua et al., 2003]. Furthermore, the morphology of a lava flow provides clues to the plumbing system of the volcano and the evolution of the plumbing system over time, as demonstrated by the study of pahoehoe and ‘a‘a in the historical records of Kilauea and Mauna Loa [Rowland and Walker, 1990]. For example, Rowland and Walker [1990] were able to infer that the relatively smooth surfaced pahoehoe flows are typical of an open conduit system where magmatic gases decouple from the liquid resulting in long periods of sustained flow at low volumetric flow rates [Rowland and Walker, 1990]. Conversely, ‘a‘a flows are typically the products of high discharge rates from the vent, likely the result of rapid loss of volume from the magma storage chamber [Rowland and Walker, 1990].

The correlations between magma supply, conduit geometry and resulting lava flow types on basaltic shields made by Rowland and Walker [1990] aid in the interpretation of the Hurst exponent for pahoehoe and ‘a‘a. Studies have shown that flow rate [Kauahikaua et al., 2003; Rowland and Walker, 1990] and crystallinity [Cashman et al., 1999] can be inferred from the textures observed in cooled lava flows. On Kilauea Volcano, lava is often erupted as fairly smooth-surfaced or ropy pahoehoe and later transitions to rubbly, clinkery-surfaced ‘a‘a, as the volumetric flow rate of a given packet

of lava increases [Kauahikaua et al., 2003; Rowland and Walker, 1990]. The increase in volumetric flow rate may occur as the result of an increase in slope, a blockage in the lava pathway along the ground, or an increase in effusion rate at the vent [Kauahikaua et al., 2003]. The higher volumetric flow rate causes the lava flow to exceed the strain rate necessary to disrupt the moving flow surface structure [Kauahikaua et al., 2003]. Surface disruption of the moving flow results in a rough surface texture on the meter to sub-meter scale, typical of an ‘a‘a flow [Rowland and Walker, 1990]. In addition, studies of solidified lava crystallinity indicate a higher percentage of plagioclase microlites in solidified ‘a‘a versus solidified pahoehoe, suggesting crystals may also play a role in the transition from pahoehoe to ‘a‘a [Cashman et al., 1999]. Assuming no subsequent modification of a flow surface (for example, by weathering), the results of the Cashman et al. [1999] study suggest that inferences regarding the crystallinity of a remotely sensed lava flow may be made based upon the surface roughness.

2.3. Summary

We therefore seek to quantify the small-scale topographic differences among the surfaces of lava flows on Kilauea Volcano in Hawaii in preparation for future identification and analysis of geologically similar lava flows on Mars. Constraining the spatial and temporal variations of flow formation processes on Mars will provide an additional tool for use in geological mapping and interpretation, thus providing a more complete picture of surface evolution. In addition, we hope to constrain the physical processes affecting the roughness of flows in Kilauea caldera, and by analogy, for flows on Mars. Using the basaltic flows of Kilauea as an analog to Mars is likely appropriate, as

previous investigations of the spectral character of the surface of Mars indicate that the dominant composition of the surface materials is basaltic [Bandfield et al., 2000]. In addition, newly identified volcanic features have been revealed by data from instruments such as the Thermal Emission Imaging System (THEMIS) visible camera [Mouginis-Mark and Christensen, 2005]. The recently mapped volcanic constructs on Mars include features such as elongate vents, akin to the terrestrial volcanic fissures that have fed several of the caldera-filling Kilauea flows, and may provide ideal locations for topographic roughness analysis in future work.

3. Data

The terrestrial topographic data used in this study are evenly spaced DEMs that cover a range of horizontal and vertical resolutions (Figure 1). The datasets and the techniques for collecting these data are described in detail in the following sections.

3.1. TOPSAR

The 10 meter/pixel TOPSAR DEM covers an area ~40 km by 12.8 km [Rowland et al., 1999] and the data coverage extends from the coastline up to the summit caldera of Kilauea Volcano (Figure 2). The C-band data (5.6-cm wavelength) were collected on 30 September 1993 using an airborne synthetic aperture radar [Rowland et al., 1999]. A detailed field investigation of the accuracy of these TOPSAR data by Rowland et al. [1999] demonstrates that the vertical accuracy of the dataset is approximately 1-2 meters.

3.2. Airborne LIDAR

The airborne LIDAR data were collected in January 2004 by Airborne 1, a commercial company (http://airborne1.com/), and cover an area ~7.7 km by 4.9 km on the southern portion of the summit caldera of Kilauea Volcano, overlapping the TOPSAR data described above [Mouginis-Mark and Garbeil, 2005]. The footprint of the LIDAR instrument was 30 cm and multiple flight lines were flown across the caldera [Mouginis-Mark and Garbeil, 2005]. The data have been processed and gridded with a resolution of 1 m/pixel and a vertical accuracy of ~2 cm [Mouginis-Mark and Garbeil, 2005] (Figure 3).

3.3. Tripod-mounted LIDAR

We used a tripod-mounted LIDAR (T-LIDAR) system to obtain high resolution DEMs (2-3 cm pixel spacing) of 225-625 m^2 areas within Kilauea caldera (Figure 4). The data were collected from 5-7 June 2007. We employed an Optech ILRIS-3D scanning LIDAR instrument and the technical overview can be obtained at http://www.optech.ca/i3dtechoverview-ilris.htm. The laser is a 1.5 μm, Class 1 (eye safe) instrument with a 40º x 40º field of view. The ILRIS-3D has a sampling rate of 2500 points per second and a company-stated accuracy of 7 mm at 100 m distance. In order to balance survey time, posting and surface coverage, the area surveyed at each field site was ~ 400-1000 m^2 surveyed at a posting of 4 mm in the near field, with point spacing as large as 2-3 cm in the far field. To minimize the effect of large point spacing and shadowing in the far field, a minimum of two separate scan directions with widely varying azimuths (minimum of 150º separation) were collected at each field site. The

instrument outputs a point cloud with x, y and z coordinates, typically composed of several sub-scans, depending on the size of the area under consideration. Post-processing of the xyz data is performed using the PolyWorks software package from InnovMetric. A full description of the software package can be found at http://www.innovmetric.com/. Internal alignment of sub-scans is performed first, followed by alignment of adjacent scan areas. Once the point clouds for one entire field site were aligned, the data were gridded using the Generic Mapping Tools (GMT) with a grid cell resolution of 2 cm for sites B-F and 3 cm for site A.

4. Field sites

Six field sites, representative of the range of roughness at Kilauea, and for which previous roughness estimates were available [Campbell and Shepard, 1996], were used to test our new 2D method (Table 1). The surfaces selected as field sites cover several different eruptions within the caldera (Figures 3, 5), including the 1885, April and September 1982, and July and September 1974 flows. Hurst exponent and surface roughness (y-intercept) maps were generated using the methods described below for both the TOPSAR and airborne LIDAR datasets, and the maps were examined to determine the variations in roughness within the caldera. GPS coordinates of these locations were recorded to verify the location of the field sites within the geo-referenced airborne LIDAR and TOPSAR maps.

Site A is located within a ponded pahoehoe unit (Figure 3), a product of the July 1974 eruption within the Kilauea caldera (Figure 5). The surface is composed of large solidified lava plates, flat or sometimes slightly curved and generally 2-5 m in extent

(Figure 4a, 6a). Overall surface relief within the unit is low, typically on the order of 30-40 cm at the decameter horizontal scale, and the majority of the surface roughness is covered by cm-sized glass chips spalled off of the exterior of the flow. Festoons are visible on the surface of the 1974 flow when observed from ~30 meters elevation (from the Byron Ledge Trail on the caldera wall). Sparse vegetation (widely spaced bushes < 1 m high) has begun to take root in the cracks between the large plates.

Site B is located near the base of the nearly vertical caldera wall just west of Halemaumau pit crater (Figure 3) in an area of smooth pahoehoe flows erupted in September 1974 (Figure 5). The pahoehoe flows exhibit expanses of large plates similar to Sites A and C, with interspersed areas of folded lava flows with individual folds on the order of 20-30 cm across and 10-20 cm high (Figure 6b). The surface is highly broken up and cm-sized glass chips litter the area between folds. The site is downwind from the actively degassing Halemaumau pit crater and the April 1982 line of spatter cones within the caldera, which appear to have resulted in the chemical alteration of the flows by the sulfur dioxide continually released from the cooling magma reservoir. The glassy selvages on the pahoehoe flows are coated with a white material, which previous work has shown is likely a combination of alteration products such as a phyllosilicate (clay minerals), palagonite and iron and aluminum hydroxides [Konhauser et al., 2002]. Additionally, recent work by Minitti et al. [2007] find that alteration products of glass-rich basalts from Kilauea are predominantly hydrated silica with minor amounts of iron, titanium and sulfur-bearing minerals. They note that these products are likely to have formed by the leaching and/or dissolution of glass-rich basalts in aqueous, oxidizing, or acidic conditions, with subsequent deposition of insoluble minerals [Minitti et al., 2007].

Site C is located within a ponded pahoehoe flow from the September 1982 eruption within the caldera (Figures 3 and 6). The ponded flow exhibits festoon ridges with an approximate wavelength of 1-1.5 m. Few folds or toes are evident on the surface of the unit, and the typical relief of the festoons is < 50 cm on the decameter horizontal scale (Figure 6c). Similar to Site A, the primary contributions to the surface roughness at horizontal scales less than one meter are small glass chips spalled from the exterior of the basalt flow.

Site D is located within the same September 1982 flow unit as Site C (Figure 5), yet exhibits a noticeably rougher texture on the meter to decimeter scale (Figure 6d). Site D is near the vent area for the September 1982 eruption (Figure 3), and is characterized by tumuli, billows and pahoehoe toes with an overall relief of ~2-3 m on the decameter horizontal scale. The surfaces of the tumuli still appear highly glassy, with elongate vesicles exposed where the glassy rind has been spalled. The tumuli are also characterized by extrusions of highly degassed pahoehoe toes that result in smooth, featureless lobes within the flow field.

Site E is the roughest site investigated in this study and is located in blocky, jumbled pahoehoe flows just south (down flow) of the April 1982 spatter ramparts that extend east-northeast from Halemaumau (Figures 3 and 6). The jumbled pahoehoe flow exhibits tilted plates typically 80-100 cm across (with a few plates up to 3 m across) characterized by surfaces covered by jagged pieces of broken vesicles. There is little smooth, glassy material in this location. Unfortunately, the TOPSAR and airborne LIDAR data do not provide overlapping coverage of any true ‘a‘a flows, so this site was used as a proxy for a rougher ‘a‘a-like flow. Indeed, our experience with LIDAR data for

Mauna Iki, a satellitic shield on the east rift zone of Kilauea, shows that the low signal return from ‘a‘a surfaces makes it very difficult to produce a LIDAR DEM from a true ‘a‘a flow.

Site F is located within a devitrified, oxidized pahoehoe flow field identified as the oldest flow on the caldera floor (Figure 5). In the field, the relief within the exposed flow field is on the order of 2-3 meters, with tumuli appearing to form the majority of the relief. Individual pahoehoe toes are typically 1-2 meters across near their termini and the surfaces of the pahoehoe billows have lost their glassy selvage, leaving a zone of vesicle concentration exposed to the atmosphere (Figure 6f). The flows appear matte brown-gray to the naked eye and re-vegetation has been initiated in the cracks between billows. Although vegetation was present here and at Site A, we did not remove it from any of the three datasets, as the vegetation was sufficiently sparse and widespread that we believe the surface roughness will not be significantly affected. This location is not one of the sites used by Campbell and Shepard [1996] in their roughness study of Kilauea, but was selected due to the relatively high Hurst exponent derived from the airborne LIDAR DEM.

5. Two-dimensional roughness method

Previous workers have extensively discussed the development of models for calculating the statistical roughness of self-affine natural terrestrial surfaces using several different approaches [Butler et al., 2001; Campbell and Shepard, 1996; Shepard et al., 1995; Shepard et al., 2001; Turcotte, 1992]. The traditional approach utilizes profiles or transects across a surface of visually homogenous apparent roughness, often in

orthogonal directions, to calculate RMS deviation or variance (the square of RMS deviation) for increasing step sizes [Campbell and Shepard, 1996; Shepard et al., 1995]. However, the roughness of natural surfaces is often anisotropic [Shepard et al., 2001], leading to a bias in the calculated RMS deviation and resulting Hurst exponent and making a map-based roughness calculation a potentially powerful approach to understanding surface roughness. In the profile method, unit boundaries are pre-selected on the basis of visually derived apparent roughness, whereas in the map-based analysis, unit boundaries are not pre-determined. In addition, using a two-dimensional analysis enlarges the available roughness dataset from select, directional-dependent profiles to a non-preferential analysis of the entire surface under investigation. One caveat of using the 2D roughness method is that, as the cells become larger, inclusion of topography outside the desired region leads to contamination of the surface roughness of that particular unit. We propose a method for minimizing contamination in Section 7.a.iii.

Calculation of the statistical roughness parameters in two dimensions requires the use of a DEM and modification of the commonly used profile-based roughness calculation methods. Here we first describe the approach in terms of previous models followed by the adaptations made in this study in order to maximize the full potential of the data in two dimensions.

As mentioned above, RMS deviation is the RMS height difference between points separated by a lag or step. The RMS deviation is a function of lag or step size and for use in profile studies is given by

$$v(\Delta x) = \sqrt{\frac{1}{n}\sum_{i=1}^{n}\left[z(x_i) - z(x_i + \Delta x)\right]^2} \qquad (1)$$

where n is the number of samples, z is the elevation, and Δx is the step size. The RMS deviation of self-affine surfaces scales with the distance between samples along a one-dimensional profile (Δx) [Shepard et al., 2001]. The relationship between the RMS deviation and the step size is given by

$$\upsilon(x) = \upsilon(\Delta x_0)\left[\Delta x / \Delta x_0\right]^H = \upsilon_0\left[\Delta x / \Delta x_0\right]^H \tag{2}$$

where H is the Hurst exponent ($0 < H < 1$). The RMS deviation and step size are plotted against one another on a log-log graph, known as a deviogram, for which the slope of the line is the Hurst exponent and the y-intercept of the linear fit represents topographic variation at that range of scales. Previous work has shown that the Hurst exponent can change as a function of scale, indicating that different underlying geologic processes may be affecting the roughness of the surface [Shepard and Campbell, 1999; Shepard et al., 2001].

To calculate the roughness of a region, we start with an equally spaced DEM and divide it into square sub-groups of pixels, or cells, of a predetermined size. In order to obtain enough data points for statistically valid results, each of these cells is 10 times larger than the maximum step size used for calculation of the Hurst exponent [Shepard et al., 2001]. Next, all possible offsets (steps) between pixels are identified and the RMS deviation of a point on the surface as a function of step size is then calculated for all pixel pairs within the cell and is given by a modified version of equation 1:

$$\upsilon(\Delta x,\Delta y) = \sqrt{\frac{1}{m}\frac{1}{n}\sum_{i=1}^{m}\sum_{j=1}^{n}\left[z(x_i,y_j) - z(x_i+\Delta x, y_j+\Delta y)\right]^2} \tag{3}$$

where m and n are the number of samples in the x and y directions, z is the elevation, and Δx and Δy equal the step size in the x and y directions. The deviation needs to be calculated for all step sizes of the same magnitude, though this may represent different lateral and vertical shifts of the DEM, so the scalar distance of a shift is determined by

$$\Delta d = \sqrt{\Delta x^2 + \Delta y^2} \,. \tag{4}$$

Similar to the profile case, the RMS deviation of self-affine surfaces is a power law that scales between scalar distance (Δd) and υ(x,y):

$$\upsilon(x,y) = \upsilon(\Delta d_0)\left[\Delta d / \Delta d_0\right]^H = \upsilon_0\left[\Delta d / \Delta d_0\right]^H . \tag{5}$$

We use the calculated RMS deviation and the step size to derive a deviogram, Hurst exponent and y-intercept for each cell. For each cell, the y-intercept of the log-log plot is then mapped as an image, providing a quantitative 2D view of surface roughness within the entire available topography dataset. Additionally, the Hurst exponent is also mapped as an image, providing a map view of the scaling properties of each cell in the topography dataset.

A similar 2D approach has been used for investigation of river-bed roughness [Butler et al., 2001]. A 2D variogram (the square of the deviogram) was used to calculate directionally dependent estimates of the fractal dimensions of gravel-bed rivers, based on an equation similar to the one we describe above [Butler et al., 2001]. The primary difference between the two equations is that in the work of Butler et al. [2001], the 2D method was used directionally to assess homogeneity of the river bed, as opposed to using it in a mapping sense, as we do in this study. Butler et al. [2001] find that the method identifies two characteristic fractal bands within the river; one band associated

with the sub-grain scale and one band associated with the grain scale. Butler et al. [2001] suggest that the anisotropic signal of the downstream flow is revealed by 2D fractal analysis, providing a more complete picture of the structure of gravel-bed rivers. The findings of Butler et al. [2001] suggest that the 2D analysis is a useful tool for determining roughness characteristics of natural, potentially anisotropic surfaces such as lava flows.

6. Kilauea results: Application to T-LIDAR, airborne LIDAR and TOPSAR data

Maps of the Hurst exponent and y-intercept were generated from the TOPSAR, airborne LIDAR and T-LIDAR data using the two-dimensional technique described in the previous section. The Hurst exponent and y-intercept maps were generated for cell sizes of 300 m and 1000 m for TOPSAR (Figure 7), to 30 m and 100 m for airborne LIDAR (Figure 8), down to 0.9 m and 1.5 m for T-LIDAR (Figure 9). The 300 m cell size TOPSAR Hurst exponent map illustrates the scaling behavior of the topography for step sizes from 10 to 30 m (Figure 7a), while the 1000 m cell size map illustrates the scaling behavior for step sizes from 10 to 100 m (Figure 7b). The 30 m cell size airborne LIDAR Hurst exponent maps illustrate the scaling behavior for step sizes from 1 to 3 m (Figure 8a) and the 100 m cell size Hurst exponent map illustrates the scaling behavior from 1 to 10 m (Figure 8b). The T-LIDAR Hurst exponent maps illustrate the scaling behavior of Site A from 0.02 to 0.09 m in 0.9 m cells (Figure 9a) and from 0.02 to 0.15 m in 1.5 m cells (Figure 9b). For comparison of the scaling behavior to the topographic variation, the y-intercept of the linear fit in log-log space is illustrated in maps with the same cell sizes as the Hurst exponent maps, where high values of the y-intercept indicate

higher variance in the topography, or a rougher surface (Figures 7c,d; 8c,d; 9c,d). The TOPSAR data were useful in obtaining an overview of the roughness of the entire volcano, but the spatial resolution and vertical accuracy were far too coarse to differentiate flows within the caldera. As mentioned in Section 3.a., the vertical accuracy of the TOPSAR dataset is 1-2 m [Rowland et al., 1999], significantly larger than the observed roughness of the majority of the lava flows in this study. As a result, we primarily focus on the T-LIDAR and airborne LIDAR results.

In general, the calculated absolute roughness variations correlate well with observed geology. The results for the step sizes between 0.02 m and 0.15 m (T-LIDAR) are consistent with the geology observed in the field for each of the sites (Figure 10). At the smallest scales (T-LIDAR), Sites A and C have the lowest RMS deviation, while Sites B and D have the next highest values and Sites E and F are the roughest (have the highest RMS deviation at 1 m step size). At the 1 to 10 m step sizes (airborne LIDAR), Sites D, E and F have the highest RMS deviations and highest average Hurst exponents (Table 1), while the ponded pahoehoe flows at sites A, B and C exhibit the lowest RMS deviations and lowest average Hurst exponents (Figure 11). At step sizes between 10 and 100 m (TOPSAR), the sites closest to the caldera wall, particularly sites A and B (Figure 3), exhibit a marked increase in RMS deviation at the large scales due to the influence of the nearly vertical cliffs bounding the caldera (Figure 11). The y-intercepts of the linear fit to the deviograms also provide useful information regarding the topographic variation (Table 2). Sites A, B and C all have the lowest y-intercepts at the T-LIDAR and airborne LIDAR scales (and thus have less variance), while sites D, E and F are all rougher (have more variance) at the 0.02 to 10 m scales (Table 2). The inconsistency of the topographic

variation across the airborne LIDAR and TOPSAR datasets at Sites E and F will be discussed in the following sections.

6.1. Site A

The deviogram from site A exhibits a low Hurst exponent at T-LIDAR scales (H=0.28±0.09), moderate Hurst exponent at the airborne LIDAR scale (H=0.40±.002) and a fairly high Hurst exponent at the TOPSAR scale (H=0.78±0.05) (Table 1; Figure 11a). The y-intercepts of the linear fit of the log-log plot are 0.02 m for T-LIDAR, 0.16 m for airborne LIDAR and 0.37 m for the TOPSAR data (Table 2). In the T-LIDAR deviogram, there appears to be a slight change in behavior at ~ 0.10 m, where the slope of the deviogram becomes steeper with increasing step size (Figure 11a). The small change in the Hurst exponent at ~10 cm step size is likely reflecting the spallation of glass chips from the surface of the ponded flow and the resulting increase in measured RMS deviation from the presence of cm-sized glass chips littering the surface at the smallest scales and a decrease in the variance of the surface roughness (y-intercept) due to infilling of topography at the decimeter scale. No statistically valid change in the Hurst exponent is observed in the airborne LIDAR deviogram; the RMS deviations increase consistently with increasing step size. The difference in the y-intercepts of the T-LIDAR (0.02 m) and airborne LIDAR (0.17 m) data reflects the increase in topographic variance with increase in scale, which is likely the result of increased variance from the large (2-5 m diameter) lava plates that form the surface of the flow. The deviogram is smooth but steep at the TOPSAR scale, which is likely due to the influence of the caldera wall located ~170 m from the field site. As would be expected based on the lack of inflation

features observed at Site A, the deviogram does not appear to exhibit any marked change at 15 m, which is often indicative of the influence of inflation features such as tumuli [Campbell and Shepard, 1996]. The slope of the deviogram does not change across the 50 m inflection typical of surfaces in the region that are influenced by the pre-existing topography [Campbell and Shepard, 1996]. The lack of both inflation features and a signature of the pre-existing topography is consistent with the observation that the July 1974 pahoehoe flow ponded against the eastern wall of the caldera.

6.2. Site B

Site B exhibits moderate Hurst exponents at the T-LIDAR (H=0.46±0.06) and airborne LIDAR scales (H=0.36±0.01) and a high Hurst exponent at the TOPSAR scale (H=0.69±0.03) (Table 1; Figure 11b). The y-intercept values for Site B are 0.05 m for the T-LIDAR data, 0.10 m for the airborne LIDAR data and 0.77 m for the TOPSAR data (Table 2). The T-LIDAR deviogram does not show any statistical change in Hurst exponent over the 0.02 to 0.14 m step size range. In the airborne LIDAR deviogram, there is a slight increase in slope at ~2-3 m, indicating a decrease in overall topographic variance above ~ 2 m. The decrease in variance at this scale is likely the result of infilling of topography from spallation of glass chips and pieces of the broken up surface. This site is the only one to exhibit large degrees of hydrothermal alteration materials on the surface and we note that the alteration is not detected as smoothing in the small step sizes, but is likely contributing to the lower topographic variance at meter-scale sizes due to the friable and easily disturbed nature of the flows. The deviogram is steep at the TOPSAR scale, likely to be due to the influence of the caldera wall located ~50 m west-southwest

from the field site. The large variations of the calculated RMS deviation between the airborne LIDAR and TOPSAR datasets are unique to Sites A and B, and we believe the high roughness in the TOPSAR data is partially due to the proximity of the sites to the caldera wall (in addition to the relatively low vertical accuracy of the TOPSAR, as discussed above). The effects of the caldera wall, the cell size and the resulting RMS deviation and Hurst exponents will be discussed in the discussion section.

6.3. Site C

Site C exhibits a moderate Hurst exponent at the T-LIDAR scale (H=0.51±0.14), low Hurst exponent at the airborne LIDAR scale (H=0.23±0.03) and a moderate Hurst exponent at the TOPSAR scale (H=0.44±0.09) (Table 1; Figure 11c). The y-intercepts are 0.03 m for T-LIDAR, 0.15 m for airborne LIDAR and 0.72 m for TOPSAR (Table 2). The airborne LIDAR data show a slight reduction in deviogram slope for scales larger than ~2.2 m, resulting in a decrease in the Hurst exponent from 0.32 to 0.23. The higher Hurst exponent at scales below 2 m is likely the result of the festoon ridges and small-scale flow features causing high topographic variation at scales smaller than ~2 m (the approximate spacing of the ridges). The lower Hurst exponent at scales above ~2 m is the result of lower topographic variance due the low relief of the lava plates above 2 m step sizes. In addition to the meter-scale roughness variations observed in the airborne LIDAR data, there is also a decrease in Hurst exponent from 0.51 to 0.45 in the TOPSAR data for scales larger than ~30 m. The decrease in Hurst exponent observed at these large step sizes is possibly the result of the large ponded flow that did not travel down any obvious

slopes. Campbell and Shepard [1996] observed a similar smoothing trend in flows that ponded behind a topographic barrier versus flows that traveled down slope.

6.4. Site D

Site D exhibits a high Hurst exponent at the T-LIDAR scale (H=0.78±0.08), moderate-high Hurst exponent at the airborne LIDAR scale (H=0.64±0.02) and high Hurst exponent at the TOPSAR scale (H=0.73±0.05) (Table 1; Figure 11d). The y-intercepts for Site D are 0.09 m for T-LIDAR, 0.17 m for airborne LIDAR and 0.48 m for TOPSAR (Table 2). The T-LIDAR scale Hurst exponent is particularly high at this site due to the low RMS deviations at the short step sizes as a result of the highly smooth, glassy nature of portions of the flow surface scanned by the laser. The change from low RMS deviations to higher RMS deviations at the larger step sizes results in a steep deviogram and thus a high Hurst exponent. There are no apparent changes in Hurst exponent in the T-LIDAR deviogram. No obvious breakpoints in the Hurst exponent are observed in the airborne LIDAR deviogram, but an increase from 0.67 to 0.73 is observed in the TOPSAR data for step sizes greater than 40 m. This increase in RMS deviation at longer step sizes is potentially the result of the increase in topographic variance due to several vents in the region that are composed of piles of layered pahoehoe flows left behind in the conduit when the lava pond collapsed (Figure 6d).

6.5. Site E

Site E exhibits moderate Hurst exponents at the T-LIDAR (H=0.50±0.01), airborne LIDAR (H=0.55±0.01) and TOPSAR scales (H=0.43±0.19) (Table 1; Figure

11e). The y-intercepts of the T-LIDAR (0.22 m) and airborne LIDAR (0.40 m) data are the highest of the six field sites and the y-intercept of the TOPSAR data is the lowest of the six field sites (0.34 m) (Table 2). Site E has the highest degree of topographic variation at the 0.02 to 10 m scales (it is the roughest site). Upon examination of the individual deviograms, we do not observe a change in the Hurst exponent in the T-LIDAR deviogram, although there is a decrease in Hurst exponent from 0.61 to 0.53 for step sizes larger than ~3 m in the airborne LIDAR deviogram. There is a definite decrease in the Hurst exponent in the TOPSAR deviogram from 0.53 to 0.45 for step sizes larger than ~ 32 m. Additionally, the derived Hurst exponent for Site E between step sizes of ~3 and 32 m is essentially identical, despite the RMS deviations being calculated from different datasets. The high topographic variance of the Site E flow is likely to be the result of the proximity to the spatter ramparts that served as vents for the April 1982 eruption on the floor of the caldera. The resulting flows were emplaced and subsequently jumbled as material was fed from the vent, breaking up the solidified surface before flowing away from the source vent. The breakpoint in the airborne LIDAR deviogram at 3 m is consistent with the size of the largest plates in the region of Site E. The jumbled flows and large plates contribute more variance (roughness) to the topography at step sizes smaller than ~3 m.

6.6. Site F

Site F exhibits fairly high Hurst exponents in the T-LIDAR (H=0.67±0.02) and airborne LIDAR (H=0.63±0.02) data and fairly low Hurst exponent in the TOPSAR data (H=0.32±0.19) (Table 1; Figure 11f). The y-intercepts at Site F are 0.17 m for both T-

LIDAR and airborne LIDAR and 0.49 m for TOPSAR (Table 2). The T-LIDAR deviogram does not appear to have any breakpoints, indicating that the surface roughness at step sizes between 0.02 and 0.14 m scales at a constant rate. There is a breakpoint in the airborne LIDAR deviogram, where the Hurst exponent decreases from 0.68 to 0.54 for scales larger than ~5 m, consistent with increased topographic variance from the tumuli observed at this field site. The tumuli contribute to the higher topographic variance for scales smaller than ~5 m and the resulting Hurst exponent is lower. There is also a breakpoint in the TOPSAR deviogram, where the Hurst exponent decreases from 0.54 to 0.28 for scales larger than ~28 m. Interestingly, as is the case with the very rough April 1982 flow containing Site E, the Hurst exponent for step sizes between 5 m and 28 m is the same in both the airborne LIDAR and TOPSAR data.

7. Discussion

This study of surface roughness analysis techniques was motivated by the desire to understand the effects of dataset resolution on the identification of emplacement and modification processes on young volcanic terrains. The results indicate that surface roughness analysis methods in two dimensions show promise as useful tools when investigating the emplacement history and subsequent modification of lava flows in Hawaii, and by inference other terrestrial basaltic shield volcanoes. The results for six field sites on Kilauea indicate that there are breakpoints in the deviogram slope at a range of wavelengths, consistent with a surface formed by several physical processes. The processes contributing to the surface roughness of a given lava flow include rate of flow (if flowing down a slope rather than topographically ponded), flow inflation, degassing,

vesiculation, crystallization and processes associated with cooling of the flow (spallation of glass chips, cracking of the surface) [Gaddis et al., 1990]. The roughness signatures of these processes are recorded on the surface of the flow, allowing interpretation of the history of the flow after emplacement. For example, we observe higher topographic variance at scales of 5-10 m for Sites D, E and F. Sites D and F are both located within compound pahoehoe flow fields and exhibit inflation features such as tumuli and pahoehoe toes. Site E is characterized by jumbled, rafted plates of spiny pahoehoe, which cause the RMS deviation and subsequent y-intercept to be high at step sizes from 0.02 m up to 10 m. Site D is characterized by glassy surfaces at the small scale, and by inflation features at step sizes from 1-10 m (y-intercepts of 0.09 m and 0.17 m for T-LIDAR and airborne LIDAR, respectively). While the deviogram for Site E is characterized by the highest RMS deviations up to the 10 m scale, the steep deviogram for Site D is the result of an increase in topographic variance with increasing scale. In contrast to the lava flows that formed compound and jumbled pahoehoe fields, the three field sites where the pahoehoe was topographically ponded exhibit statistical roughness values that are consistent with topographic confinement of the flow. Sites A, B and C are all ponded pahoehoe flows with lower topographic variance than Sites D, E and F at the 5-10 m scale, indicating that the confining caldera walls played a role in preventing the formation of features that would result in higher degrees of topographic variance at those scales.

7.1. Comparison to previous methods

Results from Campbell and Shepard [1996] using the traditional profile method over the same flows are moderately consistent with our results for the two-dimensional

surface roughness method, although differences in the Hurst exponent (Table 1) and RMS deviation at 1 m are noted (Table 3). We compare our Hurst exponent, H, to their fractal dimension, D, using the relationship $D = 3 - H$ for an isotropic surface [Shepard et al., 2001] where $D_{(2D)}=D_{(1D)}+1$. One caveat of this comparison is that if the surface is anisotropic, the relationship between $D_{(1D)}$ and $D_{(2D)}$ is not as simple as adding 1 to the $D_{(1D)}$ fractal dimension, and thus $D_{(2D)}$ for an anisotropic surface will be a value between $D_{(1D)}$ and $D_{(2D)}$ for an isotropic surface [Goff, 1990]. This will in turn translate into a change in the Hurst exponent. Assuming the profiles and cells are located within the same flow, the degree of agreement between the 1D and 2D results may indicate whether or not the surface exhibits anisotropy. In subsequent work, we plan to improve the model to calculate anisotropy in the surface. Campbell and Shepard [1996] do not provide uncertainties for their D values, but the estimated uncertainty for the Hurst exponent values given by Shepard et al. [2001] (using the Campbell and Shepard [1996] data) is ±0.05.

7.1.1. Step sizes < 1 m

The largest difference between our results and those of Campbell and Shepard [1996] at scales <1 m occur for sites A and B, both ponded pahoehoe flows with large slightly curving plates 2-5 m in diameter. The Hurst exponents calculated by Campbell and Shepard [1996] are significantly higher than the Hurst exponents calculated in this study (Table 1). For Site A, our value for the Hurst exponent of 0.28±0.09 for step sizes from 0.03-0.15 m using the T-LIDAR data is significantly lower than the 0.71 calculated by Campbell and Shepard [1996] at scales less than 1 m. The value of the Hurst exponent at Site B given by Campbell and Shepard [1996] for scales less than 1 m is 0.69 and the

value from this study is 0.46±0.06. One potential cause of the discrepancies between the results is the inherent difference in dataset resolution. The T-LIDAR data have been gridded to a DEM with 3 cm spacing for Site A and 2 cm spacing for Site B, while the Campbell and Shepard [1996] profile-derived data have a minimum 25 cm horizontal spacing. While the 25 cm spacing of the profile would miss small-scale roughness, the increased resolution of the T-LIDAR readily detects the cm-scale glass chips littering the surface, resulting in an increased RMS deviation at the smaller scales. Higher RMS deviations at smaller step sizes and RMS deviations similar to Campbell and Shepard [1996] at longer step sizes result in flatter deviograms and lower values for the Hurst exponent in the T-LIDAR data. Conversely, the calculated Hurst exponent for Site C, the other ponded pahoehoe flow in the study area, is very similar in both this study (0.51±0.14) and the Campbell and Shepard [1996] results (0.53).

The calculated Hurst exponent for step sizes < 1 m at Site D is higher in this study than the Campbell and Shepard [1996] profile-derived data. The Hurst exponent calculated in 2D is 0.78±0.08 and the value calculated from the profile data is 0.64. This site is characterized by very smooth areas of extruded glassy pahoehoe near the bases of 1-2 m high tumuli, resulting in very low roughness at small scales and higher roughness at longer step sizes. It is likely the profile data did not "sense" the highly smooth small-scale region, but did "sense" the roughness of the more vesicular surfaces and inflation features at the longer step sizes. The low small-scale roughness and higher roughness at the longer step sizes in the T-LIDAR data result in a steep deviogram and a high Hurst exponent. The Hurst exponent calculated in this study for Site E is similar to that calculated by Campbell and Shepard [1996] (Table 1). These differences illustrate how

the Hurst exponent is influenced by resolution at small scales and by regional morphology at large scales.

7.1.2. Step sizes > 1 m

Sites with the largest degree of difference between the Hurst exponent from Campbell and Shepard [1996] and this study at scales greater than 1 m are Sites B and C (Table 1). It is important to note that Campbell and Shepard [1996] only calculated the Hurst exponent up to scales of 3-5 m, depending on the site, while our study calculated the Hurst exponent along the entire deviogram for scales from 1 to 10 m. For Site B, the Hurst exponent value from Campbell and Shepard [1996] for step sizes greater than 1 m is 0.58, significantly higher than the Hurst exponent of 0.36±0.01 calculated from the airborne LIDAR DEM in this study. At Site C, the Hurst exponents for scales above 1 m are significantly different between the value derived from the airborne LIDAR (0.23±0.03) and the value derived from the profile in the Campbell and Shepard [1996] study (0.70). One potential cause for our significantly lower Hurst exponent values is that Campbell and Shepard [1996] only calculated H up to ~4 m step sizes due to the presence of a breakpoint in the deviogram, while our calculation of H using airborne LIDAR used up to 10 m step sizes. If the 1D H was calculated using the entire deviogram, H is significantly closer to the airborne LIDAR value. Additionally, the vertical accuracy of the airborne LIDAR data is 2 cm [Mouginis-Mark and Garbeil, 2005], while the vertical accuracy of the 1D data is ~ 1 cm [Campbell and Shepard, 1996]. The lower vertical accuracy of the airborne LIDAR data limits the size of the topographic changes that can be sensed, essentially smoothing out the surface at the shorter step sizes.

As calculated from the airborne LIDAR data, the RMS deviations at 1 m from the 2D study are higher than those calculated from the 1D study [Campbell and Shepard, 1996] (Table 3). The Site A RMS deviation from the 2D study is 16.0 cm, while the 1D study reported a value of 4.78 cm (Table 3). The value for Site B is much closer, where the 2D study reports a value of 10.5 cm and the 1D study reports a value of 9.01 cm (Table 3). The location of the 1D profile for Site A may have been in a different place than the field site selected in this study, or the presence of vegetation within the 2D dataset may have artificially inflated the RMS deviation. Site B, downwind from Halemaumau, does not have any vegetation on the lava flows. The RMS deviations for Sites C, D and E (14.8, 17.6 and 37.8 cm, respectively) are all higher in the 2D roughness data than in the 1D (3.89, 10.30 and 21.36 cm, respectively), although the magnitudes of the values relative to one another are similar (Table 3). This may be one instance in which the higher RMS deviations derived from the 2D technique indicate a degree of surface anisotropy at these sites. Sites A and C both have festoon ridges on the surface of the flows and Sites D and E are both near vent regions. Although measurement of the absolute degree of anisotropy is beyond the scope of this current work, it is not improbable that there is surface anisotropy that is detected in the 2D roughness analysis.

In addition to the above possibilities for the differences between the 1D and 2D Hurst exponent and RMS deviation values, it is possible that local variations in flow morphology resulting in anisotropic roughness may have biased the results from the profile transect method of sampling. It is possible that the Campbell and Shepard [1996] study measured the flows along or across a flow axis, resulting in a higher estimate of roughness than may be appropriate for the entire surface of the flow. In contrast, the

DEM-based roughness averages the roughness of the entire surface at each step size, resulting in a smoother surface at the longer step sizes and a potentially more accurate representation of the surface roughness. Recent work on the identification of lava flow structures using Fourier transforms on DEMs by Lescinsky et al. [2007] also suggests that linear topographic profiles may provide inaccurate information on surfaces that exhibit directionality during formation. In addition to accounting for bias introduced by feature anisotropy, the larger sample utilized in the 2D method provides more points, resulting in better averages of the roughness of the entire surface.

7.1.3. Interpretation

The results from the roughness analysis show that the calculated RMS deviation and the derived Hurst exponent are influenced by the size of the cell used. To assess this effect, we performed an analysis of the cell size used versus a reference RMS deviation of 1 m for each of the six field sites (Figure 12a). We also examine the relationship between the cell size and Hurst exponent (Figure 12b) and between the RMS deviation at 1 m and Hurst exponent (Figure 12c). In addition to the examination of these relationships in 2D, we also analyzed the effect of cell size (profile length) on the resulting Hurst exponent in 1D using data from Campbell and Shepard [1996].

The results indicate that generally, as cell size increases, the RMS deviation at 1 m remains fairly constant until a particular cell size is reached and then the RMS deviation changes, either increasing or decreasing depending upon the unit under consideration (Figure 12a). The cell size at which the RMS deviation at 1 m changes typically corresponds to the size of the geomorphologic unit, which when exceeded results in the inclusion of other surface units or steep topography. Exceptions to this

general trend exist, particularly Sites B and E. Site B is located in close proximity to the western caldera wall, which appears to influence the calculated RMS deviation in these cells, depending on the absolute location of the cell within the DEM. In some cases, the cell falls entirely within the caldera floor, while other cell sizes incorporate the caldera wall. There are three distinct trends in Figure 12a where the cell sizes with the lowest RMS deviation are those that do not incorporate the signature of the caldera wall, the cells with moderate RMS deviation are influenced by the drastic height difference from the caldera wall, and the cells with the highest RMS deviation are dominated by the signature of the caldera wall. In Figure 12a, the RMS deviations of Site E appear to be relatively constant until a cell size of approximately 100 meters, above which the RMS deviation doubles. As the cell size increases for Site E, the RMS deviation decreases to values near those calculated for cell sizes less than 100 m. The increase in RMS deviation at a cell size of 100 m is likely the result of the cells becoming large enough to incorporate the spatter ramparts adjacent to the fissure that fed the flow. In addition, the decrease in RMS deviation as the cell size continues to increase is likely the result of the averaging of the smoother, surrounding surfaces into the calculated RMS deviation for the area.

The Hurst exponent exhibits degrees of variation with changes in cell size and it appears to be dependent on the intrinsic roughness of the surface (Figure 12b). The smoother surfaces (the ponded flows of Sites A, B and C) generally have lower Hurst exponents until the cell size that exceeds the boundaries of the flow is reached. As discussed relative to the RMS deviation, the Hurst exponent for Site B varies between high H values and low H values, depending on where exactly the cell is located within

the map and whether or not it includes the steep caldera wall (Figure 12b). The rougher surfaces of Sites D and E exhibit fairly constant behavior until, we believe, the boundaries of the flows are reached (Figure 12b). The Hurst exponents calculated at Site F decrease fairly constantly with increasing cell size.

As demonstrated in the above discussion, cell size is an important factor in the mapping and investigation of the surface roughness of lava flows and should be considered when undertaking roughness mapping of any surface. Using the 2D surface roughness calculation method in mapping mode requires that the user edit out data that clearly do not belong to a unit of interest, such as steep topography adjacent to the unit. Additionally, the range of length scales used to calculate H significantly affects the resulting Hurst exponent, particularly in the 1D case. In a comparison of the Hurst exponent calculated for the 1D and 2D data versus the minimum step size, we note that the 2D method produces significantly more consistent results, despite decreasing the range of the deviogram used (Figure 13). This test was performed to approximate using the smaller range of the deviogram as used by Campbell and Shepard [1996]. The calculation of the surface roughness over the entire surface instead of a one-dimensional sample of the topography appears to lead to more consistent results regardless of the portion of the deviogram used.

7.2. Influence of topography

As a lava flow is emplaced, the underlying topography is one of the main controls of flow velocity. Existing topography has a strong effect on terrestrial lava flow emplacement and recently has been discussed regarding flow emplacement on Mars,

where Glaze and Baloga [2007] find that the scale of existing topography exhibits a strong influence on resulting flow thickness regardless of the overall thickness of the lava flow being emplaced [Glaze and Baloga, 2007]. We observe variations in surface roughness that correlate well with the influence of the underlying topography on the resulting flow morphology. The surface roughness of flows emplaced and subsequently ponded is readily distinguished from the surface roughness of flows that were emplaced while flowing across existing topography in the deviograms of the sample volcanic surfaces in Kilauea caldera (Figure 11). The flows that were ponded against topographic barriers have lower RMS deviations at the meter and tens of meter scales (Figure 11). These flows do not exhibit significant inflation features or flow features in the field, consistent with the low RMS deviations at the meter and tens of meter scales. The flows that exhibit inflation features such as tumuli and/or compound flow emplacement features such as lobes have higher RMS deviations at the meter and tens of meter scales than the ponded flows. Campbell and Shepard [1996] also observed a trend of decreasing roughness from flows on slopes to flows that were topographically confined during emplacement. In addition to topographic controls, the vent areas of several of the example flows are significantly rougher than the flows that were fed from the vent system. For example, Site D is located within the vent area for Site C, and is characterized by a significantly higher RMS deviation at meter scales, due to the compound flows that dominate the area of Site D. Site E is located just down flow from the vent that fed the April 1982 lava flows, and the spatter ramparts that fed the flows are significantly rougher than the actual flows as well.

We conducted a field survey of the caldera and noted that there was at least one location where the calculated surface roughness was not an expression of the actual surface, but the result of underlying flow topography dominating the roughness at the scale of the measurement. The influence of the underlying topography was observed when the airborne LIDAR Hurst exponent map and high-resolution images were compared to field observations of the western region of the caldera. In the images and in the field, a finger-like flow extends across the surface of a homogenously smooth pyroclastic deposit. In the field, the pahoehoe flow is a thin veneer (~20-30 cm thick) over a pyroclastic deposit and displays the same smooth surface morphology along the length of the flow. The roughness data indicate that this flow is rougher closer to Halemaumau pit crater and smoother out toward the outer caldera wall. The change in roughness that is detected by the Hurst exponent maps at the 3, 5 and 10 m scale is likely to be the result of the underlying topography overprinting the surface signature. Also, the flow has a slightly ropy texture near the source, likely contributing to the rougher signature in the proximal regions of the flow. The above example suggests that surface roughness data extend the potential range of interpretations, as we are able to determine whether underlying topography or other emplacement processes influence the surface.

8. Conclusions

Using known relationships for RMS deviation and Hurst exponent we have calculated 2D maps of surface roughness for six field sites in Kilauea caldera at three different dataset resolutions. The 2D roughness maps of the six field sites indicate that geological processes involved in the emplacement of young volcanic terrains leave

signatures that can be identified in the surface roughness data. Although processes such as flow inflation cannot be uniquely identified based solely on the surface roughness maps or the individual deviogram for that surface, combining surface roughness data with high-resolution image data provides additional information regarding the character of the surface under investigation.

Testing of the 2D surface roughness analysis has shown that it is important to consider the size of the cells used in the investigation. If the cell size exceeds the size of the unit under analysis, the surface roughness value will include surrounding terrain and result in an incorrect value. When mapping units with previously unidentified boundaries, such as on Mars or another planet, it is important to consider this mixing effect on roughness analysis.

The resolution of the dataset is also of critical importance. If the horizontal resolution of the dataset is lower than the size of features that characterize the roughness of the surface, the results for the Hurst exponent or RMS deviation will be biased. Additionally, if the surface feature is dominated by the underlying topography and the dataset resolution is below the scales that characterize the surface roughness, the underlying topography will dominate the signal and information regarding the character of the surface under investigation will be lost.

Future applications of this technique include applications to high-resolution topography datasets and topographic and surface roughness analysis of flow features on Mars, particularly in volcanic areas imaged by the HiRISE camera. We anticipate detailed analysis of high-resolution images and DEMs derived from stereo imaging of

young volcanic terrains on Mars will be highly conducive to studies of the spatial and temporal relationships among lava flows.

Acknowledgements

The funding for this work was provided by NASA's Mars Fundamental Research Program grant #NNG0-5GL98G (FSA, PI; PMM, Co-I). We wish to gratefully acknowledge Bruce Campbell for providing the 1D topographic data used in this analysis. ARM would like to thank Mikki Osterloo and Keith Nowicki for proving to be excellent field assistants and especially for carrying the T-LIDAR and accompanying batteries across Kilauea caldera. We appreciate Tom Farr and Michael Shepard for thorough reviews of an earlier version of this work that substantially improved the final manuscript. This is HIGP publication #1669 and SOEST publication #7515.

Tables

Table 1. Comparison of Hurst exponents derived from T-LIDAR and airborne LIDAR data to Hurst exponents derived from profiles over the same flow units published by Campbell and Shepard [1996] and Shepard et al. [2001] ("S et al."). Error in 2D data calculated from error generated from measurement uncertainty and standard calculation error. Site indicates the site label used in this study. "C & S" site indicates Campbell and Shepard [1996] site nomenclature. T-LIDAR Hurst exponents given for scales from 0.02-0.15 m. C & S < 1 m Hurst exponents calculated from 1D data with minimum 25 cm point spacing [Campbell and Shepard 1996]. Airborne LIDAR Hurst exponents given for scales from 1-10 m. C & S > 1 m Hurst exponents calculated from 1D data with minimum 25 cm point spacing for scales between 1 and 3-5 m. S et al. Hurst exponents (H_1) calculated using Campbell and Shepard [1996] 1D data up to breakpoint (if present) or up to 10% of the profile length. H_2 calculated after breakpoint (if present).

Site	C & S Site	T-LIDAR *H*	C & S <1 m *H*	Airborne LIDAR *H*	C & S >1 m *H*	S et al. H_1	S et al. H_2 breakpoint (m)
A	10	0.28±0.09	0.71	0.40±0.02	0.39	0.66	0.41 (1.3)
B	9	0.46±0.06	0.69	0.36±0.01	0.58	0.59	-
C	1	0.51±0.14	0.53	0.23±0.03	0.70	0.65	0.07 (5.5)
D	2	0.78±0.08	0.64	0.64±0.02	0.70	0.69	0.38 (5)
E	3	0.50±0.01	0.46	0.55±0.01	0.50	0.40	-
F	-	0.67±0.02	-	0.63±0.02	-	-	-

Table 2. Y-intercepts of linear fits to log-log plots of RMS deviation and step size (i.e. the deviogram) derived from T-LIDAR, airborne LIDAR and TOPSAR data for each of the six field sites. Y-intercept is RMS deviation at 1 m. Site indicates the site label used in this study. "C & S Site" indicates Campbell and Shepard [1996] site nomenclature. Y-intercept values are in meters.

Site	C & S Site	T-LIDAR y-intercept (m)	Airborne LIDAR y-intercept (m)	TOPSAR y-intercept (m)
A	10	0.02	0.16	0.37
B	9	0.05	0.10	0.77
C	1	0.03	0.15	0.72
D	2	0.09	0.17	0.48
E	3	0.22	0.40	0.34
F	-	0.17	0.17	0.49

Table 3. Comparison of RMS deviation at 1 m derived from airborne LIDAR DEM to RMS deviation at 1 m derived from profiles over the same flow units published by Campbell and Shepard [1996]. Site indicates the site label used in this study. "C & S Site" indicates Campbell and Shepard [1996] site nomenclature. Campbell and Shepard [1996] 1 m RMS deviations calculated from 1D data with minimum 25 cm point spacing. RMS deviations are given in centimeters.

Site	C&S Site	Campbell &Shepard (1996) (cm)	This study (cm)
A	10	4.78	16.0
B	9	9.01	10.5
C	1	3.89	14.8
D	2	10.30	17.6
E	3	21.36	37.8
F	-	-	16.4

Figures

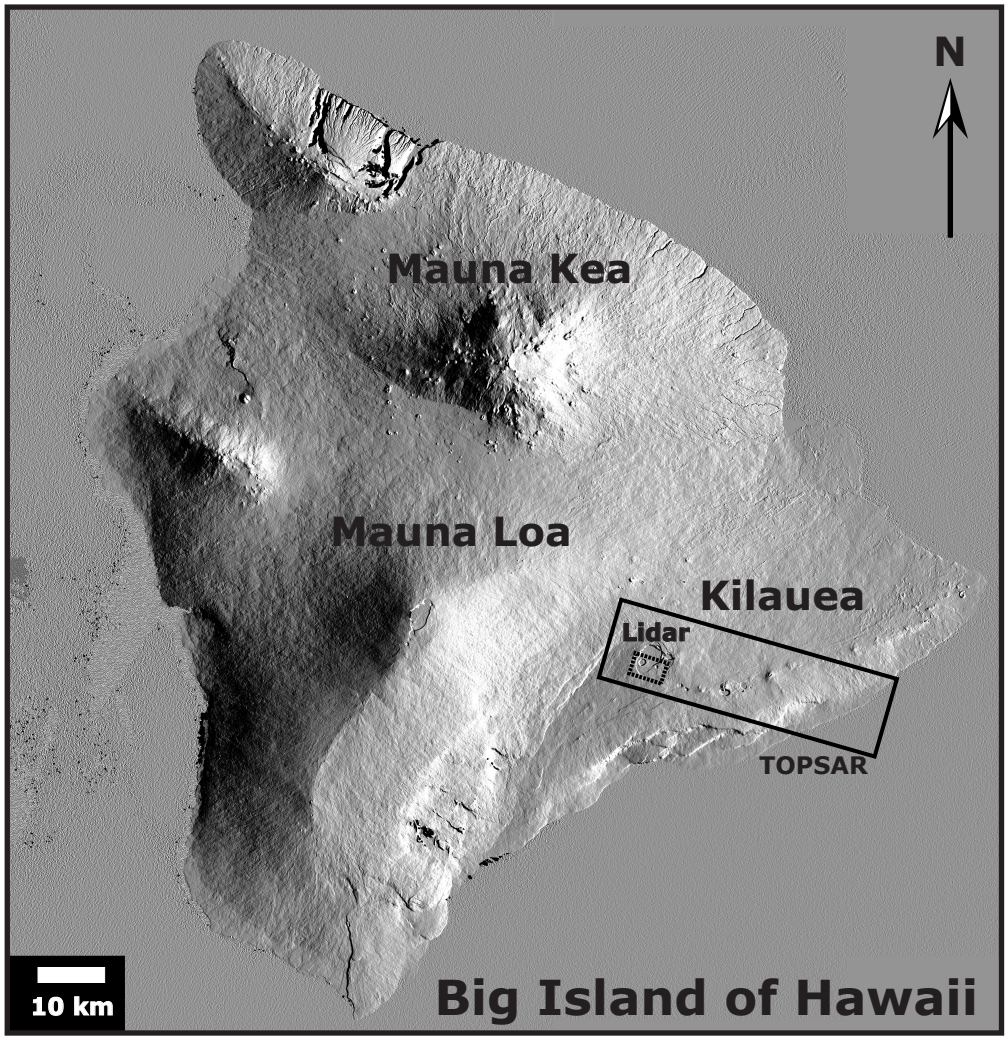

Figure 1. Shaded relief image of the Big Island of Hawaii derived from 30 m/pixel Shuttle Radar Topography Mission (SRTM) elevation data. Illumination is from the east. The coverage of the TOPSAR and airborne LIDAR datasets are identified by the solid and dashed boxes, respectively. The coordinates of the upper left corner are 20º18’49.00”N, 156º9’47.00”W. The coordinates of the lower right corner are 18º58’51.00”N, 154º48’49.00”W.

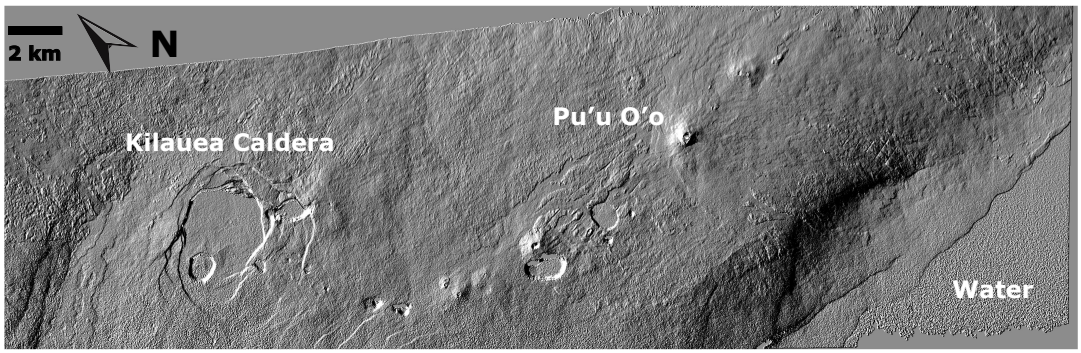

Figure 2. TOPSAR shaded relief with 10 m/pixel posting. Illumination is from the southeast. Location of Kilauea caldera and Pu'u O'o are identified.

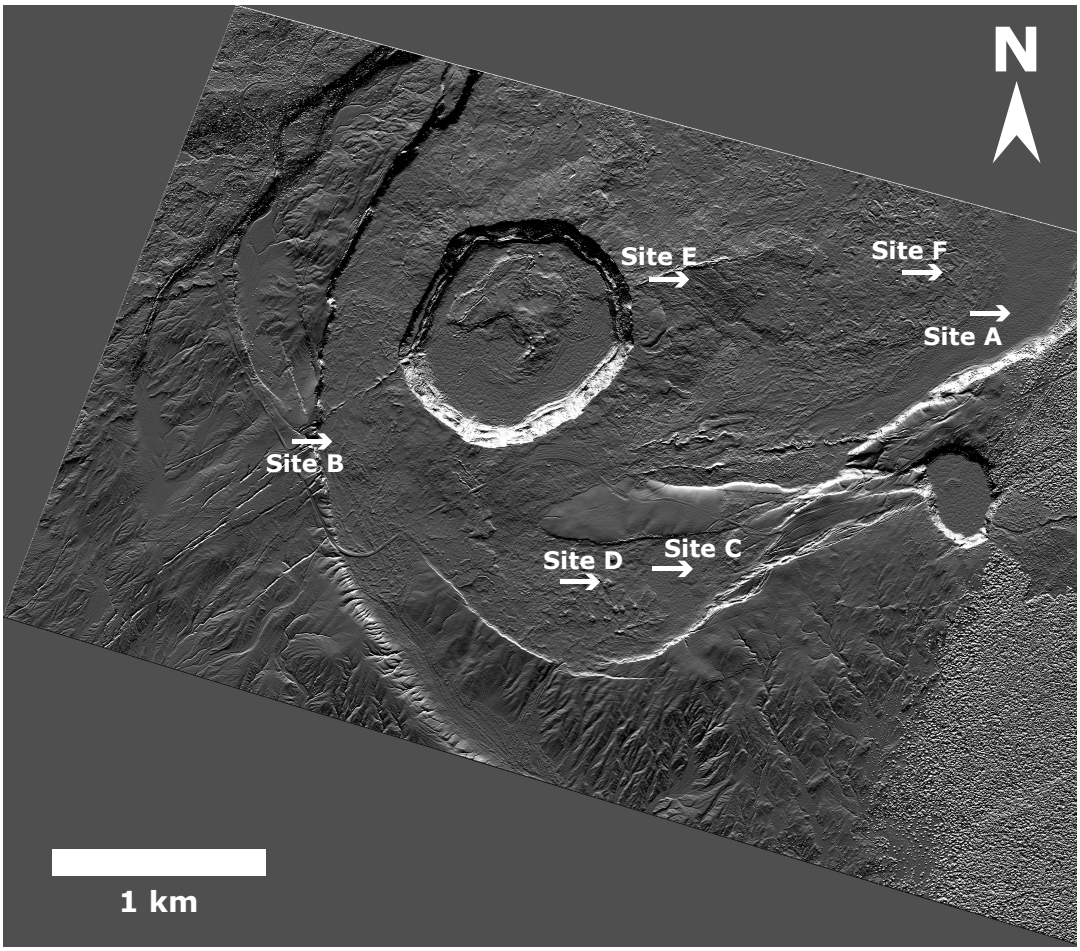

Figure 3. Airborne LIDAR shaded relief with 1 m/pixel posting. Illumination is from the north. Data cover southern half of Kilauea caldera. Arrows identify the locations of the field sites within the caldera.

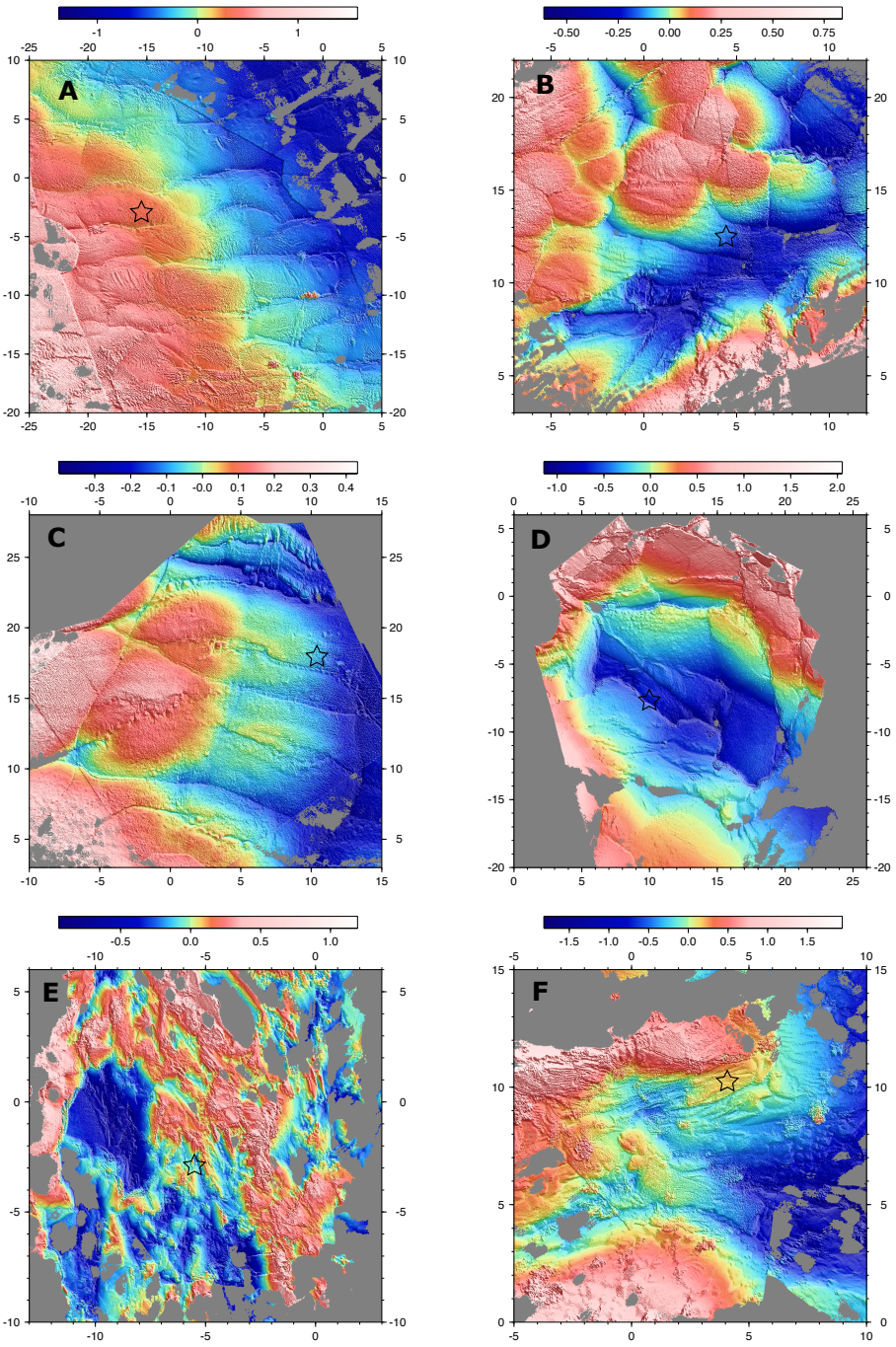

Figure 4. T-LIDAR topographic data. Elevations are in meters and are relative to local datum at each field site. X and Y coordinates are also in meters. Stars indicate location of cell used in subsequent deviogram analysis. a) Site A (19º24’27.979”, 155º15’42.901”); b) Site B (19º24’7.416”, 155º17’30.179”); c) Site C (19º23’48.859”, 155º16’32.696”); d) Site D (19º23’46.659”, 155º16’47.400”); e) Site E (19º24’32.381”, 155º16’33.850”); f) Site F (19º24’33.990”, 155º15’53.676”).1.

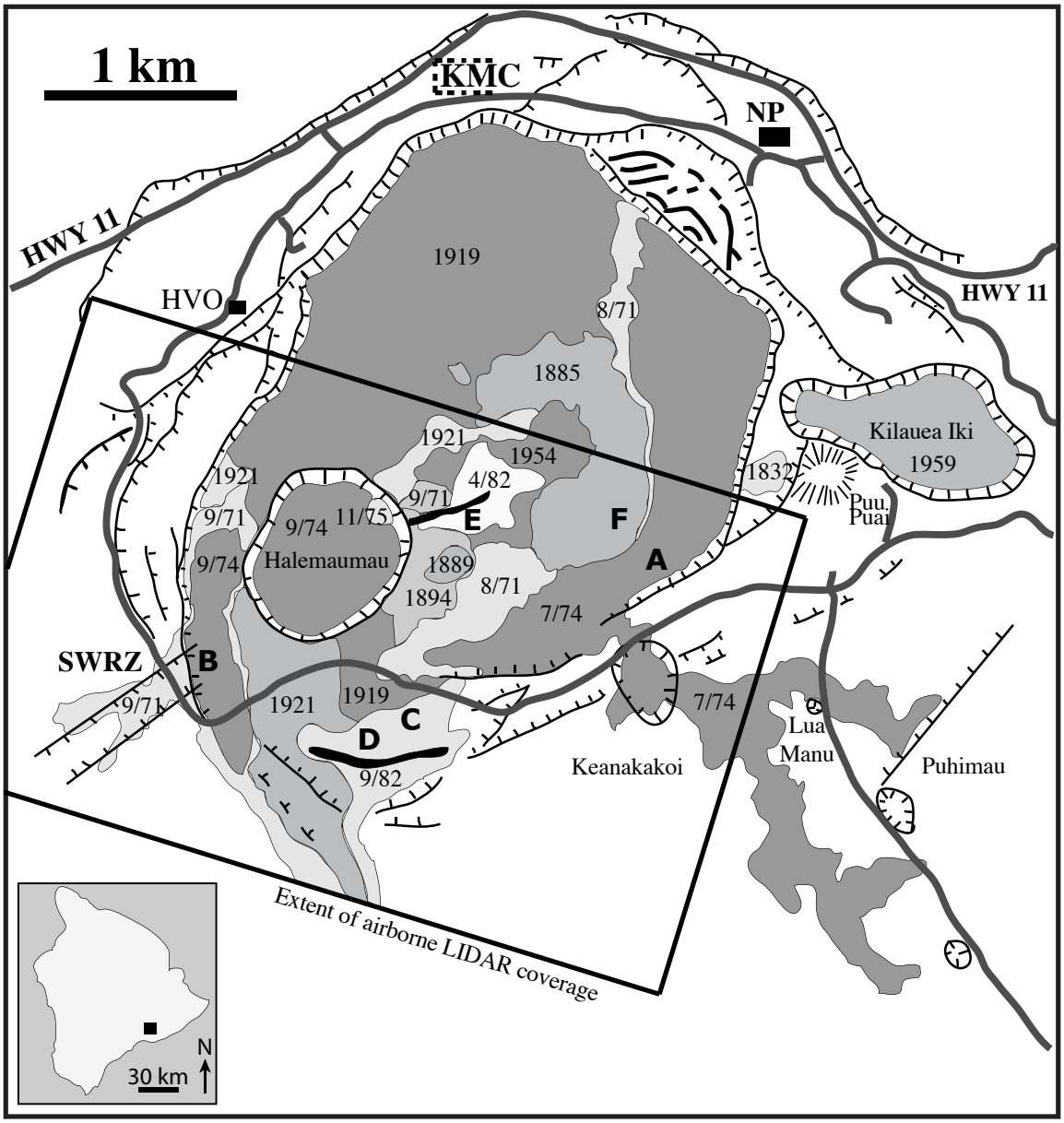

Figure 5. Map of Kilauea caldera detailing recent lava flows and structural features. After Mouginis-Mark and Garbeil [2005]. Inset shows Big Island study area location. Bold letters indicate field sites. KMC: Kilauea Military Camp, NP: National Park Headquarters, SWRZ: Southwest Rift Zone, HVO: Hawaii Volcano Observatory.

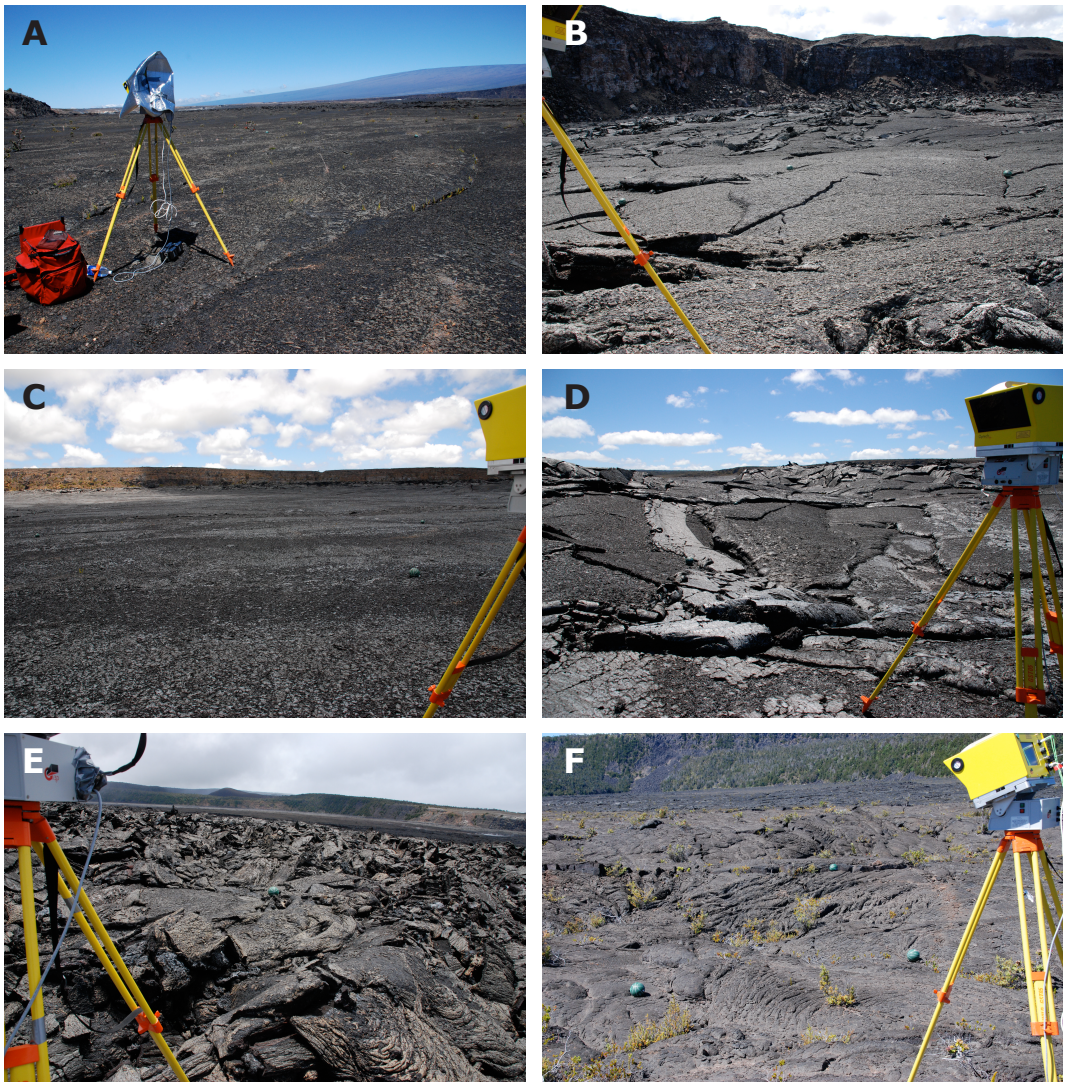

Figure 6. Representative images of field sites. Note mini-basketballs (~16 cm diameter), tripod LIDAR unit and tripod for scale. a) Site A. Ponded pahoehoe with cm-sized glass chips on 2-5 m slightly convex plates. Mauna Loa is visible in the distance. b) Site B. Ponded pahoehoe flows with low proportion of cm-sized glass chips on 2-5 m slightly convex plates. The WNW portion of the Kilauea caldera wall is visible in the distance. c) Site C. Ponded pahoehoe with cm-sized glass chips on slightly convex plates. The southern, tephra-covered portion of Kilauea caldera wall is visible in the distance. d) Site D. Near-vent inflated pahoehoe flows with glassy selvage. e) Site E. Near-vent jumbled pahoehoe flows. The eastern wall of Kilauea caldera is visible in the distance. The cone on the wall is Pu'u Puai, the tephra cone formed in the Kilauea Iki 1959 eruption. f) Site F. Inflated, devitrified compound pahoehoe flows.

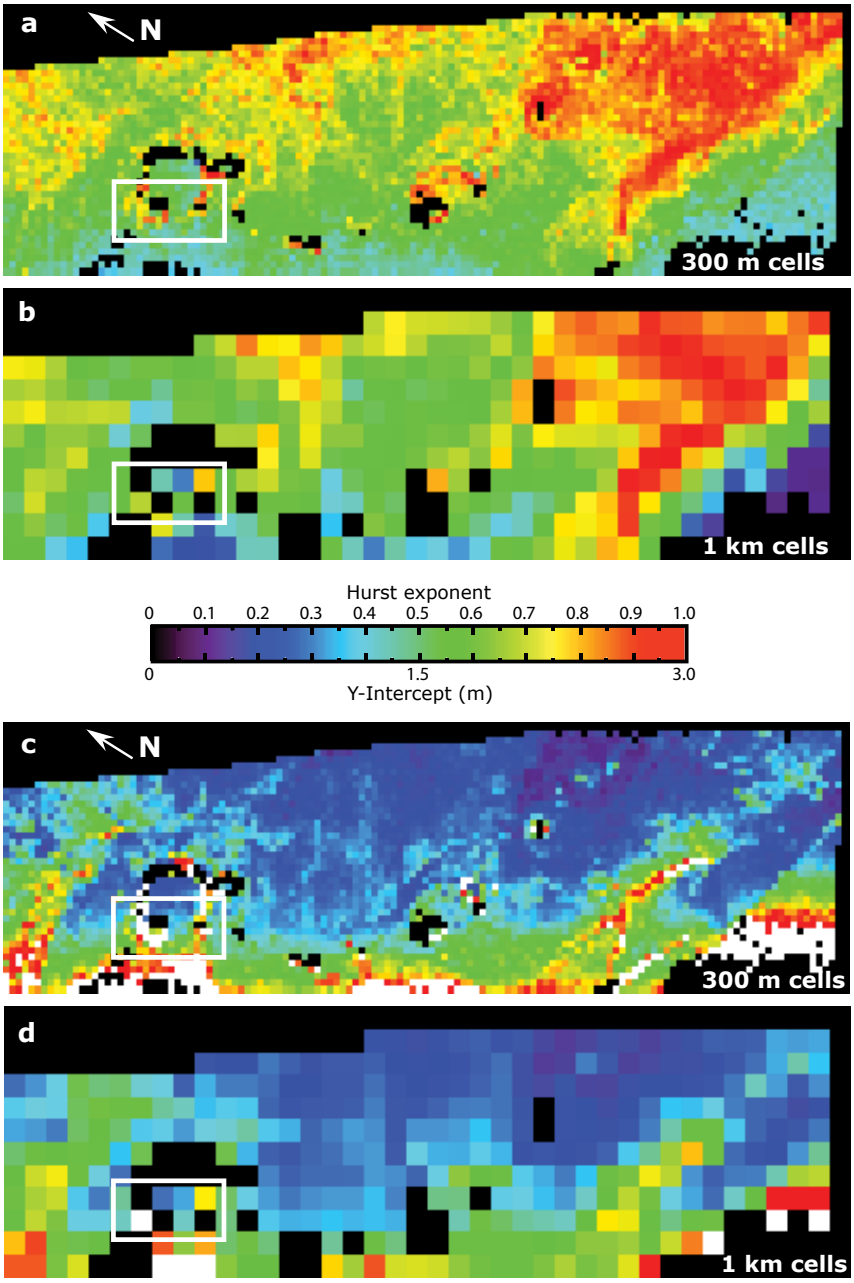

Figure 7. TOPSAR Hurst exponent and y-intercept maps covering same area as shown in Figure 2. White boxes identify approximate location of airborne LIDAR data in Figure 8. a) Hurst exponent, 300 m cells; b) Hurst exponent, 1 km cells; c) Y-intercept, 300 m cells; d) Y-intercept, 1 km cells.

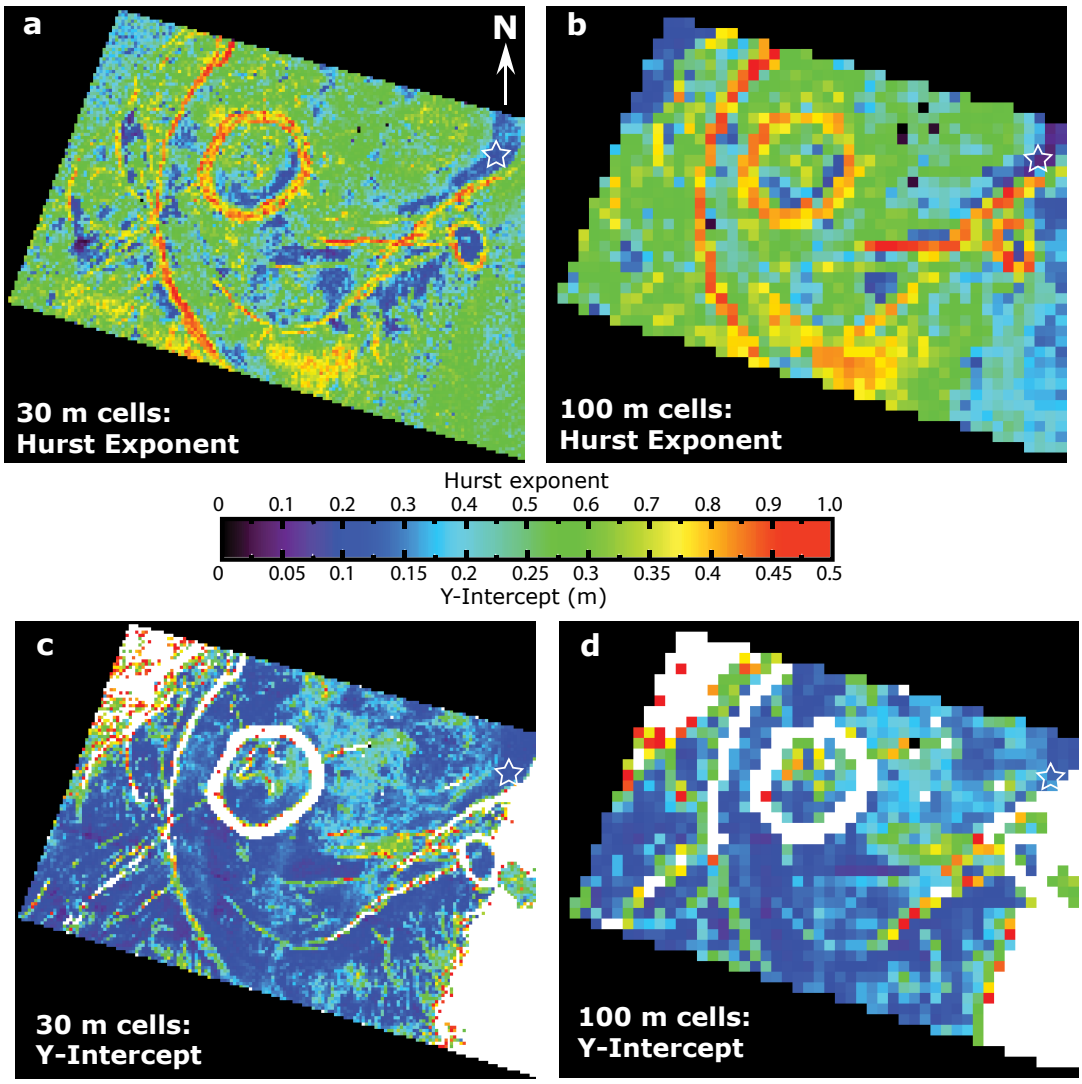

Figure 8. Airborne LIDAR Hurst exponent and y-intercept maps covering same area as shown in Figure 3. White stars identify approximate location of T-LIDAR data shown in Figure 9. a) Hurst exponent, 30 m cells; b) Hurst exponent, 100 m cells; c) Y-intercept, 30 m cells; d) Y-intercept, 100 m cells.

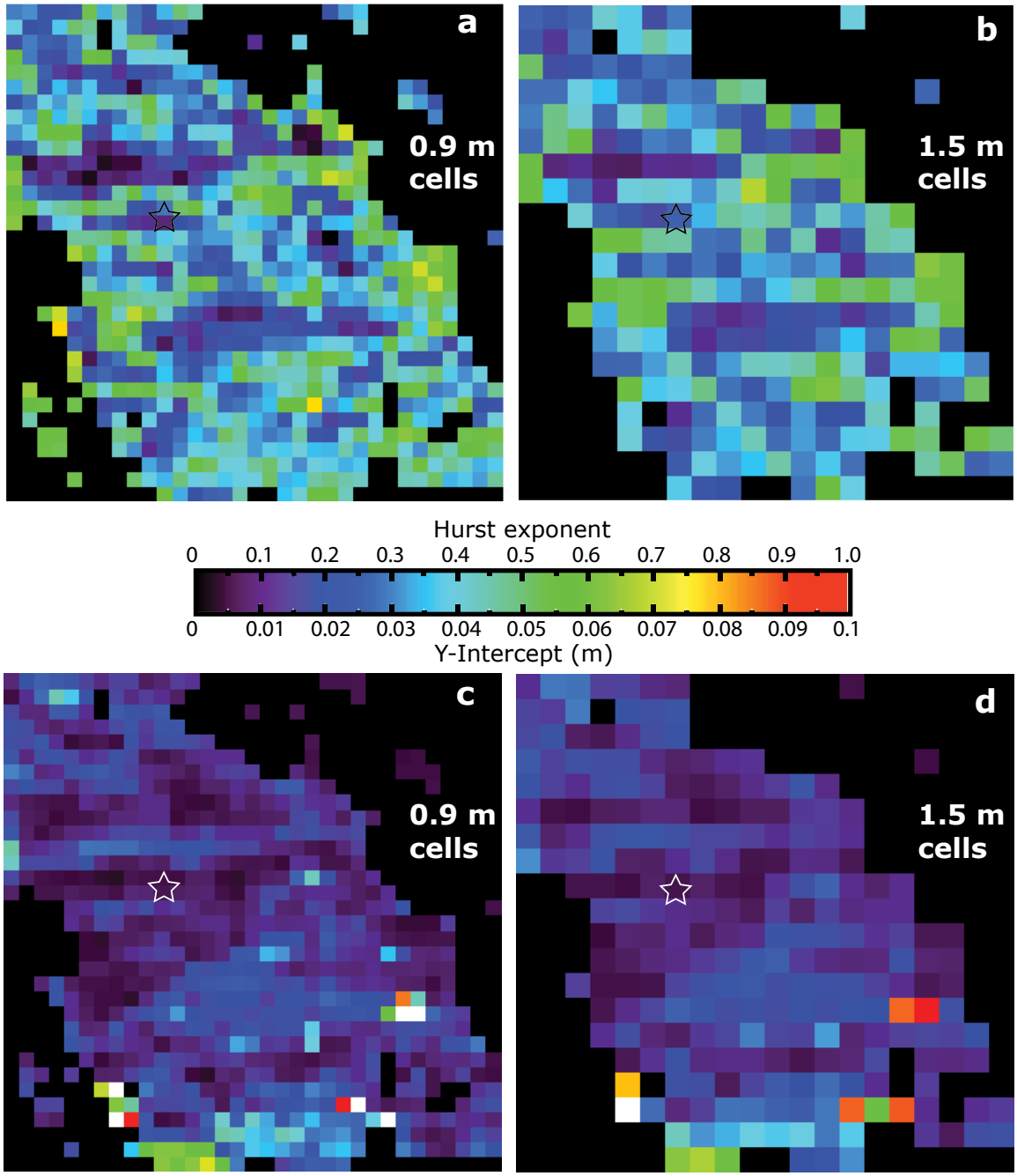

Figure 9. Example tripod-mounted (T-LIDAR) Hurst exponent and y-intercept maps from Site A. Stars indicate location of cell used in this analysis. a) Hurst exponent, 0.9 m cells; b) Hurst exponent, 1.5 m cells; c) Y-intercept, 0.9 m cells; d) Y-intercept, 1.5 m cells.

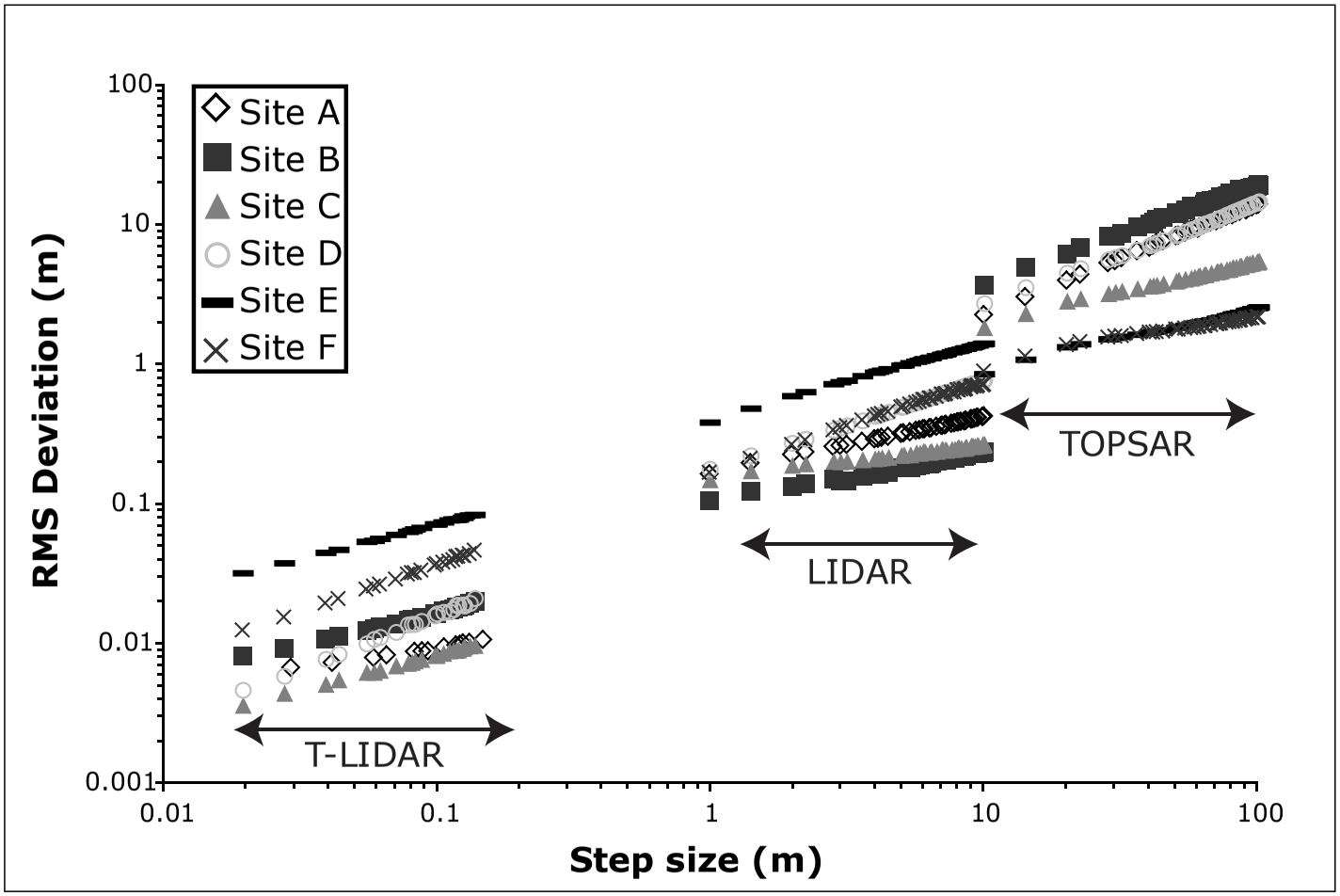

Figure 10. Deviograms of six field sites at 3 dataset resolutions. Gap between T-LIDAR data and airborne LIDAR data is the result of insufficient coverage of the T-LIDAR data to obtain roughness data at longer step sizes. Photos showing each site are in Figure 6.

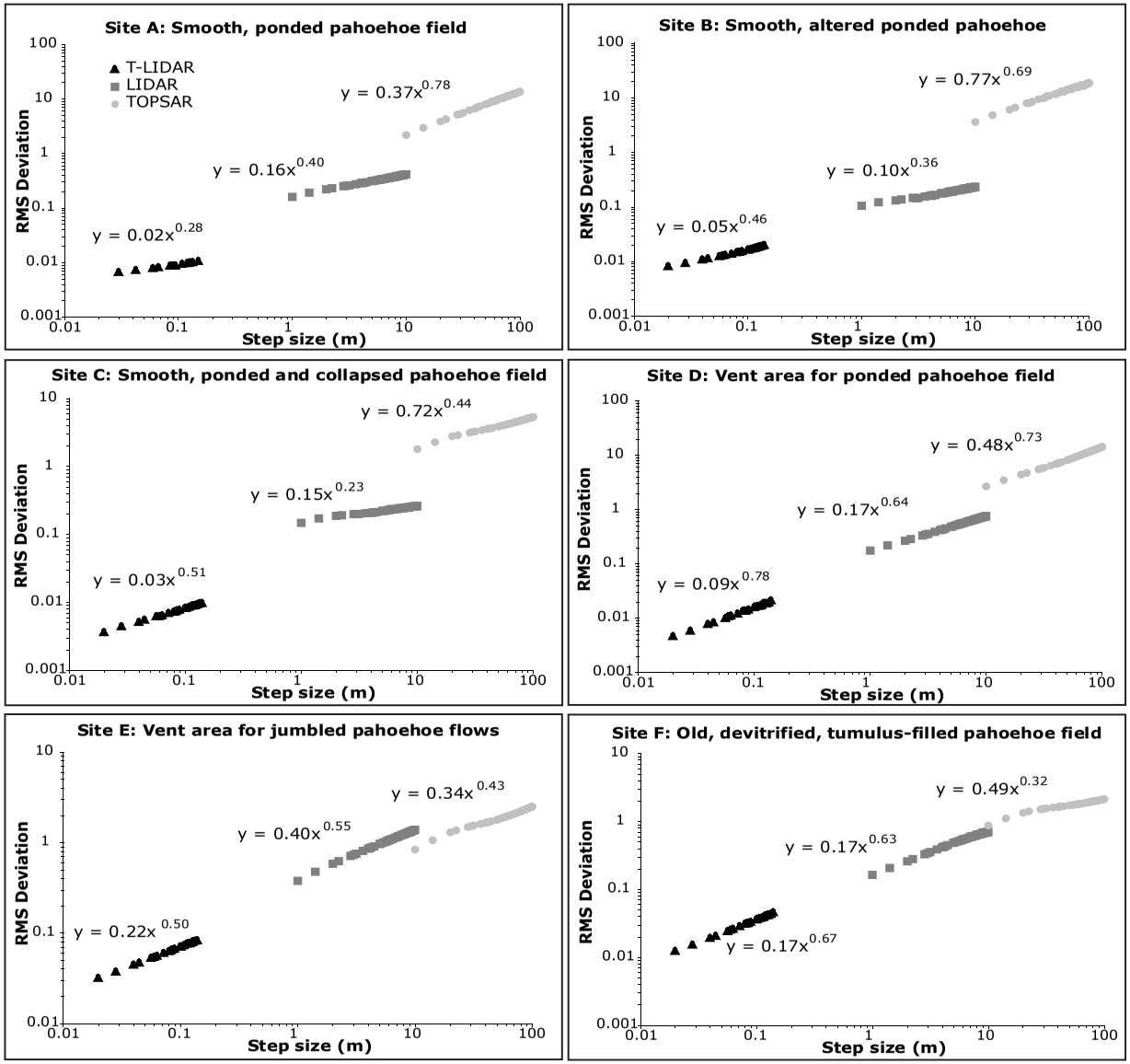

Figure 11. Deviograms of field areas described in text. Black triangles represent deviations obtained from T-LIDAR-derived topography. Dark gray squares represent deviations obtained from airborne LIDAR-derived topography. Light gray circles represent deviations calculated from TOPSAR-derived topography. Offsets are the result of differences in cell size and represent effect of averaging different surfaces in each cell. Hurst exponents are exponents of power laws fit to each dataset. In order to maximize the available information, the vertical scale varies among graphs. a) Site A; b) Site B; c) Site C; d) Site D; e) Site E; f) Site F.

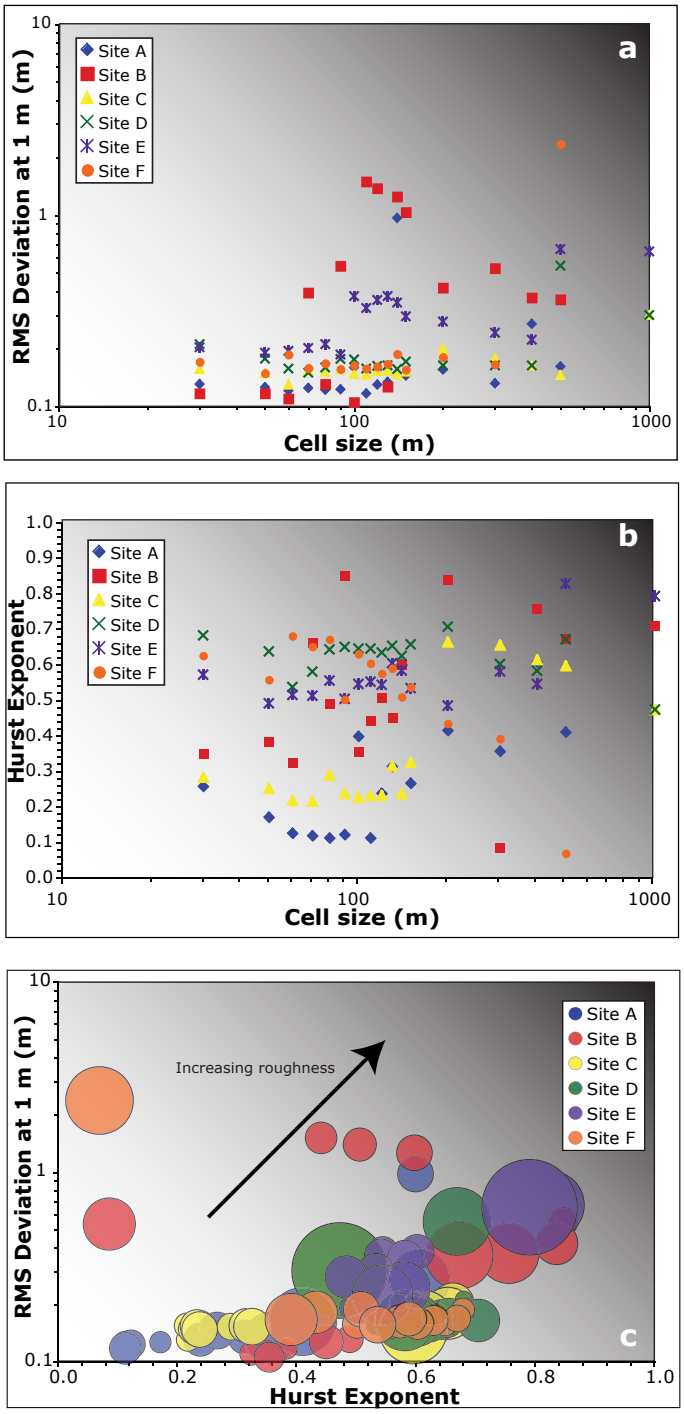

Figure 12. Comparison of RMS deviation at 1 m, Hurst exponent and cell size calculated from the 1 m/pixel airborne LIDAR data at each field site. a) RMS deviation at 1 m vs. Hurst exponent for each cell size. b) Hurst exponent vs. cell size. c) RMS deviation at 1 m (reference scale) vs. cell size where cell size is represented by the size of the circle.

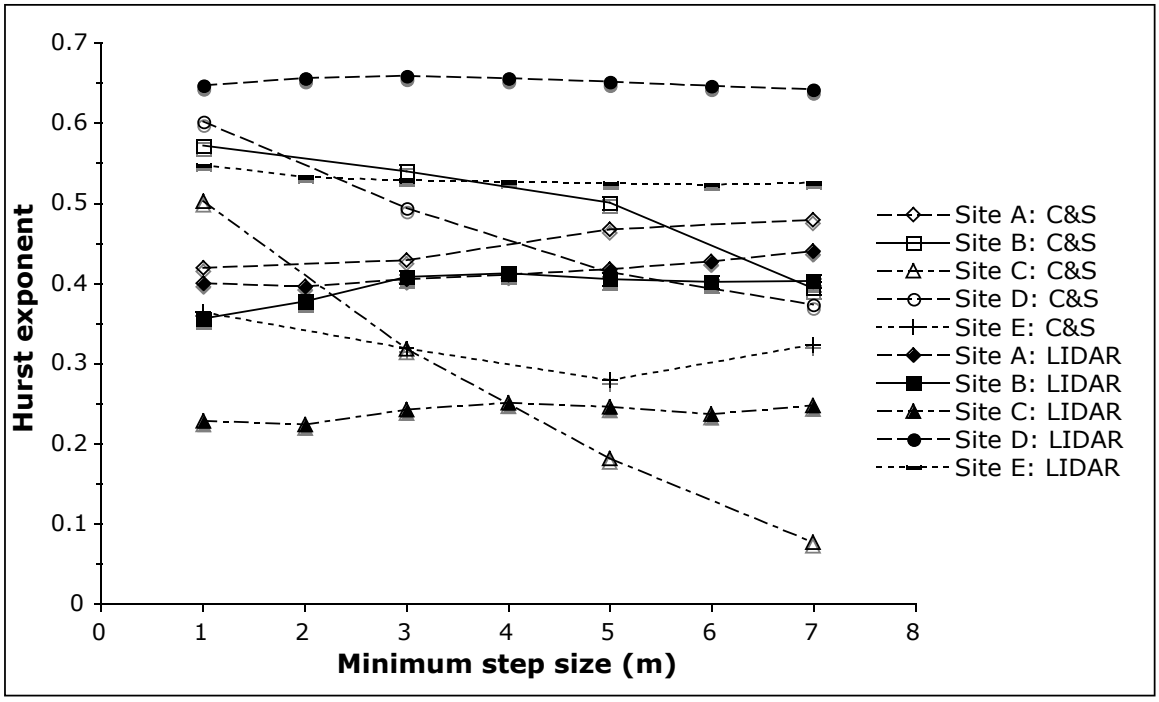

Figure 13. Comparison of Hurst exponent calculated for decreasing deviogram sizes in 1D (Campbell and Shepard [1996] data) and 2D (airborne LIDAR data). Maximum step size for all tests was 10 m. Data from Campbell and Shepard [1996] calculated using 2D method in 1D. Note higher degree of Hurst exponent variation in 1D data in comparison to airborne LIDAR 2D data. Open symbols denote Campbell and Shepard [1996] Hurst exponents and filled symbols denote 2D Hurst exponents from this study.

CHAPTER 4. POSSIBLE IMPACT MELT AND DEBRIS FLOWS AT TOOTING CRATER, MARS

To be published as Morris and Mouginis-Mark

Abstract

Candidate examples of impact melt flows and debris flows have been identified at Tooting crater, an extremely young (<2 Myr), 29 km diameter impact crater in Amazonis Planitia, Mars. Using HiRISE, CTX and THEMIS VIS images and a stereo-derived HiRISE DEM, we have studied the rim and interior wall of Tooting crater to document the morphology and understand the formation of several flow features. Four flow types have been identified; including impact melt sheets and three types of debris flows. The flow features are predominantly located on the southern rim and interior wall of the crater. Extensive structural failure has modified the northern half of the crater and we interpret this to have resulted in the destruction of any impact melt emplaced, as well as volatile-rich wall rock. The impact melt flows are fractured on the meter- to decameter scale, have ridged, leveed lobes and flow fronts, and cover an area > 6 km x 5 km on the southern rim. The debris flows are ~ 1-2 km in length, and the flow widths vary from a few tens of meters to > 300 m. The debris flows exhibit varying morphologies, from a channelized, leveed flow with arcuate ridges in the channel, to a rubbly flow with a central channel but no obvious levees.

1. Introduction

For years the study of impact craters on Mars has been used to examine the spatial and temporal variations in surface properties of the target materials [Barlow and Perez, 2003; Carr et al., 1977; Mouginis-Mark, 1979; 1981; Osinski, 2006]. Several different lobate ejecta morphologies are observed on Mars [Barlow et al., 2000] and an ongoing debate concerns the mode of ejecta emplacement for these craters. The two proposed models are formation by fluidization of the solid ejecta through their interaction with volatiles derived from the target [Carr et al., 1977; Mouginis-Mark, 1979], or by interaction of ejecta with the atmosphere [Barnouin-Jha and Schultz, 1998; Schultz and Gault, 1979]. The former mechanism is the most widely accepted and has been used as evidence for volatiles in the Martian crust at the time of crater formation [Barlow et al., 2000]. In almost all cases, the age (i.e., degradation state) of the crater precludes the confident identification of landforms considered to be most diagnostic of volatiles being in the target at the time of crater formation. The study of the impact ejecta of young, large craters on Mars is believed to have the potential to provide information regarding the distribution of landforms that could support or refute the idea that ejecta are fluidized by target volatiles [Mouginis-Mark and Garbeil, 2007].

Mouginis-Mark [1987], upon examining Viking Orbiter images (8-17 m/pixel) of selected 16-26 km diameter impact craters in the equatorial region of the southern hemisphere, noted several landforms that may be indicative of the state of volatiles in a target material at the time of crater formation. The morphological analysis of landforms within the ejecta blankets and interiors of the impact craters addressed the question of whether the volatiles were frozen or liquid [Mouginis-Mark, 1987]. Mouginis-Mark

[1987] suggested that the retention of small-scale features such as pressure ridges, scour marks and sharp distal ramparts implies the relatively high mechanical strength of the crater ejecta and argues against the presence substantial amounts of liquid water in the ejecta. Additionally, Mouginis-Mark [1987] proposed that large, volatile-rich blocks appear to have been transported and deposited by the ejecta flow of two small craters at Schiaparelli basin, and suggested that the collapse features around the blocks are evidence for subsidence due to melting or evaporation of ice. In contrast, Mouginis-Mark [1987] also observed limited evidence for surface flow of liquid, expressed as numerous, small channels (190-650 m wide) on the crater walls and ejecta blanket of Cerulli crater. Additionally, Mouginis-Mark [1987] suggests that more extensive slumping of the crater interior would likely indicate the incorporation and release of liquid water in the crater walls and ejecta blanket.

Recent high resolution imaging data from the Context Imager (CTX; 6 m/pixel) [Malin et al., 2007] and the High Resolution Imaging Science Experiment (HiRISE; 0.25-0.30 m/pixel) [McEwen et al., 2007a] have provided an unprecedented look at the surface geology of several pristine, geologically recent craters. Enhanced resolution has enabled detailed geomorphic and topographic analysis of features associated with the craters, and has reinforced the role of volatiles in the impact cratering process [McEwen et al., 2007b; Mouginis-Mark et al., 2007; Tornabene et al., 2007].

We have examined images from the visible wavelength of the Thermal Emission Imaging System (THEMIS VIS; ~17-18 m/pixel) [Christensen et al., 2004], as well as CTX and HiRISE data to identify the distribution and geomorphology of different types of lobate flow features on the southern rim and interior wall of Tooting crater (Figure 1)

that may relate to the distribution of volatiles. In addition to the image data, we have also produced two HiRISE stereo-derived, and Mars Orbiter Laser Altimeter (MOLA)-controlled, digital elevation models (DEMs) of the southern and southwest rims where particularly interesting flows can be found. The HiRISE DEMs were produced by Harold Garbeil and are generated by cross-correlating stereo images to derive pixel offsets and relative position for the image pair. Following the generation of the offset file, individual MOLA shots are used to register the DEM and provide absolute elevations. To validate the results of the calculation, the predicted heights are compared to the actual MOLA shot values and the resulting correlation is generally greater than 98%.

In this analysis, we first describe the distribution of four types of flows, and then focus on the topographic analysis of a specific flow to evaluate its mode of formation and relationship to the cratering event itself. Our analysis of the four flow types (which constitute two major flow groups) helps us understand the role of volatiles in the crater formation and ejecta emplacement process, as well as the preferential distribution of the flows, and flow formation sequence. There are two mechanisms proposed for the origin of the flows described in the following sections. The first mechanism is a formation due to the flow of impact melt formed from the target rock due to shock wave compression and release during the impact event [Melosh, 1989]. The second proposed formation mechanism is the mobilization of impact ejecta by incorporation of volatiles released during the impact event.

2. Geologic Setting of Tooting crater

Tooting crater is ~29 km in diameter (Table 1), is located at 23.4ºN, 207.5ºE, and is classified as a multi-layered ejecta crater [Barlow et al., 2000]. Inspection of THEMIS

VIS images of Tooting crater reveals that there are 13 smaller impact craters ≥ 54 m in diameter superposed on the ejecta blanket, which has an area of ~8120 km^2 [Mouginis-Mark and Garbeil, 2007]. Using the 2004 iteration of the Martian crater-count isochron [Hartmann, 2005; his table 2], gives an age for Tooting crater that is < 2 My.

Tooting crater formed on virtually flat, young, layered basalt lava flows within Amazonis Planitia [Tanaka et al., 2005], where there appear to have been no major topographic features prior to the impact event [Mouginis-Mark and Garbeil, 2007]. The depth of the crater and the thickness of the ejecta blanket have been determined by subtracting the elevation of the surrounding landscape (-3872 m) from the individual MOLA elevations of the crater rim and ejecta blanket [Mouginis-Mark and Garbeil, 2007]. The measured depth of the crater floor below the northern rim crest is 1567 m and the measured depth of the crater floor below the southern rim crest is 1851 m [Mouginis-Mark and Garbeil, 2007]. The width of the final crater cavity appears to have been increased by structural failure (slumping due to terrace formation) on the north/northeastern half of the crater that is essentially absent on the south/southwestern half of the crater (Figure 2). The proposed pre-slump diameter is ~26.4 km (Figure 2), about 2.5 km less than the existing crater diameter (~29 km). Garvin and Frawley [1998] established the relationship $d=0.25D^{0.49}$, where d is the depth and D the diameter, both in km, for 98 of the most unmodified Martian craters. Using this relationship and the proposed pre-slump diameter, Tooting crater is predicted to have a depth of 1302 m, but in reality it is ~1.3 times deeper on the northern floor and ~1.5 times deeper on the southern floor.

The structural failure of the southern crater wall appears to be less extensive than that observed on the north/northeastern wall of the crater where two major terrace blocks are identified (Figure 2). Additionally, the south/southwestern half of the crater exhibits extensive smooth material with lobate flows on the inner crater wall, whereas this material is nearly non-existent on the north/northeastern portion of the crater. A study of the ejecta distribution reveals that, for a given radial distance from the cavity rim, the ejecta blanket is ~100 m thicker on the northeastern portion of the ejecta blanket than on the southwestern portion [Mouginis-Mark and Garbeil, 2007]. Additionally, Mouginis-Mark and Garbeil [2007] note that the maximum radial distance of the ejecta is greatest at an azimuth of 30º (~NE) and smallest at 210º (~SW). Based upon the asymmetry in the distribution of the ejecta blanket (both the maximum range and the ejecta volume), the northeastern direction is the inferred downrange direction (Figure 1) resulting from a presumed oblique impact [Mouginis-Mark and Garbeil, 2007].

3. Types of flows observed in HiRISE and CTX data

Four types of flow features are observed in CTX and HiRISE images, either on the outer rim or the inner wall of the southern portion of Tooting crater (Figure 2, boxed areas), and these flow features exhibit a range of flow morphologies. In addition, there are two small flows observed on the northern rim. We will discuss all of these flows in following sections. Prior to this study, none of these flow types have ever been observed at a Martian crater. This suggests that these observations are therefore, very valuable to the study of impact cratering dynamics on Mars.

3.1. Flow Type 1: Smooth, polygonally fractured material

Several flows can be identified on the southern rim of Tooting crater (Figure 3). Extensive smooth, polygonally fractured material with lobate flow fronts is the largest unit mapped in this study (Figure 3b). As revealed in the HiRISE-derived DEM, the fractured materials are present at elevations between ~200 m above and ~400 m below the break in slope that defines the edge of the southern rim (Figure 4). As observed from HiRISE image PSP_001538_2035, the materials extend from the edge of the cavity rim to at least 6 km away from the south-southeastern rim. Where the material is present on the edge of the rim, it exhibits some degree of coherence, as there are obvious overhangs and a high degree of erosion beneath the overhang (Figure 5a). The horizontal extent of the rim overhang is unknown, although we estimate there is at least several meters of material suspended above the fluted rim and eroded talus slopes. The materials in this region exhibit decameter- to meter-scale polygonal fractures (Figure 5b). These fractured materials appear to be laterally continuous, although near the tops of steep slopes they have formed lobes (Figure 4).

We note that there are very few boulders on the surface of the fractured materials resolved in the HiRISE images (minimum size of features resolved ~90 cm [McEwen et al., 2007a]), although some flow fronts do exhibit a concentration of boulders (Figure 5b). On the surface of the southern rim, the presence of meter-scale boulders and fractured material appear to be mutually exclusive. There are very few impact craters on the surface of the fractured materials, and those craters that are observed in the HiRISE images are typically < 40 m in diameter.

In addition to the polygonally fractured materials, there are also ridged, lobate, flow-like features present on the rim of the cavity (Figure 6). The lobate features generally grade into the fractured material without any obvious stratigraphic contact (Figure 3). The lobes north of a local topographic high (marked by a dashed black line in the figure) flowed toward the crater cavity, whereas the lobes to the south of the high flowed south/southwest, away from the crater cavity (Figure 4). Precise measurement of individual flow widths and lengths is difficult because the features often coalesce. These lobes exhibit a diversity of features, including transverse ridges, raised levees and boulders on their surfaces and margins. Two of the most prominent lobate features appear to originate at scarps near the crest of a local topographic high and extend north toward the crater center within topographic lows created along the boundaries between incipient slump blocks (Figure 6).

3.2. Flow Type 2: Hummocky and smooth lobes

In addition to the smooth, fractured materials and ridged, lobate materials on the southern rim of Tooting crater, there are also several hummocky and smooth flows that appear in one 2.4 km by 2.7 km area between the polygonally fractured materials to the east and smooth and pitted terrain to the west (Figure 7). These flows are grouped together based on their spatial proximity and absence of these flow morphologies in any other areas of Tooting crater imaged by HiRISE. The surfaces of these flows vary from hummocky on the meter to tens of meter scale on the largest flows to nearly smooth with knife-edged levees on the smaller flows. These surface morphologies appear to be mutually exclusive. Each flow will now be discussed.

The largest of these flows, Flow 2, is ~1260 m long and ~225 m wide, hummocky and appears to emanate directly from collapsed terrain (Figure 7). Individual MOLA shots indicate that the source for Flow 2 appears to be at an elevation of -3634 m. Unfortunately, MOLA data points are absent near the distal end of the flow so the gradient of the underlying surface cannot be determined. This flow has levees of rubbly material, each ~60 to 70 m across, that enclose a lineated channel region that is ~86 m across at its widest. The channel is ~490 m long and is characterized by linear features parallel to the direction of flow. The channel also contains several isolated, elongate features (longitudinal bars) that are similar in morphology to the levees. The largest of the elongate features is 5-6 m across and 18 m long. The central channel terminates in a low, smooth mound ~36 m long (parallel to the flow direction) and 15 m across, ~618 m from the distal end of the flow. The outer margin of Flow 2 is characterized by individual lobes on the scale of tens of meters or less in horizontal extent (parallel to the flow direction). The flow overlies material that is interpreted to be undivided sediments as well as regions of fractured material and blocky material. The distal end of Flow 2 appears to be slightly digitate and overlies hummocky pitted terrain similar to that described in Mouginis-Mark and Garbeil [2007] within the crater cavity (Figure 7b).

The smooth, smaller flows (not studied in detail here) typically exhibit coalescing morphologies, with enclosed inliers of the pre-existing surface (kipukas) visible within some flows (Figure 7c). The flows widen and narrow along their length. Some of the shortest of the small flows are on the order of tens of meters long and only a few meters across. The source regions for the smaller, smooth flows are not as obvious as for Flow 2 and the other rubbly, large flows in the region.

3.3. Flow Type 3: Hybrid lobe (Flow 3)

A third type of flow is a long flow on the southwestern interior wall of Tooting crater (Figure 8). The source region for this flow lies between two discrete wall blocks and it is characterized by a centripetal network of channels that flow toward the crater floor. The flow is ~1570 m long and its width varies between ~250 and 500 m. It is difficult to assess the elevations of the source region and distal end of Flow 3 due to the lack of MOLA shots for this specific location. The upper reaches of the flow are characterized by large boulders (2-5 m across) and discontinuous levees (Figure 9a) whereas the distal 600 m of the flow is composed of ~6 discrete lobes that are each ~10-15 m in width (Figure 9b). The distal lobes appear to be smooth with steep margins, prominent narrow levees (< 3 m wide), and appear to have very few boulders on their surfaces. The distal lobes do not appear to coalesce; rather, they appear to have progressively overridden or have been deflected by previously emplaced distal lobes. The transition from hummocky and boulder-rich to smooth with steep levees is spatially correlated with the termini of several large channel features on the slump block (Figure 8b).

3.4. Flow Type 4: Leveed, ridged, channelized flow (Flow 4)

3.4.1. Local sketch map and description of general units

The fourth flow type is located on the west-southwest rim of Tooting crater. This flow was selected as a case study due to the availability of HiRISE stereo coverage of the flow and the ability to study its entire length from the inferred source region to the distal lobes. In contrast to the location of the other flows, the availability of HiRISE stereo data and coincident MOLA data in this region enables the production of a high resolution

DEM. Flow 4 provides a unique opportunity to examine the geomorphology and topography of a young impact-related flow feature on a pristine crater (Figure 10)

Flow 4 is located within the unit defined as *Rf* by Mouginis-Mark ("rim materials with flows," 1:200K geologic map, in prep.), and is described as rim material containing blocks that may lack an overlying ejecta layer. A sketch map of the area (Figure 10b) identifies the units in this region. The flow is primarily emplaced on blocky ejecta with linear ridges that trend radially away from the crater cavity (RS, Figure 10b). Within this unit, there are also several smooth sediments or flow materials occupying the areas between linear ridges. Uphill from, and adjacent to, the ridged, blocky unit is a mountainous, massive unit with smooth sediments or perhaps other flow materials (MS, Figure 10b). In addition to the massive unit and the ridged unit is a unit composed of pitted terrain (PT, Figure 10b), which appears to be similar to the pitted terrain mapped in the region of Flow 2 and on the main Tooting crater floor [Mouginis-Mark and Garbeil, 2007].

3.4.2. Geomorphology and topography

3.4.2.1. Dimensions

Two HiRISE scenes (PSP_002580_2035 and PSP_002646_2035) cover the region encompassing Flow 4, providing the opportunity to produce a stereo-derived and MOLA-point controlled DEM of the flow and surrounding terrain at a spatial resolution of 0.25 m/pixel (Figure 11), and enabling detailed topographic analyses to be performed. Harold Garbeil produced the DEM.

A series of 19 cross-flow topographic profiles were acquired from the DEM at a spacing of ~40-75 m, and measurements of flow thickness, flow width, channel depth and

channel width were recorded at each profile location (Figure 11). For each profile (see Appendix B, profiles 1 to 19), flow thickness was measured from the elevation of the substrate just west of the flow to the top of the flow (maximum elevation of the associated profile). The height of the western levee was used due to the emplacement of post-flow sediments on the eastern side of the flow. Flow width was measured across the entire flow, including the levees. The channel depth was measured from the top of the levees to the surface of the channel, and channel width was measured across the channel (between the interior margins of the levees). In addition to the topographic measurements, flow length was measured from the individual HiRISE images. Based on slope measurements of the adjacent terrain, the general topographic gradient is approximately 2.3º. The portion of the flow where the channel developed has a slope of ~9.5º (between profiles 4 and 12; Figure 11) and the steepest portion of the flow (the cliff identified in Figure 10b) has a slope of nearly 18º (between profiles 4 and 8; Figure 11). To accentuate small-scale variations in topography, the longitudinal profile down the center of the flow was detrended by removing the long-wavelength topographic slope using a least squares polynomial fitting routine in IDL.

Flow 4 is ~1900 m in length and 1050 m from the top edge of the cliff to the lobate, distal toe (Figure 10). Three distinct sub-lobes characterize the distal portion of the flow (Figure 10). The flow width varies from a minimum of ~75 m where the flow was channeled between ridges and subsequently traveled over the cliff (Figure 10b) to a maximum of ~ 310 m at the widest part of the three sub-lobes in the distal reaches of the flow (Figure 12a). The thickness of the flow varies from a minimum of ~0.5 m at the

apex of the cliff to a maximum of 6 m just up-flow from the division into the three sub-lobes (Figure 12a).

3.4.2.2. Source area of Flow 4

The source area for Flow 4 is just south of the crater rim and it is somewhat confined by one of the linear ridges in the "NE-SW trending linear ridges with sediments or flow materials" unit (Figure 10b). Upslope from the cliff, the material that eventually comprises Flow 4 appears to have ponded behind the ridge and formed small spillover lobes. The flow eventually overtopped the small ridge and was channeled over the cliff between two of the linear ridges, forming a lobate flow with levees, a channel and discrete distal lobes. Just above the cliff, a series of braided channels intersects the upper margin of the lobate flow.

3.4.2.3. Channel, levees and flow margins

The channel begins at the edge of the cliff and ends in a slight rise just up-flow from the start of the distal sub-lobes (Figure 11). The characteristics of the northwest and southeast levees differ. The NW levee is typically rough, with a mottled surface that appears morphologically similar to the surface of the distal lobes. Along much of the channel, the SE levee is smooth but irregularly fractured, although the smooth levee disappears and a levee similar in texture to that on the NW appears ~350 m from the cliff (~570 m from profile 1; Figure 11). The width of the channel is ~61 ± 20 m. The narrowest portion of the channel is located at the apex of the cliff, where the channel is ~30 m wide. At the base of the cliff, the channel widens out to ~74 m. Within the channel are convex down-flow transverse ridges. The average spacing between ridge crests is 8

m. The individual ridges are not resolved in the DEM, and as a result we interpret that they are < 1 m high.

Using the HiRISE images and DEM, the width and depth of the channel were measured at each profile location and plotted against the distance from Profile 1 (Figure 12). Channel width and depth are inversely correlated; the deepest parts of the channel are also the narrowest parts of the channel. The channel is deepest (~4 m) and narrowest (30-40 m) between profiles 4 and 6, which is also the steepest section of the channel. Between profiles 7 and 12, the channel is notably shallower (1-2 m) and wider (65-82 m), and the topographic gradient is also generally less steep than the gradient between profiles 4 and 6. Channel width appears to be correlated with flow thickness (Table 2). As channel width increases, the thickness of the flow increases (Figure 13a). Channel depth is anti-correlated with flow thickness (Table 2, Figure 13a). Channel width is weakly correlated with flow width (Table 2). As channel width increases, the width of the flow typically increases (Figure 13b). Channel depth is anti-correlated with flow width (Table 2). As channel depth increases, flow width decreases (Figure 13b). The exception to this is profile 5, where the flow is 96 m wide, but the channel is 4 m deep and 37 m wide. Because the channel is restricted to the region of the slope between NE-SW trending ridges, it is likely the channel formed in this region as a result of flow confinement (Figure 10).

The margins of the flow exhibit a lobate nature, and the lobes are spatially correlated with slight topographic highs that cross the interior of the flow (Figure 11). The lighter toned small lobes on the edges of the flow can be traced across the interior region, forming topographically higher “fronts” that are obliquely angled to the flow

direction. The lobes on the margins of the flow are ~10-20 m in length, and a few meters in width. These bright topographically high features are called pulse fronts (PF, orange lines drawn on the flow in Figure 10b).

At least three large-scale flow lobes characterize the region of the distal portion of the flow (Figure 10). The two outer lobes appear to be bifurcated components of the same flow and the central, farthest-reaching lobe was emplaced separately. The lobe farthest to the west is ~27 m wide and 4 m thick, the central lobe is ~146 m wide and 4 m thicker than the western lobe, and the eastern lobe is ~91 m wide and ~2 m thick (Profile 17, Figure 11). The distal toe of the central lobe superposes pitted terrain similar to that observed on the northern crater floor and at the distal end of Flow 2 (Figure 10b).

There are ~1 m-high linear features that are generally parallel to the flow direction, identified in the sketch map by purple lines, and they are located primarily along the channel (Figure 10b). The most prominent of the linear features is located between the central channel and the smooth SE levee. In addition to the channel-bounding features, there are also flow-parallel linear features near the region where the distal portion of the flow is divided into three sub-lobes (Figure 10b).

The surface of the flow is covered by boulders that range from the minimum resolvable size (~90 cm, [McEwen et al., 2007a]) up to several meters across (Figure 10b). Above the cliff, the boulders are concentrated in the center of the flow, often occurring in "boulder chains." Below the edge of the cliff the boulders are mostly located along the outer margins of the flow lobes. A few boulders are located in the upper reaches of the channel, just below the base of the cliff, but otherwise the channel is devoid of large boulders. Toward the distal end of the flow, near the dispersed, lobate

margin, boulders are concentrated along the margins of the western, central, and eastern sub-lobes.

3.4.2.4. Surface roughness

The surface roughness of the flow may provide information regarding the down-slope evolution of the material in the flow. Previous studies of the surface roughness of lava flows on Kilauea Volcano documented centimeter- to meter-scale variations in surface roughness that reflect variations in the type of lava flow under investigation [Chapter 3; Campbell and Shepard, 1996; Shepard et al., 2001]. Based on the topographic variability, distinctions can be made between ponded pahoehoe flows, compound pahoehoe flows, and slabby, near-vent pahoehoe flows [Chapter 3 figures 8 and 9; Shepard et al., 2001], and here we employ a similar approach in studying the changes in surface roughness on Flow 4. Assuming that surface roughness changes are the result of rheological changes within the flow during emplacement, we have examined the topographic variability in order to estimate the potential amount of surface roughening or smoothing that occurred down-flow. Following the methods developed in Chapter 3, we performed a scale-dependent, two-dimensional surface roughness analysis of Flow 4 and the adjacent terrain. In this analysis, the 2D topographic deviation and scaling properties of the surfaces were calculated for areas in the stereo DEM equaling 100 m^2 (10 x 10 m groups of pixels called cells) and 625 m^2 (25 x 25 m cells) [Chapter 3]. The surface roughness is quantified by first calculating the RMS deviation (the RMS difference in elevation of points separated by a horizontal step) of all points separated by a given step, up to 10% of the cell size [Shepard et al., 2001]. Next, the RMS deviation is plotted against the step size on a log-log plot called a deviogram, and a line is fit to the data to

determine the Hurst exponent (*H*, slope of the line), a value between 0 and 1 that describes the scaling behavior of the surface roughness. A low Hurst exponent indicates that, with increasing horizontal step size, the surface roughness increases at a slower rate than the increase in step size. A high Hurst exponent means the surface roughness increases at a scale comparable to the increase in horizontal step size. A surface with a Hurst exponent of 1 is self-similar. Previous studies of geologic surfaces have indicated that changes in the Hurst exponent (changes in line slope) on a deviogram may reflect different processes affecting the surface roughness at the scale at which change is observed [Chapter 3; Shepard et al., 2001]. To facilitate comparison among different surfaces, we use the y-intercept of the deviogram to provide information on the surface roughness at a horizontal reference scale, typically 1 m. Rougher surfaces in the region will have higher y-intercepts and smoother surfaces will have lower y-intercepts.

We observe differences in surface roughness between Flow 4 and the surrounding terrain in the 2D maps calculated using the above technique (Figure 14). Overall, the flow is distinctly smoother than the surrounding region as shown in the y-intercept map (Figure 14a). The flow has higher Hurst exponent, indicating that it roughens at nearly the same rate as the horizontal scale increases (Figure 14b). In the y-intercept map, the channel levees exhibit higher y-intercept values (i.e., are rougher) than both the channel itself and the distal lobes (Figure 14a). The Hurst exponents of the channel and levees are fairly high (0.8-0.9) in the 10 m cell size map, suggesting that the flow increases in roughness at the same rate as horizontal step size increases from 0.25-1 m (Figure 14b). The lobes down-flow from the channel are smooth (lower y-intercept), with a lower Hurst exponent, indicating that, within a cell, the surface does not roughen with increasing step

size. The distal lobes of Flow 4 are significantly smoother than the surrounding terrain (Figure 14a) and the Hurst exponents are higher than the surrounding terrain (Figure 14b).

When examined using similar cell sizes, overall, Flow 4 exhibits higher Hurst exponents and similar roughness to the pahoehoe flows described in Chapter 3. Portions of Flow 4 exhibit surface roughness and Hurst exponent (scaling behavior) similar to the topographic characteristics derived from the airborne lidar data for sites D and F (compound flow fields) in Kilauea caldera [Chapter 3]. The regions of Flow 4 most similar in topographic roughness to the Kilauea compound pahoehoe flows are above the point where the flow is channeled over the cliff and on the distal lobes. With the exception of site E, the jumbled near-vent Kilauea pahoehoe flow, the channelized region of Flow 4 is rougher (higher y-intercepts) and has higher Hurst exponents than all the Kilauea pahoehoe field sites. The Hurst exponents of the ponded pahoehoe flows on Kilauea are a factor of two less than the those of all points measured on Flow 4, indicating that the surface of Flow 4 smoothes at a slower rate than the ponded flows in Kilauea caldera at the meter scale. The topographic characteristics of the proximal and distal regions of Flow 4 are similar to the compound flows of Kilauea caldera. The topographic characteristics of the middle section of Flow 4 are rougher than all the sites in Kilauea caldera except site E, the jumbled pahoehoe flow. This indicates that at the meter scale, Flow 4 exhibits topographic characteristics that are comparable to the compound pahoehoe flows in Kilauea caldera.

4. Discussion

The diversity of flow morphologies observed in this study argues against a common origin for all flows identified on the southern rim and interior wall of Tooting crater. Two mechanisms are proposed for the origin of the flows: flows of impact melt/melt-bearing material and/or sediment flows. Assuming a relatively homogenous target material, were these all flows of impact melt, melting of a target material with similar rheology would likely produce melts with comparable rheologies, distribution and preserved flow characteristics. Alternatively, the morphological differences in the discrete flows may be the result of heterogeneities in the target, differences in thermal histories, or the variable influence of underlying topography. Based on our observations, we suggest that the Type 1 flows (fractured flows with lobate flow fronts) on the southern rim of the crater are sheets of impact melt and Flows 2, 3 and 4 are debris flows.

4.1. Two major flow groups

4.1.1. Type 1 flows: Possible impact melt

The location of the Type 1 fractured flows on the southern rim of the crater and the morphology of the flows are both consistent with observations of materials interpreted to be cooled sheets and flows of impact melt on lunar craters such as Copernicus [Howard, 1975], Necho [Hawke and Head, 1977] and King [Heather and Dunkin, 2003]. The ridged lobes within the flow suggest that the material behaved as a cohesive, laminar material, as opposed to a turbulent flow. The fractured material exhibits a high degree of coherence, as demonstrated by the overhang of material over the rim edge (Figure 5a). It is unlikely that a desiccated, non-metamorphosed sedimentary deposit would maintain sufficient mechanical strength to form the overhangs observed on the crater rim. The surfaces of the fractured flows appear to have very few craters,

suggesting that they were emplaced after the termination of the primary phase of ejecta fallout. Studies of lunar craters indicate that during an impact event, the last material to be emplaced is any impact melt that may be produced [Wilhelms, 1987]. Additionally, impact melt deposits are typically emplaced onto the proximal region of the ejecta blanket [Wilhelms, 1987]. The ridged, lobate flow features in the fractured sheet flows are morphologically similar to lobate, channelized flows of impact melt on King crater, on the far side of the Moon [Heather and Dunkin, 2003].

The fractured flows have few boulders exposed on the surface, indicating that one (or more) of the following occurred: 1) any boulders on the pre-flow surface were scraped off by and pushed ahead of the flow during emplacement; 2) the material flowed around and ended up burying any pre-existing boulders; 3) any coeval boulders sank through the material and remain covered by the deposit; or 4) the flowing material did not include boulders. We observe concentrations of boulders only at disrupted flow fronts, so we discount option (1). The one exception to the lack of boulders is the rubbly lobate flow in Figure 5b. This flow grades into the fractured unit, and it appears as if the viscosity of the material increased prior to the initiation of motion on this rubbly lobe. If, during emplacement, the material represented impact melt, post-emplacement motion of a partially cooled flow would result in a broken-up, jumbled surface as observed in Figure 5b. Additionally, if option (2) occurred, we may expect to see evidence of flow around boulders, such as linear grooves in the surface. We do not observe this morphology, so we also discount option (2). It is difficult to determine whether boulders were initially present and subsequently sank through the material or whether the deposit lacked boulders upon emplacement. If the boulders were large relative to the thickness of the

flow, lumps or small topographic highs within the surface of the flow might identify boulders that were emplaced and subsequently sank. Additionally, it is unlikely that all boulders would have sunk through the flow, which would result in some boulders left partially exposed. We do not observe features consistent with lumps or partially exposed boulders within the surface, suggesting that option (3) is unlikely. We are thus left with option (4), that the deposit was emplaced boulder-free. The presence of the fractured flows in the near-rim region of the southern portion of Tooting crater, the lack of meter-scale or larger boulders and the lack of evidence for re-impacting of the surface by crater ejecta is consistent with the emplacement of a veneer of impact melt during the modification stage of the cratering event, prior to terrace formation during the crater relaxation stage.

4.1.2. Discrete flows: Debris flows

All of the discrete flows in this study are closely associated with channels, gullies and apparent sedimentary flow features. The source for Flow 2 appears to be a region of collapse adjacent to a local topographic high (Figure 7), suggesting a late-stage outflow of material from the subsurface. Flow 3 appears to be sourced just down-slope of a highly channeled/gullied wall block on the inner wall of the cavity (Figure 8). Flow 3 is spatially associated with gullies and sedimentary flows, yet it is interesting to note that the flow exhibits morphology similar to pyroclastic flow deposits emplaced during the 1980 eruption of Mount St. Helens (Figure 15). These volcanic flow deposits were fluidized by a gas phase, likely primary magmatic gases and entrained atmosphere [Wilson and Head, 1981]. The upper reaches of Flow 4 are also spatially associated with gullies sourced from the mountain block to the northwest of the flow. Flow 4 is located just down-slope

from a region of ponded smooth sediments with extensive channels that emanate from the smooth pond and intersect with Flow 4 just above the cliff (Figure 10). The spatial correlation between the discrete flows and channels and gullies likely to have formed by the action of liquid water suggests that the discrete flows are the product of the interaction of impact ejecta and liquid water.

Flows 2, 3 and 4 exhibit morphologies distinct from the fractured, lobate flow-front group as well as morphologies distinct among the three discrete flows. The discrete flows appear to be types of sediment/debris flows and we interpret the morphology differences to differences in amount of incorporated volatiles. All three flows have channels with levees and Flows 3 and 4 both exhibit narrow, flow-parallel linear features on the outer levees. The existence of the narrow linear ridges is reminiscent of the levees observed on sediment flows in Azerbaijan [Hovland et al., 1997]. Individual flows identified by Hovland et al. [1997] (their Figure 6) have the same narrow ridges and similar pressure ridges (albeit at a smaller scale) as the ones identified here at Tooting crater. This similarity suggests that these specific Tooting flows are likely not impact melt flows. Flow 2 lacks narrow, linear ridges, and the levee thickness and morphology are the same as the thickness and morphology in the post-channel portion of the flow, suggesting that plug flow did not form the channel. Rather, a secondary event, such as the release of liquid water, likely carved the lineated channel. The smaller, smoother flows near Flow 2 appear to lack the rubbly surface present on the larger, longer Flow 2 (Figure 7). The difference in flow morphology could reflect the relative abundances of liquid and incorporated ejecta, as Flow 2 originates at an obvious collapse structure, whereas the smaller flows do not. The smaller flows may represent slower, less catastrophic seepage

of volatiles from the topographic high adjacent to the region of Flow 2 and the associated flows.

Terrestrial studies of the depositional processes of experimental debris flows from flume experiments find that the resulting deposits are lobate, with steep blunt margins and marginal levees [Major, 1997]. The experiments were run down a 95 m long, 2 m wide chute with a slope of 31º [Major, 1997]. Individual experiments varied the amount of water in the sediment and determined that in the experiments, arcuate surface ridges were observed only on deposits from unsaturated flows, suggesting that ridges may be used as indicators of relative water content of the flow source [Major, 1997]. Additionally, Major [1997] notes that unsaturated flows accrete toward the source region from the distal end of the deposit and saturated flows primarily accrete in vertical increments by progressive overriding of previously deposited material. The morphologies of the unsaturated experimental deposits appear to be similar to Flow 4.

A comparison of Flow 2 and Flow 4 suggests that there may be local variations in the volatile content, source and mechanism for formation. Flow 2 is located on the southern rim of the crater and Flow 4 is located on the southwestern rim of the crater. Flow 2 emanates from a collapse feature, and the surface of the flow is rubbly and covered with boulders, consistent with the down slope movement of collapse debris (Figure 7a). The source for Flow 4 is likely to be sediments collected on the southwestern rim of Tooting crater, with volatile input from the ponded material on the mountain block to the northwest. The surface of Flow 4 lacks extensive boulder populations (Figure 10a) and the surface roughness calculation indicates that between step sizes of 0.25 and 1 m, Flow 4 maintains a relatively consistent smooth surface down the length of the flow

(Figure 14a). Flow 4 has a channel with well-formed levees, whereas the channel on Flow 2 appears to be a late-stage feature that eroded the pre-existing flow. In addition, Flow 4 exhibits pulse fronts down-flow (Figure 10b), while Flow 2 does not (Figure 7). The channel in Flow 4 is occupied by material exhibiting concave-down arcuate ridges and the channel in Flow 2 appears essentially emptied (or highly dissected at a late stage), with flow-parallel lineations and longitudinal bars within the channel (Figure 16a, c). The distal toes of the flows differ, as Flow 4 widens out into a tri-lobed flow with blunt, steep margins (Figure 16b) and Flow 2 narrows down-slope with somewhat digitate, individual lobes (Figure 16d).

Comparison of Flow 4 flow and channel dimensions with the Mauna Loa, Hawaii, 1984 Flow 1A ‘a’a flow [Glaze and Baloga, 2006] provides insight into the flow morphometry compared to a known lava flow (Table 2). Surprisingly, there are few terrestrial lava flows where the geometry of the flow has been tabulated, but one such flow is the Mauna Loa 1984 Flow 1A. This ‘a’a flow is 13 km in length, and thickens from 5 m near the source to 15 m at the distal toe. Generally, the measurements of Flow 4 morphometry are more correlated than those for the measured ‘a’a flow, suggesting Flow 4 behaves in a manner that is inconsistent with observed behavior of a known basaltic lava flow. In addition, we do not believe that Flow 4 is a pahoehoe flow, as pahoehoe flows typically do not form large-scale channels and levees [Kilburn, 2000].

Topography may play a role in the channel measurements discussed above. Examination of the topographic gradient of Flow 4 between individual profiles indicates that generally, as topographic gradient increases, flow width and flow thickness decrease (Figure 17a). In contrast, the local gradient appears to have a limited effect on channel

width and depth (Figure 17b). Generally, as local gradient increases, channel depth increases and channel width decreases. Unfortunately, topographic data for the Mauna Loa flow are not available, but topography may have played a key role in the flow measurements obtained from Glaze and Baloga [2006].

The discrete flows observed on Tooting crater exhibit a range of morphologies at HiRISE scale, from very smooth, with few boulders (e.g. distal region of Flow 3, Figure 9b), to rubbly and boulder-rich (e.g. Flow 2, Figure 7b). The differences in the flow morphologies may indicate differences in formation mechanism for the discrete, channelized flows. The lobate margins with prominent levees in the channel region of Flow 4 suggest that surges occurred during flow formation, similar to the observed formation of large-scale experimental debris flows [Iverson, 1997; Major, 1997]. The many-lobed margins and lack of pulse fronts of Flow 2 suggest that each individual lobe was emplaced individually, rather than as a coherent body with static margins. Assuming that the source of the material in the flows was similar crater ejecta, the main controls on the resulting flow morphology may be the relative amounts of volatiles and sediment, the size distribution of the sediment, and the underlying topography.

4.2. Volatiles

The discrete, channelized flows examined in this study appear to be related to the incorporation of volatiles and the resulting mobilization of the ejecta sediments. The two potential sources for the volatiles are 1) "bleeding" of water from the freshly exposed aquifer within the newly formed crater cavity or 2) *in situ* dewatering of the impact ejecta and wall blocks. Precipitation from the atmosphere is also possible, but probably unlikely, as it would have to be highly localized. A previous study of Mojave crater,

Mars, has suggested that impact-induced precipitation provided water that formed channels and fan features observed on much of the crater interior [Williams et al., 2004]. Presumably, the effect of precipitation would be evident on all portions of the crater, and as flow features are nearly absent on the northern rim, it is unlikely that rain contributed to the volatiles in the ponded sediments. A recent high-resolution study of Mojave Crater has provided evidence for depositional fan formation due to impact-induced overland fluid flow, although the amount and source of the fluid have not been constrained [Williams and Malin, 2008]. Dewatering of the exposed cavity wall, or of the emplaced ejecta seem to be most plausible, and both have been suggested by several previous studies [McEwen et al., 2007b; Mouginis-Mark et al., 2007; Tornabene et al., 2007].

The target material in which Tooting crater was formed is interpreted to be young, layered basalt flows [Tanaka et al., 2005]. In HiRISE and CTX images of Tooting crater, we observe layers in the walls, slumped wall blocks, and on the outer portion of the crater rim not covered by the proposed impact melt, and agree that these are layered basalt flows. Additionally, we observe extensive gullying on the southwestern wall block in the crater interior (identified as "gullied wall material" in Figure 8), as well as just upslope from the location where Flow 4 crosses the apex of the cliff face on the crater rim (Figure 10b). The presence of gullied material on the wall blocks on the southern interior of the crater suggests that volatiles were present in the target material at the time of crater formation. Potential evidence of a pre-existing aquifer in the young, layered basalt flows is observed to the southeast of the crater ejecta blanket, where braided channels intersect the north side of a depression (white box in Figure 1). The depression may have been a source for liquid water that flowed on the surface and formed the braided channels. The

channels suggest liquid was present on or near the surface in this region. It appears that the volatiles were present prior to the impact, as secondary craters from the cratering event that formed Tooting crater have been found on the channels. Additionally, the gullies in the near-rim crater ejecta (Figure 10) suggest that liquid water was also present on the surface adjacent to the crater cavity.

4.3. Flow Distribution

The flows on the rim and interior wall of Tooting crater are dominantly observed on the southern and southwestern side of the crater. A survey of the entire rim and interior wall of the crater reveals that only two small flows are present on the northern rim of the crater (the general location is identified in Figure 2). The location of the flows is coincident with the inferred up-range portion of the crater cavity. Additionally, large-scale terrace formation is more extensive on the northern and northeastern portions of the crater, coincident with the preferential deposition of much of the material ejected from the cavity (Figure 1).

Based on known crater formation mechanics, we infer that the proposed impact melt flows formed at the terminal end of the crater excavation stage (prior to terrace formation), and were likely equally distributed around the crater cavity. The lack of flow features on the northern rim may be the result of one of two related scenarios. In the first scenario, the flows formed equally at all azimuths, but were subsequently destroyed due to terrace formation on the northern half of the crater. In the second scenario, terrace formation occurred after impact melt emplacement and prior to debris flow formation, resulting in the inability of the northern half of the crater to form debris flows due to the

emplacement of the volatile-rich wall rock and near-rim ejecta onto the crater floor during terrace formation.

In the first scenario, we assume that the impact melt and debris flows formed equally at all azimuths. We propose that terrace formation post-dated flow emplacement, destroying any impact melt and/or debris flows present on the outer rim of the northern/northeastern portion of the crater, and subsequently burying flows on the interior wall. Dewatering of the target material and/or impact ejecta occurred prior to terrace formation, resulting in debris flows on the outer rim and inner cavity walls.

In the second scenario, we assume terrace formation occurred prior to debris flow emplacement, but after impact melt deposition. In this scenario, we propose that volatile-rich materials were emplaced on the crater floor during terrace formation on the northern half of the crater. On the southern half of the crater, the volatile-rich materials remained intact and subsequently dewatered, forming the debris flows observed on the south/southwestern region of the crater.

Although we cannot explicitly determine the relative timing of flow emplacement and terrace formation, the proposed large-scale failure of a volatile-rich wall has implications for other attributes of the crater interior. The crater cavity is nearly 200 m shallower on the northern floor than the southern floor [Mouginis-Mark and Garbeil, 2007]. Dewatering channels, absent on the walls and crater rim near the terrace blocks on the northern wall, may have been destroyed, while the pitted floor appears to be located primarily where the terrace blocks formed. The presence of the pitted terrain on the northern half of the crater floor may suggest that any volatile-rich material present in the wall and on the rim was slumped into the cavity and subsequently dewatered. The loss of

volatiles resulted in the formation of pits due to the mass deficits within the crater floor (voids created as volatiles were lost from the material slumped onto the crater floor).

We have observed that the volatile source may have been stratified within the target material, as some wall blocks appear to have dewatering channels, while others at a lower elevation in the crater cavity lack channels and gullies (Figure 8). The only two flow features observed on the northern crater rim are located between the two major terrace blocks, consistent with the first scenario, suggesting the debris flows formed at all azimuths around the crater but were preferentially destroyed by structural failure on the northern half of the crater.

4.4. Proposed flow formation sequence

Based on the above findings, we suggest the following sequence of events for the formation of the flows observed on the southern/southwestern rim and interior wall of Tooting crater.

1) Prior to the impact event, the surface of Amazonis Planitia was essentially featureless and composed of a series of layered lava flows [Tanaka et al., 2005]. Within the crater wall, we observe wall blocks with extensive gullying at higher elevation than blocks that lack dewatering features (Figure 8). The absence of flow features on the stratigraphically lower crater wall suggests a pre-impact layered target, where the upper layers were volatile-rich in comparison to the lower layers.

2) An impactor approached from the southwest, moving northeast, and struck the layered basaltic lava flows.

3) Ejection of the initial volatile-rich impact ejecta.

4) Late in the ejection phase, impact melt was ejected from the crater and emplaced on the near-rim ejecta. Studies of the Ries impact structure in Germany by Osinski et al. [2004] indicate that the near-rim deposits of melt-rich lithologies were not ballistically emplaced. Osinski et al. [2004] suggest that the deposit was emplaced outward from the crater cavity as an impact melt-rich, ground-hugging flow during the final stages of crater formation. This is consistent with our observation of few craters and boulders on the surface of the flows.

As discussed in the previous section, the relative timing of the crater modification and flow formation is still ill constrained. The next portion of the proposed timing of the cratering event will discuss the two possible scenarios identified in Section 4.3 and the implications for each scenario.

4.4.1. Scenario 1: Flows formed prior to terrace formation

5) The crater cavity began collapsing. During cavity collapse, the near-rim impact melt (fractured flows) began flowing both toward and away from the cavity, forming ridged, lobate flow features (Figure 6). An incipient terrace block began forming on the southern wall of the crater, causing the impact melt (Figure 6) to flow toward the excavated cavity, but cavity collapse ended before a major terrace block could form on the southern rim.

6) The impact melt on the southern crater rim cooled, forming contraction fractures on the surface of the material. Concurrently, the ejecta below the polygonally fractured material began dewatering, resulting in the formation of smooth sediment flows observed on the southern half of the crater, including the sediment fan observed upslope from the collapse forming Flow 2 (Figure 7a).

7) The debris flows formed on the outer rim and interior wall, as volatiles were released from the ejecta on the outer rim and target material within the wall.

8) Terrace formation ceased, destroying the flows emplaced on the outer northern rim and interior wall. The complete structural failure of the northern portions of the crater may have destroyed any impact melt emplaced on the northern rim of the crater. A possible reason for the structural failure of the northern wall is the over thickening of the impact ejecta deposit [Mouginis-Mark and Garbeil, 2007], and the subsequent mechanical failure of the crater wall/rim. The volatile-rich wall material on the northern half of the crater was deposited on the crater floor, where it began dewatering. The pitted material is potentially the result of volume loss of blocks of ice in the crater floor.

4.4.2. Scenario 2: Flows formed after terrace formation

5) As in Scenario 1 above, the first step in Scenario 2 is the initiation of terrace formation. During cavity collapse, the near-rim impact melt (fractured flows) began flowing both toward and away from the cavity (Figure 6).

6) Terrace formation ceases, emplacing volatile-rich material on the northern crater floor. Similar to Step 7 in Scenario 2, volatile-rich material is emplaced on the crater floor.

7) The last flows to form were the more discrete flows, namely Flows 2, 3 and 4, but even these had diverse origins that may indicate a difference in timing. Flow 2 appears to have formed from collapse, likely an outburst of volatiles (either water or melted subsurface ice) and sediment on an over steepened slope. The rubbly surface morphology of Flow 2 is distinct from the morphology of Flows 3 and 4. These flows (3 and 4) appear to be the result of less fluidized material moving down slope. The ability of

Flow 4 and the upper region of Flow 3 to support boulders on the surface are consistent with Flows 3 and 4 comprising material with less fluidization than of Flow 2. Flow 3 originated near the top of the crater wall in a region characterized by extensive gully formation. There is no evidence for down-flow pulses of material in Flow 3, and the channels within the levees are smooth, appear to be fairly elevated with respect to the surrounding terrain, and lack any obvious plastic surface deformation. The multiple lobes observed in the distal reaches of Flow 3 suggest a protracted period of flow formation. Flow 4 originates on the outer surface of the edge of the crater rim and exhibits evidence of both plug flow and multiple down-flow pulses of material.

4.4.3. Implications for volatile distribution

In the two above scenarios, the relative timing of flow formation and crater relaxation imply differences in subsurface volatile distribution. If Scenario 1 occurred, and flows formed equally around the crater, the volatile source is likely laterally extensive. The observation that wall blocks near Flow 3 exhibit vertical variations in gullying suggests that the volatile source is likely not vertically extensive. If Scenario 2 occurred, and flows formed after the cessation of terrace formation, the volatile source is likely less laterally extensive. Formation of debris flows in an area restricted to the southern outer rim of the crater suggests that the volatile source was laterally heterogeneous and localized to the region of the flows.

4.5. Future targeting

The identification of flows of sediment, likely lubricated by water released during or closely after (perhaps only a few days?), an impact event could imply processes unique to Tooting crater, as the evidence of sediment flows at older craters is likely to have been

destroyed. The combination of a young, fairly large crater that formed in young, layered basaltic target materials may be the key to identifying preserved impact melt and impact-induced debris flows and a search of high-resolution data may reveal additional craters with similar morphologic features. Potential targets include volcanoes such as Ascraeus Mons, Arsia Mons, Olympus Mons, Alba Patera and Elysium Mons. These shield volcanoes have lava flows on their flanks and have strong radar depolarized echo strengths [Thompson and Moore, 1989], indicating that the materials exhibit higher strength than the plains materials, and may be more likely to have formed and retained flows related to volatile release. Analyses of rayed craters on Mars (2-10 km diameter) indicate that these craters are among the youngest craters in their size class, occur preferentially on young volcanic plains, and may have formed preferentially in volatile-rich targets [Tornabene et al., 2006]. These rayed craters (Zunil, Zumba, Gratteri, Tomini and Dilly) may be potential areas to target for identification of additional flows comparable to the ones described here for Tooting crater.

The preferential preservation of the impact melt and formation of debris flows on the southern portion of Tooting crater is likely related to the large-scale terrace collapse on the northern half of the crater. In order to test this hypothesis, we suggest a survey of the rim deposits and interior cavities of fluidized ejecta (rampart) craters > 15 km in diameter using CTX images. The presence and/or absence of materials as identified above may provide clues to the precise processes occurring in the formation of the impact-related flow features. For example, our interpretations may need to be revisited if impact melt is identified at distances > 1 crater radius away from the crater rim (the maximum distance on the Moon as observed by Hawke and Head [1977]; even less

extensive distribution would be expected in the higher gravity of Mars), and extensive terrace formation has occurred. Furthermore, discovery of pitted material, a notably shallower floor, and extensive flow features on a crater will indicate that the preferential preservation of flow features on Tooting crater is not the result of slumping, but the features may have only formed on the southern half of the crater rim.

5. Conclusions

The ongoing debate concerning the emplacement of multi-layered ejecta craters seeks to determine whether the ejecta were fluidized by volatiles in the target [Carr et al., 1977; Mouginis-Mark, 1979] or by entrainment of atmosphere [Barnouin-Jha and Schultz, 1998; Schultz and Gault, 1979]. The identification of volatile-rich sediment flows may indicate that the fluidization of ejecta layers in craters may in part be due to the interaction of volatiles derived from the target and the crater ejecta, as we have observed evidence for volatiles in the target material prior to the impact event that formed Tooting crater.

We find that Tooting crater, a young, multi-layered ejecta crater that formed in a layered target of young lava flows containing volatiles, may present evidence for impact melt production and volatile release in the recent history of Mars. We have observed four different types of flows on the rim and interior wall of Tooting crater. Coherent, low-viscosity impact melt was emplaced on the rim of the crater and cooled fairly rapidly while collecting and flowing short distances on slopes both toward and away from the cavity. Sediment flows with variations in the initial emplacement mechanism (collapse versus flow of water-laden sediment on slopes) and in the amount of volatiles are observed. Our investigation reveals that the flows (impact melt and debris flows) appear

to be preferentially located on the southern rim and interior wall. The absence of similar flows in the northern part of the crater may be due to the destruction of impact melt and volatile-rich crater ejecta by terrace formation. These features provide evidence for volatiles in the subsurface that were liberated by the impact event.

Acknowledgements

We thank Harold Garbeil for the production of the HiRISE DEMs used in this analysis. Alfred McEwen, Chris Okubo and Livio Tornabene are thanked for their efforts to acquire the excellent HiRISE coverage of Tooting crater that is now available. Scott Anderson was very helpful in the production of the algorithms used to generate Figure 14. This research was supported by NASA grant NNX06AC61G from the Planetary Geology and Geophysics Program and by NASA grant NNG0-5GL98G from the Mars Fundamental Research Program.

Tables

Table 1. Summary of morphometric data for Tooting crater. Data are a combination of measurements from this study and the study of the crater geometry and ejecta by Mouginis-Mark and Garbeil [2007].

Location	23.4ºN	207.5ºE	
Diameter	29 km		
Area of ejecta blanket	~8120 km^2		
Rim height	386 m (min.)	893 m (max.)	628 m (avg.)
Rim height/ Diameter ratio	0.133	0.031	0.022
Crater depth	1567 m (north)	1851 m (south)	
depth/Diameter ratio (*d*/*D*)	0.054 (north)	0.064 (south)	
Age	≤ 2 My*		

*Based upon the number of superposed impact craters larger than 54 m (4 pixels) in diameter and the cratering chronology of Hartmann et al. [2005].

Table 2. Correlation coefficients for Flow 4 and Mauna Loa 1984 Flow 1A lava flow. Mauna Loa data are from Table 2 in Glaze and Baloga [2006]. Flow 4 measurements were obtained from the HiRISE images and DEM. Correlation coefficients determined by plotting measurements against each other (similar to plots in Figures 12 and 13).

Measurements	Correlation coefficients (*R*)	
	Flow 4	Mauna Loa 1984 Flow 1A*
Flow width vs distance	0.67	0.68
Channel width vs distance	0.85	0.57
Flow thickness vs distance	0.65	0.37
Channel width vs flow width	0.62	0.40
Flow width vs flow thickness	0.44	0.21
Channel width vs flow thickness	0.84	0.05
Channel depth vs distance	-0.75	n/d
Channel depth vs flow width	-0.48	n/d
Channel depth vs channel width	-0.86	n/d
Channel depth vs flow thickness	-0.93	n/d

*Data from Table 2 in Glaze and Baloga [2006]
n/d = no data

Figures

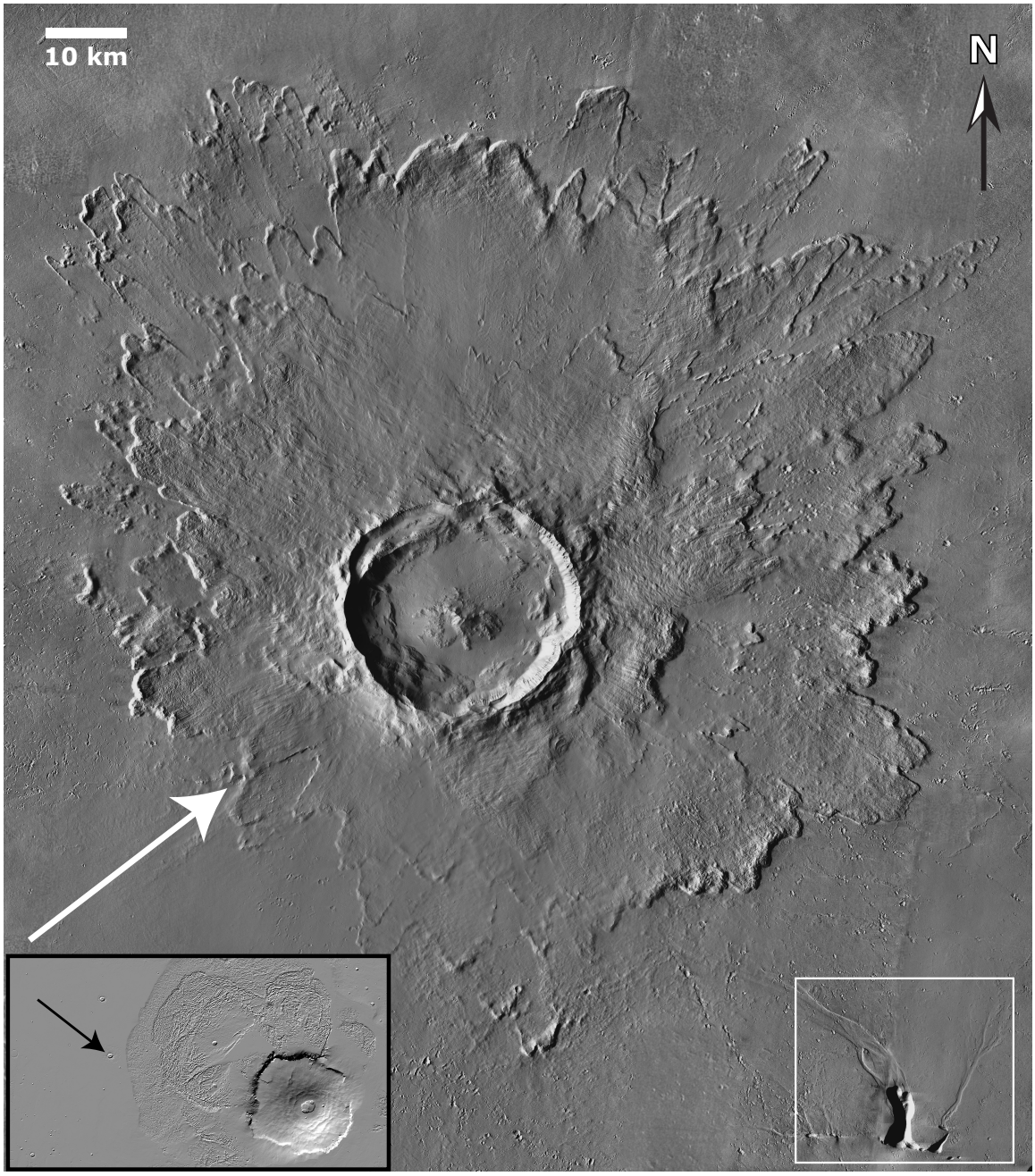

Figure 1. Mosaic of THEMIS VIS images detailing Tooting crater and surrounding ejecta blanket. Inset image shows black arrow pointing to the location of Tooting crater on Amazonis lava flows to the west of the Olympus Mons aureole. Tooting crater is located at 23.4ºN and 207.5ºE. Interior crater cavity is ~29 km across. White arrow points in the inferred downrange direction [Mouginis-Mark and Garbeil, 2007]. White box outlines depression adjacent to braided channels, which may have served as a source for volatiles prior to the impact cratering event.

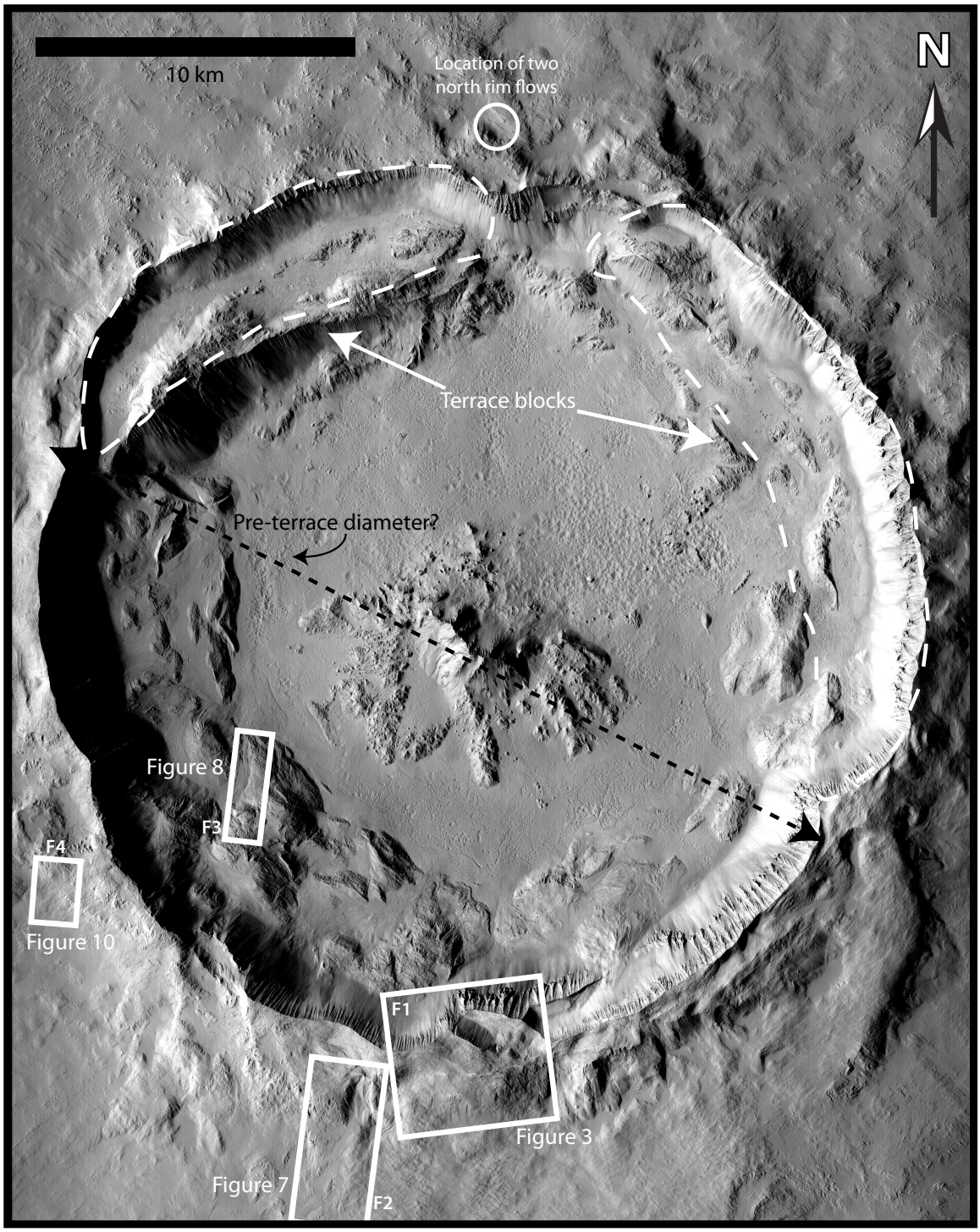

Figure 2. Portion of CTX image P03_002158 detailing Tooting crater cavity and the proximal rim materials. Tooting crater is ~29 km in diameter and the southern floor is nearly 200 m deeper than the northern floor. Dashed black line identifies proposed pre-terracing crater diameter of ~26.4 km and dashed white lines indicate terrace blocks. White circle identifies location of two small north rim flows. White boxes outline areas covered by subsequent figures. F1, F2, F3 and F4 indicate figures associated with flow types 1-4.

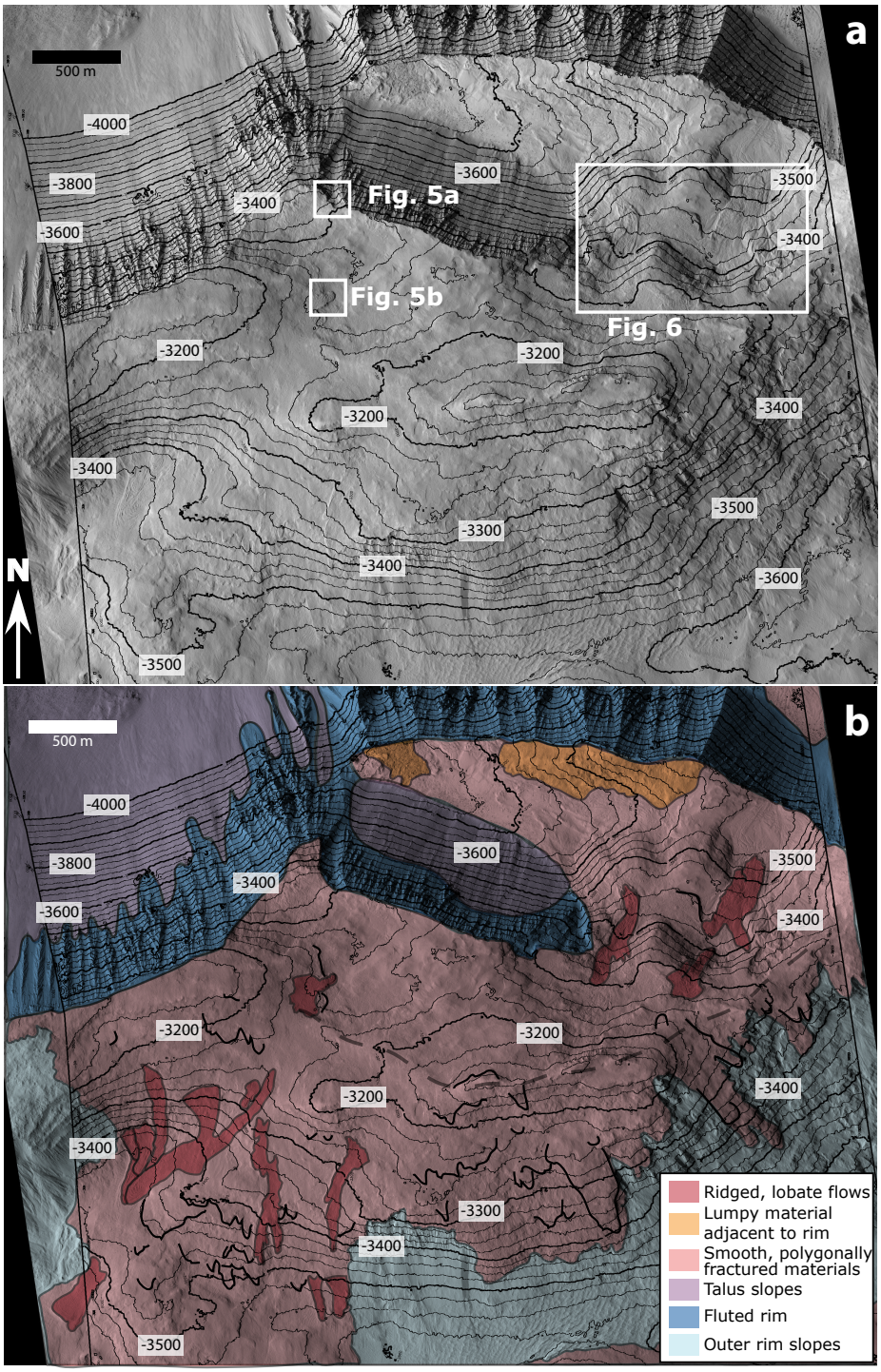

Figure 3. a) Portion of HiRISE image PSP_001538_2035 detailing extensive sheet-like fractured flows and ridged, lobate flows (Type 1 flows). The center of the crater is towards the top of the image. See Figure 2 for location. b) Sketch map detailing surface units described in text. Black lines in smooth, fractured material unit are flow fronts that do not form distinct, discrete flow lobes. Dashed line indicates crest of local topographic high (see also Figure 4).

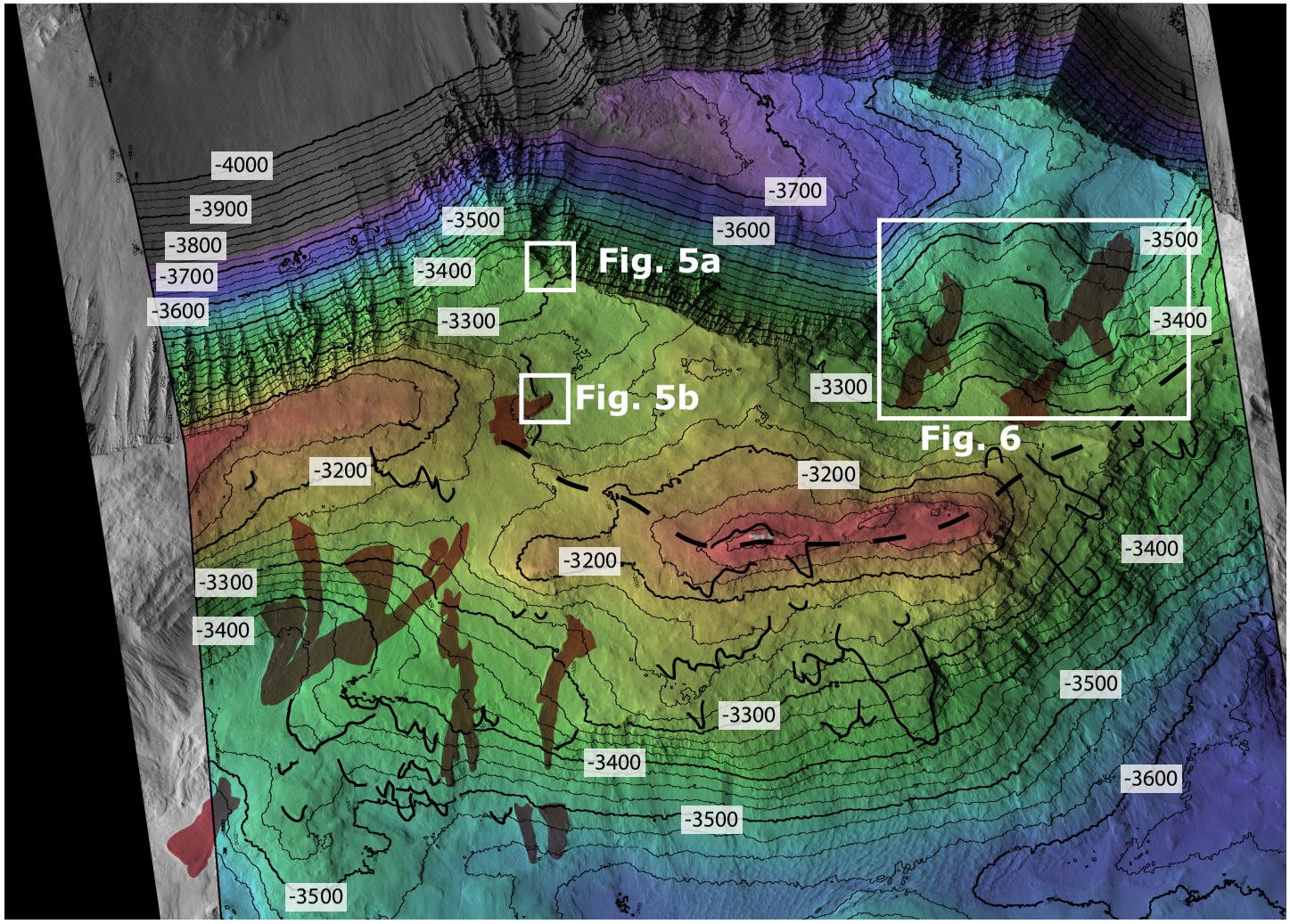

Figure 4. Stereo-derived DEM of region of fractured flows and lobate flow fronts on southern rim of crater, generated from HiRISE images PSP_001538_2035 and PSP_002538_2035. Elevations on contours are in meters relative to the Mars MOLA datum. Contour interval is 25 m. Lobate flows (red-brown), flow fronts and topographic divide (dashed line) are overlaid on topography.

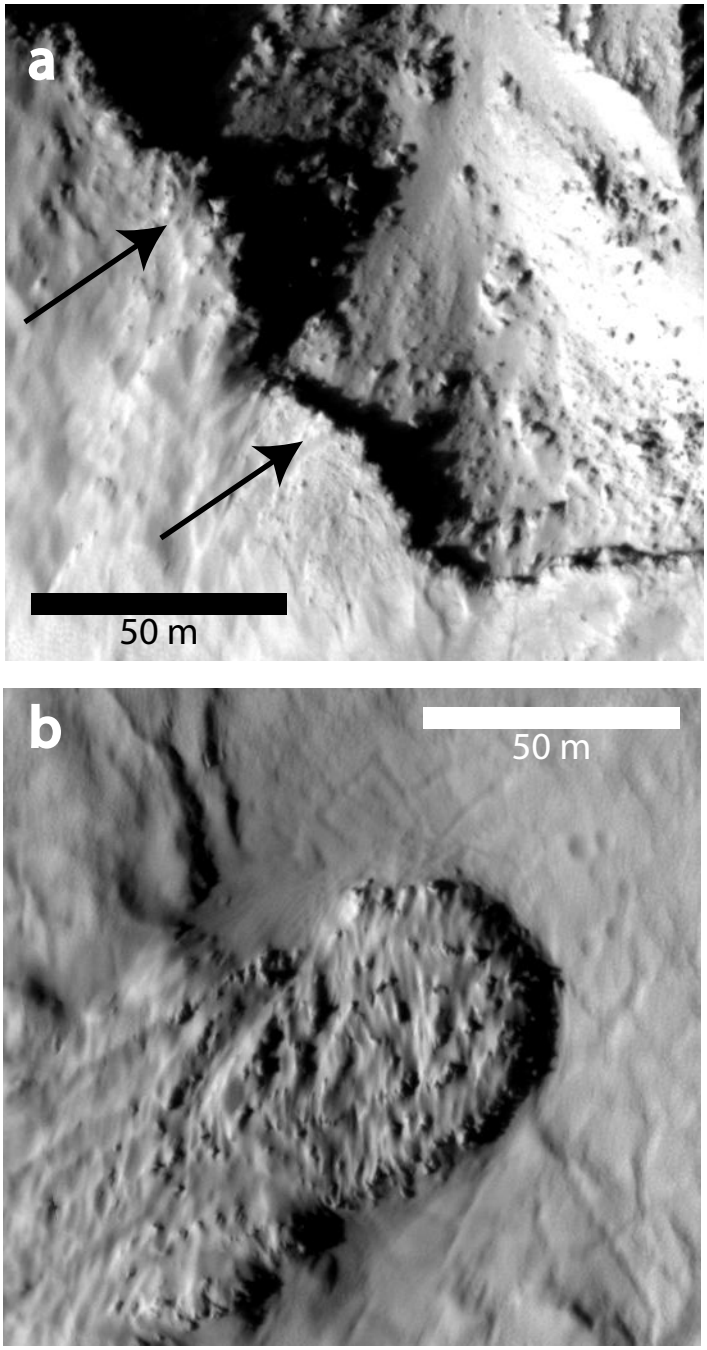

Figure 5. Portion of HiRISE image PSP_001538_2035 detailing extensive sheet-like fractured flows and ridged, lobate flows. a) Close-up of rim overhang of polygonally fractured flows. Illumination is from the lower left. Black arrows indicate location of rim overhang. Note long shadows on slope below rim. b) Close-up of fractured sheet materials and ridged flow with bouldery surface. Illumination from the lower left. Boulders on flow surface are ~2-5 m in diameter.

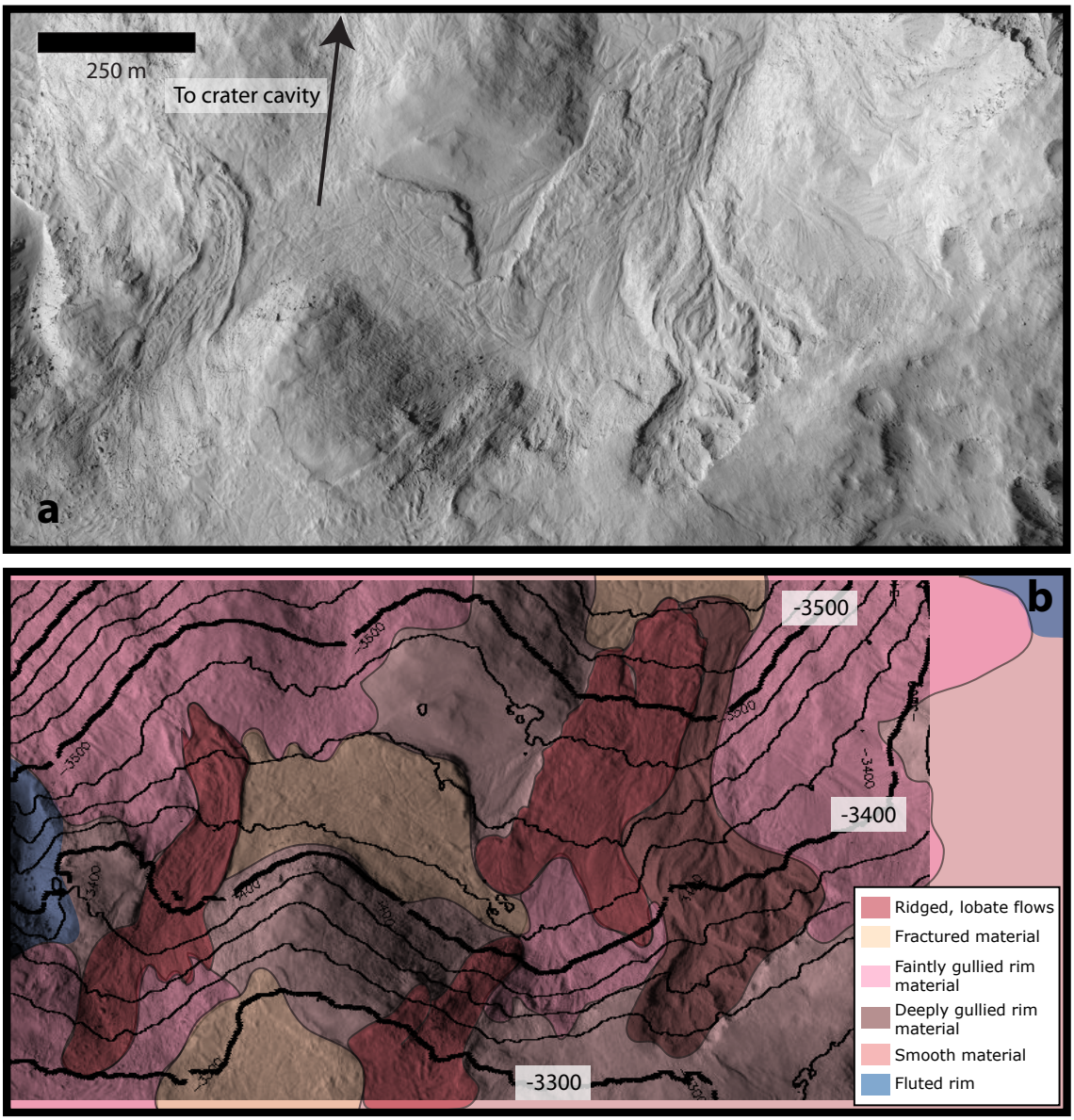

Figure 6. a) Portion of HiRISE image PSP_001538_2035 detailing lobate flows within and adjacent to fractured, sheet-like materials. Flow direction is toward crater cavity, to the north. Location of this sub-scene is shown in Figure 3. North is to the top. b) Sketch map identifying units described in text. Contours are at 25 m intervals and are referenced to the MOLA datum [Zuber et al., 1992].

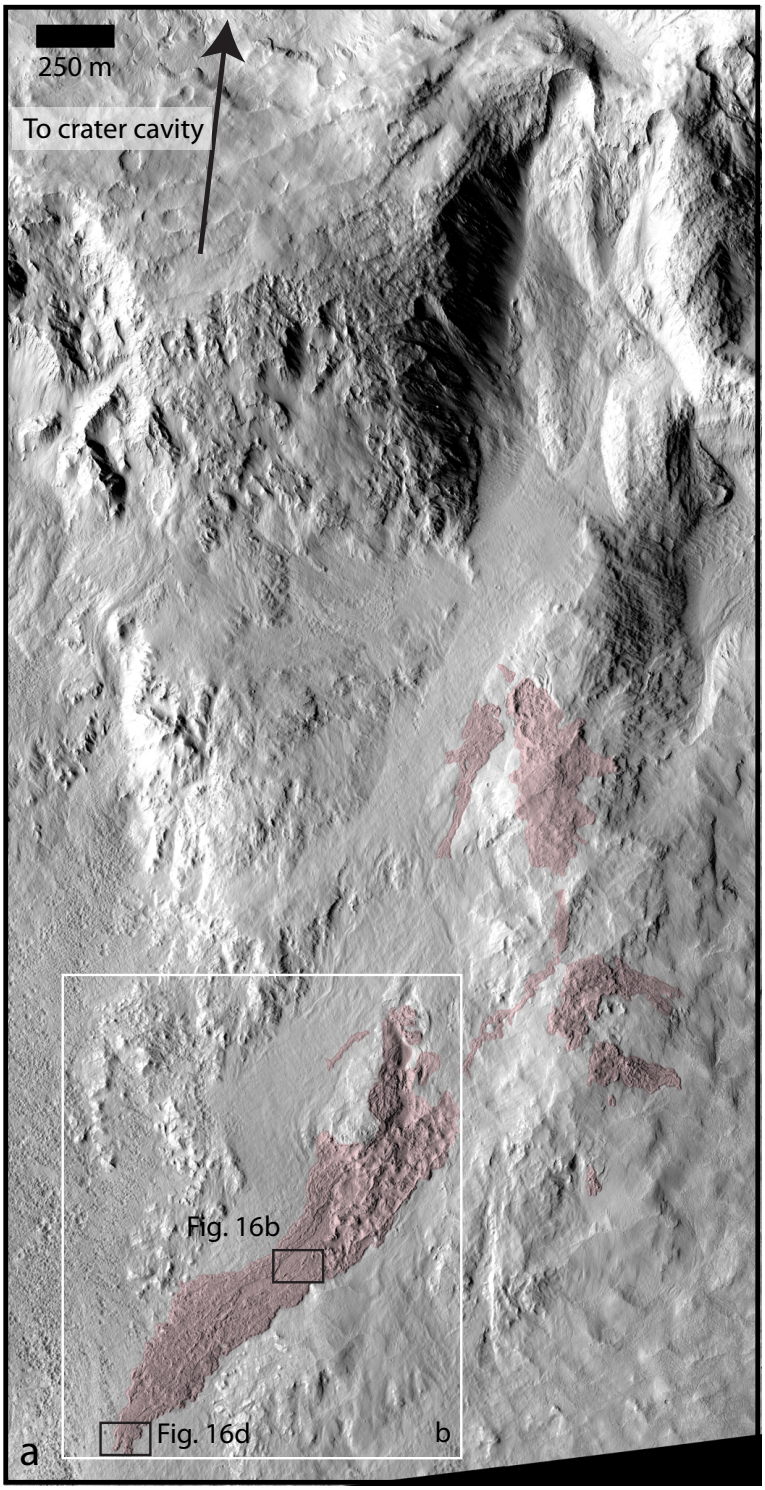

Figure 7. a) Portion of HiRISE image PSP_007406_2035 detailing region of smooth and hummocky flows. See Figure 2 for location. Individual flows shaded with pinkish red. White box outlines location of 7b. Black boxes outline location of Figure 16b, d. b) Flow 2. Note channel near collapsed source region. Box outlines location of 7c. c) Small smooth flow. Illumination is from the west. Arrows point to enclosed portions of the pre-existing surface (kipukas).

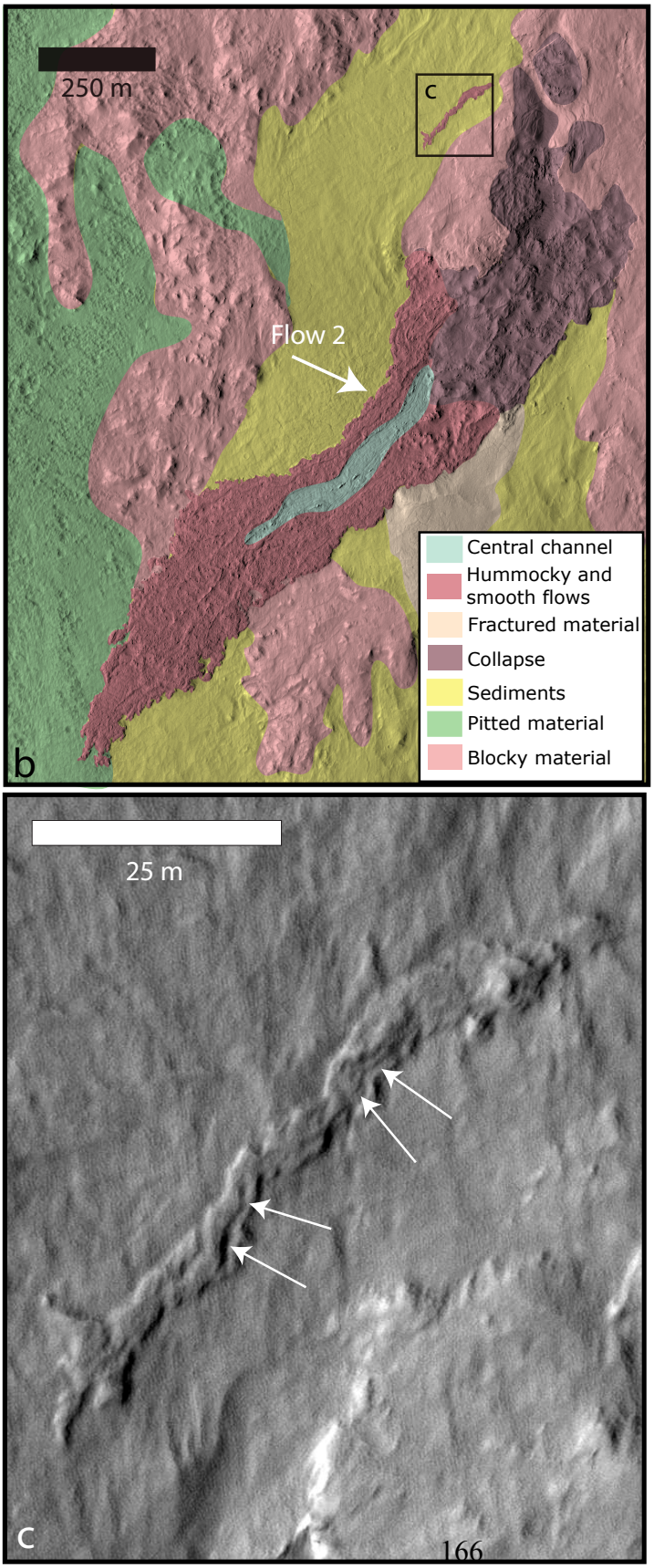

Figures 7b and 7c.

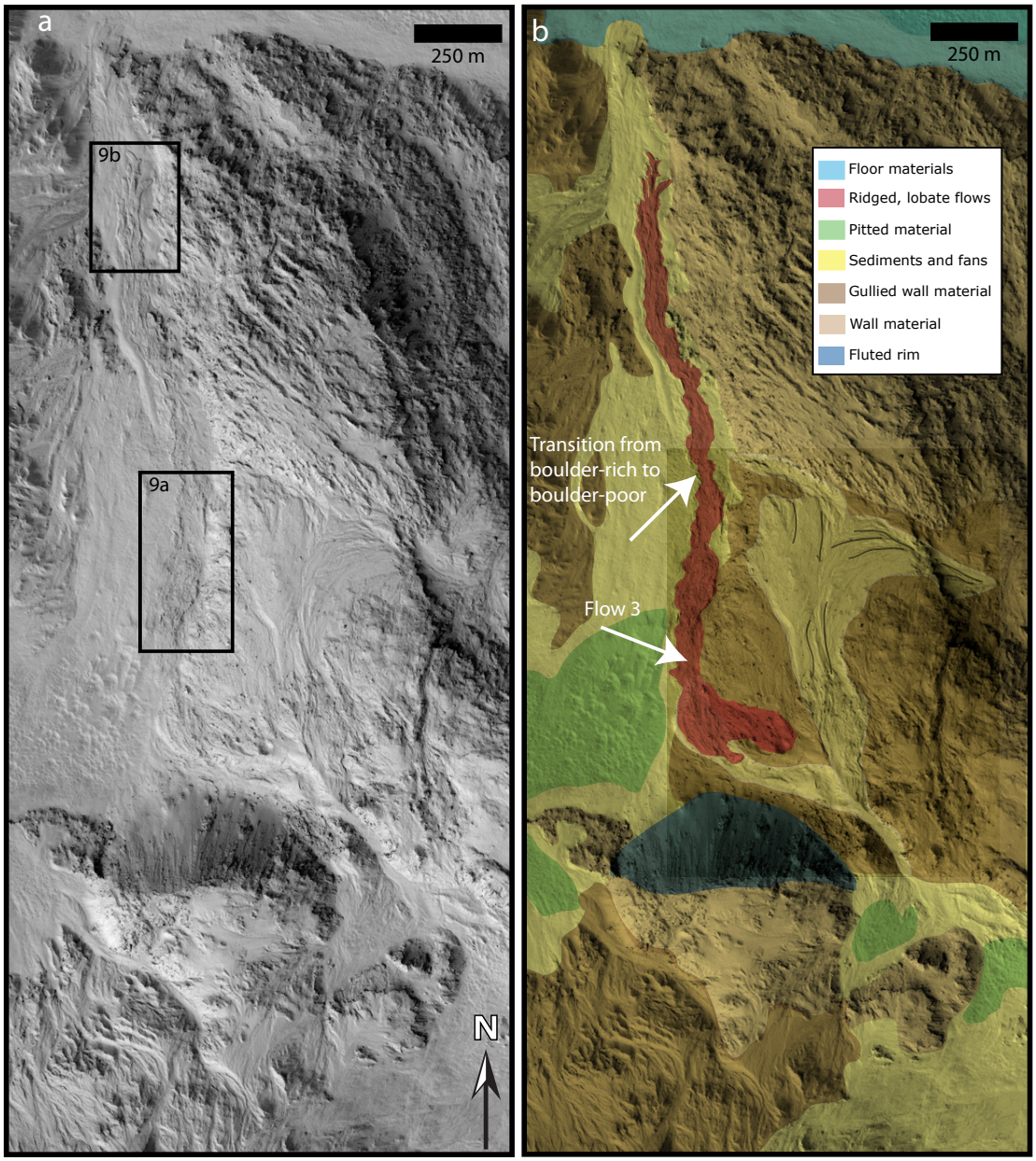

Figure 8. a) Portion of HiRISE image PSP_005771_2035 detailing the morphology of the southwestern inner wall of Tooting crater and showing Flow 3 from source to distal lobes. See Figure 2 for location. Direction of flow is towards the top of the image. Illumination is from the southwest. b) Sketch map of region shown in (a). Lines on yellow unit indicate individual channels.

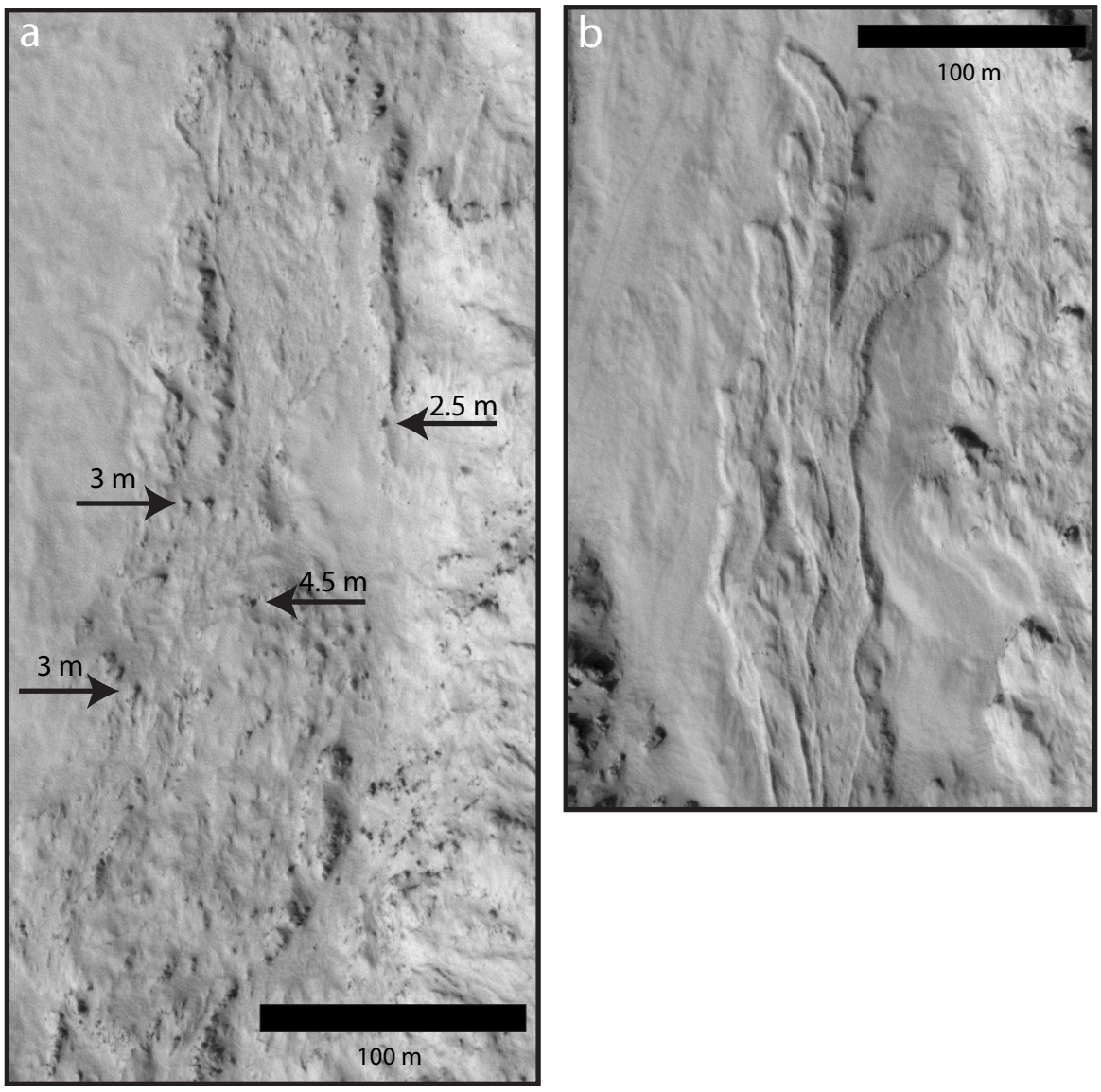

Figure 9. Portions of HiRISE image PSP_005771_2035 detailing Flow 3 morphology. North is up. See Figure 8 for location. a) Close-up of upper region of Flow 3. Note boulder-rich, hummocky surface. Example boulders are identified by arrows and boulder widths above the arrows. b) Close-up of distal lobes of Flow 3. Note smooth flows with distinct levees towards the bottom of the image.

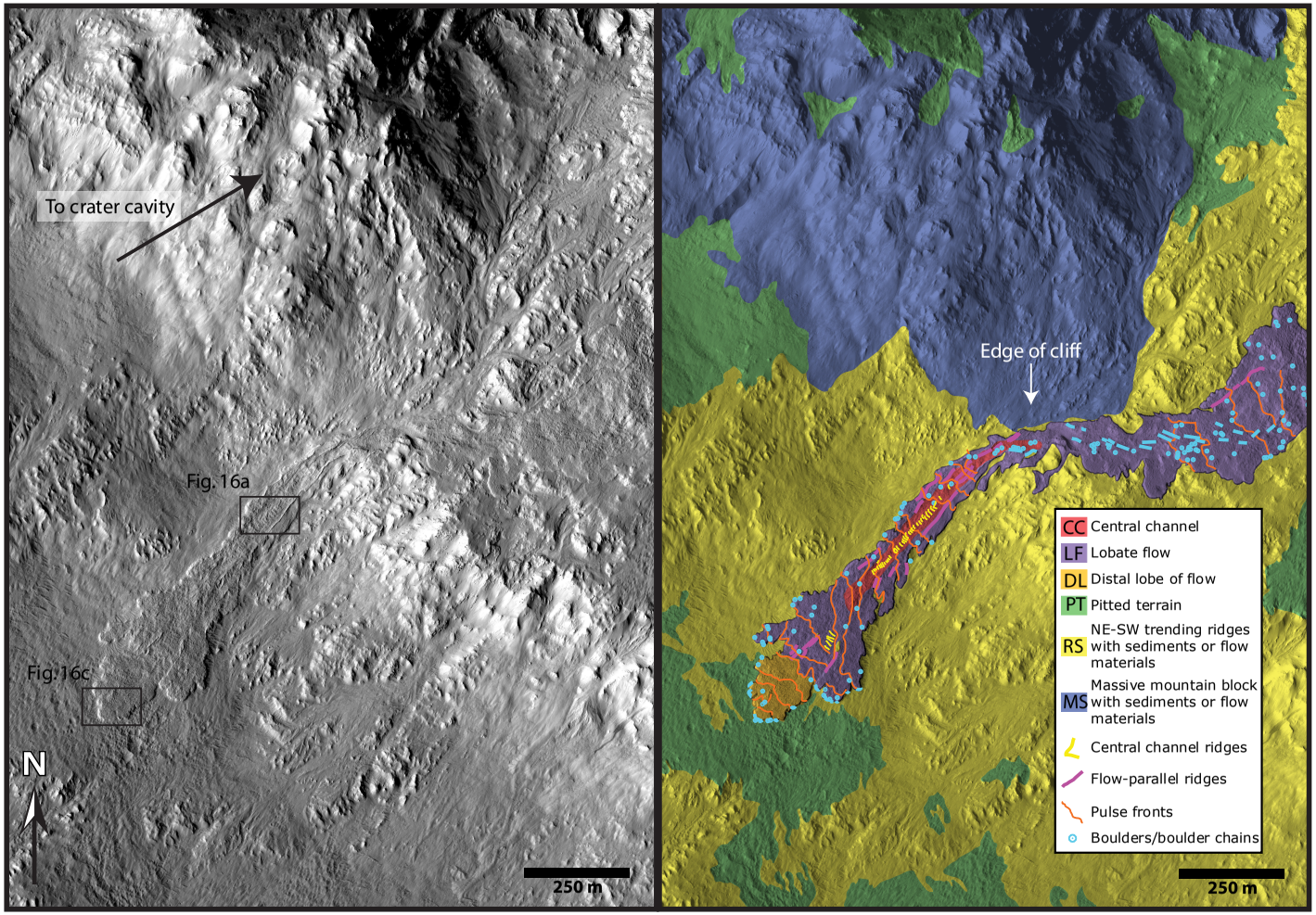

Figure 10. a) Portion of HiRISE image PSP_002646_2035 detailing Flow 4 (case study flow). See Figure 2 for location. Flow direction is from the upper right to the lower left of the image. Black boxes outline location of Figures 16a, c. b) Sketch map of region shown in (a).

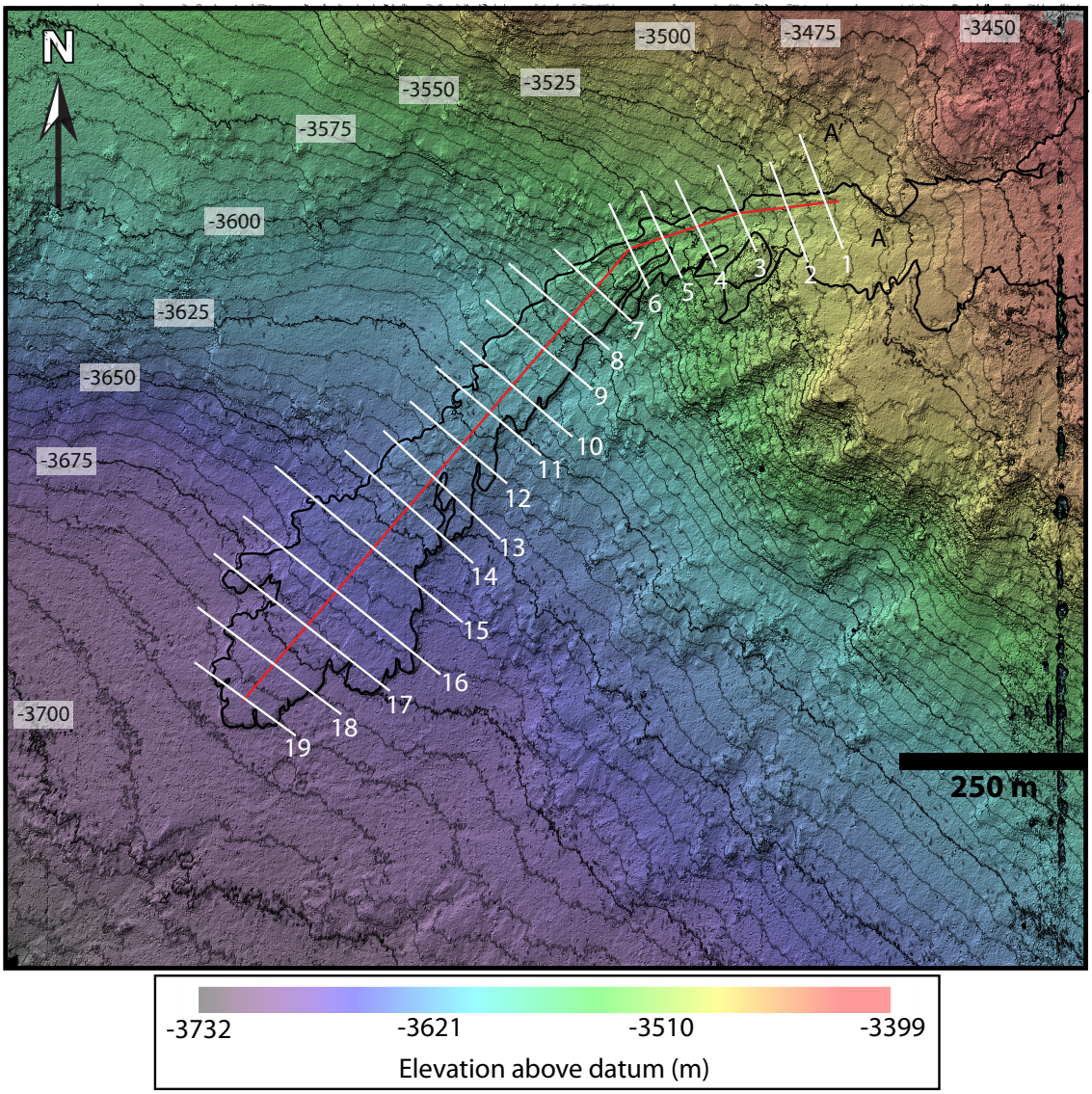

Figure 11. Portion of stereo-derived DEM of Flow 4, generated from HiRISE images PSP_002646_2035 and PSP_002580_2035. DEM elevation was controlled using individual MOLA shots and used the HiRISE data at a pixel spacing of 0.25 m/pixel. Black vertical bar near right edge of image is artifact of DEM creation. Image is color-coded topography with 5 m contours over shaded relief. Outline of Flow 4 is shown in black. Illumination is from the northwest. Cross-flow topographic profiles are identified by white lines and associated numbers. The red line identifies the down-flow topographic profile. See Appendix B for individual cross-flow profiles.

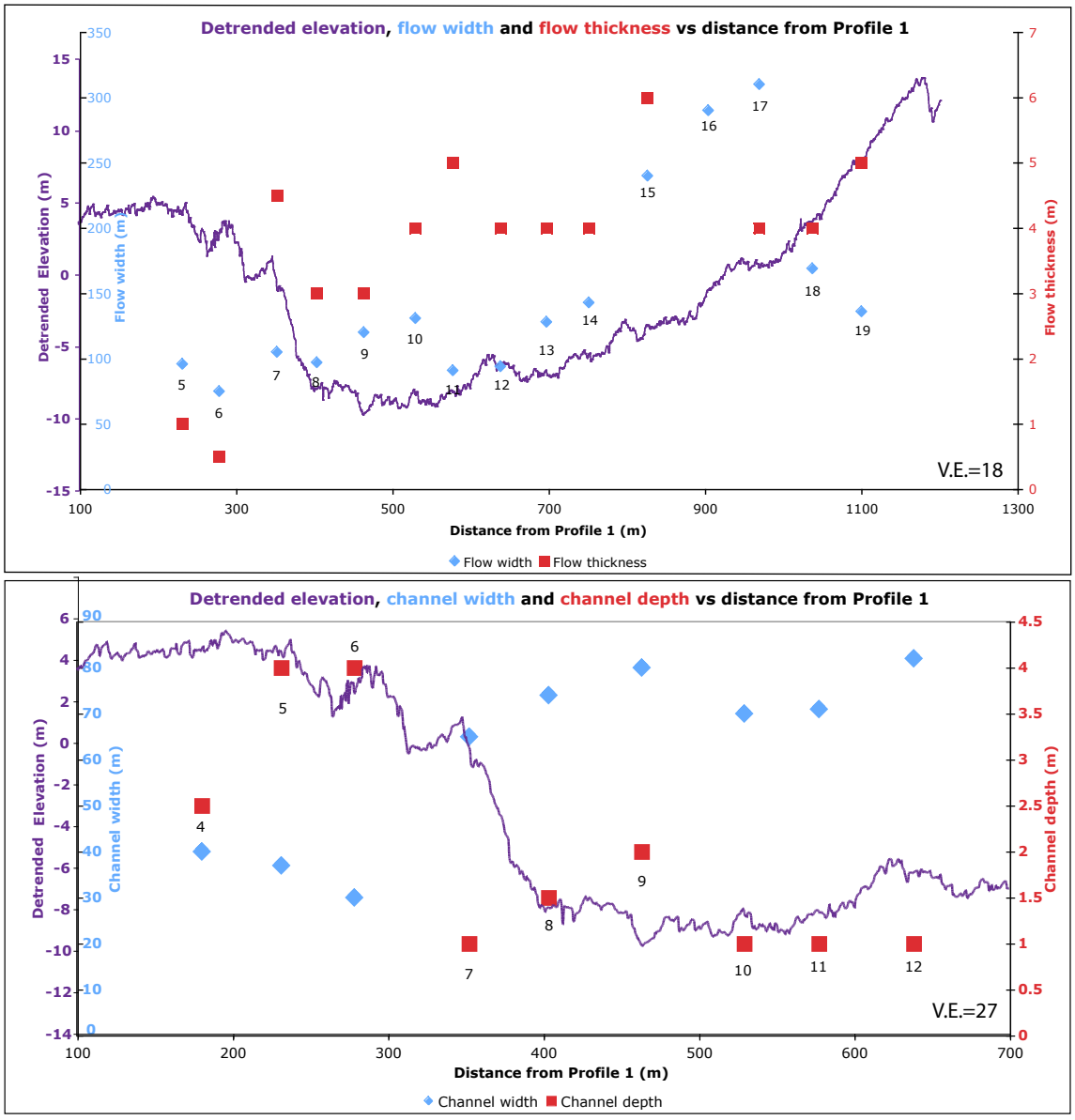

Figure 12. Graphs of detrended elevation, flow width, flow depth, channel width and channel depth for Flow 4. Measurements were obtained from stereo-derived DEM of Flow 4 and HiRISE image PSP_002646_2035. Numbers correlate to locations of cross-flow profiles identified on Figure 11 and the location of the detrended elevation profile is identified by a red line in Figure 11. a) Graph of detrended elevation, flow width and flow thickness. b) Graph of detrended elevation, channel width and channel depth.

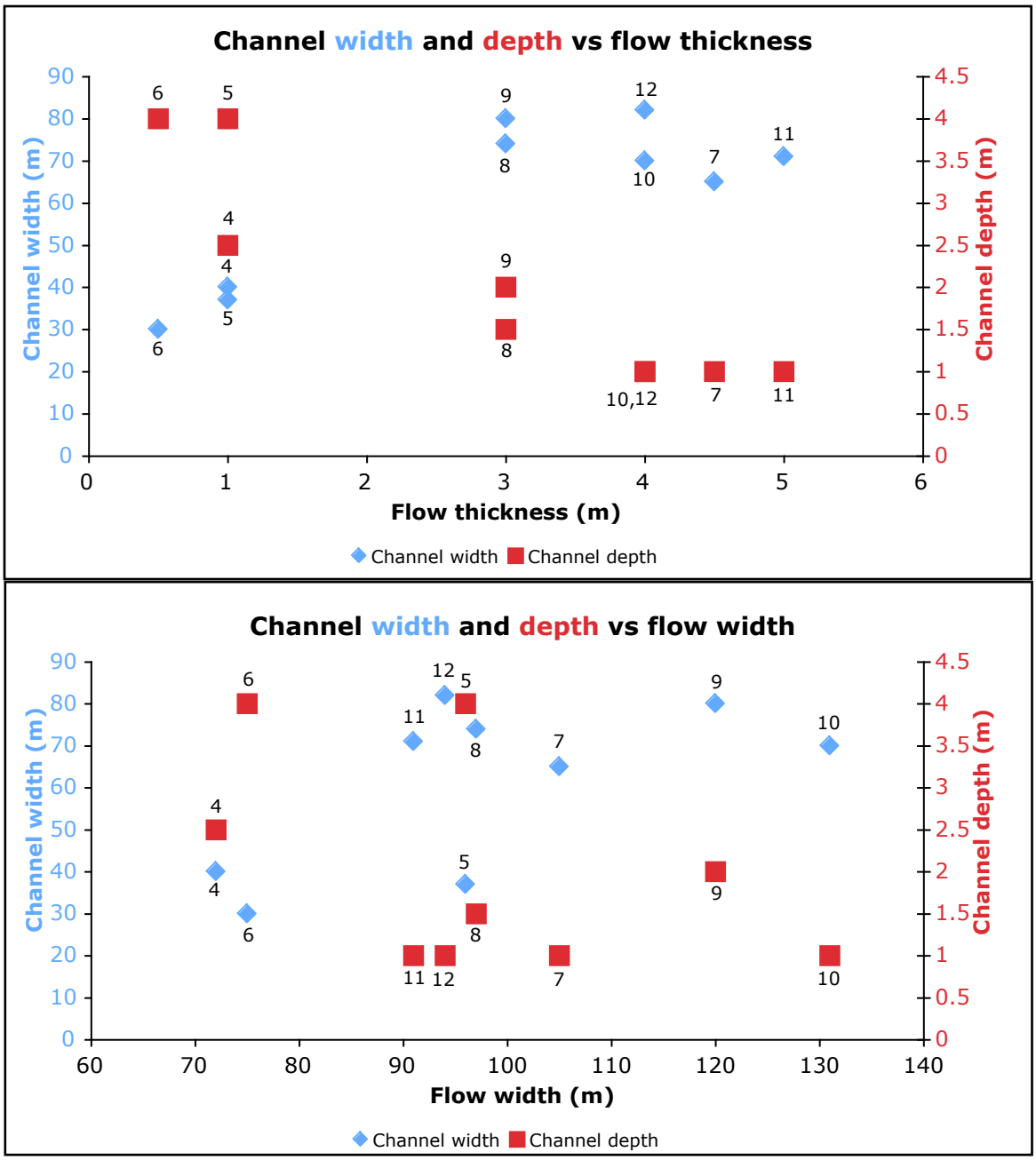

Figure 13. Graphs of channel width and depth plotted against flow thickness and flow width. Measurements were obtained from stereo-derived DEM of Flow 4 and HiRISE image PSP_002646_2035. Numbers correlate to locations of cross-flow profiles identified on Figure 11. a) Channel width and channel depth plotted against flow thickness. b) Channel width and channel depth plotted against flow width.

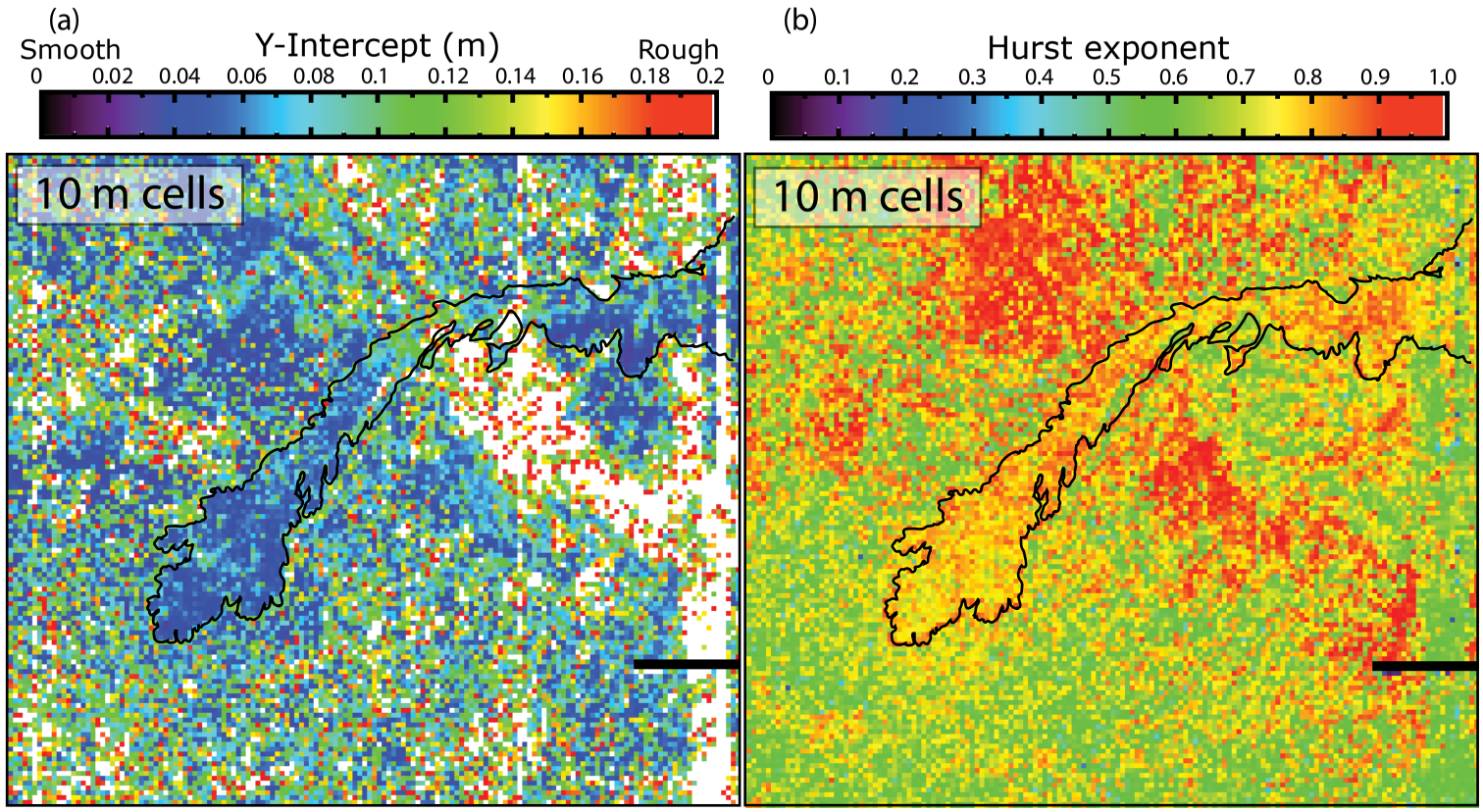

Figure 14. Maps of surface roughness characteristics of Flow 4 following techniques of Chapter 3. Topography data are from a stereo-derived DEM and the area is same as that covered by Figure 11. Each pixel is 10 m x 10 m. Flow 4 is outlined by a black line in both maps. The black bar in lower right of each image is missing data. a) Y-intercept of deviogram line fit, representing surface roughness at a reference scale (1 m). Note that the flow down-slope from the cliff is of almost uniform color, indicating a constant surface roughness along the flow. b) Hurst exponent map, representing scaling properties of surface roughness. See text for description of Hurst exponent.

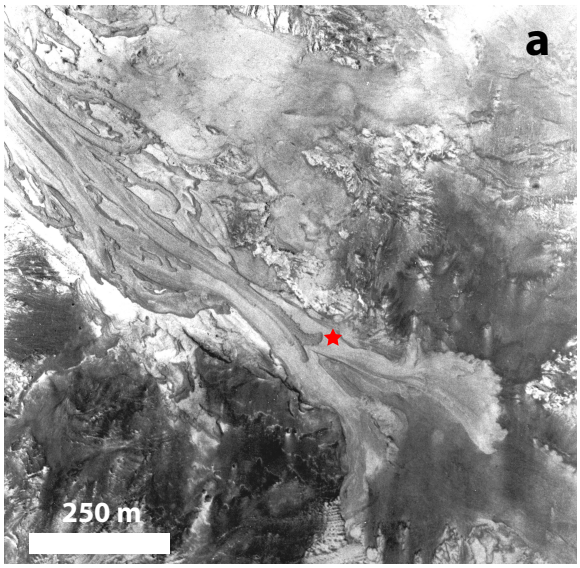

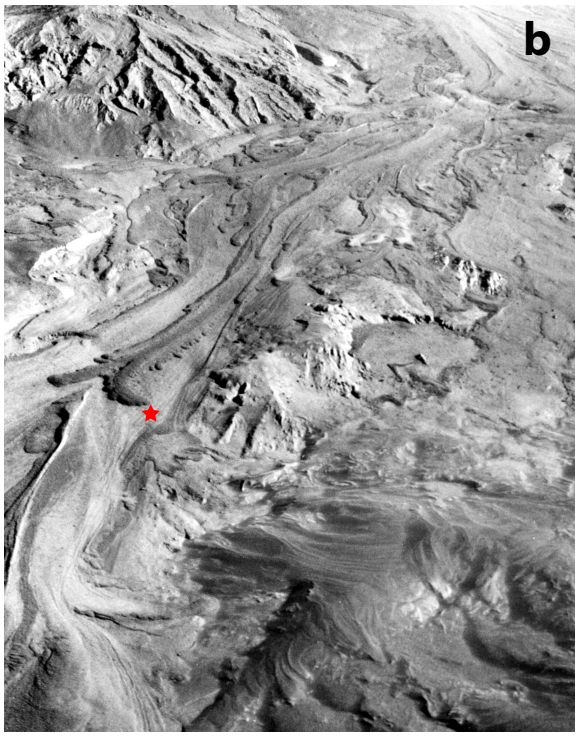

Figure 15. Example pyroclastic flow deposits from Mount St. Helens Volcano, Washington, showing the morphology of a granular flow fluidized by magmatic gases and entrained atmosphere. Compare to the Flow 3 morphology. Photos courtesy of USGS-Cascades Volcano Observatory. a) Vertical aerial view of Mount St. Helens flows showing July 22 and August 7, 1980 pyroclastic flows. Flow direction is from top left. Photo by N. Banks, Skamania County, Washington, July 31, 1980. Portion of Figure 298, U.S.G.S. Professional paper 1250. b) Oblique aerial view of lobes of pyroclastic-flow deposits of July 22 and August 7, 1980 eruptions of Mount St. Helens, showing generally constant width and thickness of deposits. Same area as (a). Star indicates same feature. Direction of flow is towards lower left. Photo by J.W. Head, Skamania County, Washington, 1980, Figure 299, U.S.G.S. Professional paper 1250.

c) Portions of HiRISE image PSP_005771_2035 detailing distal lobes of Flow 3, which display similar morphology to Mount St. Helens pyroclastic flows. Flow direction is towards the top of the page.

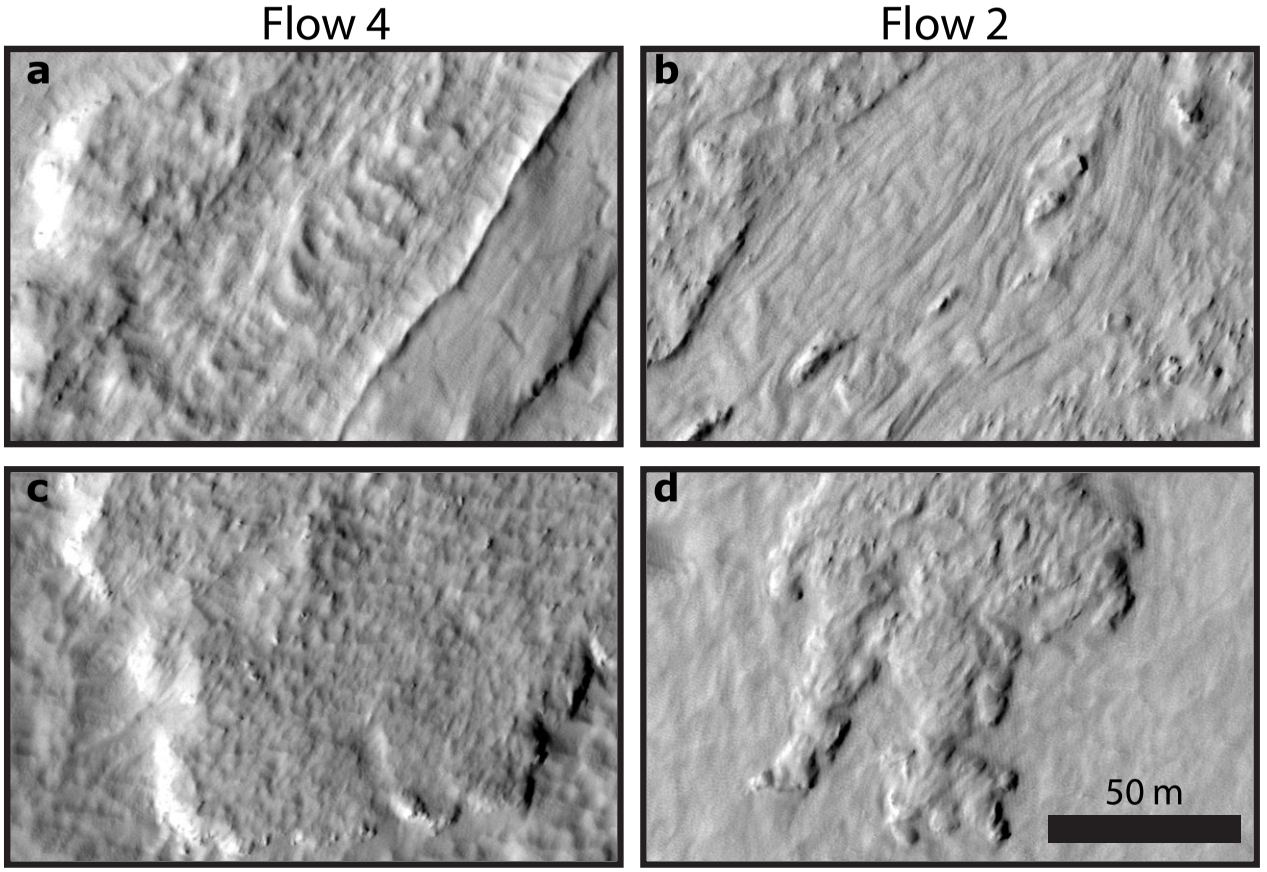

Figure 16. Comparison of the surface morphology of Flow 4 and Flow 2. Locations of boxes are shown in Figure 10 (for (a) and (c)) and Figure 7 (for (b) and (d)). Scale is the same for all four images and north is up. a) Portion of HiRISE image PSP_002646_2035 detailing a region of the central channel of Flow 4. Illumination is from the southwest. b) Portions of HiRISE image PSP_007406_2035 detailing a region of the central channel of Flow 2. Illumination is from the west. c) Portion of HiRISE image PSP_002646_2035 detailing the distal lobe of Flow 4. Illumination is from the southwest. d) Portions of HiRISE image PSP_007406_2035 detailing the distal lobes of Flow 2. Illumination is from the west.

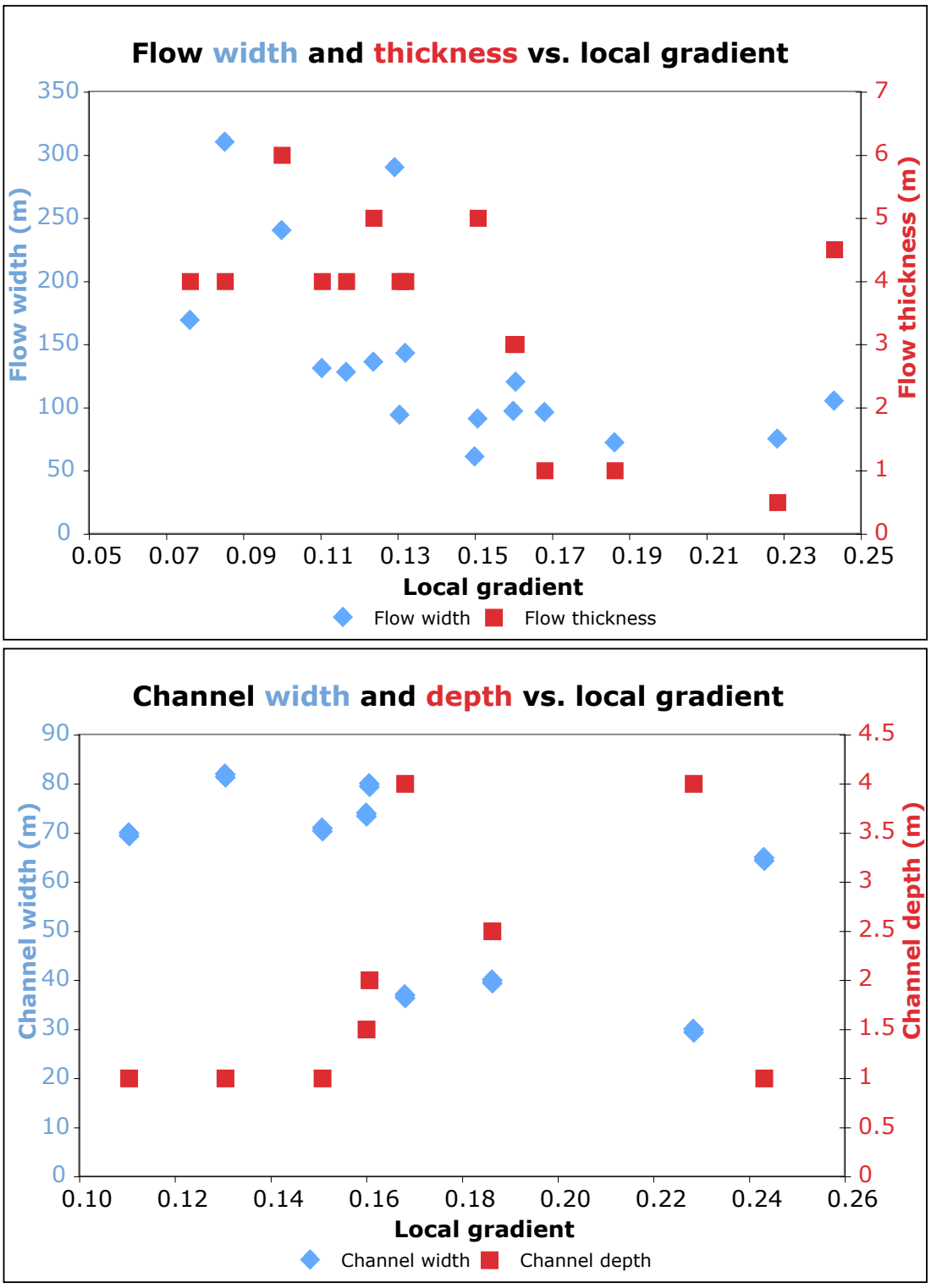

Figure 17. Graphs of flow width and thickness and channel width and depth plotted against local gradient. Measurements were obtained from stereo-derived DEM of Flow 4 and HiRISE image PSP_002646_2035. a) Flow width and flow thickness plotted against local gradient. b) Channel width and channel depth plotted against local gradient.

APPENDICES

1. Appendix A: Additional Hrad Vallis Crater Data (Chapter 2)

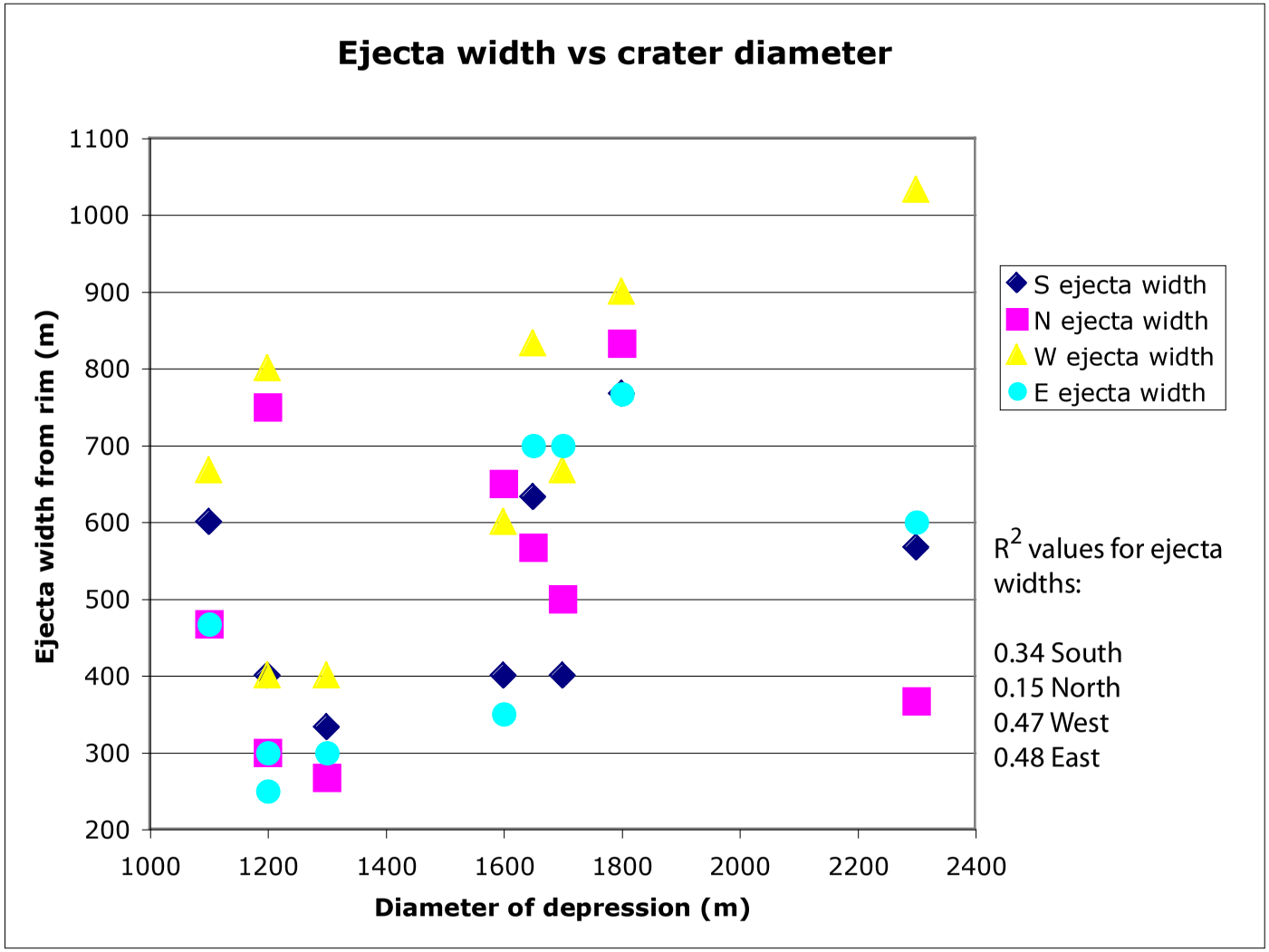

Figure 1. Graph of thermally distinct crater diameter versus ejecta width for azimuths corresponding to South, North, East and West of each crater. Correlation coefficients for each azimuth are also given.

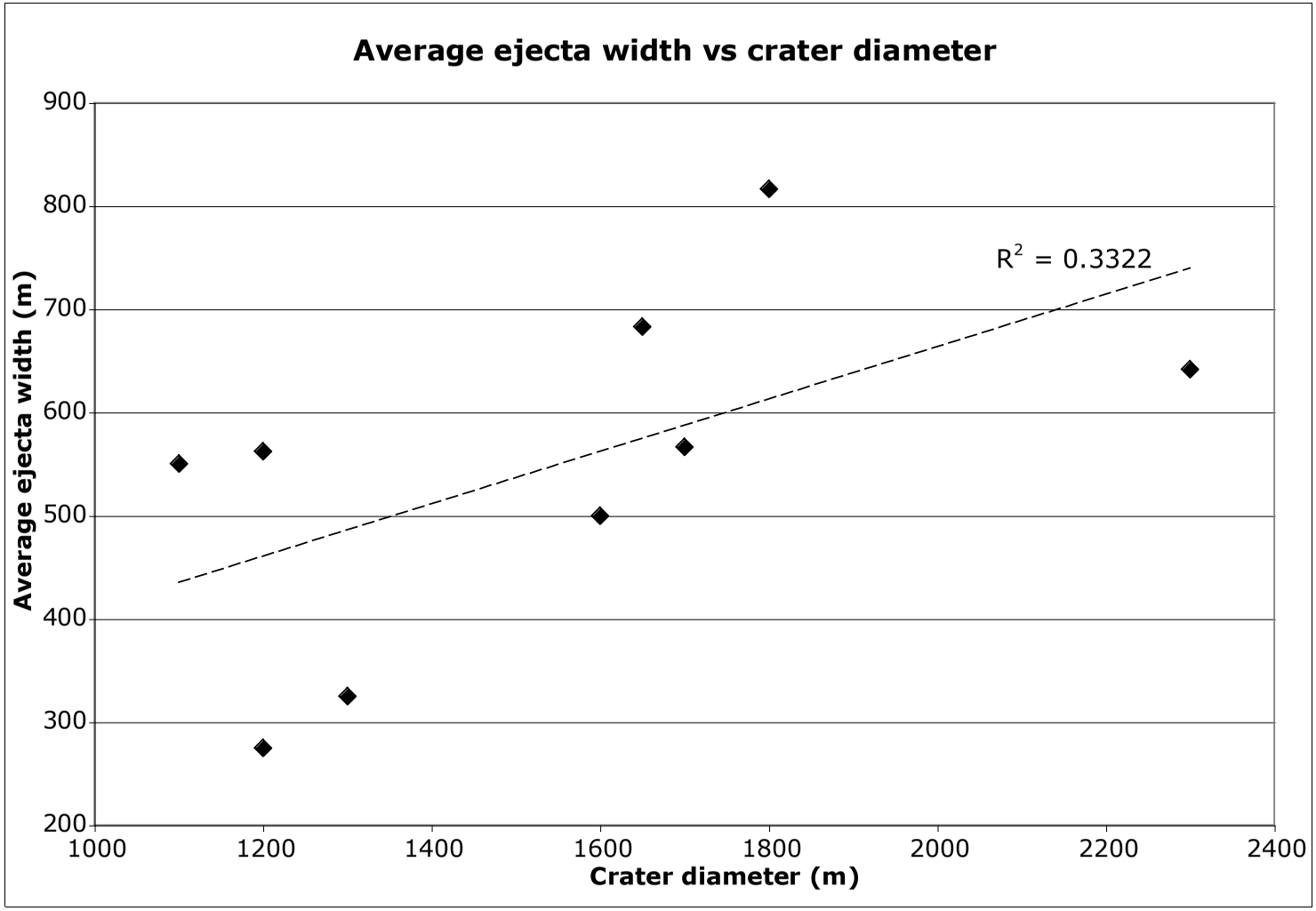

Figure 2. Graph of thermally distinct crater diameter versus average ejecta width.

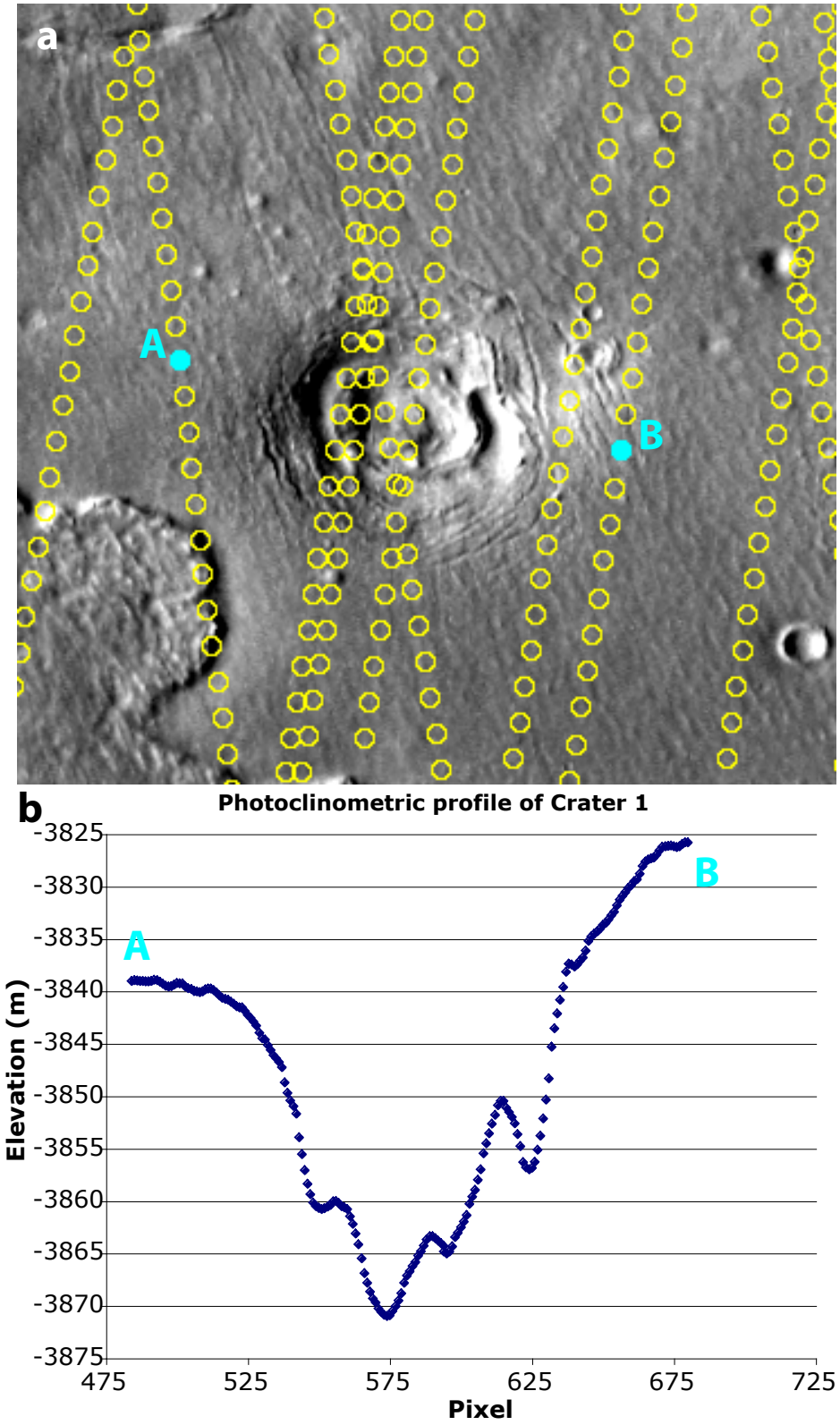

Figure 3. Photoclinometric profile of Crater 1 using MOLA shots as endpoints. a) THEMIS VIS image V05263019. Yellow circles indicate locations of MOLA shots. b) Photoclinometric profile.

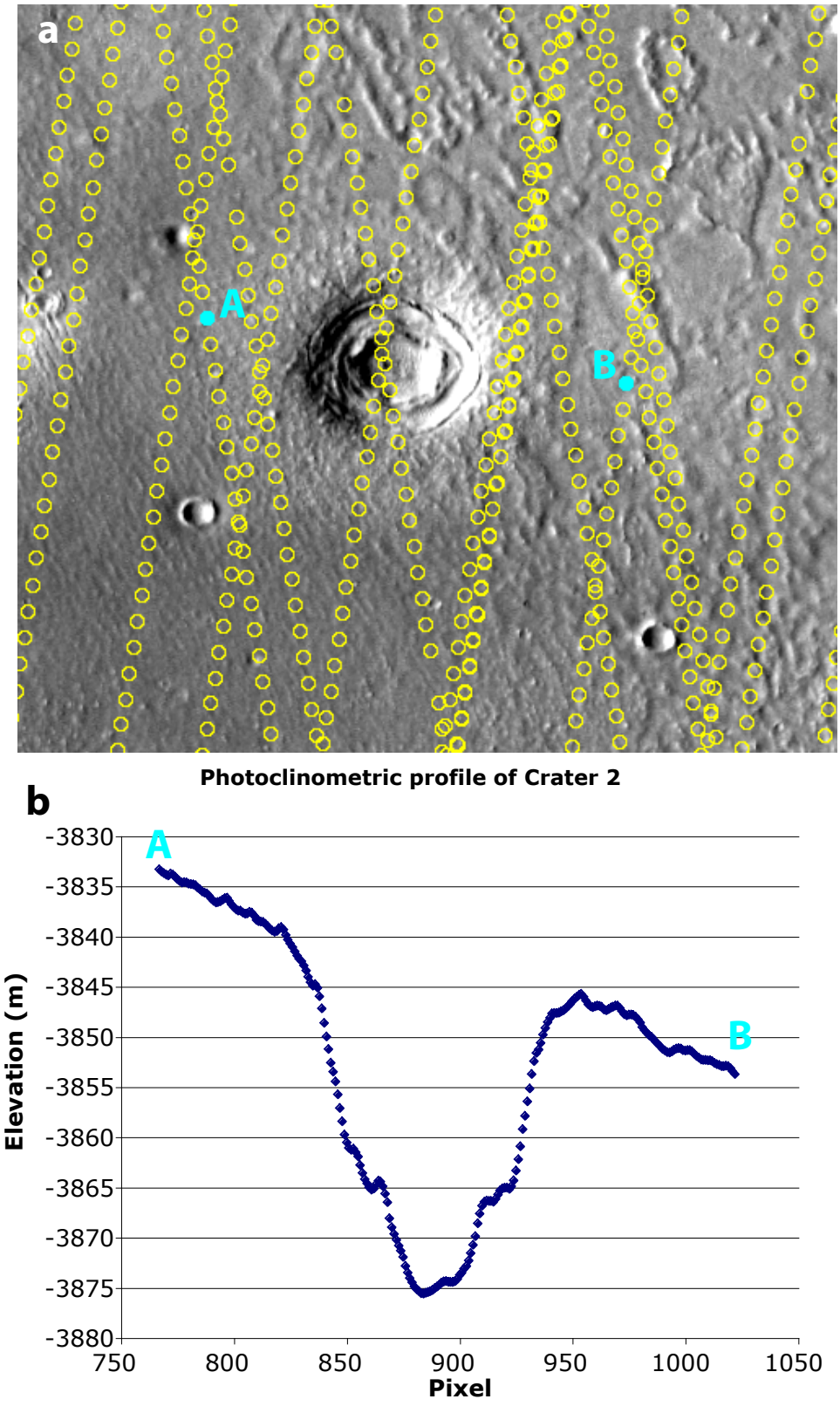

Figure 4. Photoclinometric profile of Crater 2 using MOLA shots as endpoints. a) THEMIS VIS image V05263019. Yellow circles indicate locations of MOLA shots. b) Photoclinometric profile.

2. Appendix B: Individual Topographic Profiles From Flow 4 (Chapter 4)

In the following profiles, the vertical exaggeration for each profile is different, but has been done on a case-by-case basis in order to highlight the topographic variability. Also note that the profiles are oriented east to west.

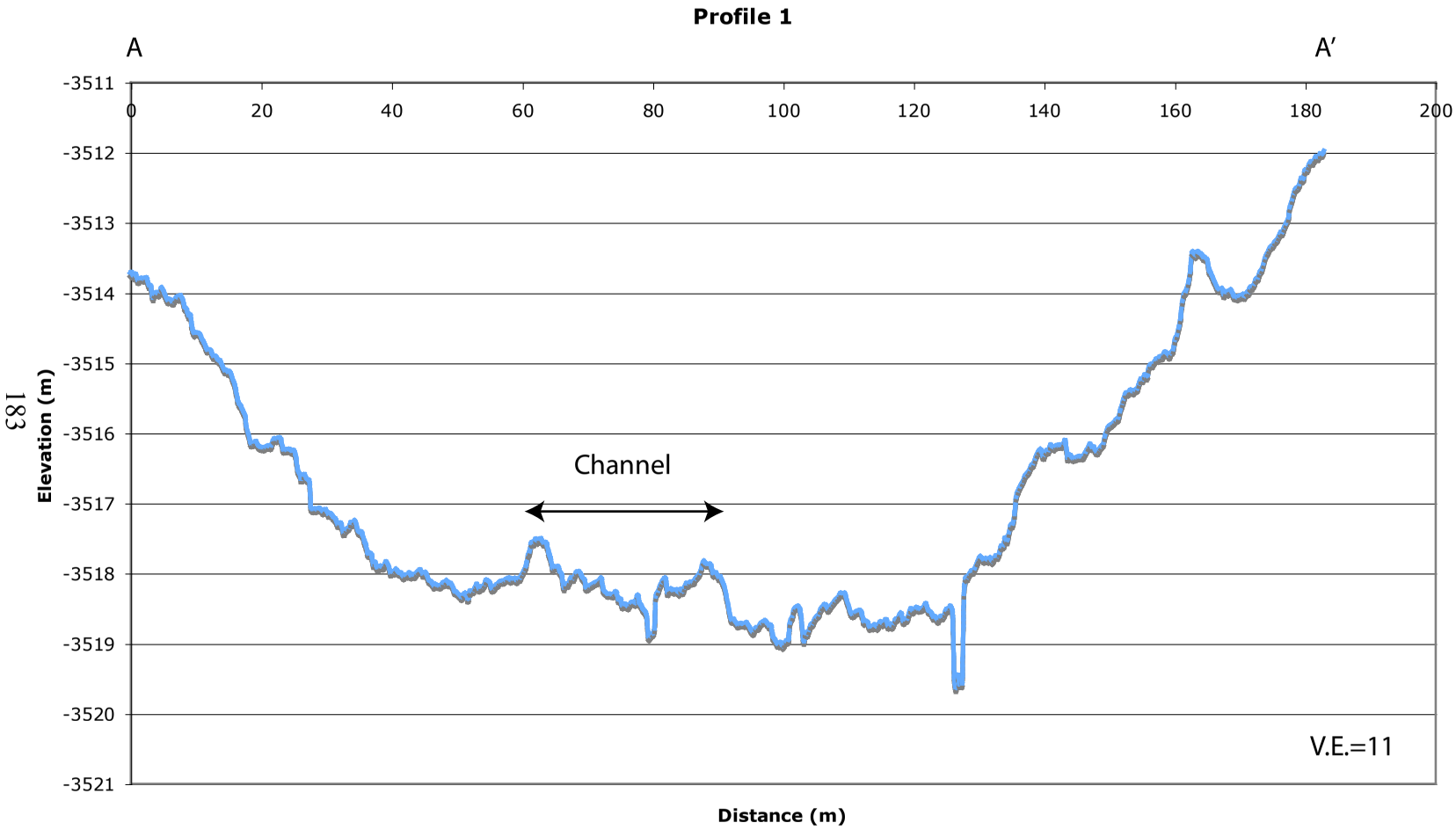
Profile 1
A
A'
-3511
-3512
-3513
-3514
-3515
-3516
-3517
-3518
-3519
-3520
-3521
0
20
40
60
80
100
120
140
160
180
200
Elevation (m)
Channel
V.E.=11
Distance (m)

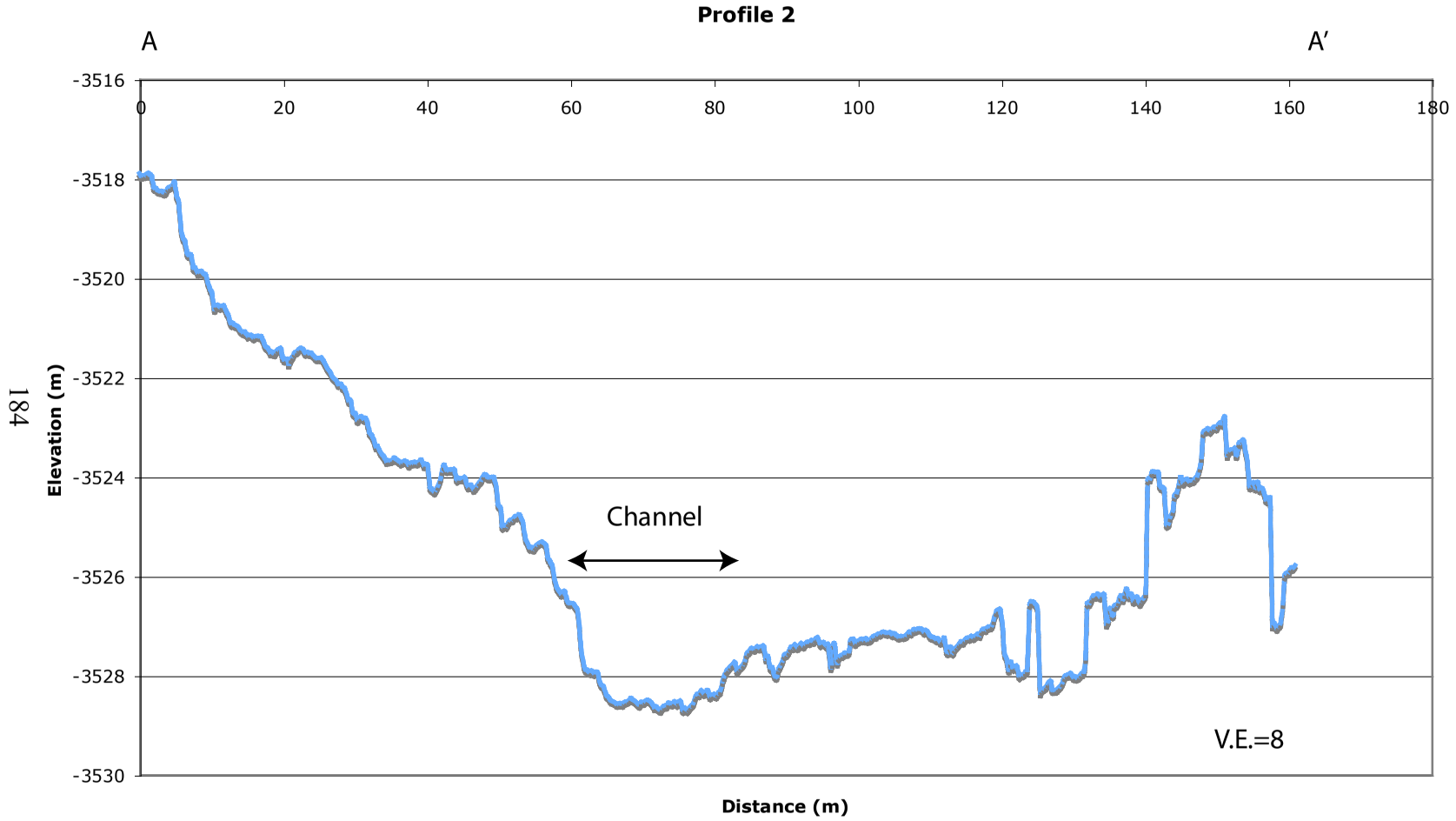
Profile 2
A
A'
-3516
-3518
-3520
-3522
-3524
-3526
-3528
-3530
0
20
40
60
80
100
120
140
160
180
Elevation (m)
Channel
V.E.=8
Distance (m)

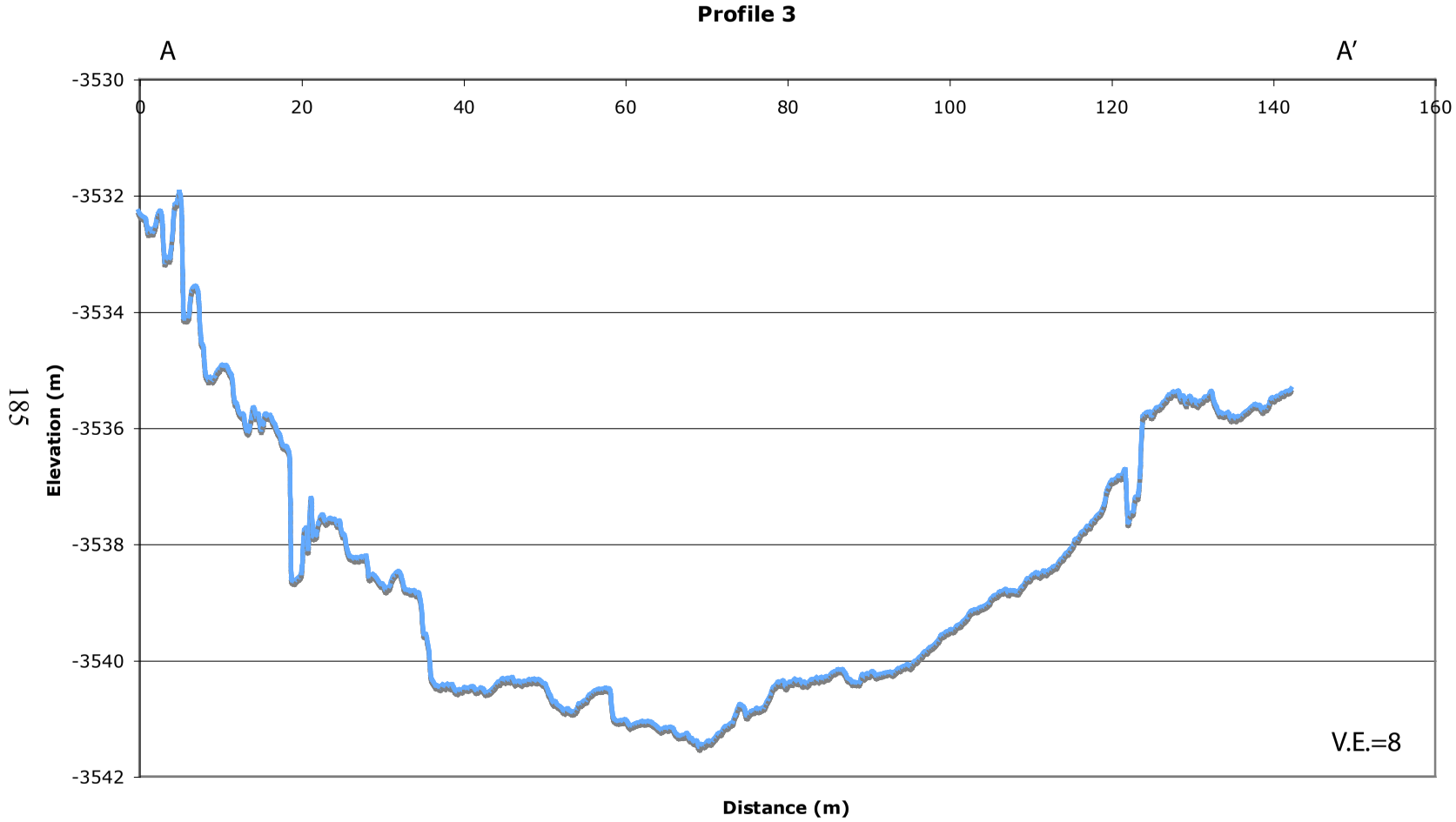
Profile 3
A
A'
-3530
-3532
-3534
-3536
-3538
-3540
-3542
0
20
40
60
80
100
120
140
160
Elevation (m)
Distance (m)
V.E.=8

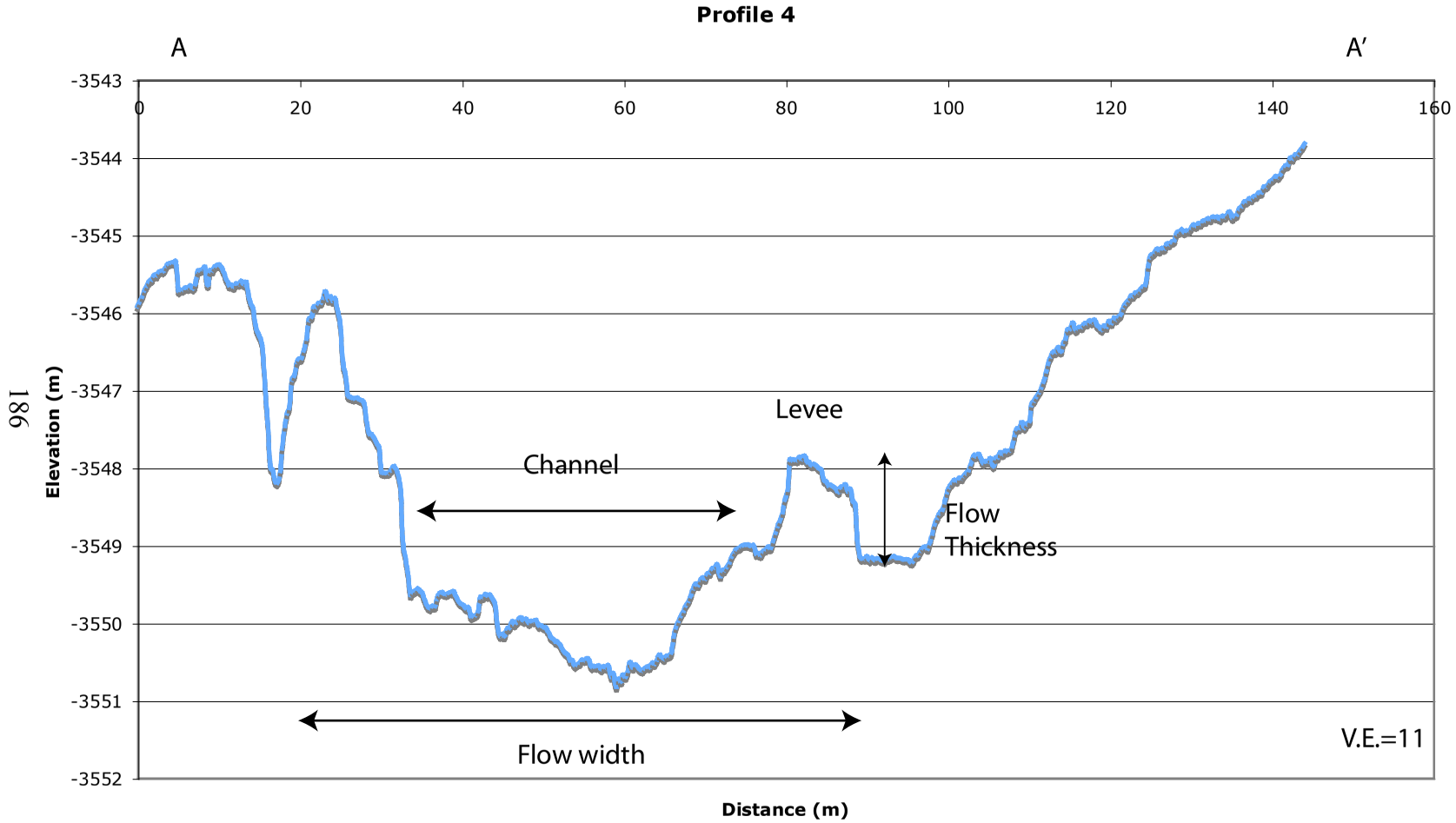
Profile 4
A
A'
-3543
-3544
-3545
-3546
-3547
-3548
-3549
-3550
-3551
-3552
0
20
40
60
80
100
120
140
160
Elevation (m)
Distance (m)
Levee
Channel
Flow
Thickness
Flow width
V.E.=11

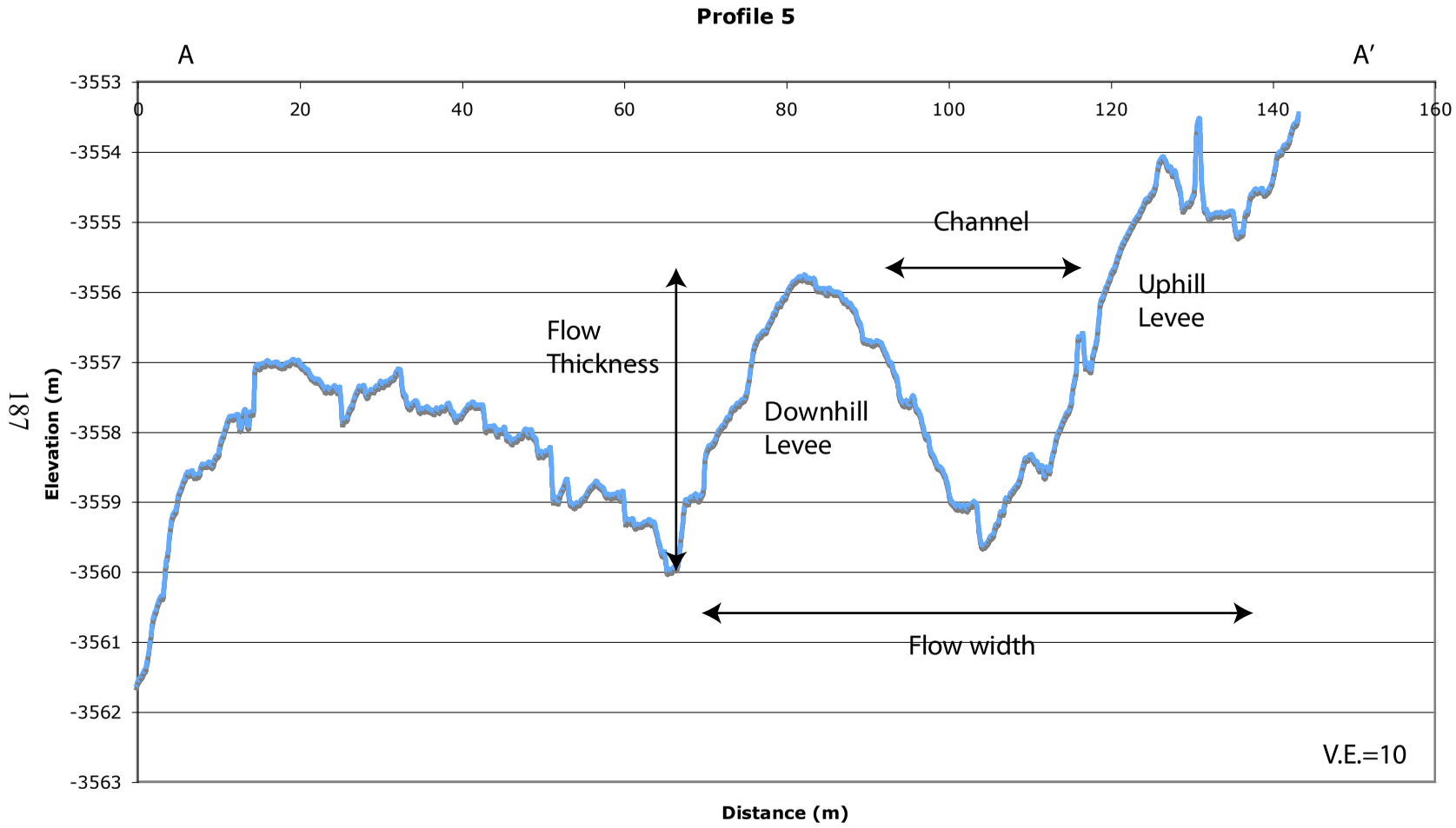
Profile 5
A
A'
-3553
-3554
-3555
-3556
-3557
-3558
-3559
-3560
-3561
-3562
-3563
0
20
40
60
80
100
120
140
160
Elevation (m)
Distance (m)
Channel
Uphill
Levee
Flow
Thickness
Downhill
Levee
Flow width
V.E.=10

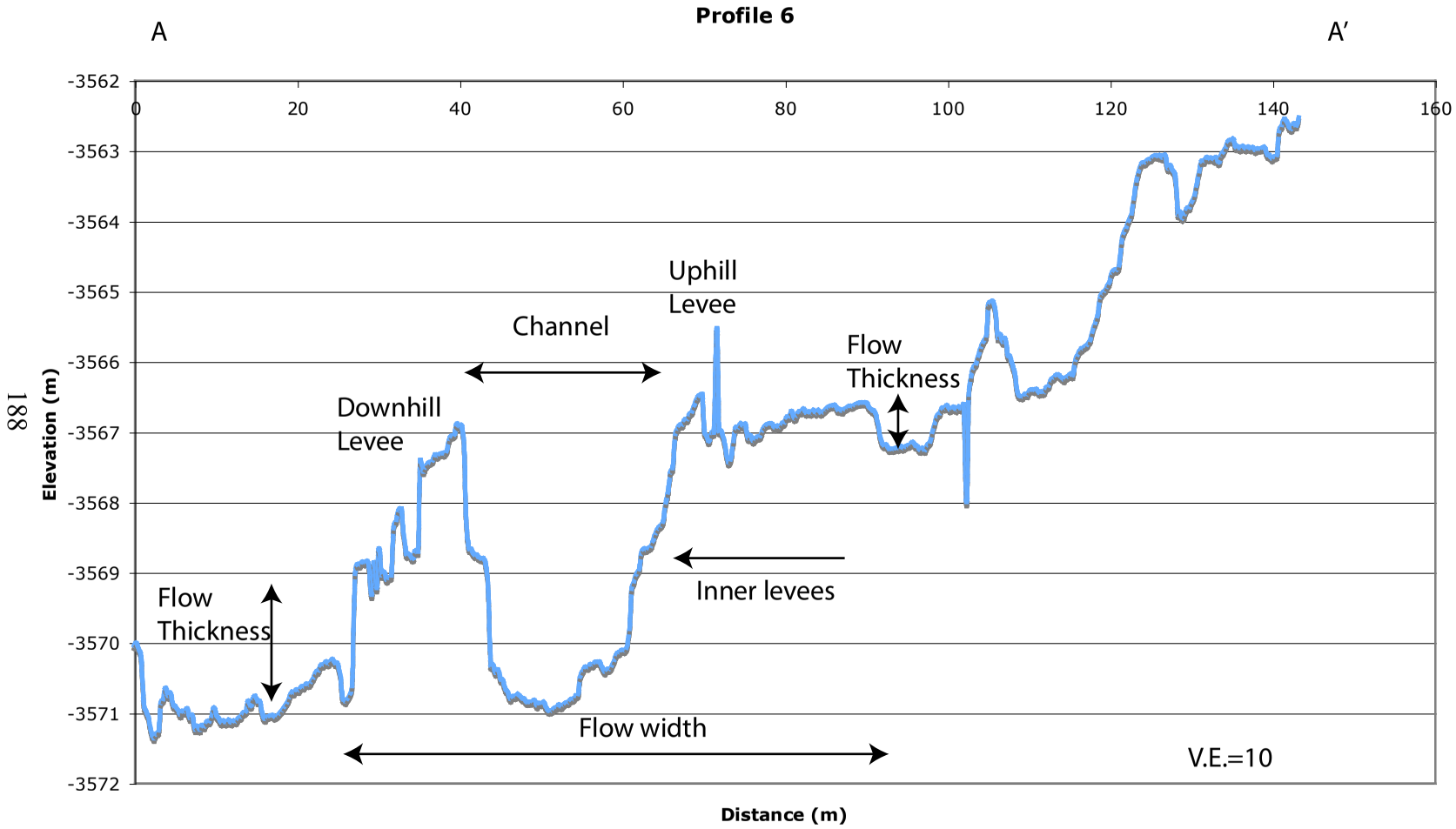
Profile 6
A
A'
-3562
-3563
-3564
-3565
-3566
-3567
-3568
-3569
-3570
-3571
-3572
0
20
40
60
80
100
120
140
160
Elevation (m)
Distance (m)
Uphill
Levee
Channel
Flow
Thickness
Downhill
Levee
Inner levees
Flow
Thickness
Flow width
V.E.=10

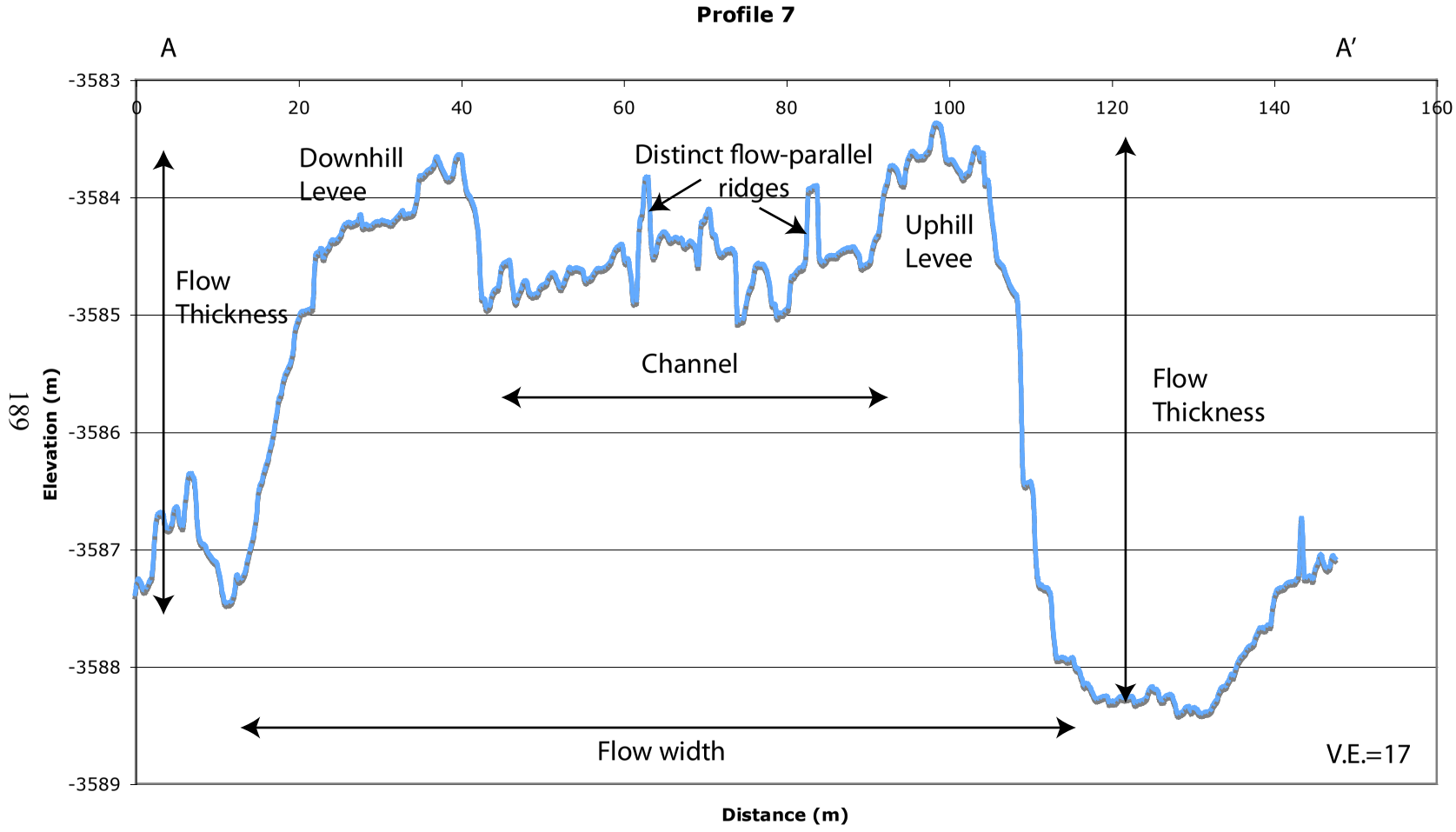
Profile 7
A
A'
-3583
-3584
-3585
-3586
-3587
-3588
-3589
0
20
40
60
80
100
120
140
160
Downhill Levee
Distinct flow-parallel ridges
Uphill Levee
Flow Thickness
Channel
Flow Thickness
Flow width
V.E.=17
Elevation (m)
Distance (m)

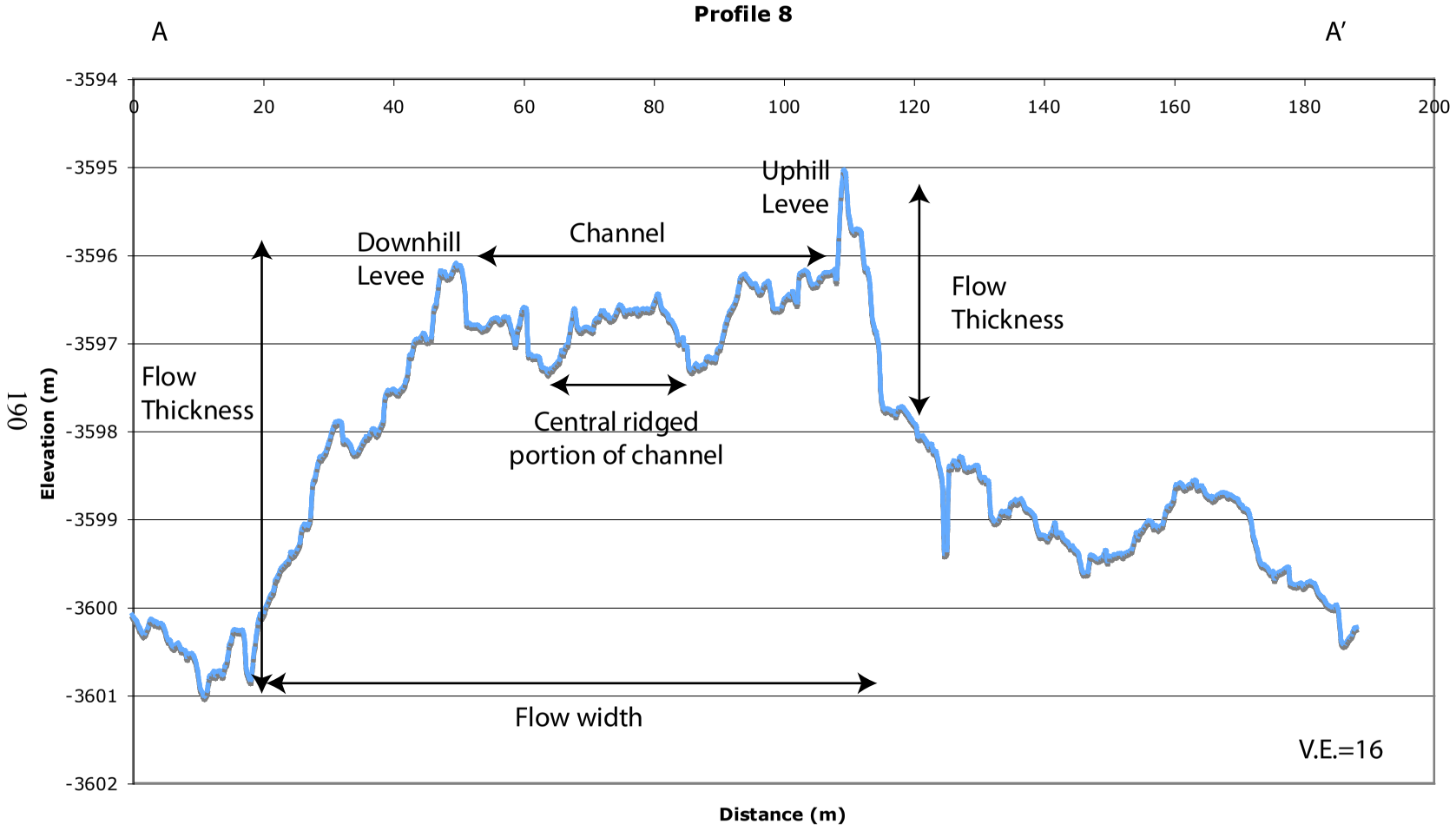
Profile 8
A
A'
-3594
-3595
-3596
-3597
-3598
-3599
-3600
-3601
-3602
0
20
40
60
80
100
120
140
160
180
200
Elevation (m)
Distance (m)
Uphill
Levee
Channel
Downhill
Levee
Flow
Thickness
Flow
Thickness
Central ridged
portion of channel
Flow width
V.E.=16

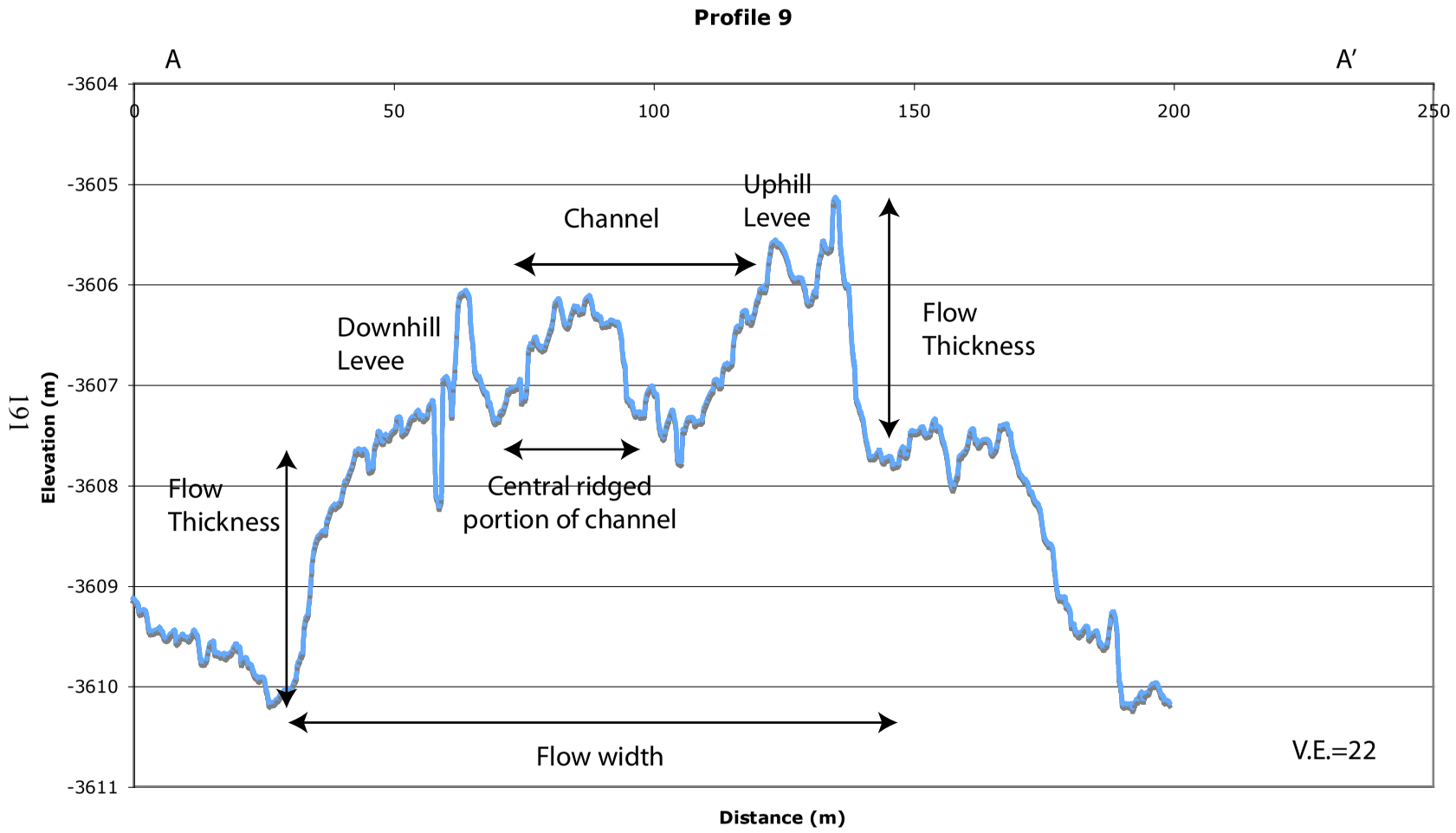
Profile 9
A
A'
-3604
-3605
-3606
-3607
-3608
-3609
-3610
-3611
0
50
100
150
200
250
Elevation (m)
Distance (m)
Channel
Uphill Levee
Downhill Levee
Flow Thickness
Flow Thickness
Central ridged portion of channel
Flow width
V.E.=22

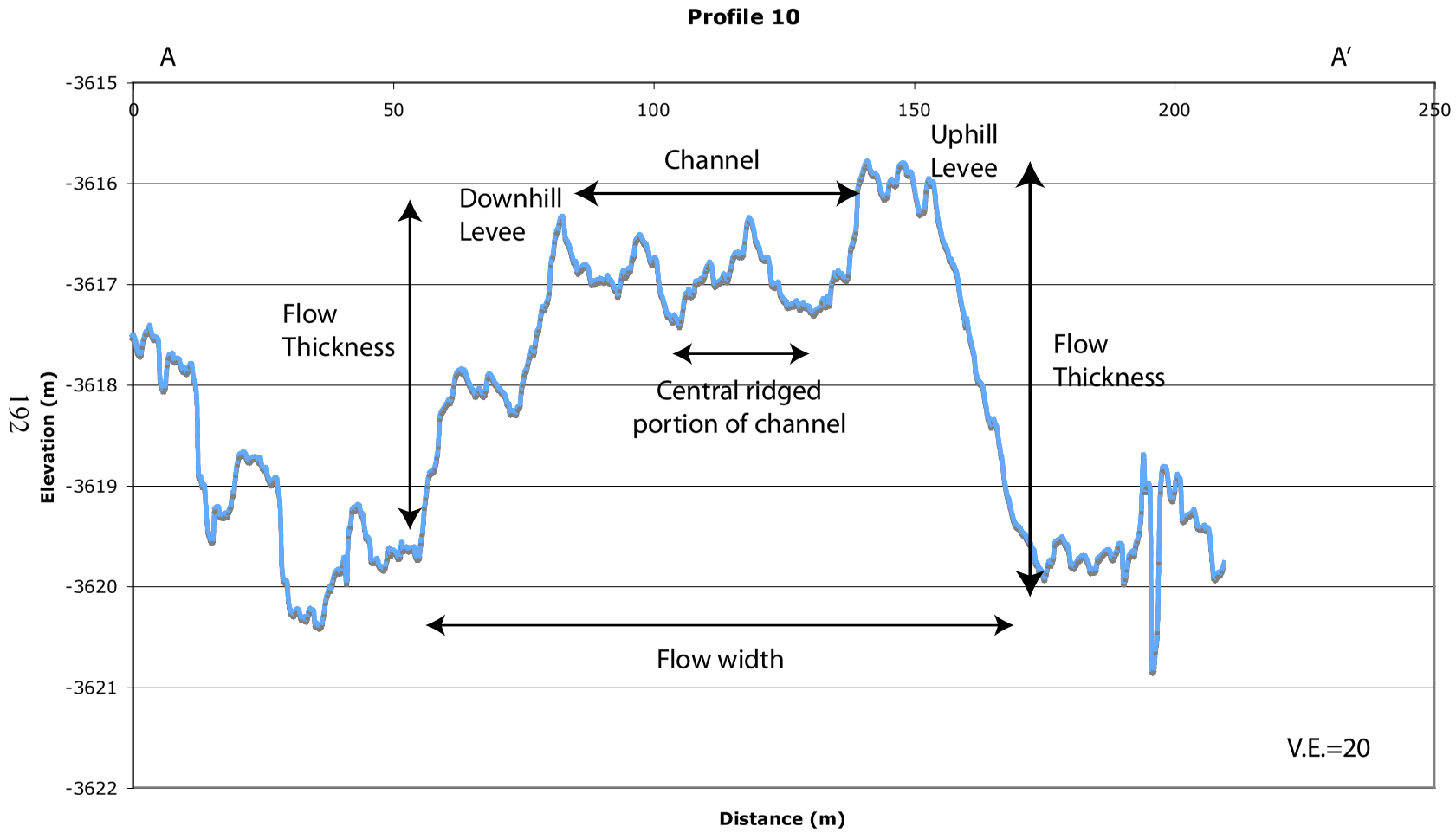
Profile 10
A
A'
-3615
-3616
-3617
-3618
-3619
-3620
-3621
-3622
0
50
100
150
200
250
Channel
Uphill
Levee
Downhill
Levee
Flow
Thickness
Flow
Thickness
Central ridged
portion of channel
Flow width
V.E.=20
Elevation (m)
Distance (m)

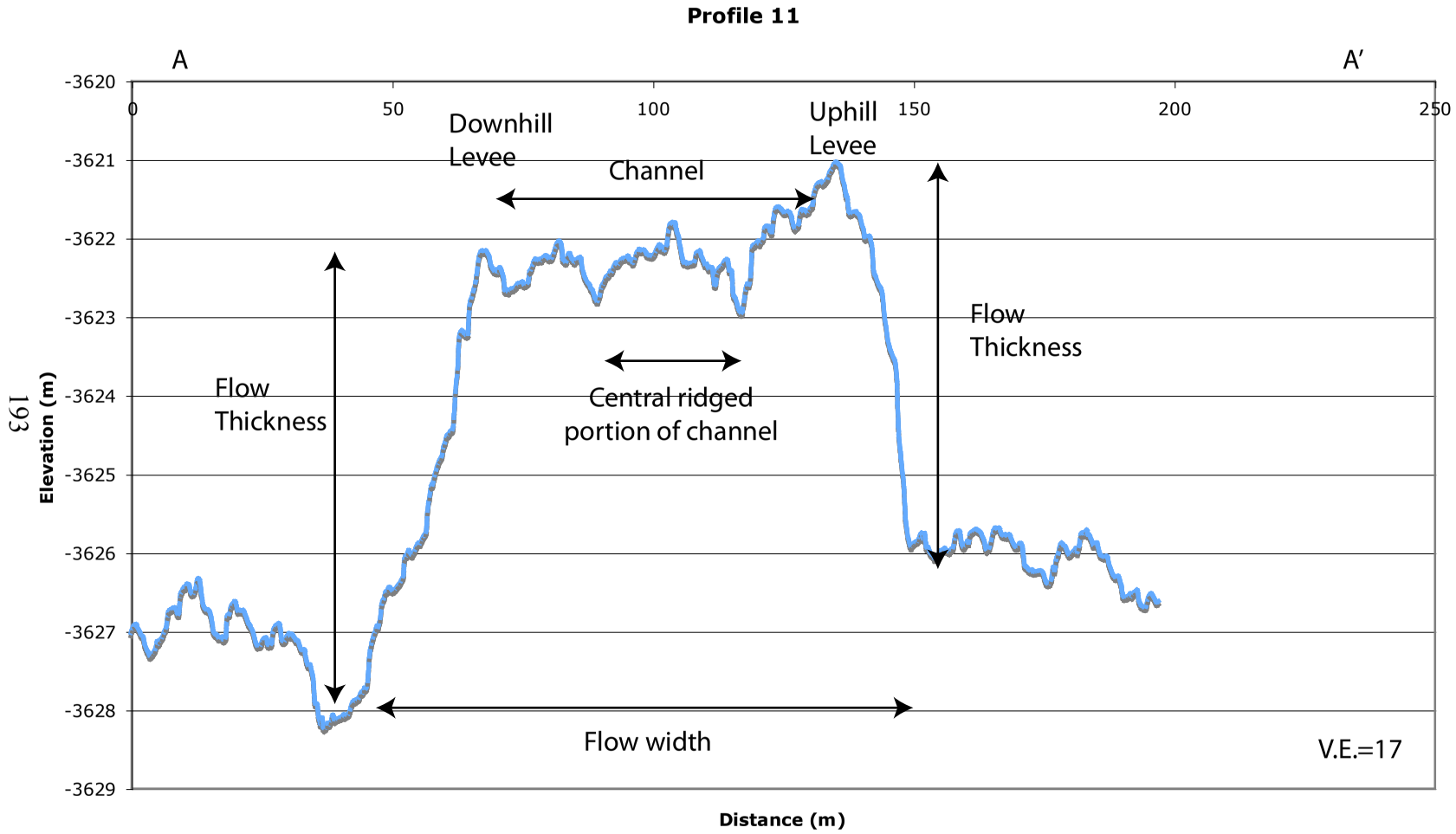
Profile 11
A
A'
-3620
-3621
-3622
-3623
-3624
-3625
-3626
-3627
-3628
-3629
0
50
100
150
200
250
Downhill Levee
Channel
Uphill Levee
Flow Thickness
Central ridged portion of channel
Flow Thickness
Flow width
V.E.=17
Elevation (m)
Distance (m)

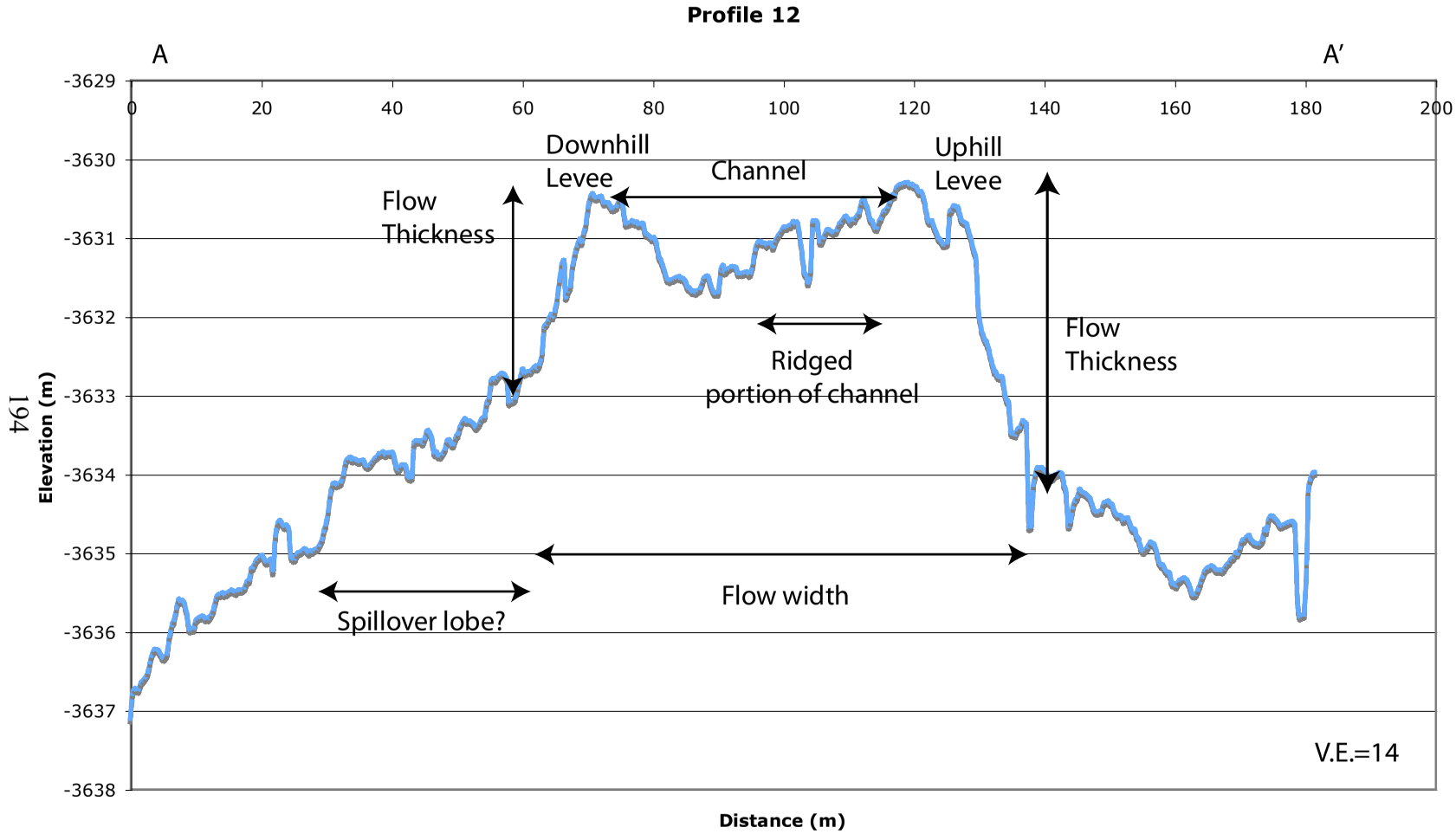
Profile 12
A
A'
-3629
-3630
-3631
-3632
-3633
-3634
-3635
-3636
-3637
-3638
0
20
40
60
80
100
120
140
160
180
200
Downhill Levee
Channel
Uphill Levee
Flow Thickness
Ridged portion of channel
Flow Thickness
Flow width
Spillover lobe?
V.E.=14
Elevation (m)
Distance (m)

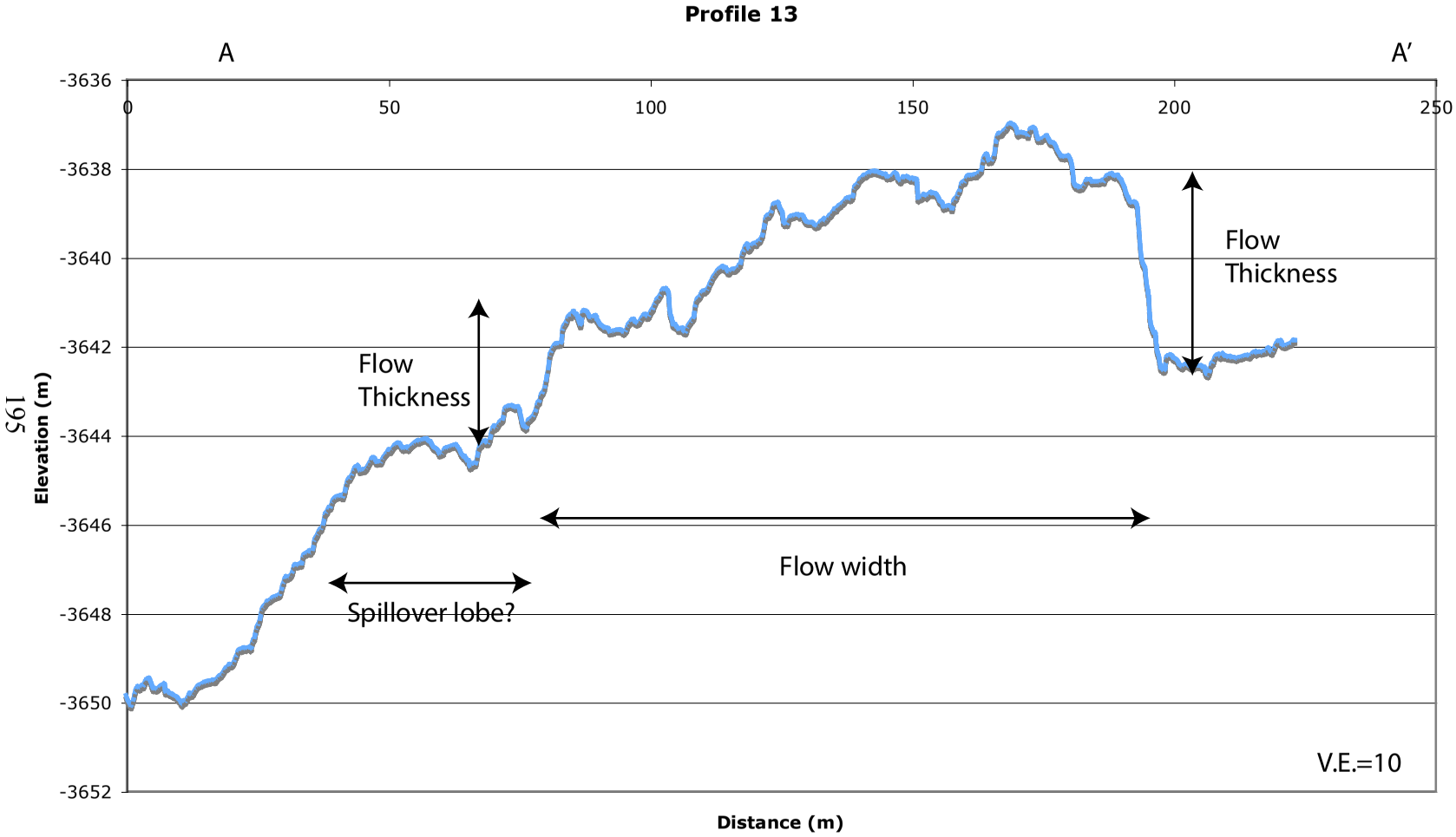
Profile 13
A
A'
-3636
-3638
-3640
-3642
-3644
-3646
-3648
-3650
-3652
0
50
100
150
200
250
Elevation (m)
Distance (m)
Flow
Thickness
Flow
Thickness
Flow width
Spillover lobe?
V.E.=10

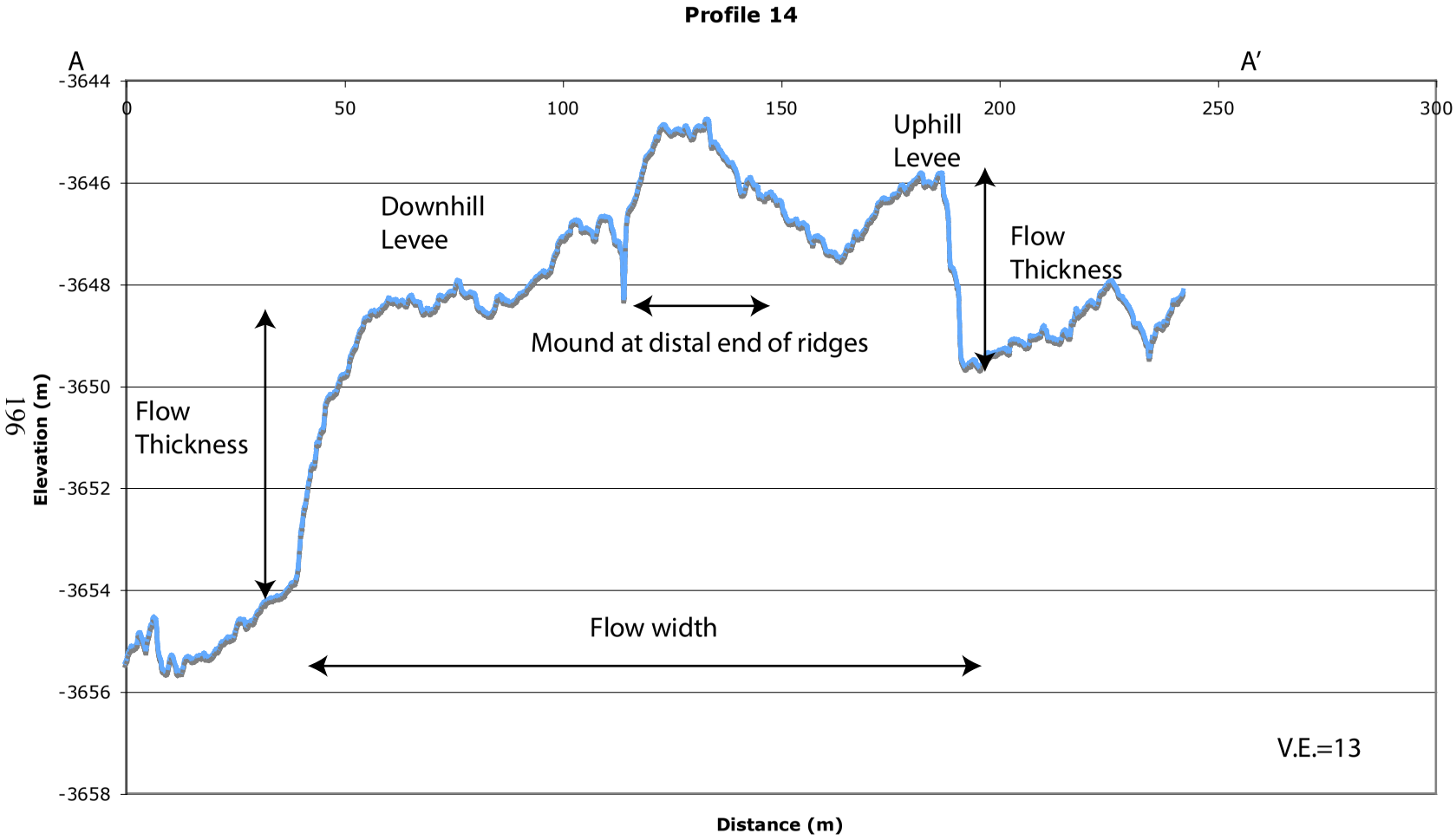
Profile 14
A
A'
-3644
-3646
-3648
-3650
-3652
-3654
-3656
-3658
0
50
100
150
200
250
300
Uphill
Levee
Downhill
Levee
Flow
Thickness
Mound at distal end of ridges
Flow
Thickness
Flow width
V.E.=13
Elevation (m)
Distance (m)

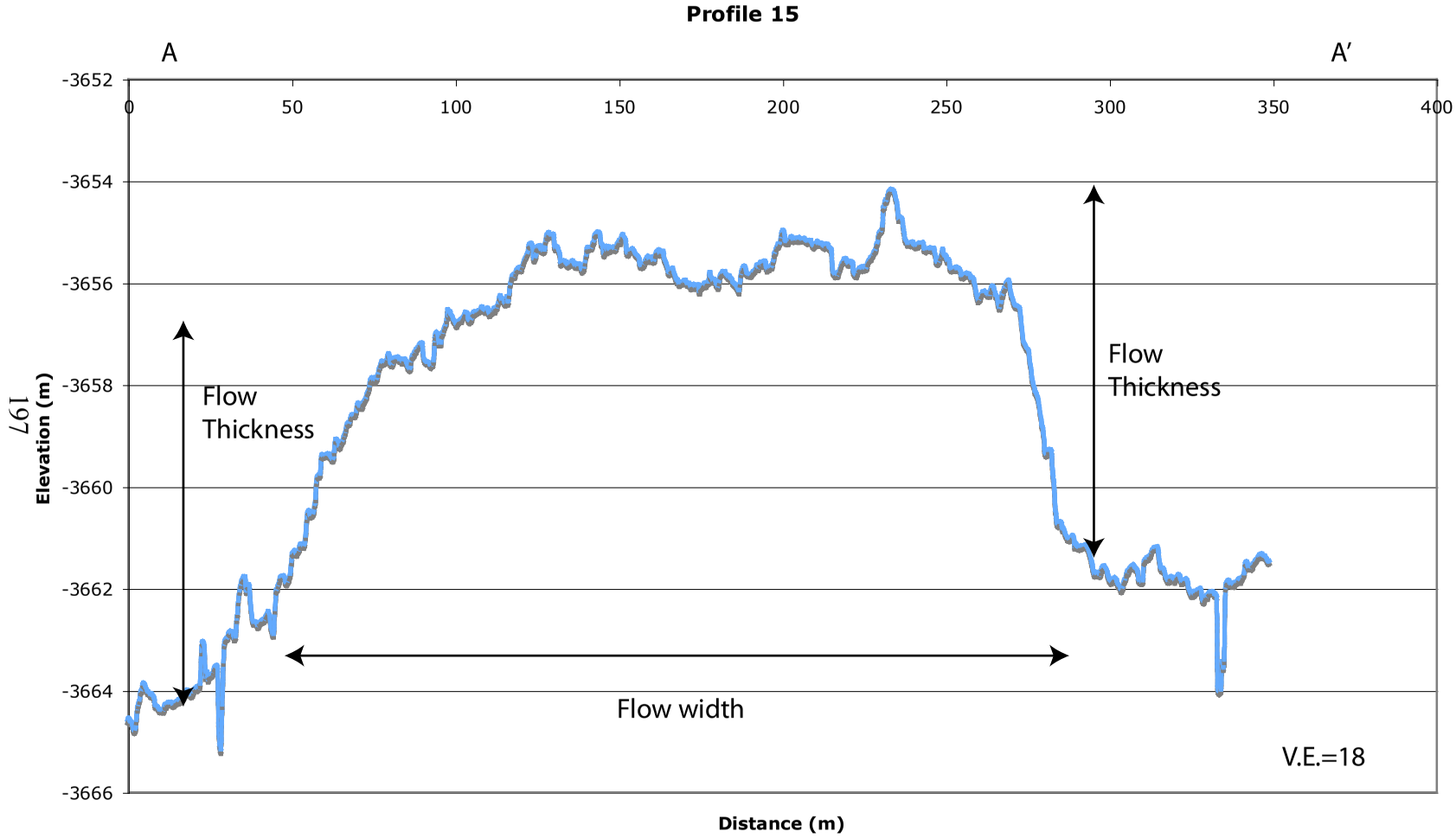
Profile 15
A
A′
-3652
-3654
-3656
-3658
-3660
-3662
-3664
-3666
0
50
100
150
200
250
300
350
400
Elevation (m)
Distance (m)
Flow
Thickness
Flow
Thickness
Flow width
V.E.=18

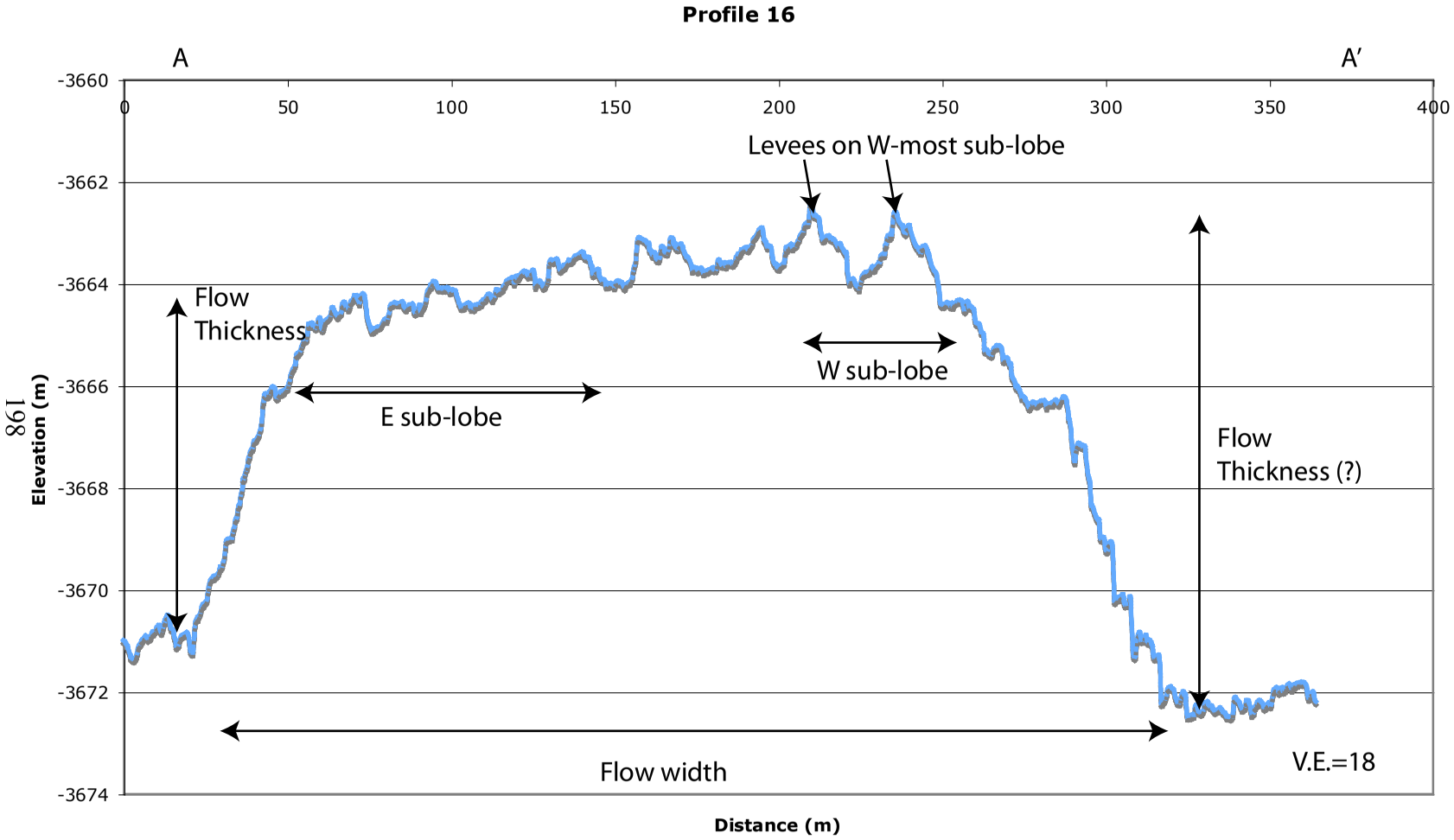
Profile 16
A
A'
-3660
-3662
-3664
-3666
-3668
-3670
-3672
-3674
0
50
100
150
200
250
300
350
400
Levees on W-most sub-lobe
Flow
Thickness
W sub-lobe
E sub-lobe
Flow
Thickness (?)
Flow width
V.E.=18
Elevation (m)
Distance (m)

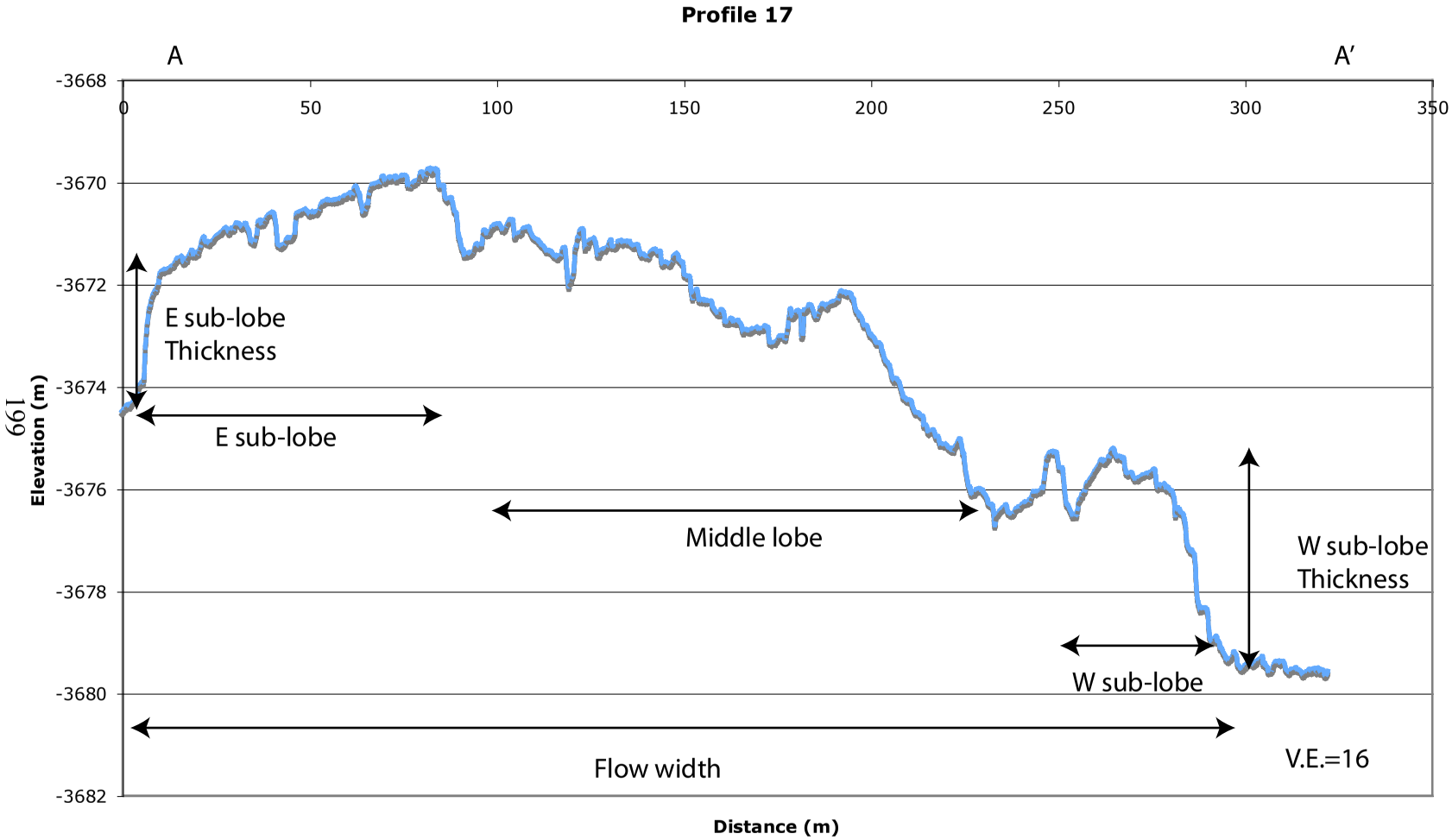
Profile 17
A
A'
-3668
-3670
-3672
-3674
-3676
-3678
-3680
-3682
0
50
100
150
200
250
300
350
E sub-lobe
Thickness
E sub-lobe
Middle lobe
W sub-lobe
Thickness
W sub-lobe
Flow width
V.E.=16
Elevation (m)
Distance (m)

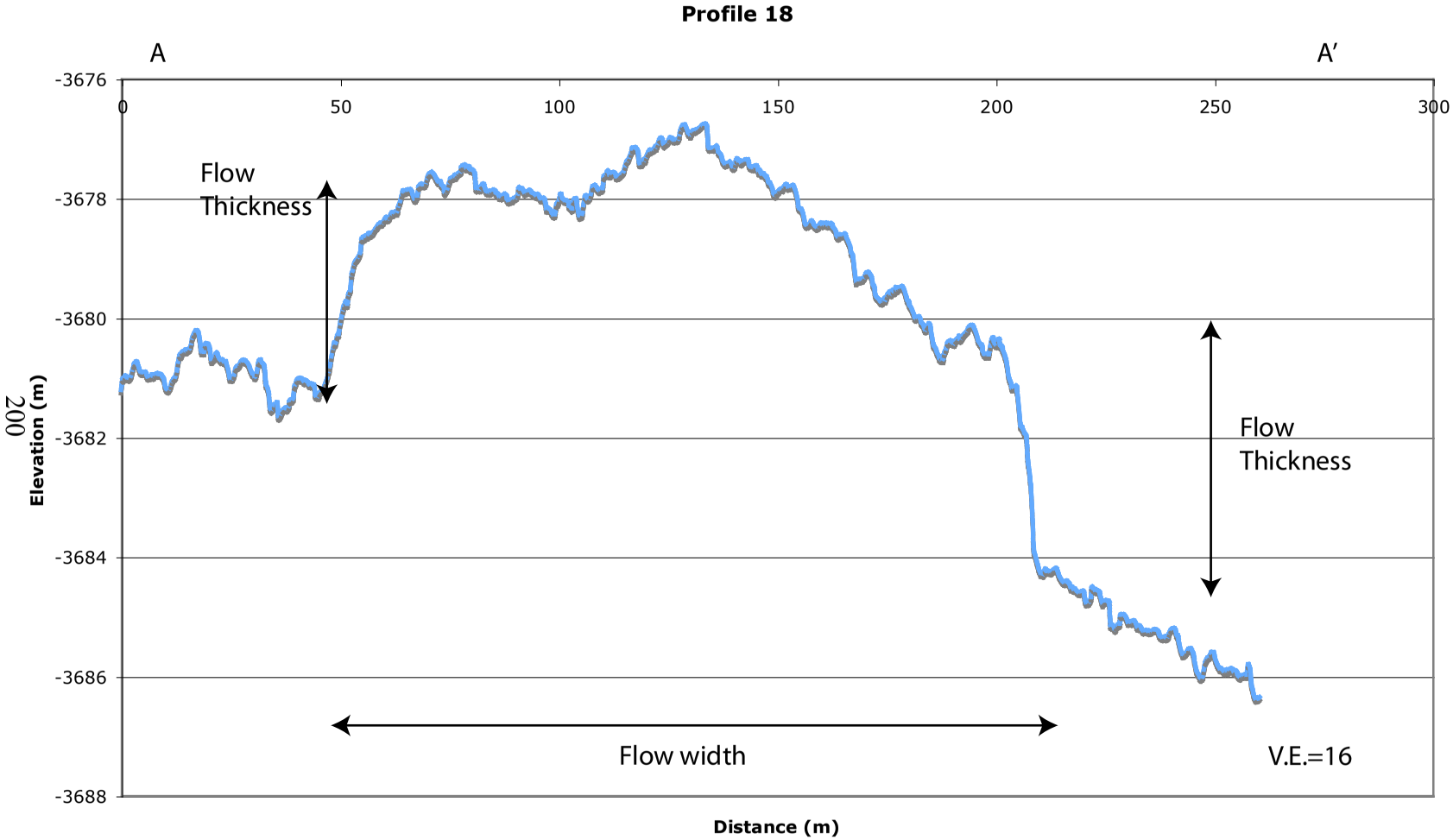
Profile 18
A
A'
-3676
-3678
-3680
-3682
-3684
-3686
-3688
0
50
100
150
200
250
300
Flow
Thickness
Flow
Thickness
Flow width
V.E.=16
Elevation (m)
200
Distance (m)

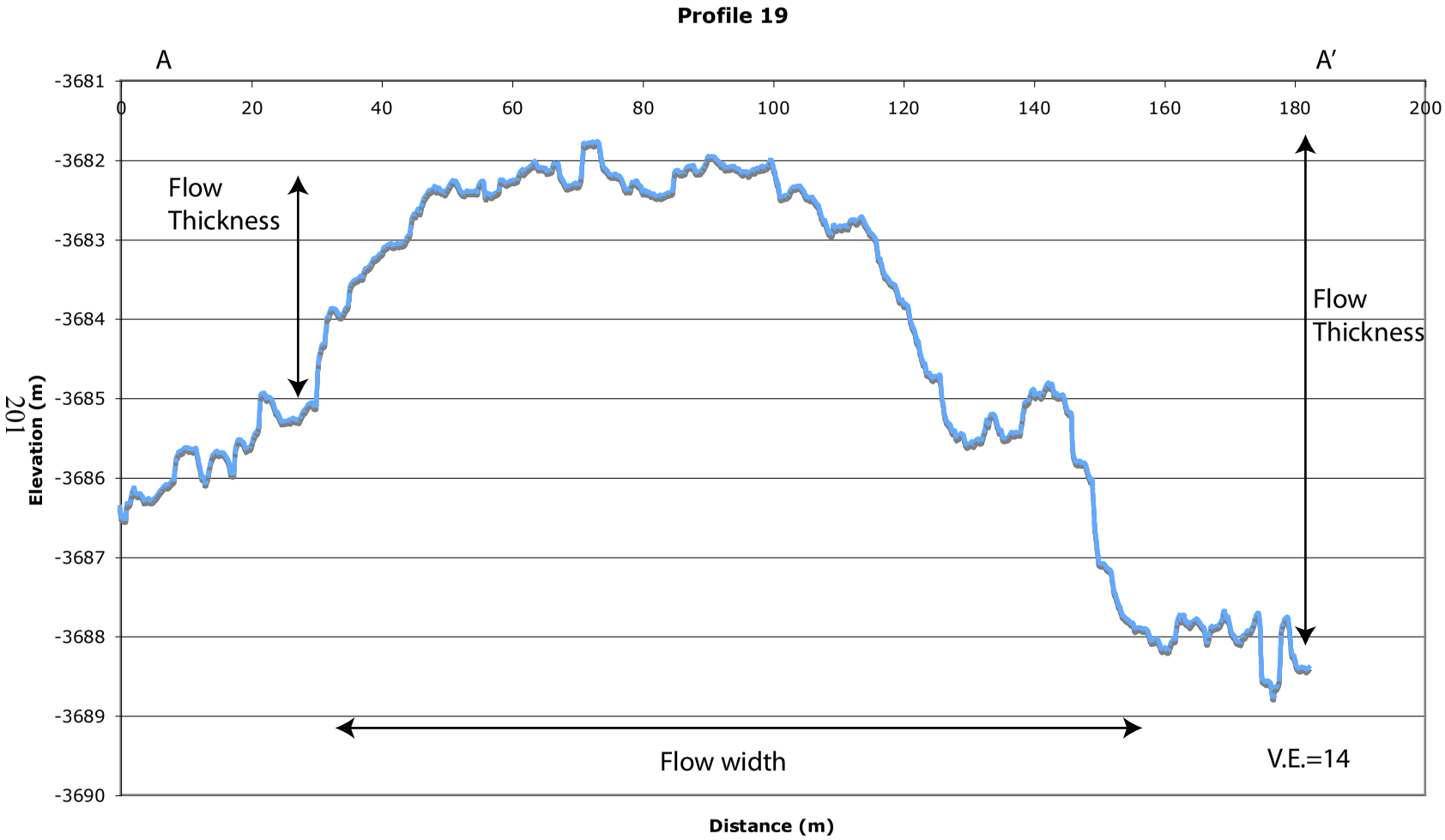
Profile 19
A
A'
-3681
-3682
-3683
-3684
-3685
-3686
-3687
-3688
-3689
-3690
0
20
40
60
80
100
120
140
160
180
200
Flow Thickness
Flow Thickness
Flow width
V.E.=14
Elevation (m)
Distance (m)

201

REFERENCES

Allen, C. C. (1979), Volcano-ice interactions on Mars, Journal of Geophysical Research, 84, 8048-8059.

Anderson, F. S., A. F. C. Haldemann, N. T. Bridges, M. P. Golombek, T. J. Parker, and G. Neumann (2003), Analysis of MOLA data for the Mars Exploration Rover landing sites, Journal of Geophysical Research, 108, doi:10.1029/2003JE002125.

Ansan, V., N. Mangold, P. Masson, E. Gailhardis, and G. Neukum (2008), Topography of valley networks on Mars from Mars Express High Resolution Stereo Camera digital elevation models, Journal of Geophysical Research, 113, doi:10.1029/2007JE002986.

Baker, V. R. (2001), Water and the martian landscape, Nature, 412, 228-236.

Bandfield, J. L., V. E. Hamilton, and P. R. Christensen (2000), A global view of Martian surface compositions from MGS-TES, Science, 287, 1626-1630.

Barlow, N. G., J. M. Boyce, F. M. Costard, R. A. Craddock, J. B. Garvin, S. E. H. Sakimoto, R. O. Kuzmin, D. J. Roddy, and L. A. Soderblom (2000), Standardizing the nomenclature of Martian impact crater ejecta morphologies, Journal of Geophysical Research, 105, 26733-26738.

Barlow, N. G., and C. B. Perez (2003), Martian impact crater ejecta morphologies as indicators of the distribution of subsurface volatiles, Journal of Geophysical Research, 108, doi:10.1029/2002JE002036.

Barnouin-Jha, O. S., and P. H. Schultz (1998), Lobateness of impact ejecta deposits from atmospheric interactions, Journal of Geophysical Research, 103, 25739-25756.

Betts, B. H., and B. C. Murray (1993), Thermally distinct ejecta blankets from Martian craters, Journal of Geophysical Research, 98, 11043-11059.

Boynton, W. V., W. C. Feldman, S. W. Squyres, T. H. Prettyman, J. Bruckner, L. G. Evans, R. C. Reedy, R. Starr, J. R. Arnold, D. M. Drake, P. A. J. Englert, A. E. Metzger, I. Mitrofanov, J. I. Trombka, C. d'Uston, H. Wanke, O. Gasnault, D. K. Hamara, D. M. Janes, R. L. Marcialis, S. Maurice, I. Mikheeva, G. J. Taylor, R. Tokar, and C. Shinohara (2002), Distribution of hydrogen in the near surface of Mars: Evidence for subsurface ice deposits, Science, 297, 81-85.

Brown, S. R., and C. H. Scholz (1985), Broad bandwidth study of the topography of natural rock surfaces, Journal of Geophysical Research, 90, 12,575-12,582.

Butler, J. B., S. N. Lane, and J. H. Chandler (2001), Characterization of the structure of river-bed gravels using two-dimensional fractal analysis, Mathematical Geology, 33, 301-330.

Campbell, B. A., R. R. Ghent, and M. K. Shepard (2003), Limits on inference of Mars small-scale topography from MOLA data, Geophysical Research Letters, 30, doi:10.1029/2002GL016550.

Campbell, B. A., and M. K. Shepard (1996), Lava flow surface roughness and depolarized radar scattering, Journal of Geophysical Research, 101, 18941-18951.

Carr, M. H. (1979), Formation of martian flood features by release of water from confined aquifers, Journal of Geophysical Research, 84, 2995-3007.

Carr, M. H. (1996), Water on Mars, 229 pp., Oxford University Press, New York.

Carr, M. H., and G. D. Clow (1981), Martian channels and valleys: Their characteristics, distribution, and age, Icarus, 48, 91-117.

Carr, M. H., L. S. Crumpler, J. A. Cutts, R. Greeley, J. E. Guest, and H. Masursky (1977), Martian impact craters and emplacement of ejecta by surface flow, Journal of Geophysical Research, 82, 4055-4065.

Cashman, K. V., C. R. Thornber, and J. P. Kauahikaua (1999), Cooling and crystallization of lava in open channels, and the transition of pahoehoe lava to aa, Bulletin of Volcanology, 61, 306-323.

Chapman, M. G., C. C. Allen, M. T. Gudmundsson, V. C. Gulick, S. P. Jakobsson, B. K. Lucchitta, I. P. Skilling, and R. B. Waitt (2000), Volcanism and ice interactions on Earth and Mars, in Environmental Effects on Volcanic Eruptions, edited by J. R. Zimbelman and T. K. P. Gregg, pp. 39-73, Kluwer Academic/ Plenum Publishers, New York.

Christensen, P. R., J. L. Bandfield, J. F. B. III, N. Gorelick, V. E. Hamilton, A. Ivanov, B. M. Jakosky, H. H. Kieffer, M. D. Lane, M. C. Malin, T. McConnochie, A. S. McEwen, J. Harry Y. McSween, G. L. Mehall, J. E. Moersch, K. H. Nealson, J. W. R. Jr., M. I. Richardson, S. W. Ruff, M. D. Smith, T. N. Titus, and M. B. Wyatt (2003), Morphology and composition of the surface of Mars: Mars Odyssey THEMIS results, Science, 300, 2056-2061.

Christensen, P. R., B. M. Jakosky, H. H. Kieffer, M. C. Malin, H. Y. J. McSween, K. H. Nealson, G. L. Mehall, S. H. Silverman, S. Ferry, M. Caplinger, and M. Ravine (2004), The Thermal Emission Imaging System (THEMIS) for the Mars 2001 Odyssey mission, Space Science Reviews, 110, 85-130.

Christiansen, E. H. (1989), Lahars in the Elysium region of Mars, Geology, 17, 203-206.

Christiansen, E. H., and R. Greeley (1981), Mega-lahars (?) in the Elysium Region, Mars, Lunar and Planetary Science Conference, XII, 138-140.

Craddock, R. A., and A. D. Howard (2002), The case for rainfall on a warm, wet early Mars, Journal of Geophysical Research, 107, doi:10.1029/2001JE001505.

De Hon, R. A. (1992), Polygenetic origin of Hrad Vallis region of Mars, Proceedings of Lunar and Planetary Science, 22, 45-51.

De Hon, R. A., P. J. Mouginis-Mark, and E. E. Brick (1999), Geologic map of the Galaxias Quadrangle (MTM 35217) of Mars, Map I-2579, U.S. Geological Survey.

Fagents, S. A., P. Lanagan, and R. Greeley (2002), Rootless cones on Mars: A consequence of lava-ground ice interaction, in Volcano-Ice Interaction on Earth and Mars, edited by J. L. Smellie and M. G. Chapman, pp. 295-317, Geological Society of London, London.

Gaddis, L. R., P. J. Mouginis-Mark, and J. N. Hayashi (1990), Lava flow surface textures: SIR-B radar image texture, field observations, and terrain measurements, Photogrammetric Engineering and Remote Sensing, 56, 211-224.

Garvin, J. B., and J. J. Frawley (1998), Geometric properties of Martian impact craters: Preliminary results from the Mars Orbiter Laser Altimeter, Geophysical Research Letters, 25, 4405-4408.

Glaze, L. S., and S. M. Baloga (2006), Rheologic inferences from the levees of lava flows on Mars, Journal of Geophysical Research, 111, doi:10.1029/2005JE002585.

Glaze, L. S., and S. M. Baloga (2007), Topographic variability on Mars: Implications for lava flow modeling, Journal of Geophysical Research, 112, doi:10.1029/2006JE002879.

Goff, J. A. (1990), "Fractal mapping of digitized images: Application to the topography of Arizona and comparison with synthetic images" by J. Huang and D. L. Turcotte, comment and reply, Journal of Geophysical Research, 95, 5159-5161.

Golombek, M. P., J. A. Grant, T. J. Parker, D. M. Kass, J. A. Crisp, S. W. Squyres, A. F. C. Haldemann, M. Adler, W. J. Lee, N. T. Bridges, R. E. Arvidson, M. H. Carr, R. L. Kirk, P. C. Knocke, R. B. Roncoli, C. M. Weitz, J. T. Schofield, R. W. Zurek, P. R. Christensen, R. L. Fergason, F. S. Anderson, and J. W. Rice Jr. (2003), Selection of the Mars Exploration Rover landing sites, Journal of Geophysical Research, 108, doi:10.1029/2003JE002074.

Greeley, R., and S. A. Fagents (2001), Icelandic pseudocraters as analogs to some volcanic cones on Mars, Journal of Geophysical Research, 106, 20527-20564.

Greeley, R., and J. E. Guest (1987), Geologic map of the eastern equatorial region of Mars, Map I-1802-B, United States Geological Survey.

Gulick, V. C., and V. R. Baker (1989), Fluvial valleys and martian paleoclimates, Nature, 341, 514-516.

Hamilton, V. E., P. R. Christensen, H. Y. J. McSween, and J. L. Bandfield (2003), Searching for the source regions of martian meteorites using MGS TES: Integrating martian meteorites into the global distribution of igneous materials on Mars, Meteoritics & Planetary Science, 38, 871-885.

Hartmann, W. K. (2005), Martian cratering 8: Isochron refinement and the chronology of Mars, Icarus, 174, 294-320.

Hawke, B. R., and J. W. Head (1977), Impact melt on lunar crater rims, in Impact and Explosion Cratering, edited by D. J. Roddy, R. O. Pepin and R. B. Merrill, pp. 815-841, Pergamon Press, New York.

Head, J. W., J. F. Mustard, M. A. Kreslavsky, R. E. Milikken, and D. R. Marchant (2003), Recent ice ages on Mars, Nature, 426, 797-802.

Heather, D. J., and S. K. Dunkin (2003), Geology and stratigraphy of King crater, lunar farside, Icarus, 163, 307-329.

Hort, M., and C. M. Weitz (2001), Theoretical modeling of eruption plumes on Mars under current and past climates, Journal of Geophysical Research, 106, 20547-20562.

Hovland, M., A. Hill, and D. Stokes (1997), The structure and geomorphology of the Dashgil mud volcano, Azerbaijan, Geomorphology, 21, 1-15.

Howard, K. A. (1975), Geologic map of the crater Copernicus, Map I-840, United States Geological Survey.

Ivanov, M. A., and J. W. Head (2001), Chryse Planitia, Mars: Topographic configuration, outflow channel continuity and sequence, and tests for hypothesized ancient bodies of water using Mars Orbiter Laser Altimeter (MOLA), Journal of Geophysical Research, 106, 3275-3295.

Iverson, R. M. (1997), The physics of debris flows, Reviews of Geophysics, 35, 245-296.

Kauahikaua, J., D. R. Sherrod, K. V. Cashman, C. Heliker, K. Hon, T. N. Mattox, and J. A. Johnson (2003), Hawaiian lava-flow dynamics during the Pu'u 'O'o-Kupaianaha Eruption: A tale of two decades, in The Pu'u 'O'o-Kupaianaha Eruption of Kilauea Volcano, Hawaii: The First 20 Years, edited by C. Heliker, D. A. Swanson and T. J. Takahashi, pp. 63-87, US Geological Survey Professional Paper 1676.

Kieffer, S. W., and C. H. Simonds (1980), The role of volatiles and lithology in the impact cratering process, Reviews of Geophysics, 18, 143-181.

Kilburn, C. R. J. (2000), Lava flows and flow fields, in Encyclopedia of Volcanoes, edited by H. Sigurdsson, B. Houghton, S. R. McNutt, H. Rymer and J. Stix, pp. 291-305, Academic Press, San Diego.

Konhauser, K. O., P. Schiffman, and Q. J. Fisher (2002), Microbial mediation of authigenic clays during hydrothermal alteration of basaltic tephra, Kilauea Volcano, Geochemistry, Geophysics, Geosystems, 3, 1075, doi:1010.1029/2002GC000317.

Kreslavsky, M. A., and J. W. Head (2000), Kilometer-scale roughness of Mars: Results from MOLA data analysis, Journal of Geophysical Research, 105, 26695-26711.

Lescinsky, D. T., S. V. Skoblenick, and L. Mansinha (2007), Automated identification of lava flow structures using local Fourier spectrum of digital elevation data, Journal of Geophysical Research, 112, doi:10.1029/2006JB004263.

Li, R., B. A. Archinal, R. Arvidson, J. Bell, P. R. Christensen, L. S. Crumpler, D. J. Des Marais, K. Di, T. C. Duxbury, M. Golombek, J. A. Grant, R. Greeley, J. Guinn, A. Johnson, R. L. Kirk, M. Maimone, L. H. Matthies, M. C. Malin, T. Parker, M. Sims, S. Thompson, S. W. Squyres, and L. A. Soderblom (2006), Spirit rover localization and topographic mapping at the landing site of Gusev crater, Mars, Journal of Geophysical Research, 111, doi:10.1029/2005JE002483.

Li, R., R. Arvidson, K. Di, M. Golombek, J. Guinn, A. Johnson, M. Maimone, L. H. Matthies, M. Malin, T. Parker, S. W. Squyres, and W. A. Watters (2007), Opportunity rover localization and topographic mapping at the landing site of Meridiani Planum, Mars, Journal of Geophysical Research, 112, doi:10.1029/2006JE002776.

Major, J. J. (1997), Depositional processes in large-scale debris-flow experiments, Journal of Geology, 105, 345-366.

Malin, M. C., J. F. Bell III, B. A. Cantor, M. A. Caplinger, W. M. Calvin, R. T. Clancy, K. S. Edgett, L. Edwards, R. M. Haberle, P. B. James, S. W. Lee, M. A. Ravine, P. C. Thomas, and M. J. Wolff (2007), Context camera investigation on board the Mars Reconnaissance Orbiter, Journal of Geophysical Research, 112, doi:10.1029/2006JE002808.

Malin, M. C., G. E. Danielson, A. P. Ingersoll, H. Masursky, J. Veverka, M. A. Ravine, and T. A. Soulanille (1992), The Mars Observer Camera, Journal of Geophysical Research, 97, 7699-7718.

Malin, M. C., and K. S. Edgett (2000), Evidence for recent groundwater seepage and surface runoff on Mars, Science, 288, 2330-2335.

Malin, M. C., and K. S. Edgett (2003), Evidence for persistent flow and aqueous sedimentation on early Mars, Science, 302, 1931-1933.

Malin, M. C., K. S. Edgett, L. V. Posiolova, S. M. McColley, and E. Z. Noe Dobrea (2006), Present-day impact cratering rate and contemporary gully activity on Mars, Science, 314, 1573-1577.

Mandelbrot, B. B. (1982), The Fractal Geometry of Nature, W. H. Freeman, New York.

McEwen, A. S., E. M. Eliason, J. W. Bergstrom, N. T. Bridges, C. J. Hansen, W. A. Delamere, J. A. Grant, V. C. Gulick, K. E. Herkenhoff, L. Keszthelyi, R. L. Kirk, M. T. Mellon, S. W. Squyres, N. Thomas, and C. M. Weitz (2007a), Mars Reconnaissance Orbiter's High Resolution Imaging Science Experiment (HiRISE), Journal of Geophysical Research, 112, doi:10.1029/2005JE002605.

McEwen, A. S., C. J. Hansen, W. A. Delamere, E. M. Eliason, K. E. Herkenhoff, L. Keszthelyi, V. C. Gulick, R. L. Kirk, M. T. Mellon, J. A. Grant, N. Thomas, C. M. Weitz, S. W. Squyres, N. T. Bridges, S. L. Murchie, F. Seelos, K. Seelos, C. H. Okubo, M. P. Milazzo, L. L. Tornabene, W. L. Jaeger, S. Byrne, P. S. Russell, J. L. Griffes, S. Martinez-Alonso, A. Davatzes, F. C. Chuang, B. J. Thomson, K. E. Fishbaugh, C. M. Dundas, K. J. Kolb, M. E. Banks, and J. J. Wray (2007b), A closer look at water-related geologic activity on Mars, Science, 317, doi:10.1126/science.1143987.

McSween, H. Y. J., R. E. Arvidson, J. F. Bell III, D. Blaney, N. A. Cabrol, P. R. Christensen, B. C. Clark, J. A. Crisp, L. S. Crumpler, D. J. Des Marais, J. D.

Farmer, R. Gellert, A. Ghosh, S. Gorevan, T. Graff, J. A. Grant, L. A. Haskin, K. E. Herkenhoff, J. R. Johnson, B. L. Jolliff, G. Klingelhoefer, A. T. Knudson, S. McLennan, K. A. Milam, J. E. Moersch, R. V. Morris, R. Rieder, S. W. Ruff, P. A. J. de Souza, S. W. Squyres, H. Wanke, A. Wang, M. B. Wyatt, A. Yen, and J. Zipfel (2004), Basaltic rocks analyzed by the Spirit Rover in Gusev Crater, Science, 305, 842-845.

Melosh, H. J. (1989), Impact Cratering, 245 pp., Oxford University Press, New York.

Minitti, M. E., C. M. Weitz, M. D. Lane, and J. L. Bishop (2007), Morphology, chemistry, and spectral properties of Hawaiian rock coatings and implications for Mars, Journal of Geophysical Research, 112, doi:10.1029/2006JE002839.

Morrissey, M. M., and L. G. Mastin (2000), Vulcanian eruptions, in Encyclopedia of Volcanoes, edited by H. Sigurdsson, B. Houghton, S. R. McNutt, H. Rymer and J. Stix, pp. 463-475, Academic Press, San Diego.

Mouginis-Mark, P. J. (1979), Martian fluidized crater morphology: Variations with crater size, latitude, altitude and target material, Journal of Geophysical Research, 84, 8011-8022.

Mouginis-Mark, P. J. (1981), Ejecta emplacement and modes of formation of martian fluidized ejecta craters, Icarus, 45, 60-76.

Mouginis-Mark, P. J. (1985), Volcano/ground ice interactions in Elysium Planitia, Mars, Icarus, 64, 265-284.

Mouginis-Mark, P. J. (1987), Water or ice in the Martian regolith?: Clues from rampart craters seen at very high resolution, Icarus, 71, 268-286.

Mouginis-Mark, P. J., and P. R. Christensen (2005), New observations of volcanic features on Mars from the THEMIS instrument, Journal of Geophysical Research, 110, doi:10.1029/2005JE002421.

Mouginis-Mark, P. J., and H. Garbeil (2005), Quality of TOPSAR topographic data for volcanology studies at Kilauea Volcano, Hawaii: An assessment using airborne lidar data, Remote Sensing of Environment, 96, 149-164.

Mouginis-Mark, P. J., and H. Garbeil (2007), Crater geometry and ejecta thickness of the Martian impact crater Tooting, Meteoritics & Planetary Science, 42, 1615-1625.

Mouginis-Mark, P. J., L. L. Tornabene, J. M. Boyce, and A. S. McEwen (2007), Impact melt and water release at Tooting Crater, Mars, in Seventh International Conference on Mars, edited, Lunar and Planetary Institute Contribution No. 1353, Pasadena, California.

Mouginis-Mark, P. J., L. Wilson, J. W. Head, S. H. Brown, J. L. Hall, and K. D. Sullivan (1984), Elysium Planitia, Mars: regional geology, volcanology, and evidence for volcano-ground ice interactions, Earth, Moon and Planets, 30, 149-173.

Mouginis-Mark, P. J., L. Wilson, and M. T. Zuber (1992), The physical volcanology of Mars, in Mars, edited by H. H. Kieffer, B. M. Jakosky, C. W. Snyder and M. S. Matthews, pp. 424-452, The University of Arizona Press, Tucson.

Okubo, C. H., and A. S. McEwen (2007), Fracture-controlled paleo-fluid flow in Candor Chasma, Mars, Science, 315, 983-985.

Orosei, R., R. Bianchi, A. Coradini, S. Espinasse, C. Federico, A. Ferriccioni, and A. I. Gavrishin (2003), Self-affine behavior of Martian topography at kilometer scale from Mars Orbiter Laser Altimeter data, Journal of Geophysical Research, 108, doi:10.1029/2002JE001883.

Osinski, G. R. (2006), Effect of volatiles and target lithology on the generation and emplacement of impact crater fill and ejecta deposits on Mars, Meteoritics & Planetary Science, 41, 1571-1586.

Osinski, G. R., R. A. F. Grieve, and J. G. Spray (2004), The nature of the groundmass of surficial suevites from the Ries impact structure, Germany, and constraints on its origin, Meteoritics & Planetary Science, 39, 1655-1684.

Pelletier, J. D., K. J. Kolb, A. S. McEwen, and R. L. Kirk (2008), Recent bright gully deposits on Mars: Wet or dry flow?, Geology, 36, 211-214.

Plescia, J. B. (2004), Morphometric properties of Martian volcanoes, Journal of Geophysical Research, 109, doi:10.1029/2002JE002031.

Rowland, S. K., M. E. MacKay, H. Garbeil, and P. J. Mouginis-Mark (1999), Topographic analyses of Kilauea Volcano, Hawaii, from interferometric airborne radar, Bulletin of Volcanology, 61, 1-14.

Rowland, S. K., and G. P. Walker (1990), Pahoehoe and aa in Hawaii: Volumetric flow rate controls the lava structure, Bulletin of Volcanology, 52, 615-628.

Russell, P. S., and J. W. Head (2003), Elysium-Utopia flows as mega-lahars: A model of dike intrusion, cryosphere cracking, and water-sediment release, Journal of Geophysical Research, 108, doi:10.1029/2002JE001995.

Sayles, R. S., and T. R. Thomas (1978), Surface topography as a nonstationary random process, Nature, 271, 431-434.

Schultz, P. H., and D. E. Gault (1979), Atmospheric effects on martian ejecta emplacement, Journal of Geophysical Research, 84, 7669-7687.

Scott, D. H., and K. L. Tanaka (1986), Geologic map of the western equatorial region of Mars, Map I-1802-A, United States Geological Survey.

Self, S., J. Kienle, and J.-P. Huot (1980), Ukinrek Maars, Alaska, II. Deposits and formation of the 1977 craters, Journal of Volcanology and Geothermal Research, 7, 39-65.

Shepard, M. K., R. A. Brackett, and R. E. Arvidson (1995), Self-affine (fractal) topography: Surface parameterization and radar scattering, Journal of Geophysical Research, 100, 11709-11718.

Shepard, M. K., and B. A. Campbell (1999), Radar scattering from a self-affine fractal surface: Near-nadir regime, Icarus, 141, 156-171.

Shepard, M. K., B. A. Campbell, M. H. Bulmer, T. G. Farr, L. R. Gaddis, and J. J. Plaut (2001), The roughness of natural terrain: A planetary and remote sensing perspective, Journal of Geophysical Research, 106, 32777-32795.

Strom, R. G., S. K. Croft, and N. G. Barlow (1992), The martian impact cratering record, in Mars, edited by H. H. Kieffer, B. M. Jakosky, C. W. Snyder and M. S. Matthews, pp. 383-423, The University of Arizona Press, Tucson.

Summerfield, M. A. (1991), Global Geomorphology, 537 pp., John Wiley & Sons, Inc., New York.

Tanaka, K. L., and D. H. Scott (1987), Geologic map of the polar regions of Mars, Map I-1802-C, United States Geological Survey.

Tanaka, K. L., J. A. Skinner, and T. M. Hare (2005), Geologic map of the northern plains of Mars, Miscellaneous Investigations Map I-2888, U.S. Geological Survey.

Thompson, T. W., and H. J. Moore (1989), A model for depolarized radar echoes from Mars, in Lunar and Planetary Science Conference 19, edited, pp. 1199-1200, Lunar and Planetary Institute, Houston, TX.

Tornabene, L. L., A. S. McEwen, G. R. Osinski, P. J. Mouginis-Mark, J. M. Boyce, R. M. E. Williams, J. J. Wray, J. A. Grant, and the HiRISE Team (2007), Impact melting and the role of subsurface volatiles: Implications for the formation of valley networks and phyllosilicate-rich lithologies on early Mars, Abstract #3288, in Seventh International Conference on Mars, edited, Lunar and Planetary Science Institute Contribution No. 1353, Pasadena, California.

Tornabene, L. L., J. E. Moersch, H. Y. J. McSween, A. S. McEwen, J. L. Piatek, K. A. Milam, and P. R. Christensen (2006), Identification of large (2-10 km) rayed craters on Mars in THEMIS thermal infrared images: Implications for possible Martian meteorite source regions, Journal of Geophysical Research, 111, doi:10.1029/2005JE002600.

Turcotte, D. L. (1992), Fractals and Chaos in Geology and Geophysics, Cambridge University Press, New York.

Vergniolle, S., and M. Mangan (2000), Hawaiian and Strombolian eruptions, in Encyclopedia of Volcanoes, edited by H. Sigurdsson, B. Houghton, S. R. McNutt, H. Rymer and J. Stix, pp. 447-461, Academic Press, San Diego.

Ward, W. R. (1992), Long-term orbital and spin dynamics of Mars, in Mars, edited by H. H. Kieffer, B. M. Jakosky, C. W. Snyder and M. S. Matthews, pp. 298-320, The University of Arizona Press, Tucson.

Wilhelms, D. E. (1987), The Geologic History of the Moon, 302 pp., United States Geological Survey, Washington, DC.

Williams, R. M. E., K. S. Edgett, and M. C. Malin (2004), Young fans in an equatorial crater in Xanthe Terra, Mars, paper presented at Lunar and Planetary Science XXXV, Lunar and Planetary Institute, Houston, Texas.

Williams, R. M. E., and M. C. Malin (2008), Sub-kilometer fans in Mojave Crater, Mars, Icarus, in press.

Wilson, L., and J. W. Head (1981), Morphology and rheology of pyroclastic flows and their deposits, and guidelines for future observations, in The 1980 Eruptions of Mount St. Helens, Washington, USGS Professional Paper 1250, edited by P. W.

Lipman and D. R. Mullineaux, United States Geological Survey, Washington, D.C.

Wilson, L., and P. J. Mouginis-Mark (2003), Phreatomagmatic explosive origin of Hrad Vallis, Mars, Journal of Geophysical Research, 108, doi:10,1029/2002JE001927.

Zuber, M. T., D. E. Smith, S. C. Solomon, D. O. Muhleman, J. W. Head, J. B. Garvin, J. B. Abshire, and J. L. Bufton (1992), The Mars Observer Laser Altimeter investigation, Journal of Geophysical Research, 97, 7781-7797.